Quasicrystal Growth Mechanisms and Generalized Defect Detection in Crystals

by

Kelly L. Wang

A dissertation submitted in partial fulfillment
of the requirements for the degree of
Doctor of Philosophy
(Macromolecular Science and Engineering)
in the University of Michigan
2024

Doctoral Committee:

Professor Sharon C. Glotzer, Chair
Associate Professor Ashwin Shahani
Professor Michael J. Solomon
Assistant Professor Wenhao Sun

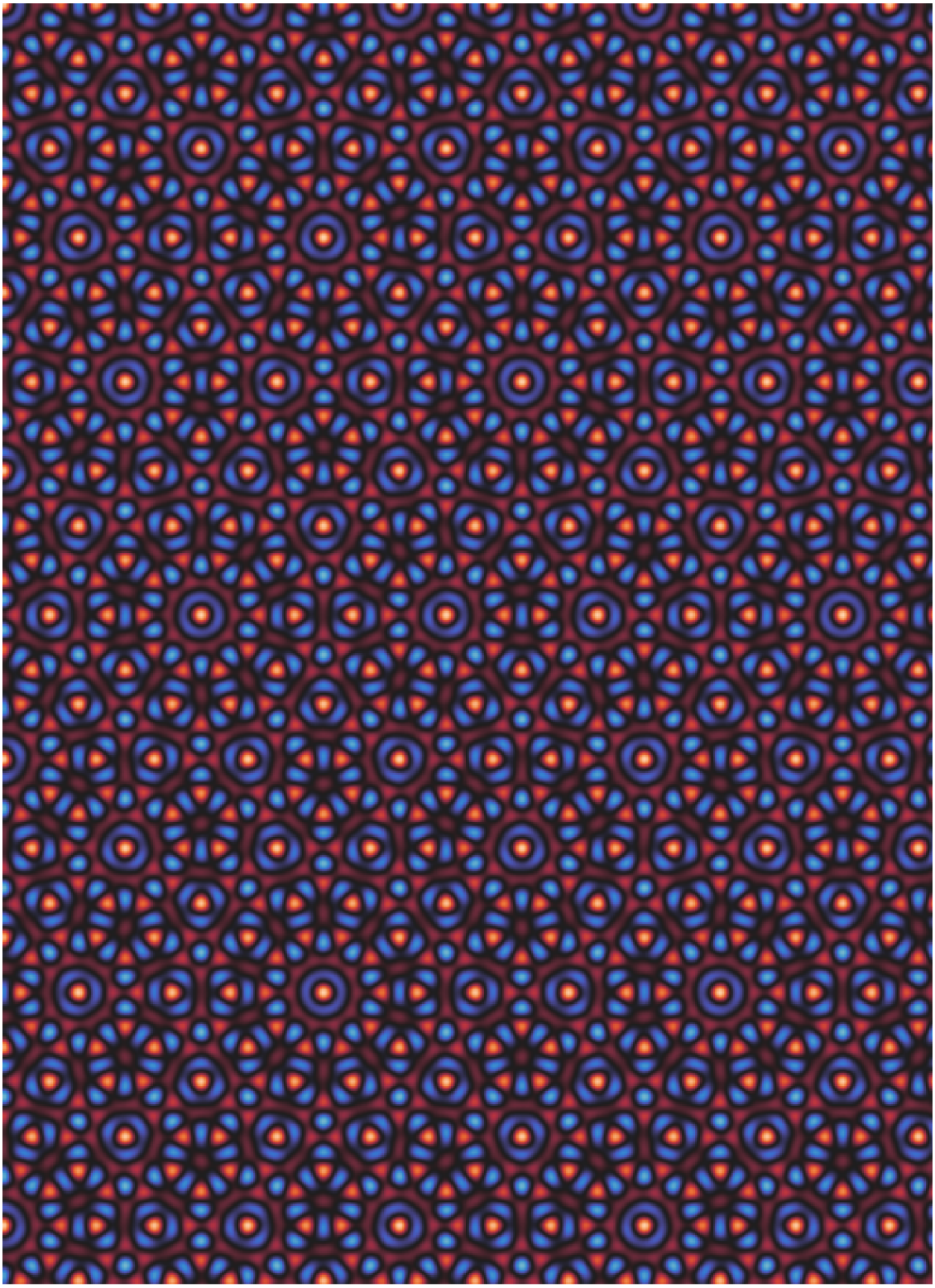

Kelly L. Wang
kelwang@umich.edu
ORCID iD: 0000-0002-7326-3835

DEDICATION

To my mother, Jingping, whose influence played a pivotal role in shaping my academic journey. To my father, Chicheng (Jack), and my partner, Tim. Thank you for your unconditional love and support.

ACKNOWLEDGMENTS

First, I would like to thank my advisor Sharon C. Glotzer for fostering an rigorous but welcoming environment for both research and collaboration. Thank you for creating a space where I could explore exciting and new questions. Your guidance, trust, and support helped me grow as a researcher, and has opened up numerous professional and academic opportunities. Thank you for the opportunity to become a part of your group.

I would also like to thank my committee members Professor Solomon, Professor Sun, and Professor Shahani for their time, expertise and insights. I would like to thank Professor Shahani, and Insung Han, in particular, for helping shape my research and showing me what questions were worth asking.

I would like to thank the Glotzer group as a whole. In particular, I'd like to thank Karen Coulter and Joshua Anderson for keeping things running and making sure we had all the resources we needed. I'd like to thank Fengyi Gao, Ray Asare, Andrew Cadotte, and Dom Fijan, in particular, for their friendship and endless hours spent discussing all sorts of research questions. I'd also like to thank Bradley Dice and Vyas Ramasubramani for both their friendship and professional mentorship.

I would like to thank my friends from Purdue, Maddie Neufeld, Riya Parikh, Andrea Pehr; my childhood friend Maggie Holt; and my friends at Michigan, including Sang won Choi, Jakin Zhang, Scott Ensel, Laura Saunders, Chris Tossas, Dan Matera, Ravi Raghani, Nick Schott, Sam DePalma, Kennedy Gibson, Nic Tjahjadi, and many others. Thank you for making my time here one worth remembering. I can't wait to see where we all head next.

I'd like to thank my parents, Jingping Liu and Chicheng (Jack) Wang, and my partner Tim Baker. Thank you Jingping for emphasizing the value of both science and art in life. Thank you to Jack for always supporting my interests and opening up new opportunities for me. Last, but not least, I'd like to thank my partner, Tim Baker. You have been with my best friend and companion for the past six years. Thank you for you endless love and support.

Lastly, much of the material in this dissertation is based upon work supported by the U.S. Department of Energy, Office of Science, Basic Energy Sciences, under Awards # DE-SC0023147 and # DE-SC0019118. Compute resources provided by the Advanced Research Computing (ARC), a division of Information and Technology Services (ITS) at the University of Michigan, Ann Arbor; the Oak Ridge Leadership Computing Facility, which is a DOE Office of Science User Facility supported under Contract DE-AC05-00OR22725; and under allocation DMR 140129 from the Extreme Science and Engineering Discovery Environment (XSEDE) [134]

TABLE OF CONTENTS

LIST OF FIGURES

FIGURE

LIST OF TABLES

TABLE

LIST OF ACRONYMS

QC quasicrystal

dec-QC decagonal quasicrystal

GB grain boundary

MD molecular dynamics

NPT isobaric-isothermal

NVT canonical

PMF tabulated potential of mean force

LGO local grain orientaions

FCC face-centered cubic

LJ Lennard-Jones

XRT x-ray tomography

PDF probability density function

FT Fourier Transform

DFT discrete Fourier Transform

iFT inverse Fourier Transform

FFT Fast Fourier Transform

TTT Tuebingen Triangle Tiling

FWHM full width at half maximum

AB Ammann-Beenker Tiling

DXA dislocation extraction algorithm

CNA common neighbor analysis

SC simple cubic

FCC face-centered cubic

BCC body-centered cubic

ML machine learning

PTM polyhedral template matching

HRTEM high resolution transmission electron microscopy

GPA geometric phase analysis

ABS acrylonitrile butadiene styrene

STEM scanning transmission electron microscopy

IUCr International Union of Crystallography

FS Fibonacci Sequence

ABSTRACT

Quasicrystals are aperiodic crystals known to exhibit properties unexpected for their composition. These materials have potential applications as solar absorbers, Teflon alternatives, and mechanical reinforcement. Unfortunately, the presence of defects, dislocations, and grain boundaries in synthesized quasicrystals impede the study and commercialization of these materials. Conventional methods to detect defects and grains assume periodicity, are limited to simple crystals, or are developed for a specific crystal structure. Although theories of defects and dislocations in quasicrystals exist, they can be difficult to implement on large systems due to their complexity and computational cost. This dissertation aims to bridge this gap by deepening our understanding of quasicrystal growth mechanisms, offering a versatile tool for defect and dislocation detection, and ultimately enhancing the quasicrystal manufacturing processes.

Due to the difficulties associated with defect detection in quasicrystals, research on the growth interactions of these materials remains limited. To address this gap in the literature, I use molecular dynamics simulation to model two novel growth behaviors discovered by our experimental collaborators. First, I elucidate how phasons, the configurational degrees of freedom imparted by aperiodicity, enables the formation of single, defect free quasicrystals upon collision of two grains with small misorientation. I show how phasons enable quasicrystals to redistribute direct space strain (i.e. phonon strain) upon collision and rotation of misoriented grains. Second, I detail the role of multiple length scales in phason-mediated coalesence mechanisms upon quasicrystal collison and engulfment of shrinkage pores. This phason-mediated mechanism results in a low-energy region at the site of growth front collision, and is agnostic to pore collision conditions. These works highlight the role phasons play in redistributing strain upon collision of growth fronts. Understanding how the presence of phasons affects quasicrystal growth behavior will give experimentalists the tools they need to develop better manufacturing processes for commercially viable quasicrystal coatings.

Although Fourier filtering is traditionally used to detect strain and dislocations in experimental crystals imaged at atomistic resolution, this technique has seen limited usage for the analysis of phason and classical strain in quasicrystals. Additionally, Fourier filtering relies on manual inspection of structural data and often requires specialized knowledge of proprietary software. For systematic studies over large parameter spaces, manual inspection becomes infeasible. Conse-

quently, Fourier filtering for defect detection has seen limited usage in simulated systems. To process the large volumes of data required for our systematic study of obstacles and temperature on quasicrystal synthesis, I develop a structure agnostic algorithm to automate defect and strain detection.

The algorithm is robust to noise and artifacts originating from disordered regions or misaligned grains, effective at segmenting misoriented grains in polycrystalline samples, and effective at identifying defects and dislocations. I leverage this algorithm to analyze phason trail relaxation in simulated quasicrystals and demonstrated the algorithm's generalizability across a diverse array of simulated and experimental crystals, including images of non-spherical particles, three dimensional experimental data, and three dimensional simulation data.

This dissertation aims to advance our understanding of quasicrystals by exploring their growth behaviors, offering a robust defect detection tool, and providing valuable insight for material scientists, crystallographers, and other researchers specializing in quasicrystals. Through the integration of molecular dynamics simulations and innovative algorithms, this research promises to facilitate significant advancements in the comprehension and commercialization of these remarkable materials.

CHAPTER 1

Introduction

Quasicrystals (QCs) are solids that possess long-range orientational order but lack transitional periodicity. These materials are known exhibit mechanical and transport properties that are highly unexpected for their composition [65]. This is due, in part, to their unique geometries [65, 99, 147]. For example, metallic QC are shown to exhibit exceptional hardness [77, 142], high thermal [65] and high electrical resistivity [117, 118], low friction [99], and exceptional corrosion resistance [65]. They are extremely brittle at room temperature and superplastic at high temperatures [65]. The conductivity of QCs, though low at room temperature, becomes much higher at elevated temperatures, making them attractive materials for heat sensing applications [65]. Researchers have also investigated QC applications in solar light absorbers [37], as an alternative to Teflon [37, 65], as mechanical reinforcement of tools as a coating or nanoparticles [37], and insulation [37, 65].

Axial QCs, in particular, can exhibit strong anisotropy in properties such as electrical resistivity [117, 118] or elasticity [27] between the periodic axes and the aperiodic plane. The anisotropy present in axial QCs could open up exotic applications for these materials, while differences in properties along the periodic axis and within the aperiodic plane mean that axial QCs, like decagonal quasicrystals (dec-QCs), are also great tools to help researchers understand how highly ordered materials behave in the presence and absence of periodicity.

Despite the the interest surrounding QCs, they have seen only seen commercial success as mechanical reinforcement in blades with extremely demanding applications (e.g. surgical tools) [37]. This is, due, in part, to the challenges surrounding the synthesis of single crystal QC that are larger than a few centimeters in dimension, and the challenges associated with analyzing QCs.

1.1 Motivation

In this work, we focus on the growth mechanisms of QCs, with the ultimate aim to understand how researchers can harness *phasons*, or the additional degree of freedom unique to aperiodic crystals like QCs, to grow large, high quality QCs for research and commerical applications.

Unfortunately, phasons are both a source of fascination surrounding QCs, and a major challenge associated with studying these materials. Phasons complicate conventional wisdom surrounding the effects of defects and dislocations on QC growth and properties, and the conventional wisdom surrounding how defects and dislocations are formed or relaxed under various growth conditions. In fact, work by Schmiedeberg et al. [76] suggests that phasons give QCs an additional mechanism to redistribute strain in physical space, allowing them to avoid the formation of grain boundaries (GBs) under conditions where periodic crystals would normally form GBs. Unfortunately, the lack of translational periodicity in QCs means that conventional measures of defects and dislocations either fail, or only allow us to measure physical space strain, defects, and dislocations. Yet, phasons give QCs access to strain relaxation mechanisms unavailable to periodic crystals. Tracking phason strain (i.e. perpendicular space strain), then, can help researchers understand the conditions and situations where phasons enable QCs to avoid the formation of large defects and dislocations.

From semiconductors [8, 111, 149] to DNA nanoparticle superlattices [91], defects and dislocations are ubiquitous in self-assembled crystals. The types and quantities of defects greatly impact the quality and properties of a given material, regardless of the crystal's scale or composition [63, 144, 149]. In some cases the introduction of defects and dislocations can diminish desired properties (e.g. suppression of phonon propagation in periodic, thermoelectric materials [149]). In other cases, the introduction of defects such as GBs can be desirable (e.g. work hardening to improve mechanical properties of metals [75] with periodic lattices or semi-crystalline polymers [112]). This has lead to widespread usage of defect engineering in the fabrication of semiconductors [111, 149] and photocatalysts [8], and in the fabrication of organic materials such as metal-organic frameworks [144] and pure carbon nanostructures [86]. Despite the advances made in defect engineering and characterization in hard solids, however, our ability to measure, analyze, and control defect formation in QCs remains limited.

1.2 Summary

In this work, we study defect formation and the relaxation of QCs under experimentally relevant and inspired growth conditions. We elucidate the growth mechanisms of dec-QCs upon collision with other, misoriented dec-QC grains, and with shrinkage pores – a common solidification defect – via systematic, large scale simulations studies. As we conducted our simulations studies of QC growth behavior, we found a marked need for reliable, efficient methods to detect strain and dislocations in, not just QCs, but also periodic crystals with complex or unknown structures. Ultimately, this led us to develop a pure-Python tool, *peakyFinders* and novel methodology to analyze order in crystals. **Taken together, this dissertation aims to elucidate the contributions of phasons of QC growth phenomena discovered by our collaborators in the Shahani group**

at the University of Michigan, and to proved a highly generalizable tool for the analysis of crystals.

1.3 Outline of Thesis

The remainder of the thesis is structured as follows: Ch. 2 reviews the basic QC concepts in the context of quasiperiodic functions and higher dimensional crystallography, and the challenges associated with analyzing these complex structures. In Ch. 3, we detail our first simulation – experimental collaboration in the Shahani group, wherein we elucidate the mechanisms driving grain coalesence and GB formation upon collision of two misoriented dec-QC grains. Our molecular dynamics (MD) simulations helped overcome the spatial and temporal limitations present in experiment, enabling us to observe grain rotation toward 0° misorientation upon collision of grains with small initial misorientation. Our results suggest that this process occurs through a dislocation-mediated mechanism that allows the dec-QCs to redistribute *phonon strain* (i.e. strain in physical space) due to lattice mismatch as *phason strain* (i.e. deviations from quasiperiodicity).

Ch. 4 details our second simulation – experimental collaboration with the Shahani group, where we elucidate the mechanisms driving coalesence upon QC collision and engulfment of shrinkage pores. In this work, we build on this idea of "phason-mediate grain coalesence" through our MD simulations of QC-pore collision. Specifically, our findings highlight the importance of more than one length scale in "phason-mediated grain coalesence" mechanisms. Over time, we see the orientational order and positional order increase, and the potential energy decrease along the region of coalescence. Remarkably, we note that the potential energy changes at a significantly faster rate than orientational order or positional order, ultimately leading to a lower energy region along the region of coalescence, than the surrounding crystal. We attribute this to the fact that the ratio of short-to-long length scales remains low along the region of coalescence when compared to the rest of the crystal. This suggests that any real-space strain introduced upon collision is able to relax because of the presence of phason fluctuations introduced upon collision, and offers further insight on the mechanisms driving "phason-mediated grain coalesence."

Then, in Ch. 5, we present *peakyFinders* and our novel, highly generalizable methodology for grain segmentation and dislocation analysis in crystals. The methodology presented in Ch. 5 is built from the intuition we gained while analysing QCs previous chapters. In Ch. 3, we used the technique presented in [43] to measure phason and phonon strain in our dec-QCs. In Ch. 4, we present some of the limitations of [43], and develop a more robust methodology. Then, finally, in Ch. 5, we extend the methodology developed in Ch. 4 to 2D and 3D periodic crystals sourced from simulation and experiment. We show how our Python package, *peakyFinders*, enables reliable, streamlined Bragg peak detection and Bragg peak filtering for a variety of 2D and 3D inputs,

and show that our existing protocol is easily extensible to a variety of 2D systems and simple, 3D crystals. Then, we show how our workflow can be extended to more complex structures and particle shapes with a few additional steps in our workflow. Ultimately, Ch. 5 highlights a new framework with which we can approach the analysis of order in complex crystals and develop fast, robust, and transparent models for structural analysis.

We conclude the thesis with an outlook in Ch. 6.

CHAPTER 2

Introduction to Quasicrystals

Here we give a brief overview of quasiperiodicity and higher dimensional crystallography in the context of quasicrystals (QCs). Next, we discuss some of the challenges associated with QC analysis. Then, we give an overview of how reciprocal space can be used to analyze order in QCs.

Before we begin our discussion on QCs and the general concept of quasiperiodicity, however, it helps to revisit the suprisingly philisophical question of *what is a crystal*?

2.1 What is a Crystal?

The International Union of Crystallography (IUCr) offers two, alternative but equivalent definitions for the word crystal. One definition focuses on direct space (what we see with our eyes), while the second focuses on reciprocal space (i.e. Fourier space).

2.1.1 The Direct Space Definition

We'll begin with the definition of *crystal* in direct space from the IUCr's Online Dictionary of Crystallography [98]:

> A solid is a crystal if its atoms, ions and/or molecules form, on average, a long-range ordered arrangement.

If we look at, say, the structures shown in Fig 2.1 **(b, c)** (top row), this may seem like a clear and intuitive definition. The order in these examples is clear due to the presence of translational periodicity. Meaning, we can easily describe the order in any region of the crystal using a simple set of local rules. In Fig. 2.1 **(b)**, the basic building blocks (i.e. the *unit cell*) is a square. While, in Fig. 2.1 **(c)**, the basic building blocks (i.e. the *unit cell*) is a hexagon. In these systems, the concept of 'long-range order' is rather straight forward.

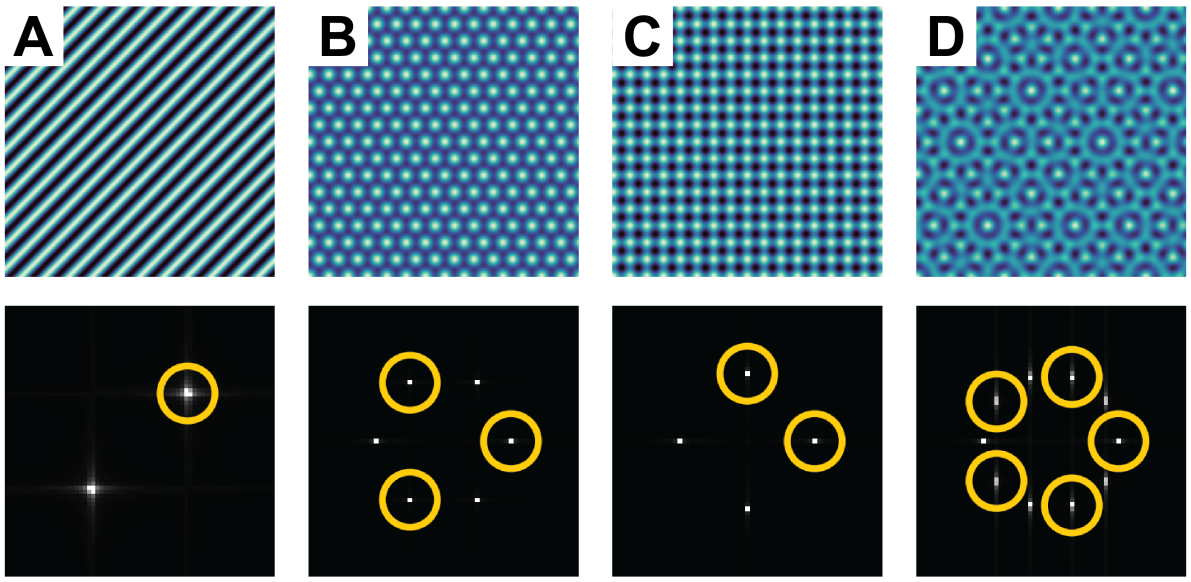

Figure 2.1: **Crystals constructed from a sum of cosines.** Real space (top) and reciprocal space (bottom) images generated from the sum of cosines with basis vectors (circled in yellow) **(a)** $\vec{b_0} = [\cos \pi/4, \sin \pi/4]$; **(b)** $\vec{b_k} = [\cos 2 * k * \pi/3, \sin 2 * k * \pi/3]$ for $k = 0, 1, 2$; **(c)** $\vec{b_0} = [1, 0]$ and $\vec{b_1} = [0, 1]$; and **(d)** $\vec{b_k} = [\cos 2 * k * \pi/5, \sin 2 * k * \pi/5]$ for $k = 0, 1, 2, 3, 4$. For reciprocal space images, plots show the power spectrum (the magnitude of the Fourier Transform (FT)).

Examining the structure in Fig. 2.1 **(d)** (top row), however, highlights a major shortcoming of the direct space definition. The structure shown in Fig. 2.1 **(d)** (top row) is clearly ordered, and yet, it is non-trivial to describe the long-range order of the system in direct space.

2.1.2 The Reciprocal Space Definition

Now, let's look at the definition of *crystal* in reciprocal space from the IUCr's Online Dictionary of Crystallography [98]:

> A material is a crystal if it has **essentially** a sharp diffraction pattern.

Meaning, the diffraction pattern, or, the reciprocal space image of that material consists of sharp *Bragg peaks*, where each peak, $H^*(\vec{q})$, can be indexed using some linear combination of basis vectors $\vec{b_k}$ in reciprocal space,

$$H^*(\vec{q}) = \sum_k^N n_k \vec{b_k}$$

where, N is the minimum number of reciprocal basis vectors $\vec{b_k}$, required to index each point in the diffraction or reciprocal space image of the crystal.

We can see the reciprocal space image of each crystal in the bottom row of Fig. 2.1.

For a single plane wave (Fig. 2.1 **(a)**), we see one pairs of Bragg peaks. For the periodic pattern with fourfold symmetry, we see two pairs of Bragg peaks, arranged in the shape of a square (Fig. 2.1 **(b)**), and for the periodic pattern with sixfold symmetry (Fig. 2.1 **(c)**), we see three pairs of Bragg peaks, arranged in the shape of a hexagon. Then, finally, when we look at the Fourier space image of that complex, yet ordered pattern in Fig. 2.1 **(d)**, we see a much simpler description of that pattern. What we see, is five pairs of Bragg peaks, arranged neatly around a ring. This last structure is something like a quasicrystal (QC) – it has long-range orientational order and long-range order, despite the lack of translational periodicity.

2.1.3 The Cosine Crystal

The reciprocal space (i.e. Fourier space) image of a crystal tells us about the dominant frequencies associated with a given structure. It is, essentially, a summary of how every point in a structure interacts with every other point in a structure.

Then, to understand why this reciprocal space image of crystals is so effective, it helps to think crystals defined by a sum of plane waves (Fig. 2.1, top row), rather than a discrete set of points,

$$H(\vec{r}) = \frac{1}{N}\sum_{k}^{N}\cos(2\pi\vec{r}\cdot\vec{b_k}) \tag{2.1}$$

where, b_k is the set of N basis vectors and $\vec{r}$ is a point in real (direct) space.

If we take the FT of Eqn. 2.1, we get a point-like Fourier spectrum, where the points can be indexed by the basis vectors $\vec{b_k}$ associated with Eqn. 2.1 (Fig. 2.1; bottom row, yellow circles correspond to basis vectors used to generate each cosine crystal),

$$F(\vec{x}) = \frac{1}{2N}\sum_{k}^{N}\delta(\vec{x}-\vec{b_k}) + \delta(\vec{x}+\vec{b_k}) \tag{2.2}$$

where $\delta(\vec{x})$ is the Dirac delta function.

If we filter a single Bragg peak in the Fourier spectrum, meaning, we take the inverse Fourier Transform (iFT) of just a single Bragg peak, $F(\vec{x}) = \delta(\vec{x}-\vec{b_k})$, we get the following:

$$\xi_k(\vec{r}) = e^{2\pi i\vec{r}\cdot\vec{b}_k} \tag{2.3}$$

Contrast this with the positional order parameter [5], which is measured with respect to some reciprocal basis vector, $\vec{b_k}$,

$$\chi(\vec{r}) = e^{i\vec{r}\cdot\vec{b}_k} \tag{2.4}$$

we see how each Bragg peak is fundamentally related to positional order.

Meanwhile, taking the iFT of a pair of filtered Bragg peaks, then, yields:

$$\xi_k(\vec{r}) + \xi_{-k}(\vec{r}) = e^{2\pi i \vec{r}\cdot\vec{b}_k} + e^{-2\pi i \vec{r}\cdot\vec{b}_k} \tag{2.5}$$

Using Euler's formula, it's possible to reformulate Eqn. 2.5 as: $\xi_k(\vec{r}) + \xi_{-k}(\vec{r}) = cos(2\pi i \vec{r} \cdot \vec{b}_k)$, giving us a more concrete, real space connection between the concepts of frequency and reciprocal space, positional order, and direct space.

From Eqns. 2.3, 2.4 and 2.5, we see that the iFT of a filtered Bragg peak or pair of Bragg peaks is fundamentally related to positional order in a given crystal.

2.2 A Brief History

Before 1991, the definition of crystal, and of long-range order in matter, was a much more rigorous and direct than the modern definition of crystal. Before 1991, crystals were defined by the presence of 3D periodicity [97, 113]. As a result, crystals were believed to be restricted to two-, three-, four-, and six-fold symmetry rotational symmetry. Other symmetries, such as five-fold or ten-fold rotational symmetry, were thought to be forbidden because they were incompatible with longe-range order.

Then, in 1982, Shechtman et al. [116] discovered quasicrystals (QCs) in rapidly cooled aluminum alloys. His discovery challenged the existing paradigm of crystallography and ultimately led to a revision in how we defined crystals [97]. This discovery, however, was initially met with immense skepticism.

It was known that aperiodic states of crystallinity existed before the discovery of QCs [35]. However, these aperiodic structures exhibited crystallographic symmetry (i.e. symmetries belonging to a crystallographic point group) [138]. *Incommensurately modulated crystals* were the first class of aperiodic crystals discovered by modern researchers [35, 64, 66]. These structures could be interpreted as periodic lattices with modulations [64, 66, 138], where the probability of finding a molecule at a certain position or some molecules in a certain orientation varies periodically. That is, incommensurately modulated crystals could be interpreted as a periodic-average lattice where the displacements of positions from ideal lattice sites is highly correlated such that they follow a wave. If follows, then, that incommensurately modulated crystals did not violate the premise that crystals must have symmetry that is compatible with periodicty, despite appearing aperiodic.

Shortly following the discovery of incommensurately modulated crystals, came the discovery of *incommensurate composite crystals* [34, 66]. Incommensurate composite crystals consist of two or more subsystems with mutually incommensurate interactions [34, 138]. Think, for example,

of a system composed of two types of periodic lattices, stacked in alternating layers along an axis where the periodicity of each lattice is incommensurate with the other. This means that, like QCs and incommensurately modulated phases, incommensurate composites lack translational periodicity, yet they still possess some basic, periodic structure in physical space [138]. This means that incommensurate composite crystals, too, possess crystallographic symmetries [138].

QCs, in contrast, cannot be described as periodic or periodic-average in physical space. In fact, they exhibited symmetries once believed to be impossible in three dimensional matter with long-range order. As a result, Shechtman's findings were dismissed [121]. Shechtman was in luck, however. A mere 150 miles away, Paul Steinhardt and his student, Dov Levine, had been independently worked towards a theory to describe order in the "non-periodic" Penrose tiling [121]. What they had determined was that the Penrose tiling exhibited *quasiperiodic* order, and that there may a whole, new class of ordered material, which they named *quasicrystals* [84, 121].

Then, in 1984, two years after Shechtman's initial discovery, the two teams published their findings within two month of each other in *Physical Review Letters* [84, 116]. Though contention remained in the early days of this discovery, with two-time Nobel prize winner, Linus Pauling being the first and most notable [121]. Still, as time went on, QCs gained acceptance into the scientific mainstream [121], and Shechtman was ultimately awarded the Nobel Prize Chemistry in 2011 for his discovery [1].

2.3 Quasiperiodicity

Here, we return view of crystals as a sum of plane waves, rather than points presented in Sec. 2.1.3. This view particularly helpful in capturing the long-range positional order associated with quasicrystals (QCs) because it allows us to reduce the complex, local structures and rules associated with QCs to a simple set of equations (Fig. 2.1 **(d)**, Sec. 2.1.3).

Mathematically-ideal QCs are solids that possess long-range orientational order and long-range translational order [85], but lack transitional periodicity [85]. Rather, the order in these structures are defined by the presence of *quasiperiodicity*.

When we say a function is *quasiperiodic*, we mean that a function is aperiodic – or, the function lacks a period, but has sharp peaks in Fourier space [14, 66]. This means that, unlike a periodic function, $f(\vec{x})$, where there exits some translation, $\vec{b}$, associated with the period of the function,

$$f(\vec{x}) = f(\vec{x} + \vec{b}) \tag{2.6}$$

quasiperiodic functions are *almost periodic* [14, 17, 66], a concept first introduced by mathematician Herald Bohr [17].

An almost periodic function is defined as a function, $f(\vec{x})$, where there exists a 'dense' set of translations, $\vec{b}$, such that,

$$||f(\vec{x}) - f(\vec{x} + \vec{b})|| < \epsilon \tag{2.7}$$

where, $\epsilon > 0$ [66] and ϵ is very small, $\epsilon << 1$ [14]. Here, $|| \cdot ||$ is the norm of a vector, $||\vec{a}|| = \sqrt{\vec{a} \cdot \vec{a}^*}$ and $\vec{a}^*$ is the complex conjugate of some vector, $\vec{a}$, and 'dense' means that for any set of $\vec{b}$ and value of ϵ, there exists at least one value of $\vec{x}$ where Eqn. 2.7 holds true.

This *almost periodic* property of quasiperiodic functions tells us that quasiperoidic functions exhibit some form of self-similarity in direct space. As a consequence, it should be possible to measure deviations from quasiperiodicity, both locally, and globally, in a meaningful way.

Arising from this loss of translational periodicity, and the presence of quasiperiodic order, is an additional degree of freedom, termed, *phasons*.

Phasons are present in all aperiodic crystals [66], though, in most *incommensurate crystals*, a class of aperiodic crystals which exhibit crystallographic symmetries, phason excitations and relaxations are continuous [66]. In these cases, phasons may be interpreted as a displacement from the periodic lattice [66]. Meanwhile, in QCs, which exhibit non-crystallographic symmetries in direct space, this model of dislocations does not apply [83].

In QCs, phasons are characterized by discrete, local changes in particle position, or *phason flips* that result in a change in *tiling* configuration [41], where *tiles* are the basic structural units of a QC. They can be thought of like a unit cell, though unlike a periodic crystal, these motifs are not arranged periodically [85], and there are typically more than one tiles associated with a given QC.

The discrete nature of phasons and phasons flips in QCs make them unique, even among aperiodic crystals. These changes in tiling configurations are representative of phason excitations and relaxations, and do not introduce real space defects into the crystal [119]. Instead, these phason excitations and relaxations are associated with changes *phason strain*, a measure of deviation from ideal quasiperiodicity [128].

This concept of phason flips and phason strain play a key role in understanding how and why QCs exhibit the unexpected behavior discussed in later chapters.

2.4 Tilings

While periodic crystals lattices may be constructed from a single repeating unit cell, quasicrystals (QCs) lattices may be described as *tilings* of two or more repeating motifs. These repeating motifs, or *tiles*, are assembled without overlaps or gaps to form aperiodic patterns. Decoration of tile vertices with particles yields the atomic structure of QCs. In 1D, the tiles are interpreted as line segments of varying lengths, while in 2D and 3D, tiles are polygons or polyhedra.

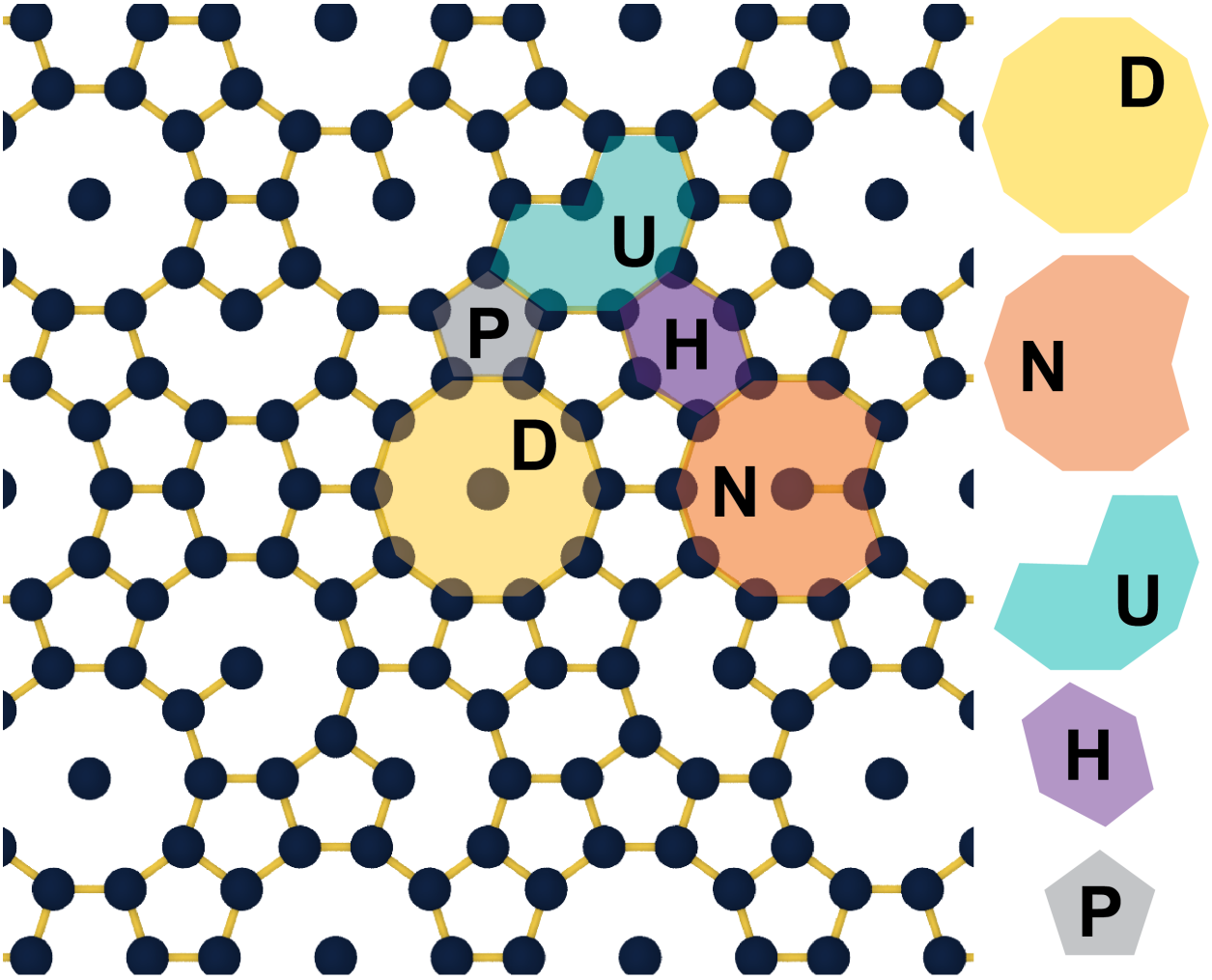

Figure 2.2: **Atom decorated Tübingen tiling.** An ideal Tübingen tiling constructed from 5 prototiles: decagon (D), u-tile (U), nonagon (N), hexagon (H), and pentagon (P). In molecular dynamics (MD) simulations of decagonal quasicrystals (dec-QCs), atoms decorate the verticies of the tiles (blue dots).

In Fig. 2.2, we show an ideal Tübingen tiling constructed from 5 prototiles: decagon (D), u-tile (U), n-gon (N), hexagon (H), and pentagon (P), and blue dots correspond to where we would expect to see atoms in an molecular dynamics (MD) simulation of a decagonal quasicrystal (dec-QC).

Here, an *ideal tiling* refers to a mathematically perfect structure with hierarchical long-range order. In contrast, a *random tiling* refers a space filling collection of prototiles associated with some *ideal tiling*. Different random tilings can have different levels of *phason strain*, where some structures are completely devoid of any quasiperiodicity (high phason strain structures), while others have near-zero phason strain (low phason strain structures).

Typically, self-assembled QCs, such as the ones that will be discussed in Ch. 3 and 5, are random tilings.

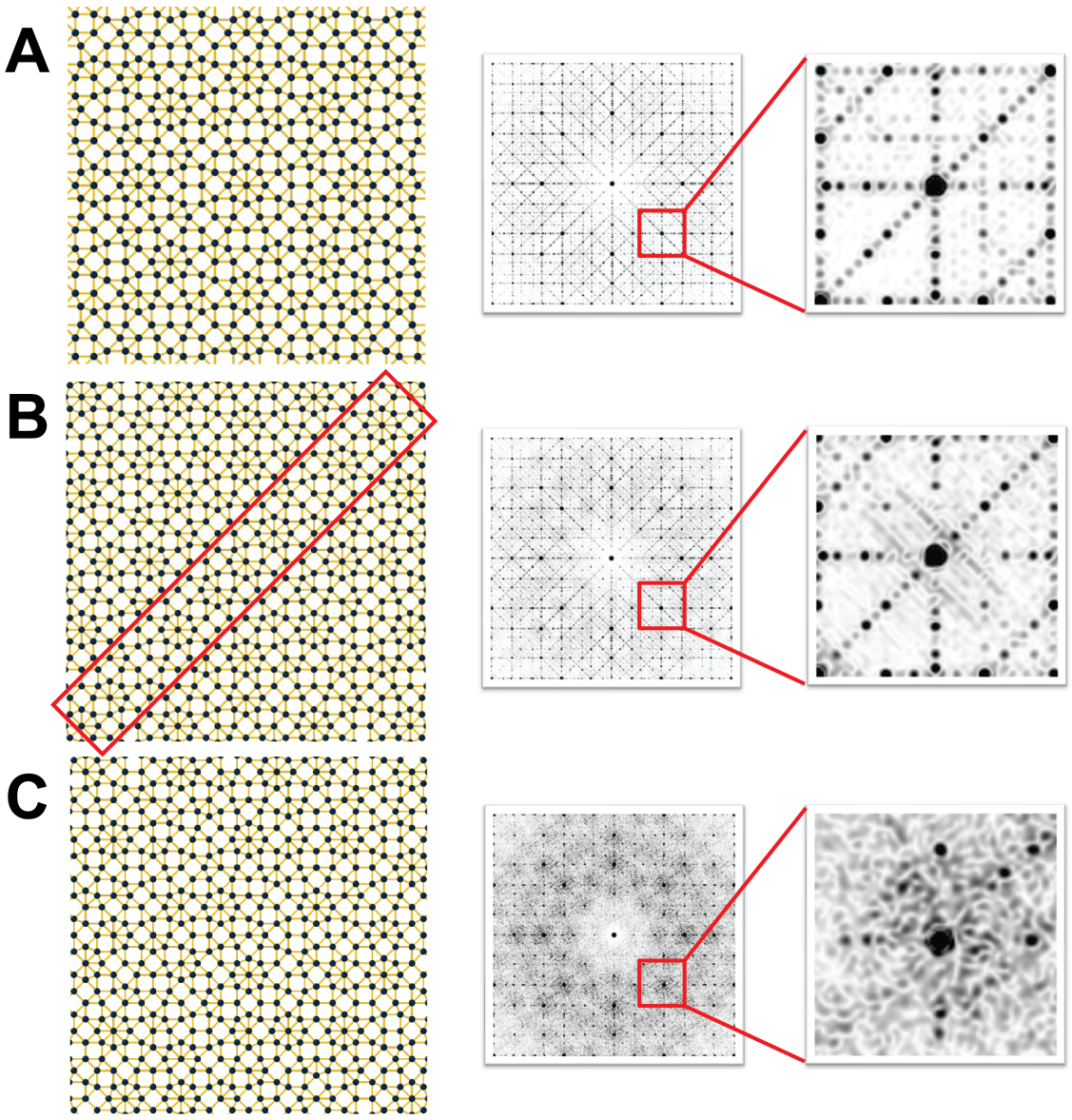

Figure 2.3: **Quasicrystals and their random-tiling counterparts.** The first column depicts **(a)** ideal Ammann-Beenker Tiling (AB) tiling **(b)** a nearly AB ideal tiling with a line of phasons introduced along a diagonal (red box), and **(c)** a random AB tiling, AB vertices are decorated with atoms decorations (blue dots). The second column shows the corresponding power spectrums, while the third column shows zoomed in insets of the power spectrum.

In Fig. 2.3, we see examples of ideal (Fig. 2.3 **(a)**), a nearly ideal AB tiling with a line of phasons engineered across the diagonal (Fig. 2.3 **(b)**), and a random tiling (Fig. 2.3 **(c)**). From the the direct (i.e. physical) space image of the tilings, it can be difficult to tell the difference between an ideal QC tiling and a random tiling. Examining the power spectrums[1] (Fig. 2.3, second and third columns), however, tells a different story.

2.4.1 Random Tilings and Reciprocal Space

In the power spectrum and the zoomed in inset of the ideal AB tiling (Fig. 2.3 **(a)**, second and third columns), we can see ideal quasiperiodicity reflected in the arrangement of Bragg peaks.

When we examine the power spectrum for the AB tiling with a line of phasons, we can see faint diagonal streaks where we expect to see lower intensity peaks (Fig. 2.3 **(b)**, third column). Yet, when we examine brighter peaks, and the overall appearance of the power spectrum remains nearly identical to that of the AB tiling (Fig. 2.3 **(a)**). Remember, that in this example, we engineered phason flips along a diagonal of the otherwise ideal AB tiling (red box in first column; Fig. 2.3 **(b)**). These phason flips were simple, local tiling flips, which only disrupted quasiperiodicity along the smallest length scale. That is why we see this change reflect on the lowest intensity Bragg peaks, but not on brighter intensity Bragg peaks.

Meanwhile, in the power spectrum for the random, AB-like tiling, the low intensity peaks are no longer visible, but the high intensity peaks remain, and power spectrum still appears similar to the ideal AB tiling when viewed from afar (Fig. 2.3 **(c)**, second and third column). This is because, at the smallest length scale (i.e. the length scale of the individual tile), we no longer have the well-defined quasiperiodic order. We know, however, that some long-range quasiperiodic order still exists in this random tiling (i.e. quasiperiodiciy still exists at the global level), due to the presence of sharp Bragg peaks.

To get a better understanding of how quasiperiodicty relates global and local order it helps to examine QC order using the hyperspace approach.

2.5 Higher Dimensional Crystallography

The hyperspace approach was derived from diffraction data [96, 126], and acts a direct extension of 3D crystallography to aperiodic structures like quasicrystals (QCs).

[1]Here, power spectrum refers to the amplitude obtained from the 2D Fourier Transform (FT) of the crystal positions. The power spectrum is the square root of the structure factor, and the square root of what diffraction typically returns. We plot the power spectrum, rather than the structure factor/FT intensity because it is easier to see lower intensity peaks, and thus, the effects of phason flips and phason excitations in reciprocal space.

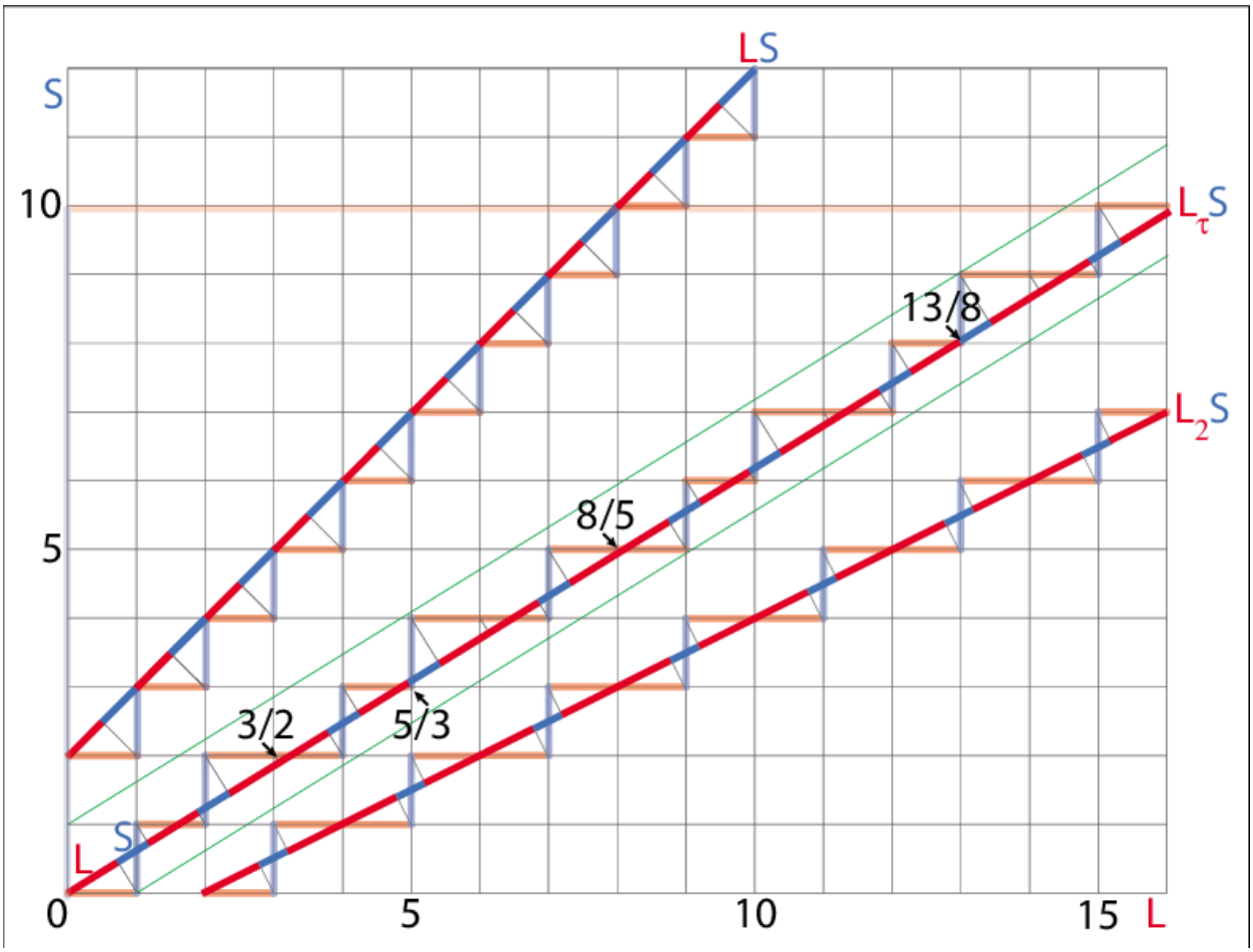

Figure 2.4: **2D embedding of 1D Fibonacci sequence and 1D periodic sequences.** The top line, labeled LS, and the bottom line, labeled L_2S, show 2D embeddings of periodic sequences, where LS corresponds to projection along a cut with slope $= 1$, and L_2S corresponds to a projection along a cut with slope $= 2$. The middle line, labeled $L\tau S$, shows the 2D embedding of the Fibonacci Sequence (FS). The bounds of the FS projection are shown in light green lines. Red corresponds to L segments in the sequence, while blue corresponds to S segments in the sequence. Source: Walter Steuer [125], licensed under CC BY-NC 4.0.

Iteration [i]	**Sequence**	**Ratio [$N_{L,i}/N_{S,i}$]**
0	L	–
1	LS	1
2	LSL	$2/1 = 0.5$
3	LSLLS	$3/2 = 1.5$
4	LSLLSLSL	$5/3 = 1.666\ldots$
5	LSLLSLSLLSLLS	$8/5 = 1.6$
6	LSLLSLSLLSLLSLSLLSLSL	$13/8 = 1.625$
...	...	...
∞	LSLLSLSLLSLLS...	$\approx \tau = 1.618\ldots$

Table 2.1: **The Fibonacci sequence and its approximates**, where $N_{L,i}$ is the number of L segments at iteration i, and $N_{S,i}$ is the number of S segments at iteration i.

Under the lens of higher dimensional crystallography, QC becomes periodic in hyperspace. In theory, this enables us to extend the established models developed for periodic, 3D crystals to QCs. In practice, however, this interpretation of QC structure is limited in its ability to analyze highly disordered structures (*i.e.* grain boundaries) and random tilings in self-assembled, quasicrystalline strucures. Still, it provides valuable tools to understand the unique symmetries of QCs.

The hyperspace space of crystal, V, can be separated into two orthogonal subspaces, $V_{\parallel}$ and $V_{\perp}$, where $V_{\parallel}$ is the *parallel* or *physical space* and corresponds to atomic positions in "real" or direct space. $V_{\perp}$ corresponds to the *perpendicular* or *internal space* and contains information about the *atomic surface*, where the *atomic surface* is a type of probability density function. Information about the atom, such as the probability an atom will appear at any given intersection of the perpendicular space and the parallel space.

A trivial example of the hyperspace image can be constructed for a 1D periodic sequence. In Fig. 2.4, we can see two examples of 1D periodic sequences in hyperspace. The top line (LS in Fig. 2.4) represents a projection of the 2D square hyperlattice onto a line with cut angle $\tan(1)$. Meanwhile, the bottom line (L_2S in Fig. 2.4) represents the projection of a 2D square hyperlattice onto a line with cut angle $\tan(2/1)$.

If we try to project all of the points from this hyperlattice down to LS or L_2S, we get a discrete, periodic sequence out. This is because we take a rational cut of hyperspace. By definition, when we take a rational cut of hyperspace, we get a line that intersects points at a regular interval defined by the slope.

2.5.1 The Fibonacci Sequence

Now, let's say we take a cut with an angle $\tan(\tau)$. Since τ is irrational, we know that this line will never intersect another point. As a consequence, if we try to project every point onto this line, we get an infinitely dense projection. Instead, we need to take a "cut window", (light green lines above and below the line labeled $L_\tau S$, Fig. 2.4), meaning, we only project points that are within some distance or boundary of our line. Given proper selection of a cut window, we get back out the Fibonacci Sequence (FS).

The 1D FS is a well-known and well-studied example of a quasiperiodic tiling. Because it is aperiodic in 1D and periodic in 2D, it is commonly used to visualize the relationships between $V_\perp$, $V_\parallel$, and V.

The FS consists of long segments, L, and short segments S, which are related by an irrational scaling factor, $L = \tau S$, where $\tau = \frac{1+\sqrt{5}}{2}$ is the golden ratio. The FS can be constructed via the following subsition rules: $L \rightarrow LS, S \rightarrow L$. In, Table 2.1 shows the generation of the FS via substitution, or, alternatively, inflation. As the FS grows, the ratio, $\frac{N_L}{N_S} \rightarrow \tau$. The sequence here, never repeats, and yet, it can be described using a simple set of rules. These substitution rules are an example of self similarity present in QCs.

2.5.2 Scaling Symmetry and Self-Similarity

Some mathematically ideal QCs possess self-similarity and non-trivial scaling symmetry [126], where self-similarity in QCs tilings can be understood in terms of *inflation* and *deflation*. In the process of inflation, every tile has a way to map onto itself – meaning, any tile in a QC can be constructed by a combination of smaller versions of the same set of tiles associated with the given QC (think back to the substitution rules of the FS). If we perform inflation, on say, an ideal FS, what we get back out is another, mathematically ideal FS composed of smaller tiles. In this inflated FS, however, the tiles (the L and S segments of the QC) are still related by the scaling factor $L = \tau S$.

Deflation is the opposite of inflation, meaning, it is possible to shrink an ideal QC down to a smaller subset of tiles without destroying quasiperiodic order. In the case of the QC, we can think of it as reversing the substitution rules: $LS \rightarrow L$ and $L \rightarrow S$. Any FS we shrink using these rules will yield a smaller version of the original FS.

While the prototiles shown in Figs. 2.2 and 2.3 do not correspond to self-similar variants of the Tübingen tiling and AB tilings, respectively, self-similar variants do exist for both.

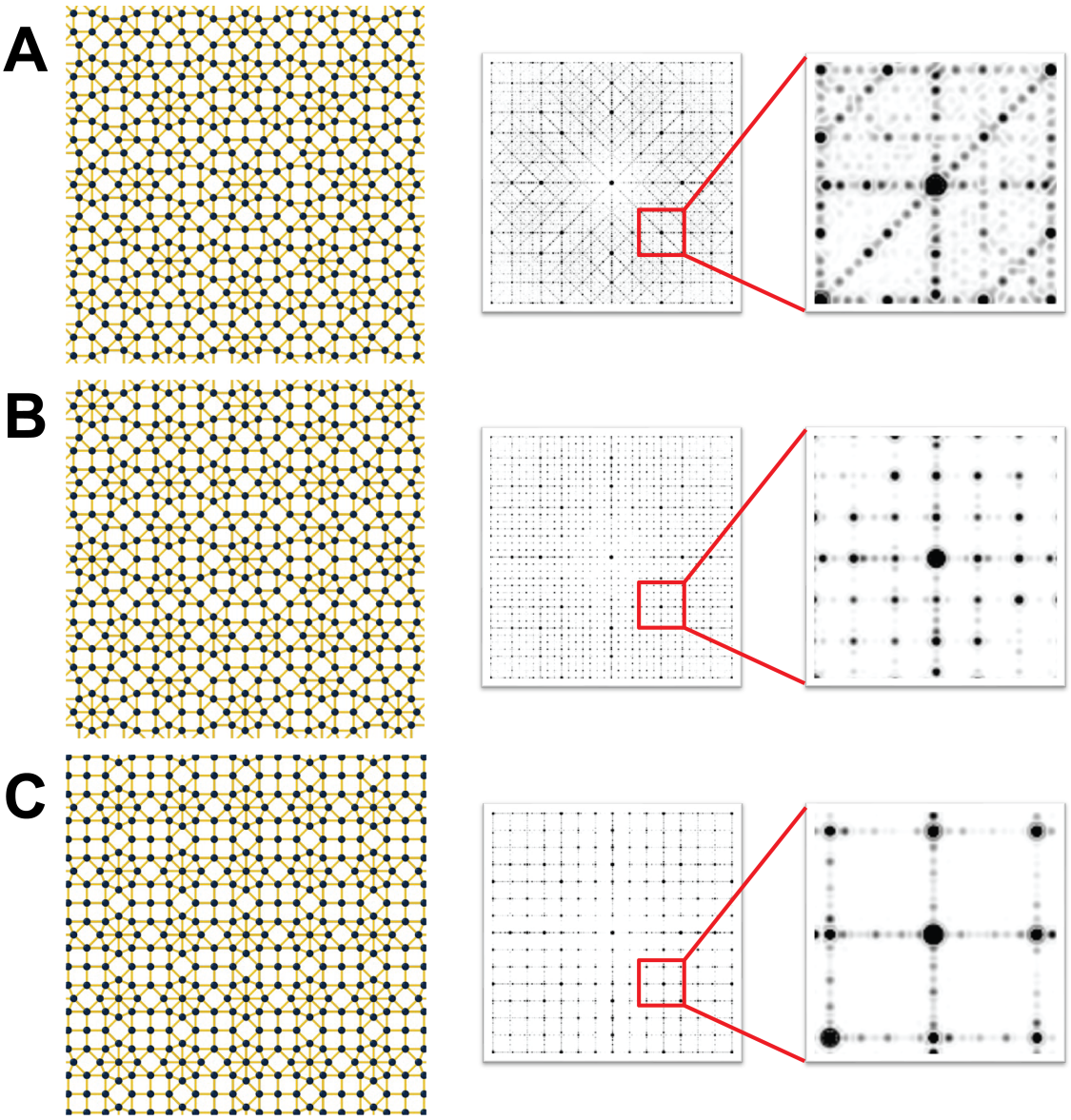

Figure 2.5: **Quasicrystals and their approximate counterparts.** The first column depicts **(a)** ideal Ammann-Beenker Tiling (AB) tiling **(b)** an AB approximate with a large unit cell, and **(c)** an AB approximate with a small unit cell. AB vertices are decorated with atoms decorations (blue dots). The second column shows the corresponding power spectrums, while the third column shows zoomed in insets of the power spectrum.

2.5.3 Approximates

In Table 2.1, we see another important property of QCs and quasycrystal like structures. If we look at the ratio $R_i = N_{L,i}/N_{S,i}$, where $N_{L,i}$ is the number of L segments at iteration i, and $N_{S,i}$ is the number of S segments at iteration i, another interesting trend emerges – during early iterations, the R_i is a poor approximation of τ. Then, as $i \to \infty$ increases, $R_{i\to\infty} \to \tau$.

In Fig. 2.4, these approximate are marked by black arrows along $L_\tau S$. We see that, at these ratios, the cut plane becomes very close to, though never quite intersects these points. This means that when angle of the cut window is varied, even slightly, we can end up get a rational *approximate*, rather than a true QC. In these cases, the sequence (or crystal) is no longer aperiodic, and a single unit cell can be drawn for the structure.

Previously, we defined *phason strain* as a measure of deviation from aperiodicity. It follows then, that approximates have higher, global phason strain than a truly aperiodic QC.

In Fig. 2.5, we can see examples of the AB tiling and its approximates. When the unit cell of the approximate is large relative to the system size (Fig. 2.5 **(b)**), it is not straight forward to tell, by eye, if the crystal is true QC or an approximate. Much like in the case of the random tiling, the deviation from aperiodicity becomes clear in the power spectrum.

2.5.4 Phason Flips and Phason Strain

Phason flips are of particular interest because they enable changes in tiling configurations without introducing defects or dislocations in physical space [119]. These changes in tiling configurations are representative of phason excitation and relaxations [119], and are known to help relax phason strain in QCs over diffusive time scales [66]. This means QCs posses an additional mechanism, by which they can relax, not just phason strain, but, potentially phonon strain as well.

Fig. 2.6 shows an example of how phason flips can enable FS to avoid the formation of dislocation or defects due to incommensurate length scales. This phason flip shown here can be thought of as either a collective shift in the particles either before or after the L segment we replaced, or as a slight compression of the ideal sequence FS. By substituting an L segment for an S segment, we make the entire FS sequence shorter, and we introduce a slight shift in the slope of the cut, effectively introducing phason strain in place of phonon strain or a dislocation.

Meanwhile, Fig. 2.7 shows an example of how phasons flips can violate quasiperiodic order and scaling symmetry locally, without disrupting long-range quasiperiodic order. The presence of two, adjacent S tiles in the FS is not possible if we follow the substitution rules, or if we only project points from hyperspace within our cut window. In fact, if we look at the location of the new coordinate in hyperspace, we see that this new point is further from the cut line than the ideal hyperspace coordinate (Fig. 2.7 **(c)**, red arrow). This type of deviation from quasiperiodicity is

distinct from the type of phason strain introduced by the previous example, shown in Fig. 2.7, and is more representative of the type of disorder we saw in the random tiling example seen in Fig. 2.3.

Schmiedeberg et al.'s [110] work, provided early evidence that phasons and phason flips may help QCs avoid the formation of small angle grain boundaries (GBs). In particular, his work showed how grain coalescence occurs more readily in dodecagonal QCs than in periodic crystals, and that phasons play a significant role in distributing stress [110] around the non-fitting structures, where the resulting phason strain can be relaxed via phason flips [41].

Our own work in Ch. 3 and 4 provide further evidence that QCs may be able to avoid the formation of phonons, defects, or dislocations via phason excitations, and highlighted the role of multiple length scales in enabling this mechanism.

2.5.5 Lifting from Physical Space to Higher Dimensional Space

The lifting and cut-and-project procedure enables researchers to map their self-assembled simulations and experiments to hyperspace, V, for analysis. This procedure has been used extensively to compute phason strain (i.e. global deviations from quasiperiodicity) in self-assembled systems [38, 40, 52, 67, 95].

The first step in this protocol is *lifting*. In this step, physical space positions are indexed using basis vectors projected from hyperspace.

A simple example of this can be constructed from the FS. Revisiting the FS, the cut plane (or line in this case), has a slope of $\tan(\tau)$. This means that the equation for our line can be expressed as: $[\tau, 1]$. Projecting our square lattice in hyperspace, $\vec{b}_1 = [1, 0]$ and $\vec{b}_2 = [0, 1]$, yields lower dimensional basis "vectors" (or, in this case, line segments $L = \tau S$) of $b_1^{\parallel} = \tau$ and $b_2^{\parallel} = 1$.

Next, we iterate through the FS and assign each point in the sequence a coordinate in higher dimension space. When we find segments with length τ will can add the associated basis vector $\vec{b}_1 = [1, 0]$ to to the previous coordinate. Meanwhile, when we find segments with length 1, we can add basis vector $\vec{b}_2 = [0, 1]$ to the previous coordinate. (Fig. 2.7 **(a)**, yellow and brown arrows correspond to higher dimensional lattice vectors).

Once all of the $V_{\parallel}$ point have been assigned higher dimensional coordinates, we can compute phason strain – or, the systems deviation from aperiodicity, as the higher dimensional coordinate's deviation from the expected slope.

The same algorithm can be extended to 2D and 3D QC, where points are indexed in higher dimensions based on their alignment with a the associated, projected basis vector.

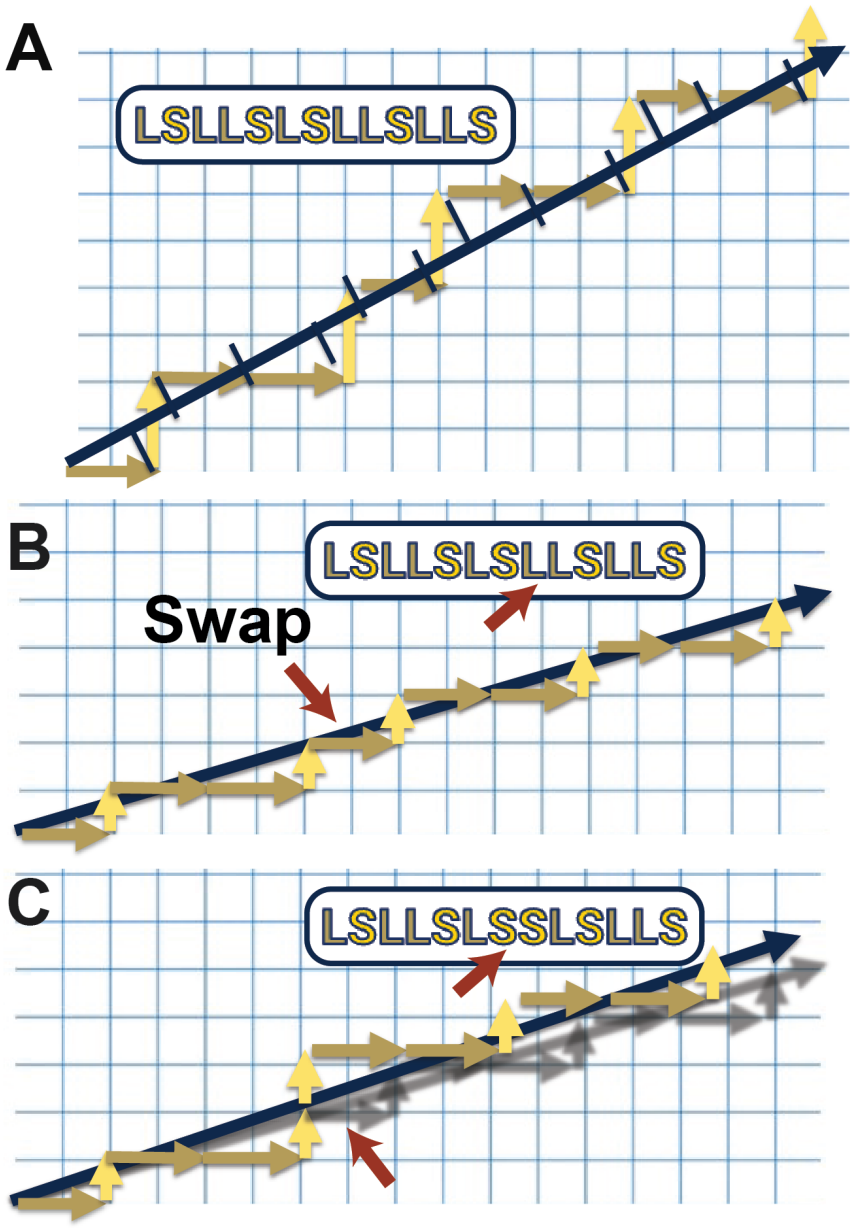

Figure 2.6: **How phason flips can introduce phason strain.** **(a)** Shows a segment of an ideal 1D FS in hyperspace, where the dark blue arrow is the parallel subspace, $V_{\parallel}$. Brown arrows (darker color) correspond to the lattice vector in hyperspace (V) for segment L, while yellow arrows (lighter color) correspond to the lattice vector in hyperspace (V) for segment S. **(b)** We substitute a L segment with a S segment (red arrows). **(c)** The phason flip causes a shift in the slope of the cut plane and a shift in the overall length of the FS sequence. The shadows show the location of the cut plane lattice vectors for an ideal FS.

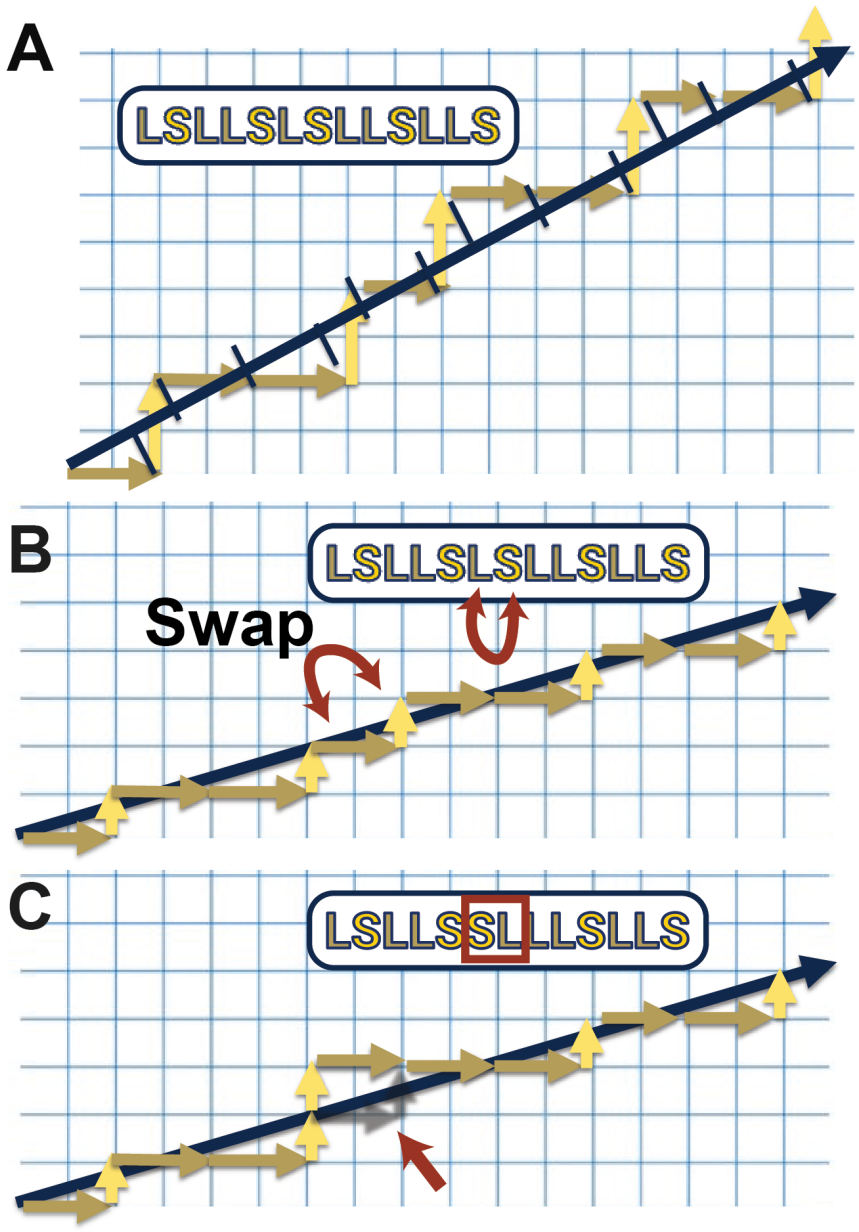

Figure 2.7: **How phason flips can disrupt quasiperiodicity locally, without introducing phason strain globally.** **(a)** Shows a segment of an ideal 1D FS in hyperspace, where the dark blue arrow is the parallel subspace, $V_{\parallel}$. Brown arrows (darker color) correspond to the lattice vector in hyperspace (V) for segment L, while yellow arrows (lighter color) correspond to the lattice vector in hyperspace (V) for segment S. **(b)** We swap a L segment with a S segment (red arrows). **(c)** The phason flip does not cause a shift in the slope of the cut plane, despite introducing a *phason defect* in perpendicular space. The shadows and red arrow show the location of ideal hyperspace coordinate.

2.6 Challenges Associated with Quasicrystal Analysis

Standard theoretical treatment of physical properties in quasicrystals (QCs) is difficult due to their aperiodic nature. To date, the higher-dimensional approach to QCs has been the most successful and ubiquitous approach to both conceptualize and analyze order in QCs [38, 40, 66, 67, 95, 119]. The hyperspace approach enables us to describe QCs as periodic structures in higher dimensions. This means the hyperspace approach is undeniably powerful, as it enables theoretical extension of 3D crystallography to QCs.

2.6.1 Structural Analysis in Higher-Dimensional Space

The hyperspace approach, however, is not without its limitations. The main challenge comes from applying higher-dimensional theories of *phonon* strain, dislocation, defects, and *phason strain* to experimental and self-assembled systems. Here, phonon strain refers to continuous, physical (i.e. "real" or parallel) space deformations to the lattice, while phason strain refers, broadly, to a measure of QCs deviations from quasiperiodicity.

Namely, these higher-dimension theories require some sort of *lifting* procedure, where we transform our physical space lattices (e.g. 2D or 3D lattices) to higher-dimensional lattices (e.g. 4D or 6D lattices), followed by projection of our high-dimensional lattice back down to a *parallel* subspace ($V_{\parallel}$; analogous to physical space) and *perpendicular* space ($V_{\perp}$; an orthogonal subspace arising from the hyperspace interpretation of quasiperiodic order) [2].

2.6.1.1 Lifting Protocols

Although the lifting and cut-and-project procedure have been used extensively to compute phason strain (i.e. global deviations from quasiperiodicity) in self-assembled systems [38, 40, 52, 67, 95], we find that these algorithms scale poorly to larger systems.

Lifting can be thought of as a shortest-path problem, where we compute a path between some reference point in a given QC, and all other connected atoms/molecules in that QC. Even ignoring the complexities and nuances associated with creating, finding and defining neighbors in a given system of particles or atoms, we see that even the most efficient shortest path algorithms has a computational complexity of $\mathcal{O}(NM)$ [69], where N is the number of vertices (particles in the QC lattice) and M is the number of edges (bonds).

[2] Although this section focuses on the drawbacks and limitations of the hyperspace approach and conventional methodologies for phason strain calculation, the hyperspace approach is still fundamental to the description of order and symmetries present in QCs. As such, it remains a staple in all texts and discussions regarding QCs. More detailed theoretical discussion regarding phason strain and hyperspace can be found in this work (Ch. 2 and Sec. 4.4.1) and in various academic texts. Some good sources include: [38, 66, 119, 126].

While the lifting protocol alone is slow and expensive, it is not necessarily prohibitive for large systems. It is, however, complicated by the presence of phonon strain and dislocations. The presence of continuous distortions to the lattice, which can arise even in the absence of some external source of strain, can cause artifacts in the subspace projections (e.g. false dislocations and grains) that can affect phason strain measurements. In simulation, we can circumvent these issues by, say, quenching each frame to remove the effects of thermal fluctuation, but this additional step only adds additional cost and complexity to the analysis pipeline.

2.6.1.2 Phason Strain Measurments

The computation of phason strain from the lifted and projected molecules/atoms is perhaps the most computationally demanding portion of the analysis. This step involves computing a Euclidean distance matrix between all parallel space positions and perpendicular space positions, followed by linear regression of $r_{\parallel}$ vs $r_{\perp}$, where $r_{\parallel}$ is the pairwise distance betwen all points with respect to all other points in $V_{\parallel}$ and $r_{\perp}$ is the pairwise distance of all points with respect to all other points in $V_{\perp}$. The distance matrix computation alone is an expensive task, with a computational complexity of $\mathcal{O}(N^2)$, where N is the number of points in the QC lattice. This step is the most computationally demanding and prohibitively expensive for the large scale simulation growth studies performed in Ch. 3 and 4, where we have simulations with up to 1 million particles and > 200 frames each.

We note that the size of these systems is necessary, since the lack of periodicity and the long-range order inherit to quasiperiodic functions and QCs means that we want to measure phason strain over as large of an area as possible. Otherwise, system size effects will affect our measurements. Additionally, our aim here is to model the growth behavior discovered by our experimental collaborators in the Shahani group at an atomistic level. The methods used by our collaborators enable them to track QC growth behavior at a macroscopic scale, but lack the spatial and temporal resolution required to perform the particle-based phason measurments discussed in this section. Molecular dynamics (MD) simulations enable us to examine QC growth at atomistic length-scales, and thus track phason strain. It follow then, that our simulations need to be sufficiently large to model the relevant phenoma, and that the analysis we use to analyze our simulations must be efficient enough to handle these large-scale simulation studies.

2.6.2 Local Particle Descriptors

The lack of translational periodicity in physical space limits the application of conventional measures of bond order [123] to QCs. Common measures of local bond order include general descriptors of bond symmetry (e.g. bond orientation order parameters [5, 16, 123]; translational order parameters [5]; Minkowski structure metrics [92]), or algorithms like common neighbor

analysis (CNA) [60], dislocation extraction algorithm (DXA) [131, 132], and polyhedral template matching (PTM) [79], which automatically match crystal structures, dislocations, and grain boundaries in simple condensed phases by comparison to a library of lattices.

Template-based methods like CNA [60], DXA [131, 132], and PTM [79] are not applicable to QC because of their explicit reliance on the concept of a single unit cell.

General descriptors of local bond order like bond angle order analysis [2], the Steinhardt order parameter [123] and Minkoski structure metrics [92], however, do not require a library of lattices to identify grains or disorder in condensed phases, but still require careful selection of particle neighbors or local symmetry to return meaningful results. In the context of QC, which have heterogenous local environments arising from the loss of translational periodicity (see Fig. 2.2 for an example), researchers must take particular care in how they define bonds, neighbors, and symmetries in their systems. Given proper selection of neighbors and parameters, local measures of order can, and have, been adapted to differentiate liquid from QCs [52, 81] and to identify local motifs in QCs [67, 81]. These measures of order, however, are often developed with specific motifs and QC structures in mind, and are not generalizable to other QC structures. They are also, still inherently measures of local order and cannot be used to measure deviation from long-range order (e.g. phason strain) on their own.

2.6.3 Machine Learning

In recent years, numerous machine learning (ML) models have been developed to classify local particle environments [11, 45, 82, 104, 120]. Though powerful, deep, supervised ML models require well-labeled data from a variety of crystal structures to return a generalizable model. However, obtaining per-particle labels of local environments in a crystal structure remains challenging and labor intensive, even in periodic crystals. This means supervised ML models tend to rely on established order parameters to label local environments in training data, and that training data is restricted to structures that researchers can already characterize, making supervised ML unsuitable for QC analysis.

Unsupervised ML attempts to circumvent issues with obtaining a variety of labeled, high quality structures that supervised models face. These typically use some combination of clustering and dimensionality reduction to classify particle environments based on particle positions and some set of general descriptors [12, 13, 26, 50, 104, 120]. These methods have been used to effectively classify structures in complex phase diagrams [120], to segment grains in polycrystalline samples [13], to separate growing grains from fluid [104], and, more recently, to identify defects in crystals [12, 26, 50].

Though effective at classification of large domains in a crystal structure, the application of

these types of models to the detection of point defects, line dislocations, and the like remains limited, even in periodic crystals. Existing models are either restricted to 2D inputs [26], rely on 3D, system specific parameters to return meaningful results [12], or they have low precision [50]. None of these models have ever been tested on QCs.

2.7 Bragg Peak Filtering

Revisiting the International Union of Crystallography (IUCr) definition of crystal, however, yields a promising hint on how we may approach quasicrystal (QC) analysis. By definition, all crystals (including QCs) have essentially sharp Bragg peaks in their diffraction patterns [48].

In periodic crystals, it has been shown that the point group symmetries present in direct (i.e. physical) space are present in the Fourier Transform (FT) of that crystal structure [19]. In the diffraction pattern of a QC, too, the rotational symmetries and scaling symmetries are preserved. In fact, it well known and documented that both phasons and phonons can cause changes to Bragg peak intensity and shape [43, 66, 88, 119] (see Figs. 2.5 and 2.3).

2.7.1 Geometric Phase Analysis

Electron microscopists have long used a type of reciprocal space analysis called geometric phase analysis (GPA) [62, 105] to analyze defects and dislocations in electron microscope and scanning transmission electron microscopy (STEM) images. This technique is powerful and precise, and can even be used to measure displacements in atomic lattices at the picometer scale ($< 10pm$) [109], though it can be prone to noise and artifacts [3].

GPA takes advantage of the relationships between reciprocal space and direct space, where defects and dislocations can be represent as distortions to a displacement field $\Delta\vec{b}_k$ in direct space [62, 105]:

$$H(\vec{r}) = \frac{1}{N}\sum_{k}^{N} \cos(2\pi\vec{r}\cdot\vec{b}_k - 2\pi\vec{r}\cdot\Delta\vec{b}_k) \tag{2.8}$$

These displacement fields, in turn, can cause distortions in the peaks seen in reciprocal space. For a crystal with thermal noise, point defects, and dislocations, we no longer have a perfect, point-like Fourier spectrum. This means that the discrete Fourier Transform (DFT) of a crystal behaves like a histogram, where the amplitude of each peak in $||F(\vec{x})||$ (i.e. power spectrum) tells us how many points contribute to a given $\vec{b}_k$. Meanwhile, broadening of these peaks tells us how many particles are strained with respect to a given $\vec{b}_k$. In some ways, we can think about the peak as a sort of 2D or 3D density functions.

[3] See Sec. 5.2.4.

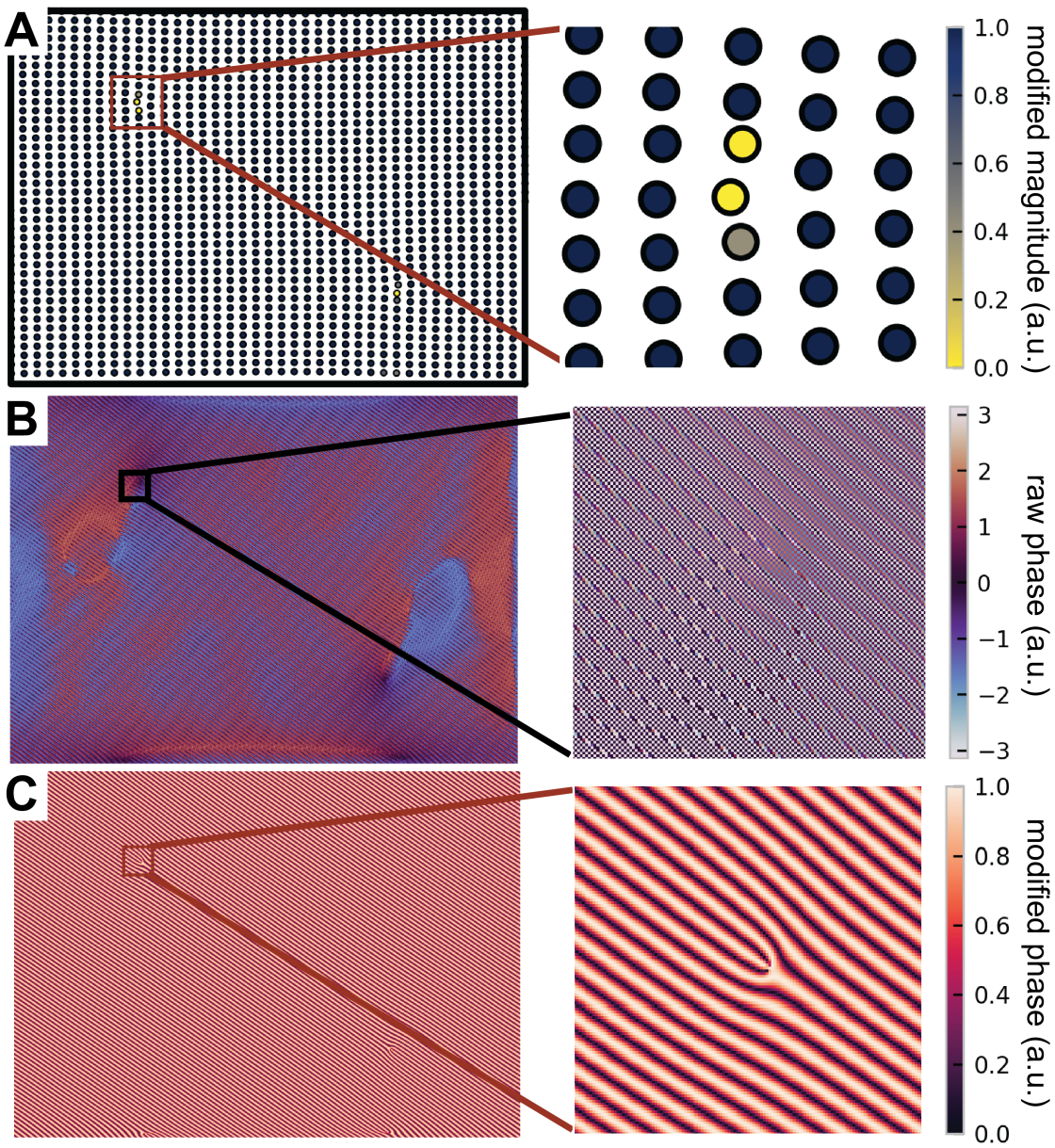

Figure 2.8: **Dislocation detection from Bragg peak filtering using *peakyFinders*.** For a 2D simulation of a dislocation pair in a square lattice: **(a)** Dislocation detected from a single, filtered Bragg peak. The magnitude of the inverse Fourier Transform (iFT) was normalized to 1, then mapped onto a sigmoid centered at 0.3 and scaled to 128. Dark blue (darker color) corresponds to regions aligned with the lattice vector. Yellow (lighter color) corresponds regions with poor alignment to the lattice vector. Values were mapped from 2D iFT images to 2D simulation points. **(b)** Modified phase of the iFT. We can see changes and distortions in the phase due to the presence of a dislocation. **(c)** Moiré interference pattern due to the dislocation shown in **(a)** and **(b)**. For clarity, phase of the iFT (**(b)**) was mapped to Eqn. 5.8. In **(b)**, blue indicates a value of 0, and yellow indicates a value of 1.

2.7.2 Bragg Peak Filtering in a Periodic Example

When we filter these Bragg peaks, we select a pair of Bragg peaks in the FT of the crystal, then zero out all values outside of the selected pair of Bragg peak. Then, we perform an iFT on the isolated Bragg peaks. The resulting FT and iFT output, ξ_k, for a pair of filtered Bragg peaks in a perfect crystal will looks something like Fig. 2.1 **(a)**. Meanwhile, taking the inverse FT of a crystal with defects or dislocations yields disortions and interference patterns (Fig. 2.8 **(b, c)**), where Fig. 2.8 **(b)** shows a result analogous to the phase Eqn. 2.8,

$$\xi_k(\vec{r}) = h_k(\vec{r})cos(2\pi\vec{r}\cdot\vec{b}_k - 2\pi\vec{r}\cdot\Delta\vec{b}_k) \tag{2.9}$$

where ξ_k denotes the iFT of the Bragg peak filtered FT and $h_k(\vec{r})$ denotes the direct space intensity of a point, $\vec{r}$, in the filtered iFT.

In GPA, we take the **phase**, ϕ. Where phase typically refers to the angular component in $cos(\phi)$ or $e^{2\pi i\phi}$. In the case of Eqn. 2.9 $\phi = 2\pi\vec{r}\cdot\vec{b}_k - 2\pi\vec{r}\cdot\Delta\vec{b}_k$. From these results, it is possible to isolate the displacement field associated with a given, $\Delta\vec{b}_k$.

2.7.3 Bragg Peak Filtering and Quasicrystals

More recently, Freedman et. al. [43] showed how Bragg peak filtering could be used to measure both phonon strain and localized phason strain in photonic QCs. In the following chapters, we will extend and build on the methodology presented in [43]. We show the strengths and limitations of this technique in QCs, then develop a novel, more generalized methodology inspired by the work presented in [43].

Here, we give an overview of Bragg peak filtering and how reciprocal space relates to phasons and higher dimensional crystallography.

While it's possible to measure phason strain from real space systems using the concepts of hyperspace, lifting, and cut-and-project discussed in the previous sections, and the algorithmis outlined in Sec. 2.6.1.1 make this analysis prohibitively expensive.

Instead, we choose to approach the analysis of QC using Bragg peak filtering and the reciprocal space image of QC. Bragg peak filtering analysis is convenient for two major reasons: (1) Fast Fourier Transform (FFT) algorithm [28] is efficient, reliable, and well established, and (2) it is fundamentally related the order in crystals and higher dimensional crystallography.

To understand how Bragg peak filtering gives us an alternative lens to measure both phononic and phasonic disorder in a QC, it helps to re-examine periodic crystals in the context of plane waves (Sec. 2.1.3) and to revisit the concept of quasiperiodic functions (Sec. 2.3).

This view of crystals as a sum of plane waves, rather than points, is helpful in capturing the

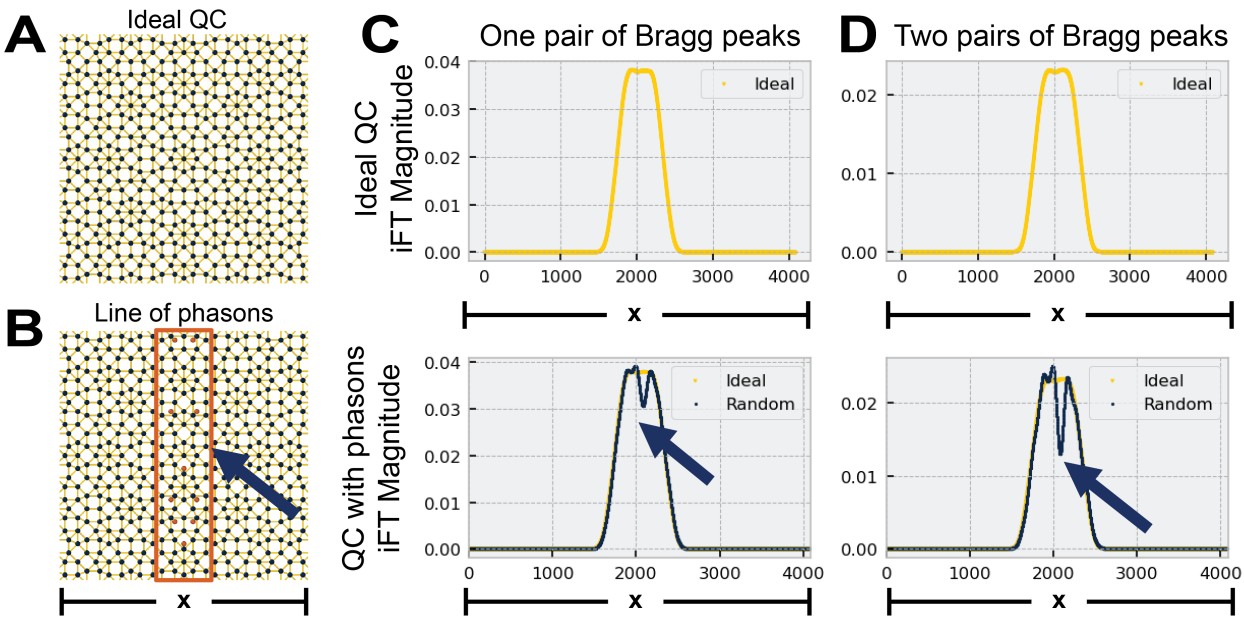

Figure 2.9: **Bragg peak filtering on a QC with engineered phason strain.** We compare the positional order parameter ξ for an **(a)** ideal Ammann-Beenker Tiling (AB) QC, and an **(b)** AB QC with an line of phasons (orange boxed region; orange points are positions from the ideal tiling). We compute the positional order ξ for the ideal AB by filtering **(c)** a pair of Bragg peaks associated with some basis vector $\vec{b}_k$ and **(d)** two pairs of Bragg peaks. We in ξ along the x-axis and compute the mean of each bin for the ideal QC (tiling shown in **a**; yellow lines in **c, d**), and the QC with a line of phasons (tiling shown in **(b)**; blue lines in **(c, d)**). Here, one set of peaks is associated with $\vec{b}_k$, and the other pair is related to $c\vec{b}_k$, where, $c = 1 + \sqrt{2}$ is the silver ratio, or the incommensurate ratio between length scales associated with AB. This is conceptually analogous to scaling $\vec{b}_k$ by the golden ratio, $\tau = \frac{1+\sqrt{5}}{2}$ and filtering by both pairs of Bragg peaks.

long-range order associated with QCs because it allows us to reduce the complex, local structures and rules associated with QC to a simple set of equations. In such cases, global deviations from aperiodicity are measured as shifts in frequency, rather than, say, violations of matching rules or distances from higher dimensional cut planes. Meanwhile, local deviations from global order, such as aperiodicity (phason strain) and real space dislocations and real-space strain (phonon strain), can be captured as displacements in phase space [43, 105] and changes in the magnitude of the Bragg peak filtered iFT, $||\xi||$, (see Fig. 2.9 and Sec. 2.1.3) where $||\cdot||$ is the norm of a vector $||\vec{a}|| = \sqrt{\vec{a} \cdot \vec{a}^*}$ and $\vec{a}^*$ is the complex conjugate of $\vec{a}$.

2.7.4 Revisiting Periodic and Quasiperiodic Functions

A simple example of can be constructed from the sum of two cosines, $f(x) = cos(2\pi x) + cos(a2\pi x)$. When a is rational, we can define a single length scale (or, the period of $f(x)$), b,

with which we can index identical environments in $f(x)$ (a.k.a. translational periodicity). When a is irrational ($a \notin \mathbb{Q}$), however, $f(x)$ becomes a quasiperiodic function, and we are no longer able to define a single period for our function $f(x)$. Yet, $f(x)$ still has sharp peaks in Fourier space at 1 and $a \notin \mathbb{Q}$, where $\mathbb{Q}$ denotes rational numbers. In this case, we are still able to describe the relation between local maxima in $f(x)$ using two incommensurate lengths, which we can compute from the frequencies associated with $f(x)$. For example, if we take $a = \tau$, where $\tau = \frac{1+\sqrt{5}}{2}$ is the golden ratio, we find that $f(x)$ is closely related to the 1-D Fibonacci Sequence (FS), where the frequencies associated with $f(x)$ give us the two length scales of the associated sequence. For the given $f(x)$, this means the distance between the local maxima of $f(x)$ corresponds to the two length scales of the sequence, and the spacings between local maxima map directly to the 1-D FS (Fig. 2.10, **(c-e)**). Unlike the periodic case, however, the values at local maxima are not equivalent.

Here, another important difference between quasiperiodic functions and periodic functions becomes apparent – periodic functions can be indexed with $D = d$ basis vectors, while quasiperiodic functions are described by $D > d$ [22], where d is the dimension of the function $f(x)$ and D is the number of basis vectors associated with $f(x)$.

In the periodic case, the number of independent basis vectors does not exceed d. As a consequence, it is not possible to reach any point outside the crystal lattice using a linear combination of the crystal's basis vectors, $\sum_k \sum_i n_i \vec{b}_k$ where $n_i \in \mathbb{R}$. That is, the linear combination of d basis vectors in d dimensions yields a unique lattice, and the d basis vectors alone are sufficient to describe both the short- and long-range the order of the crystal. In the case where $f(\vec{x}) = \sum_k \sum_i n_i \vec{b}_k$, the output of $f(\vec{x})$ is discrete. In the case where $f(\vec{x})$ is a continuous periodic function (e.g. $f(\vec{x}) = \cos(2\pi x) + \cos(a2\pi x), a \in \mathbb{Q}$), this means that $f(\vec{x}) = f(\vec{x} + \sum n_i \vec{b})$. As a consequence of this translational periodicity, any deviations from a crystal's ideal structure can be measured based on local deviations from a set of $\vec{b}_k$.

In such cases, global deviations from aperiodicity are measured as shifts in frequency, rather than, say, violations of matching rules or distances from higher dimensional cut planes. Meanwhile, local deviations from global order, such as aperiodicity (phason strain) and real space dislocations and real-space strain (phonon strain), can be captured as displacements in phase space [43, 105] and changes in $||\xi||$ Fig. 2.9, where $||\cdot||$ is the norm of a vector $||\vec{a}|| = \sqrt{\vec{a} \cdot \vec{a}^*}$ and $\vec{a}^*$ is the complex conjugate of $\vec{a}$.

2.7.5 Relation to Higher-Dimensional Crystallography

In contrast, quasiperiodic functions are described by $D > d$ basis vectors [22]. In the case of a function, $f(\vec{x}) = \sum_k \sum_i n_i \vec{b}_k$ where $n_i \in \mathbb{Z}$, the output of $f(\vec{x})$ is no longer discrete. If follows then, that in the function's space (d-dimensional space, or what we call direct space), there is no

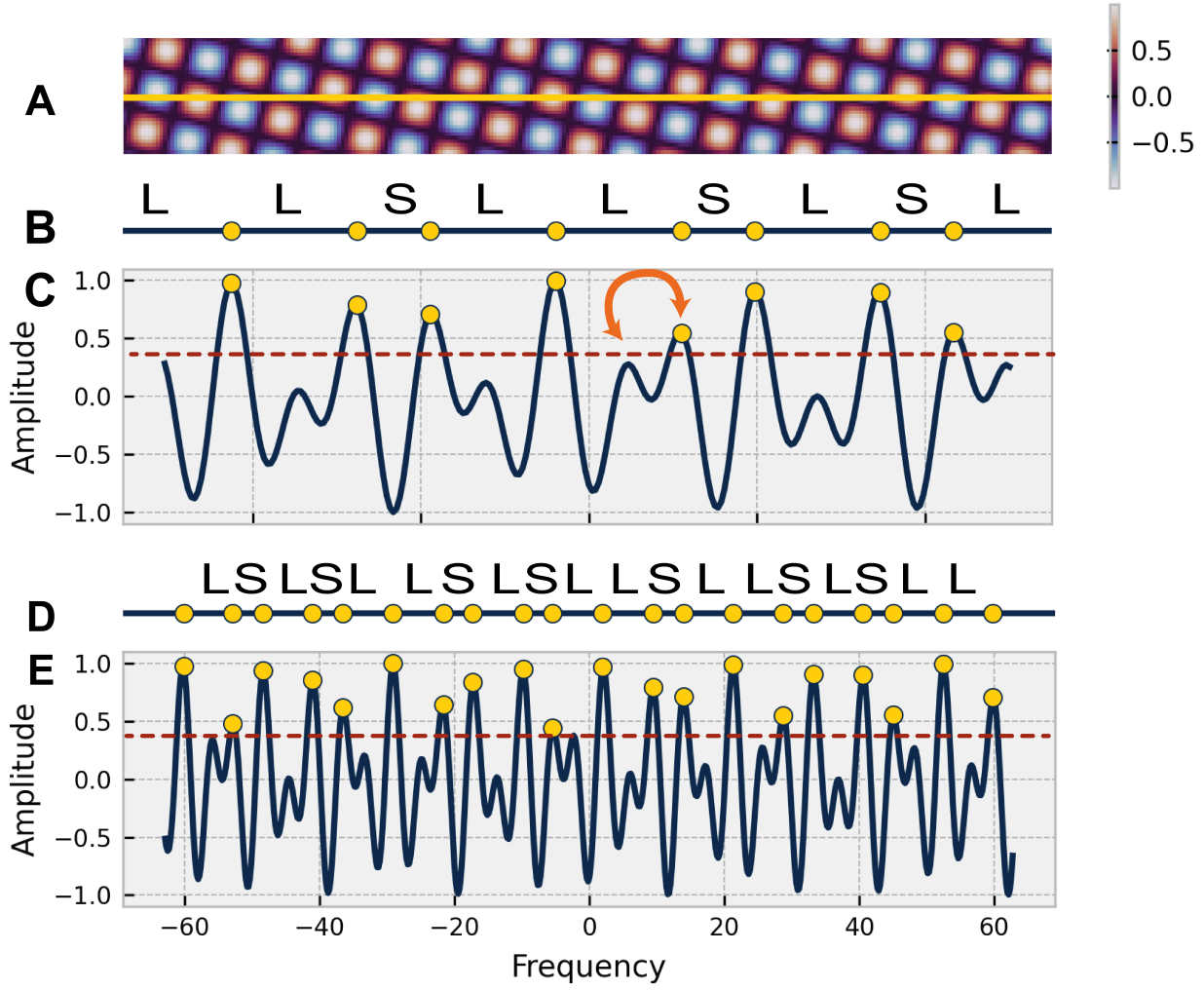

Figure 2.10: **Relationship between plane wave image of quasiperiodicity and higher dimensional crystallography.** **(a)** Two, orthogonal plane waves summed together to make a square-like cosine crystal. Here, we choose to express our basis set as $\vec{b}_1 = [\tau, 1]$ and $\vec{b}_2 = [1, -\tau]$. **(b)** The FS, reconstructed from the local maximum with values greater than 0.4 (dotted red line) in **(c)**. **(c)** Amplitudes from a slice of the hyperlattice (yellow line). The orange arrow shows an example of a phason flip. We note that, as a result of the Fourier projection-slice theorem, taking a 1D slice of the cosine crystal shown in **(a)** is equivalent to computing $f(x) = cos(x + c) + cos(\tau x + c)$ in 1D, where c is some global shift associated with where the 2D function was sliced. **(d)** shows the FS reconstruction and **(e)** the aperiodic signal over a longer interval.

one, unique lattice that can be constructed from a linear combination of $D > d$ basis vectors. Instead, it's possible to construct any lattice using $\sum_k \sum_i n_i \vec{b}_k$. This means we can construct periodic simple cubic (SC) lattices or infinitely dense lattices or lattices that may look like QCs locally, but are either periodic (*approximates*) or lack the quasi long-range translational order (e.g. some random tilings) associated with mathematically ideal QCs (i.e. phason-strain free QCs) [128] using $\sum_k \sum_i n_i \vec{b}_k$.

Similarly, in a continuous, quasiperiodic function (e.g. $f(x) = \cos(2\pi x) + \cos(a2\pi x), a \notin \mathbb{Q}$), the function $f(\vec{x} + \sum_k \sum_i n_i \vec{b}_k) \neq f(\vec{x})$, despite the fact that $\vec{b}_k$ is described by the frequencies associated with $f(\vec{x})$. Yet, if we examine a simple quasiperiodic function like $f(x) = \cos(2\pi x) + \cos(a2\pi x)$, we see that the associated basis vectors give us a convenient way to describe how the local maxima relate to each other (Fig. 2.10).

The relation discussed above shows how the set of $D > d$ basis vectors alone is insufficient in describing the structure of the QC, and that measures of local order (e.g. strain, potential energy, $||\psi_k||$) are unable to measure deviations from the complex, quasi-long range order associated with true QCs. Instead, additional restrictions and rules are necessary to describe and measure local order in a QC or QC-like structure (e.g. matching rules [47], coverings [21], cut-and-project [38, 95]).

We note, however, that it is not straightforward to decouple phason strain from phonon strain using this method. Fig. 2.9 shows how phason defects can introduce sharp dips to the iFT magnitude, $||\xi||$, when filtering one or two pairs of Bragg peaks. Dislocations and defects can also cause decreases in iFT magnitude in periodic crystals (see Chapter 5 for a more detailed discussion on Bragg peak filtering in periodic crystals). Previous studies have suggested that filtering two pairs of Bragg peaks, $\vec{b}_k$ and $\tau\vec{b}_k$, allows us to measure both phason and phonon strain, whereas filtering one pair of Bragg peaks measures phonon strain in a system [43]. Our results suggest that phason strain can still be detected when filtering a single pair of Bragg peaks – though change in $||\xi||$ is much weaker and harder to detect in these cases.

2.8 Summary

Here, we introduce the mathematical concepts needed for the research presented in this dissertation. We provide a brief introduction to quasiperiodicity, reciprocal space, and self-similarity in the context of QCs and phasons, and we discuss the strengths and limitations of existing methods for periodic crystal and QC analysis.

CHAPTER 3

Formation of a Single Quasicrystal Upon Collision of Multiple Grains

This chapter is a modified version of our published work:

> Insung Han.*, **Kelly L. Wang***, Andrew T. Cadotte, Zhucong Xi, Hadi Parsamehr, Xianghui Xiao, Sharon C. Glotzer, and Ashwin J. Shahani. "Formation of a single quasicrystal upon collision of multiple grains." *Nature Communications* 12, no. 1 (2021): 5790. * These authors contributed equally.

This paper was a joint simulation-experimental collaboration with the Shahani group, who we refer to as our collaborators in the text. All data and measurements were conducted by the Shahani group. All simulations and grain orientation analysis were conducted by me.

When grown as single crystals, quasicrystals (QCs) possess distinctive and unusual properties owing to the absence of grain boundaries. Unfortunately, conventional methods such as bulk crystal growth or thin film deposition only allow us to synthesize either polycrystalline QCs or QCs that are at most a few centimeters in size. Here, our collaborators in the Shahani group reveal through real-time and 3D imaging the formation of a single decagonal quasicrystals (dec-QCs) arising from a hard collision between multiple growing QC in an Al-Co-Ni liquid. Through corresponding molecular dynamics simulations, we examine the underlying kinetics of QC coalescence and investigate the effects of initial misorientation between the growing quasicrystalline grains on the formation of grain boundaries. At small misorientation, coalescence occurs following rigid rotation that is facilitated by phasons. Our joint experimental-computational discovery paves the way toward fabrication of single, large-scale QCs for novel applications.

3.1 Introduction

The growth mechanism of QCs has attracted great interest [68, 71] due to their unique crystal structure that cannot be explained by the presence of a unit cell [116]. Instead, QC lattices may be described by two or more space-filling motifs [40, 122], or *tiles*. The presence of multiple tiles is due to an additional degree of freedom present in QCs *phason* [119], which encompasses associated modes of phason strain and its relaxation (*e.g.* phason flips) [41, 43, 119]. Phason strain describes the deviation from ideal quasiperiodicity [128] and phason flips are characterized by discrete particle motions [41] that result in a change in tiling configuration. These changes in tiling configurations are representative of phason excitations and relaxations, and do not introduce defects into the crystal [119]. Previous studies suggest that entropic contributions can have a significant influence on QC stability [68, 71, 129]. This suggests there is degeneracy in tile configurations that preserves quasiperiodicity and that QCs can grow into low or zero phason strain structures without the need for complex phason flip sequences [129].

Although past studies on QC growth mechanisms extend our understanding of phason contributions to stability in a bulk QC [68, 71, 129], studies on phason contributions to the formation and motion of grain boundaries (GBs) remain limited [110]. Yet the latter is critically important from a practical standpoint since the formation of polycrystals is unavoidable due to finite nucleation rates below the melting point. That is, two solid nuclei may impinge on one another, retaining their structure and forming a long-lasting GB. The GBs can, in turn, deteriorate material properties. For instance, defects in quasicrystalline films render the substrate underneath more vulnerable to corrosion by providing a channel for electrolytic attack [10]. In addition, the anisotropic thermal, electrical, and frictional properties of dec-QCs can be maximized for future applications [89, 99], provided the QCs are devoid of GBs between mismatched solid crystal nuclei.

Recently, Schmiedeberg et al. [110] conducted phase field crystal simulations to determine whether and when a GB may form between two QCs. In general, they observe that grain coalescence occurs more readily in dodecagonal QCs than in periodic crystals. This finding is remarkable given that two QCs are always incommensurate. They also reported that phasons play a significant role in distributing stress [110] around the non-fitting structures, where the resulting phason strain can be relaxed via phason flips [41]. Despite the insights obtained by Schmiedeberg et al. [110], the fundamental question remains: Can coalescence take place in experimental systems? If so, how can simulations support experimental observations?

Here, our experimental collaborators in the Shahani group investigate the growth dynamics of multiple thermodynamically-stable dec-QC grains [141] upon solidification of an $Al_{79}Co_6Ni_{15}$ alloy. They used synchrotron-based, four-dimensional (*i.e.*, 3D space plus time-resolved), x-ray tomography (XRT) to resolve *grain coalescence*, or the time-dependent formation of a single dec-QC

from multiple grains. This experimental technique has opened a paradigm shift in solidification science, allowing them to capture transient microstructural dynamics in optically opaque materials [4, 7, 115]. To the best of our knowledge, our *in situ* experiments provide the first-ever demonstration of QC coalescence. On the basis of their experimental results, we performed molecular dynamics (MD) simulations to identify the mechanism of grain coalescence (or conversely, GB formation) at the atomic scale. We examine relevant crystal rotation mechanisms [23, 57, 93, 135, 140] and discuss the role of phasons in facilitating grain coalescence as well as their density as a function of misorientation between grains. Our combined efforts provide the direct evidence of single crystal formation between incommensurate structures, such as QCs.

3.2 Methods

3.2.1 Decagonal Quasicrystal Simulation

MD simulation was performed with HOOMD-blue [6] in the isobaric-isothermal (NPT) ensemble. Simulations used reduced units of energy (ϵ), length ($d = 1.02$) in arbitrary units, mass (m), and time ($\tau = \sqrt{\frac{md^2}{\epsilon}}$). Particles interacted through an oscillatory, double-well potential [32] (Fig. 3.1), previously shown to form dec-QCs,

$$V(r) = V_{\text{PMF}}(r) - \varepsilon \exp\left(-\frac{(r-d)^2}{2\sigma^2}\right) - V(r_{cut}) \tag{3.1}$$

where $V_{PMF}(r)$ is the tabulated potential of mean force (PMF) constructed from the radial distribution of a diamond-forming system [30], $\varepsilon = -1.8$, $d = 1.02$ is the location of the first minimum, σ is the width of the Gaussian applied to the first well, and $r_{cut} = 2.9d$ is the cutoff. The pair potential was smoothed and shifted to 0 at r_{cut}.

Each simulation was performed with 500,000 particles and with periodic boundary conditions in 3 dimensions. Simulations were carried out in quasi-2D boxes with final average dimensions of $360 \times 360 \times 8$ to reduce the influence of layer mismatches and rearrangements along the periodic axis and to maximize the amount of atomic rearrangements in the quasicrystalline plane. Systems were linearly cooled from a liquid-like configuration ($T^*_{init} = 1.5$) to a temperature near, but below the melting point ($T^*_{end} = 0.4$) over 100,000 timesteps. The temperature was expressed in a reduced unit of $T^* = \frac{k_b T}{\epsilon}$, where k_b is the Boltzmann constant. Each system was then held at T^*_{end} for 20 million simulation timesteps at a pressure of 3.9. Simulations consisted of two fixed seeds with a distance of 40 between the seed centers and misorientation between 0° and 18°. For each misorientation, 3-5 simulations were run to ensure consistency of the results. The computational workflow and general data management in particular for this publication was primarily supported

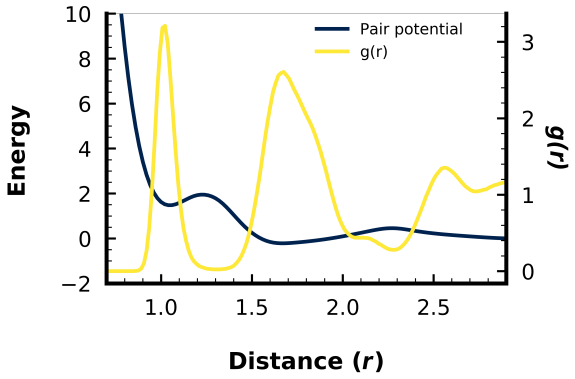

Figure 3.1: **Tabulated pair potential and radial distribution function for QC simulations.** [52] The single-component, isotropic pair potential (dark blue) used for all dec-QC simulations is derived from the potential mean of force of a diamond-forming system [30]. The radial distribution function is shown in yellow, $g(r)$, for a single seeded dec-QC simulation after 19.7×10^6 timesteps.

by the signac data management framework [3].

3.2.2 Orientational Order Parameter Analysis

We used the bond-orientational order parameter for k-atic rotational symmetry[127] to identify the local orientational symmetry of each particle m:

$$\psi_k(m) = \frac{1}{n} \sum_{j}^{n} e^{ki\theta_{mj}} \tag{3.2}$$

where n is the number of neighboring particles and θ represents the angle between local bond orientations and a fixed basis with k-atic rotational symmetry, or, the local grain orientaions (LGO). For a decagonal quasicrystal, we use the value of $k = 10$, so that $\psi_{10}(m)$ refers to the decatic order parameter. For face-centered cubic (FCC) simulations, we computed $\psi_4(m)$, or the quadratic order parameter, on the 2D projection of the crystal down the 2-fold rotational axis. We note that the projected structure resembles a simple square lattice, resulting in 4-fold, rather than 2-fold rotational symmetry in the 2D lattice. We determine neighbors for particle m as the k nearest neighbors to ensure that measurements reflect the local atomic environment of each particle. Data analysis for this publication utilized the freud library[102].

3.2.3 Face-Centered Cubic Crystal Simulations

We carried out additional MD simulations of an FCC forming system via the 6-12 Lennard-Jones (LJ) pair potential,

$$V_{LJ} = 4\epsilon \left[\left(\frac{\sigma}{r}\right)^{12} - \left(\frac{\sigma}{r}\right)^{6} \right] \tag{3.3}$$

that is truncated at $r_{cut} = 2.5 * \sigma$, where $\sigma = 1.0$, $\epsilon = 1.0$, and r is the distance from the center of a particle, expressed in units of σ. Temperature was fixed at $kT = 0.6$, and pressure was fixed at $P = 1.0$ in reduced units. All periodic simulations contained $\approx 500,000$ atoms and contained either one or two fixed seeds, with 499 atoms each, and the potential was shifted and smoothed so that both the potential and its derivative are zero at the cutoff.

3.2.4 Orientational Order Paramater Mapping

For qualitative comparison of grain rotation between two seeds with different misorientation, we normalize LGOs of individual particles based on their deviation from seed LGOs. To begin, we constructed expected histograms for two seeded simulations as bimodal distributions from histograms of single seeded reference simulations (yellow line, Fig. 3.2), where peaks correspond to the reference seed misorientation ($\theta = 0°$) and the rotated seed misorientation ($0° \leq \theta \leq 18°$, $6°$ in Fig. 3.2). We remap the LGO of individual particles to the bimodal cumulative histogram, $cf(\theta)$. This highlights small changes in misorientation and makes it possible to compare grain interactions at various misorientations without manual rescaling.

This is because the cumulative distribution $cf(\theta)$ always equals 0.5 when θ equals mean of a unimodal distribution corresponds. If we construct our bimodal distribution as a mixture of two Gaussian-like distributions with identical variance, but different means, if follows that the means in the bimodal distribution correspond $cf(\theta_{0.25}) \approx 0.25$ and $cf(\theta_{0.75}) \approx 0.75$, where $\theta_{0.25} = 0°$ and $\theta_{0.75}$ corresponds to the LGO of the rotated seed (in Fig. 3.2, $\theta_{0.75} = 6°$). Particles with LGOs different from either seed have $cf(\theta)$ of 1 or 0, and seeds with intermediate orientations have $cf(\theta)$ between 0.25 and 0.75, where LGOs with $cf(\theta)$s of 1 or 0 have the same meaning. This is because, for the 10-fold rotational symmetry found in dec-QCs, the basis vectors are invariant for rotations $36°$, meaning, LGOs of $-10°$ and $26°$ are equivalent. Here, we define intermediate orientations as angles that lie along the shortest rotation between two seeds (black region in Fig. 3.2) and unlike orientations as angles that lie along the longest rotation between two seeds (white region in Fig. 3.2). The inclusion of the extreme cases, where orientations are highly unlike either seeds, is useful in identifying liquid regions in the dec-QC during growth, such as in Fig. 3.10. It is important to note that as misorientation approaches $18°$, the difference between "intermediate" orientations and "unlike" orientations diminishes.

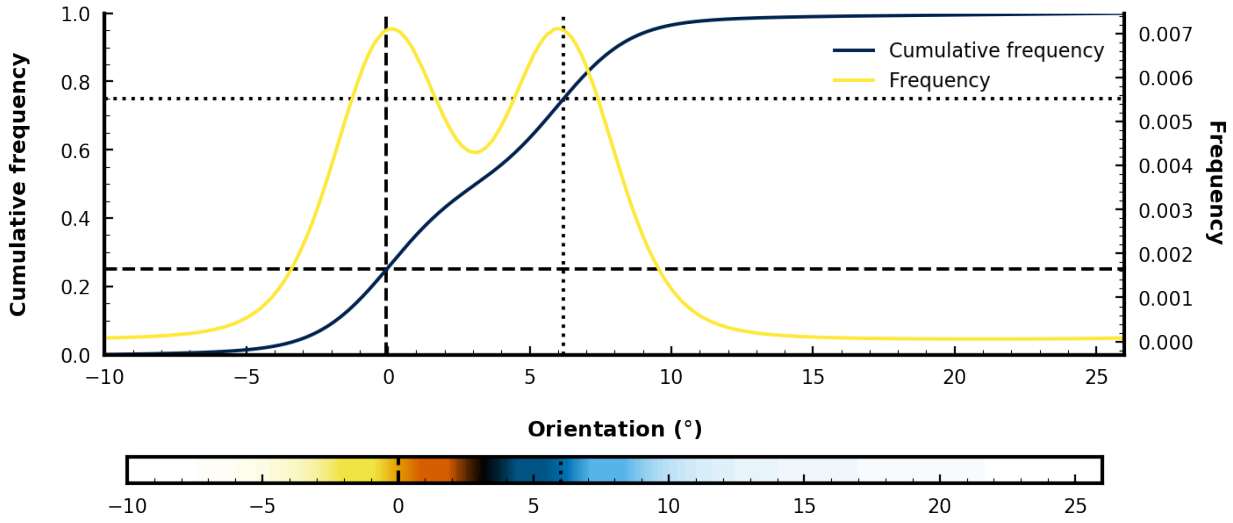

Figure 3.2: **Orientantaional order mapping for QC simulations with 6° misorientation.** [52] Mapping LGOs onto the cumulative histogram ($cf(\theta)$, blue line) of LGOs for 6° misorientation between seeds. Black dashed lines indicate the LGO when $cf(\theta_{0.25}) = 0.25$. Black dotted lines indicate the LGO when $cf(\theta_{0.75}) = 0.75$. These regions correspond to the peaks (means) in the expected bimodal histogram (yellow line, $f(\theta)$) of LGOs. Using values from the cumulative histogram, we create a colormap where alignment with the reference seed ($\theta_{0.25} = 0°$, dashed lines) corresponds to yellow-orange and alignment with the rotate seed ($\theta_{0.75} = 6°$ in this example, dotted lines) corresponds to blue. Black corresponds to LGOs between 0° and the LGO associated with the rotated seed (6° in this example), while white corresponds to $-10° < \theta < 0°$ or $16° < \theta < 28°$. Due to the 10-fold rotational symmetry of the dec-QC, the angle between each basis vector is 36°. We keep all LGOs values between $-10° < \theta \leq 26°$, where a value of 27° would be equivalent to $-9°$. This means that the white region could also be defined as an interval between $0° < \theta < \theta_{0.75}$, but the arc it represents is longer than the arc for the black region for all seed misorientations below 18°.

3.3 Results

3.3.1 Grain Coalescence Observed in X-Ray Tomography Experiments

The contents of this section were performed by and contributed by the Shahani Group.

Fig. 3.3 depicts the time-evolution of multiple dec-QCs before and after collisions in an alloy of composition $Al_{79}Co_6Ni_{15}$, upon slow cooling (1 °C/min) from above the liquidus (∼1026 °C) to below. The growth sequences of the as-grown dec-QCs were recorded via XRT every 10 mins with 20 s scan time, starting from 1020 °C (at which point the sample was in a fully liquid state). The key advantage of using XRT is that our collaborators can unambiguously visualize the morphologies, misorientations, and growth dynamics of the QCs in real-time and in 3D, without needing to repeatedly quench their specimen. Quenching is known to distort the shapes and orien-

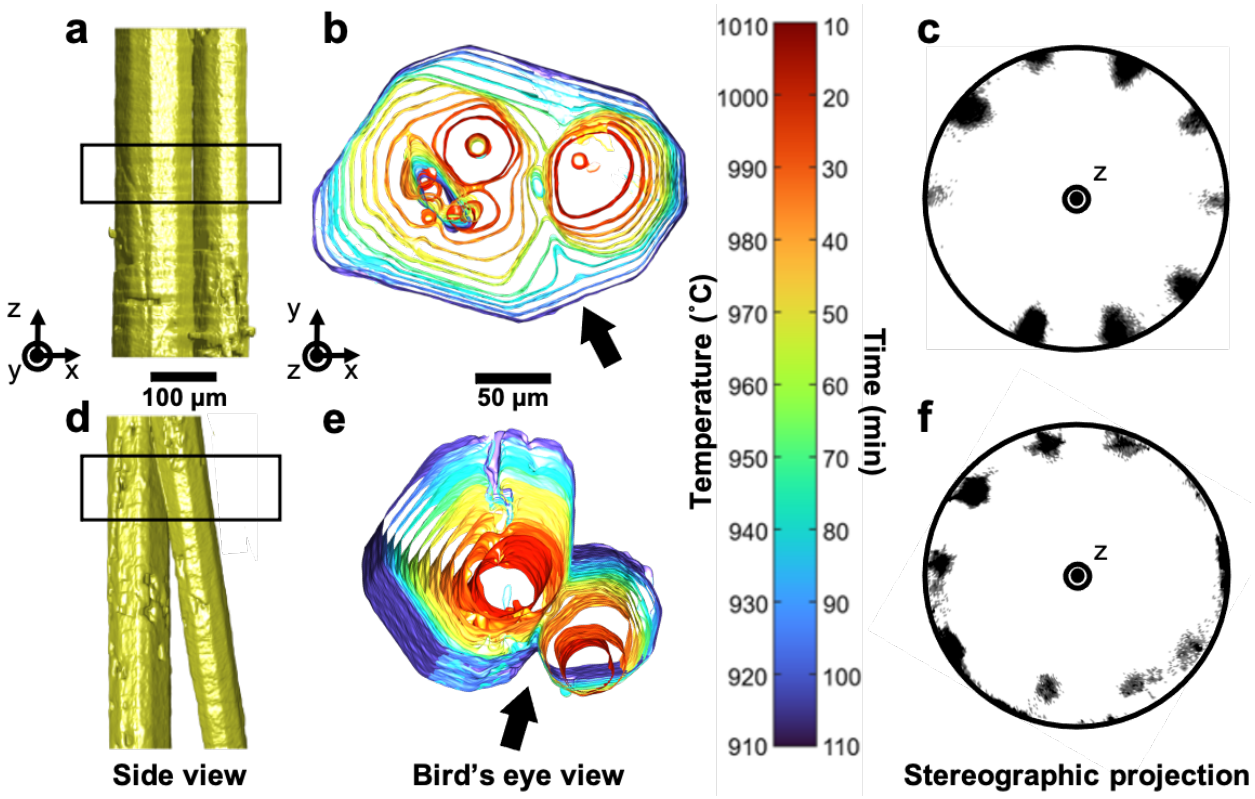

Figure 3.3: **Tracking grain impingements in real-time.** [52] **(a)** Side view ($\hat{z} - \hat{x}$ in the specimen frame) of two dec-QCs with parallel $\langle 00001 \rangle$ long axes, observed after 50 min of cooling (1 °C/min) from 1030 °C. **(b)** Birds-eye view ($\hat{x} - \hat{y}$) of quasiperiodic plane corresponding to boxed region shown in **(a)**. **(c)** Stereographic projection of interface (facet) normal vectors of the outermost isochrone (910 °C) in **(b)**. Zone axis is $\hat{z}$. Facets are evenly projected ($\sim$36° apart) as peaks along the circumference (or primitive circle) of the projection plane, which implies the formation of a single, decaprismatic QC along $\hat{z}$. The missing tenth peak can be attributed to the less developed facet in **(b)**. **(d)** Side view of dec-QCs with non-parallel $\langle 00001 \rangle$ long axes, observed at the same timestep as in **(a)**. **(e)** Birds-eye view of the boxed region shown in **(d)**. **(f)** Stereographic projection of interface normal vectors of the outermost isochrone (910 °C) in **(e)**. Zone axis is again $\hat{z}$. Quasiperiodic facets of two QCs are inclined to the projection plane, and thus the corresponding peaks do not lie on the primitive circle. Peaks are not always separated by 36° either, suggesting a superposition of two single crystal patterns and hence a bi-quasicrystalline structure. Isochrones of the solid-liquid interface in **(b)** and **(e)** are colored to illustrate the passage of time, with early times in red and late times in blue. Times and temperatures in **(b)** and **(d)** are as follows: 10 min (1010 °C), 20 min (1000 °C), 30 min (990 °C), 40 min (980 °C), 50 min (970 °C), 60 min (960 °C), 70 min (950 °C), 80 min (940 °C), 90 min (930 °C), 100 min (920 °C) and 110 min (910 °C). Thick black arrows in **(b)** and **(e)** point to the evolution of the grain boundary groove in time.

tations of the solid-liquid interfaces [25]. They confirmed the existence of dec-QCs in they sample through X-ray diffraction (XRD, see Fig. 3.4(a)) together with a thermodynamic assessment of the Al-Co-Ni system [141]. On the basis of our XRD results on a water-quenched specimen, they plot in Fig. 3.4(b) the physical scattering vector, $G_{||}$ (defined as $4\pi \sin\theta/\lambda$, where λ is X-ray wavelength), against the full width at half maximum (FWHM) of the peaks belonging to the dec-QC in Fig. 3.4(a). The linear relationship between the two quantities indicates that the contribution of phonon strain in the lattice dominates that of phason strain [51]. Therefore, we can expect that phason strain is relaxed if we consider the relatively longer time-scales of the slow cooling experiment showcased in Fig. 3.3.

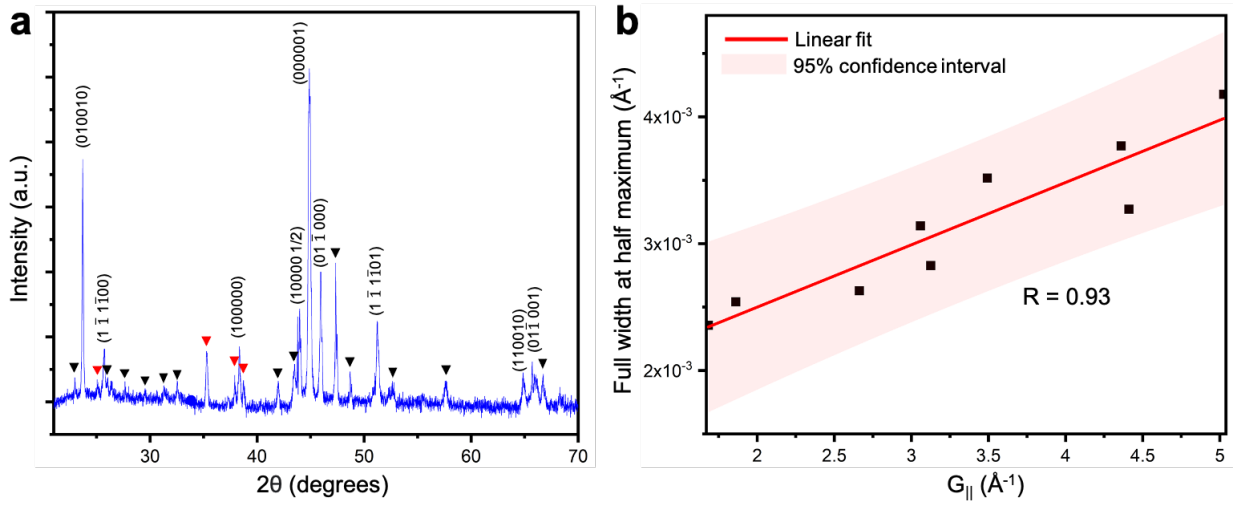

Figure 3.4: **X-ray diffraction analysis.** [52] **(a)** X-ray diffraction pattern of water-quenched $Al_{79}Co_6Ni_{15}$ alloy from an initial temperature of 1030 °C. Rapid quenching prevents peritectic transformation of dec-QCs from proceeding to completion. The diffraction peaks are indexed to confirm the presence of dec-QCs at 970 °C. The peaks indexed with black and red correspond to the Al_3Ni and aluminum oxide, respectively. **(b)** A linear fit with Pearson correlation coefficient of 0.93 is shown between $G_{||}$ and FWHM along with 95% confidence interval bounds, see text for details.

The dec-QCs in Fig. 3.3 show a decaprismatic morphology [53] with a 'long axis' parallel to $\langle 00001 \rangle$, representing the fast-growing periodic direction. Perpendicular to this direction is the aperiodic plane $\{00001\}$. Similar to our collaborators' past experiments [53, 54], the dec-QCs are 'anchored' to the oxide skin of the sample (not pictured), which acts as a fixed, heterogeneous nucleant for the dec-QCs, preventing their displacement. Grain displacement would manifest itself as negative solid-liquid interfacial velocities on one side of the grain and positive interfacial velocities on the other. They do not observe this feature here nor in our prior experiments [53]. As the dec-QCs grow, they interact with each other through *soft impingements* (overlapping diffusion

fields) and *hard impingements* (collisions)[33].

Here, we selectively focus on two different cases of hard collisions between dec-QCs with (i) parallel long axes (Figs. 3.3 **(a-c)**) and (ii) non-parallel long axes (Figs. 3.3 **(d-f)**). Figs. 3.3 **(a,d)** shows these two cases after 50 min of continuous cooling from a viewpoint perpendicular to the long axes of the dec-QCs. Figs. 3.3 **(b, e)** displays a bird's eye (or cross-sectional) view of the growth sequences from the quasiperiodic planes. When the long axes of dec-QCs are parallel (Fig. 3.3 **(b)**), we observed multiple coalescence events, the first between 20-30 min and the second between 50-60 min, the culmination of which is the formation of a single dec-QC.

3.3.1.1 Grain Boundary Groove and Young's Law

The formation of a single dec-QC is further evidenced by the absence of a GB groove (where the GB intersects the solid-liquid interfaces) [9, 94] as well as the presence of ten facets on the coalesced structure at the final time-steps; this end-state is depicted in the outermost isochrone in Fig. 3.3 **(b)** and the near-perfect symmetry of its facets is quantified via interface normal distribution [53, 70] in Fig. 3.3 **(c)**. That is, GBs may be detected in solidification experiments [18, 46, 106, 114] owing to the fact that they create macroscopic depressions (grooves) of the solid-liquid interface around the point at which they emerge into the liquid. According to Young's law [61], the groove angle, ϕ, is related to the grain boundary energy, γ_{gb}, as $\gamma_{gb} = 2\gamma_{sl}\cos(\phi/2)$, where γ_{sl} is the solid-liquid interfacial free energy. If the GB groove persists during solidification, it can be inferred that the GB is stable and fixed to the groove. However, the morphological transition from a V-shaped groove to a faceted interface ($\phi \rightarrow 0°$, see thick arrow in Fig. 3.3 **(b)**) suggests otherwise, i.e., the annihilation of the GB during grain coalescence. Interestingly, the facet orientations of the dec-QCs prior to impingement were nearly the same as those dec-QCs following coalescence. This observation is in line with the findings of Schmiedeberg et al. [110], who testify to the coalescence between two colloidal QCs with small initial misorientation in the aperiodic plane regardless of the initial distance between them. Our quantitative analysis of facet orientations as a function of time (Fig. 3.5) provides further support of this behavior. The groove itself does not move laterally along the solid-liquid interfaces on the intermediate time-scales (see arrow in Fig. 3.3 **(b)**), which would indicate that GB translation on its own is not the mechanism of coalescence.

The irregular shape of the dec-QC on the left-hand-side in Fig. 3.3 **(b)** between 40-50 min of cooling (i.e., prior to collision) can be attributed to a mutual interference of diffusion fields between the two grains.

On the other hand, in the case where the two long axes are non-parallel to each other, we observed the persistence of a V-shaped GB groove (Figs. 3.3 **(d,e)**), signifying the formation of a stable GB between the two grains. In comparison to the above scenario where the long axes are

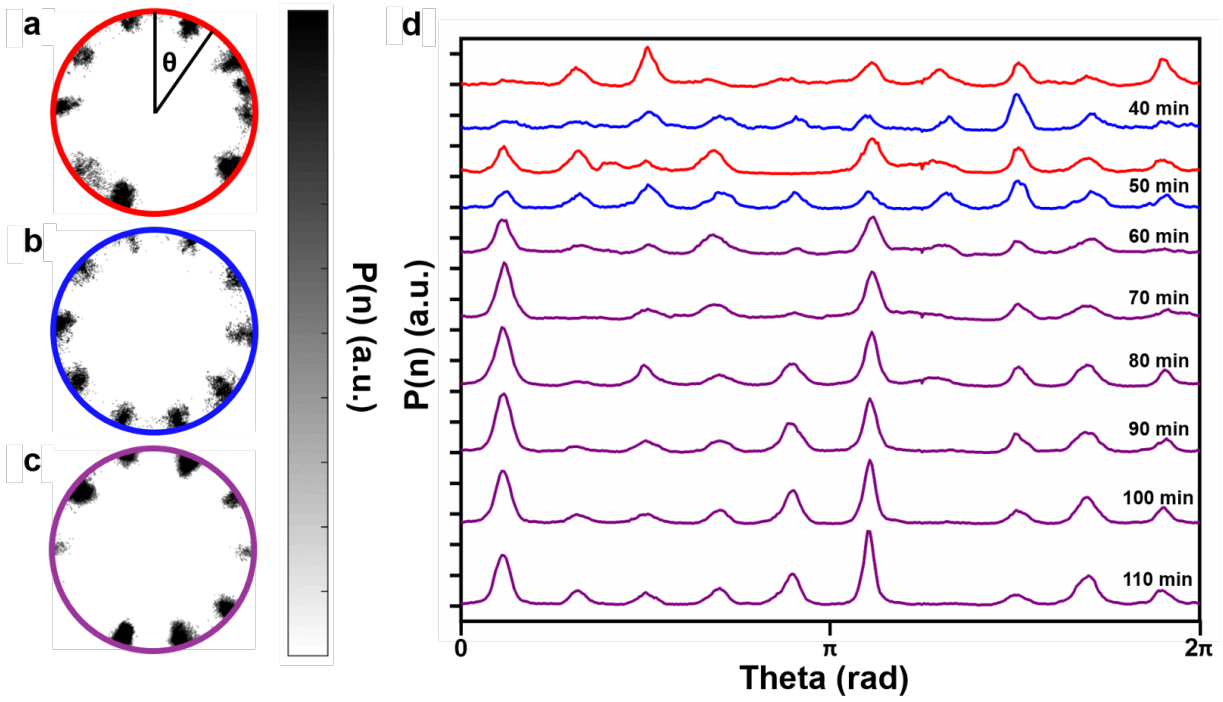

Figure 3.5: **Distribution of facet orientations.** [52] Detailed view of stereographic projections of interface (facet) orientations of dec-QC seeds on the **(a)** left-hand-side, **(b)** right-hand-side in Fig. 1(b) after 50 min of cooling and **(c)** the coalesced dec-QC after 110 min of cooling. Zone axis of projections is the specimen $\hat{z}$ direction, which corresponds to $\langle 00001 \rangle$ in all cases. It follows that the QCs in **(a,b)** possess parallel long axes and small ($> 1°$) misorientation in the aperiodic plane. $P(n)$ represents the probability (weighted by area fraction) of finding an interfacial normal, n, along a particular direction. Peaks in the distribution indicate a highly anisotropic or faceted structure. In principle, a facet should have a single (discrete) orientation. Yet the peaks have finite width, likely a result of mesh smoothing. **(d)** Radial distribution of facet orientations obtained from 40 min to 110 min. The red, blue, and purple colors represent the dec-QC seeds on left- and right-hand-side (before impingement) and the coalesced dec-QC, respectively. Angular measurements start at the 12 o'clock position of the stereographic projection and increase clockwise. Two facets (peaks) are separated by an angle of nearly 36°, which is consistent with a decaprismatic morphology of the dec-QC phase.

parallel, here the quasiperiodic lattice in one dec-QC merged with the periodic lattice of the other d-QC. Naturally, the appreciable mismatch between the two lattices resulted in the formation of a GB, and hence a V-shaped groove in Fig. 3.3 **(e)**. Quantitative support comes from the stereographic projection of interface orientations shown in Fig. 3.3 **(f)**, which represents here the superposition of two single QC patterns (cf. Fig. 3.3 **(c)**). Since contrast in XRT stems from differences in photoabsorption between the phases, we can only capture the external solid-liquid interfaces and not the GBs and atomic configurations within the solid phases. Furthermore, it is nearly impossible

to preserve the QC interfaces at room temperature for high-resolution imaging, since the decagonal phase undergoes a peritectic decomposition below 910° C [141].

3.3.2 Simulation Results

To overcome such experimental constraints, we systematically examine the effects of misorientation on grain behavior in dec-QCs using seeded MD simulations with an isotropic, single-component pair potential [32]. We focus on misorientations within the aperiodic plane $\{00001\}$, since the XRT experiments provide evidence for coalescence when the long axes are parallel (Figs. 3.3 **(a-c)**). Thus, we carry out MD simulations in quasi-2D boxes to maximize surface area along the quasiperiodic plane. We fix the initial position of dec-QC seeds in our simulations to match experimental conditions, where grains were 'anchored' to the sample surfaces. Seed positions are fixed for the entire simulation. We use the decatic order parameter, ψ_{10}, to determine the alignment of the local bond configurations about each particle. We will call this quantity the LGOs (LGO) and particles with local bond configurations that align with the reference basis will have a LGO of $\theta = 0^\circ$. A detailed description of simulation setup and analysis is provided in the Methods section.

To elucidate the mechanism behind grain coalescence in dec-QCs, we begin with characterization of GB formation as a function of misorientation. Here, we define misorientation as the rotation angle about the $\{00001\}$ axis between two seeds. We define *grain* as a region where the arrangement of particles may be described by a continuous lattice in physical space and *seed* as a set of particles belonging to the d-QC lattice with fixed LGOs. We will refer to simulations based on the misorientations between seeds, rather than the misorientations between grains, since grains can change LGOs over time but the misorientations between seeds are fixed and represent the initial conditions of d-QC grains.

Fig. 3.6 compares small (3°), intermediate (9° and 10°), and large (15°) seed misorientations between two dec-QC seeds with a fixed distance of $L = 40d$, where $d = 1.02$ is defined as the distance between $r = 0$ and the 1st neighbor shell in the isotropic pair potential [32] and each seed contains 144 atoms. Each seed accounts for ~ 0.03 % of the particles in the entire simulation.

This means that the contribution of the fixed seed to the phason dynamics around the seed could be negligible. We verify this assumption with analysis of particle flips in both fixed and unfixed seed simulations (Fig. 3.7). No significant suppression of phason dynamics was observed around the seeds in both cases. In unfixed seed simulations, we do not see grain displacement upon collision (Fig. 3.8), which suggests our use of fixed seeds do not artificially hinder grain motion and should not introduce any significant artifacts into our results. Therefore, our choice to incorporate fixed-seed simulations can be justified by the purpose of replicating solidification experiments. Temperature was fixed at $kT = 0.5$ reduced units and pressure was fixed at $P = 3.9$

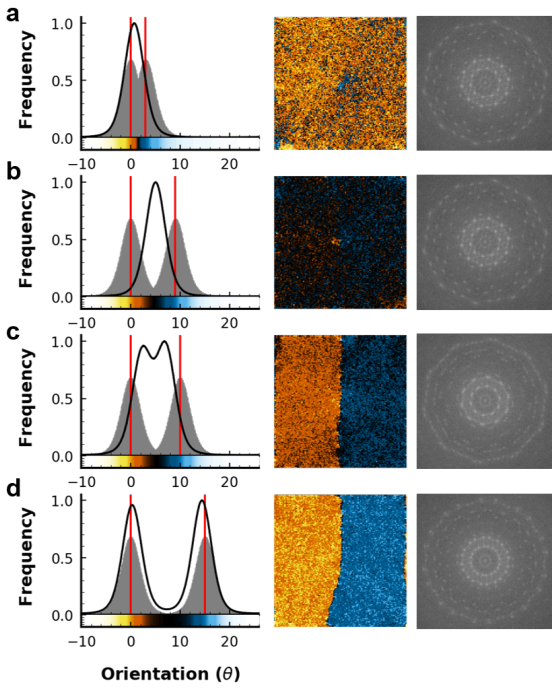

Figure 3.6: **Simulation orientation analysis.** [52] MD simulations showing changes in LGOs (θ) towards near-equilibrium configurations ($\sim$25 million simulation timesteps). Left column: Histograms of simulated (black line) and expected seed LGO distributions (grey peaks). Red lines indicate the expected LGOs of particles in each seed. Histogram bin frequencies (arbitrary units) for simulation lattice orientations were averaged after θ reached a constant value. The thickness of the black line represents the standard deviation of frequency for each bin. Grey peaks are expected probability density function (PDF) for the reference grain ($\theta = 0°$) and rotated grain. PDFs are calculated from single-seeded simulations. Peaks for the reference seed are centered at $\theta = 0°$ and peaks for the rotated seed are centered at $\theta =$ **(a)** 3°, **(b)** 9°, **(c)** 10°, and **(d)** 15°, respectively. Middle column: Spatially-binned simulation frames at 25 million timesteps for each set of seeds. Here, coarse-grained images are shown, rather than images with atomic level resolution, because they show grain rotation and GB characteristics more clearly. One pixel or cell represents 20 particles on average. All images show the aperiodic $\{00001\}$ plane of our dec-QC simulations. Colorbars for θ are below each histogram (left) and correspond to the orientation in the histogram axes, where yellow-orange corresponds to particles that align with the reference seed ($\theta = 0°$). Bright blue corresponds to particles that align with the rotated seed. Dark regions on the colorbar correspond to angles along the shortest arc between $0°$ and the rotated seed and white regions on the colorbar indicate angles along the longest arc between $0°$ and the rotated seed. White regions typically correspond to liquid regions, which are not visible in fully crystallized simulations frames (middle column), but are visible during growth, when liquid is still present in simulation. Right column: Calculated diffraction patterns based on the atomic level resolution simulations used in the middle column. Note the diffraction patterns of **(a)** and **(b)** are indicative of a single dec-QC. On the other hand, the diffraction patterns of **(c)** and **(d)** suggest the presence of two dec-QCs with different orientations.

reduced units. Further description of reduced units are provided in the **Methods** section.

3.3.3 Effects of Initial Grain Misorientation Grain Boundary Formation

When seed misorientations are $3°$ and $9°$ (Figs. 3.6 **(a, b)**), we observe unimodal histograms of θ in the bulk QC at equilibrium (left column) and a ten-fold pattern in the diffraction (right column). These results suggest that the misoriented grains rotated and the misorientation was minimized. On the other hand, when seed misorientations are $10°$ and $15°$ (Fig. 3.6 **(c, d)**), we observe bimodal histograms of θ (left column) in the bulk QC at equilibrium and overlapped, ten-fold patterns in the diffraction image (right column).

These results indicate the formation of a GB between misoriented grains. In the case of Fig. 3.6 **(a)**, one grain (yellow-orange) adopts the LGOs of the other grain (blue), see middle column. For intermediate seed misorientations (Figs. 3.6 **(b, c)**), grains rotate toward intermediate orientations (dark colored regions, middle column). In some cases, a GB is observed because misorientation is reduced, but not eliminated (Fig. 3.6 **(c)**). This is visible in the diffraction pattern (right column), where the misorientation between the two ten-fold patterns is approximately $6°$ after rotation. At large seed misorientation, i.e. $15°$, the GB is clearly defined and orientations of both seeds strongly

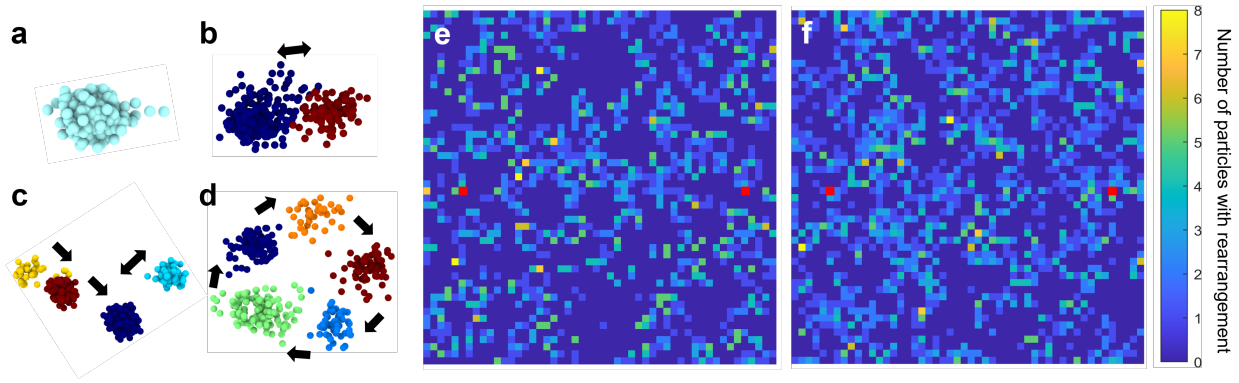

Figure 3.7: **Particle trajectory analysis.** [52] Trajectories of a single particle in a solid, dec-QC. The viewpoint is parallel to the periodic $\langle 00001 \rangle$ direction. Gaussian mixture model [100] and clustering algorithm [102] are used to classify the types of particle motion in 2D, e.g., **(a)** vibration, **(b)** oscillating phason flip, **(c)** multiple particle flips, and **(d)** cyclical motion on the pentagon vertices. Individual particle flips and coordinated particle flips [41] are involved in **(b-d)**, i.e., they may be identified if more than one cluster is detected (note each cluster is depicted in a single, unique color). The number of particles that re-order by particle flips is counted in each pixellated region of the simulations with **(e)** fixed seeds and **(f)** non-fixed seeds, in order to map the number density of particles showing phason flips. The red pixels in **(e,f)** represent the two QC seeds (the initial misorientation between them is zero). The number density of particles that flip is relatively uniform over the simulation domain in both cases.

resemble the initial seed orientations (Fig. 3.6 **(d)**). The diffraction pattern in Fig. 3.6 **(d)** shows a misorientation of ∼15°, which corresponds to the initial misorientation between the seeds (i.e., no grain rotation). Note the diffraction patterns shown here are closely related to the stereographic projections of facet orientations from experiment (Figs. 3.3 **(c, f)**). This is because the external morphology of a crystal reflects its point group isogonal with its space group [20].

In light of these trends, we can identify a critical seed misorientation, $\Delta\theta_{crit} \approx 9.5°$, for the given simulation conditions ($L = 40d$ and $kT = 0.4$), below which grains can rotate. The angle of critical value provided here is not meant to represent all cases of grain coalescence in dec-QCs, as $\Delta\theta_{crit}$ is likely a function of various thermophysical parameters (i.e., temperature, grain size, fluid viscosity, and external stress [23, 135]). Instead, we treat it as a reference point for how the behavior of dec-QCs change at $\Delta\theta_{crit}$. After grain rotation towards 0° misorientation from the small initial misorientation (3°), only a few dislocations in the GB region were detected (Figs. 3.9 **(a, c)**) in the single density mode [76], which suggests grain coalescence. In contrast, we observed an array of dislocations in the single density mode [76] from the simulations with 15° initial misorientation ($> \Delta\theta_{crit}$), indicating the formation of a GB (Figs. 3.9 **(b, c)**). That is, grain coalescence occurs only for relatively small seed misorientation angles, see Fig. 3.9 **(c)**.

We begin our analysis of coalescence by mapping the LGOs of grains grown from two seeds with misorientation 6°, well below $\Delta\theta_{crit}$, as depicted in Fig. 3.10.

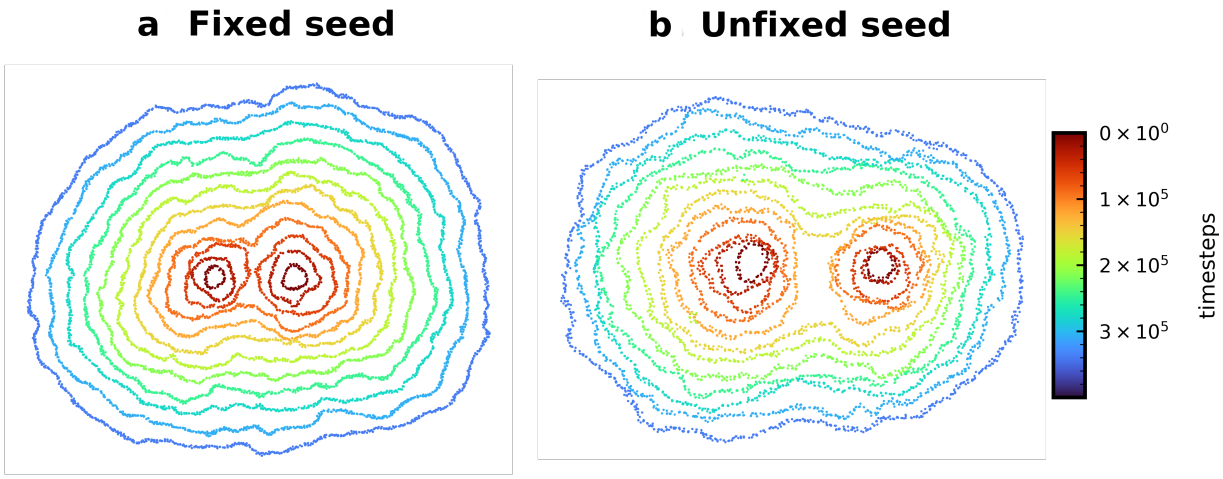

Figure 3.8: **Solid-liquid interface in simulation.** [52] Solid-liquid interfaces over 4×10^5 simulation time steps for the case of **(a)** fixed seeds ($\theta = 9°$, $L = 40d$) and **(b)** unfixed seeds. To simulate, two seeds with $\theta = 9°$ and $L = 40d$ were placed in the fluid. For the **(a)** fixed seed case, seeds positions were fixed for the entire simulation. Particles in the **(b)** unfixed seed simulation were allowed to move freely following nucleation. Interfaces are colored according to time step. Differences in collision time between the two systems is likely stochastic.

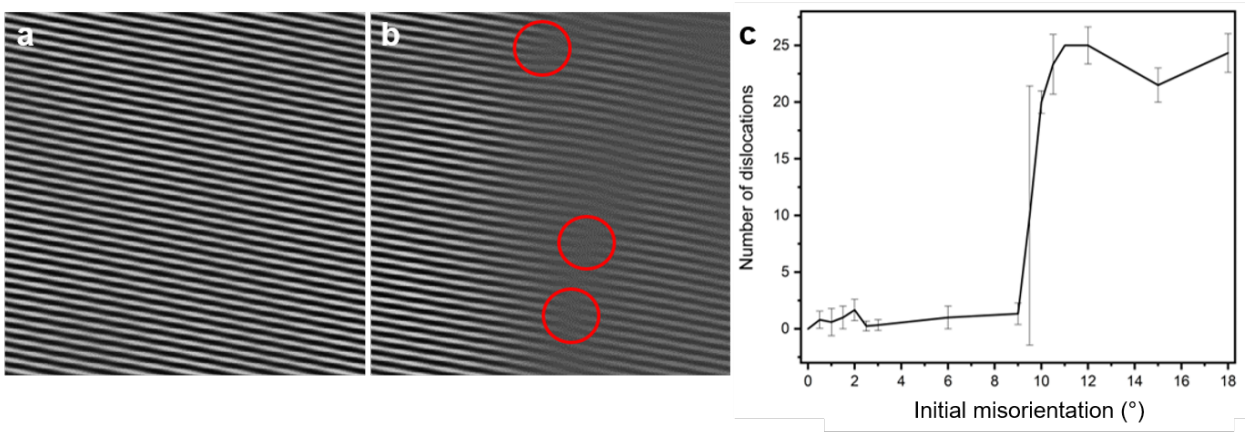

Figure 3.9: **Number of dislocations along the grain boundary.** [52] Real-space images of a single density mode [76], in the region where QCs collide, taken from the last frame in MD simulation ($\sim 2.5 \times 10^7$ simulation timesteps) with **(a)** 3° and **(b)** 15° initial misorientations. Dislocations are highlighted with red circles. **(a)** and **(b)** are cropped to provide a magnified view from the images that represent full volume. **(c)** Relationship between the initial misorientation and number of dislocations along the grain boundary in the coalesced structure. We find that there are few dislocations (if any) at low ($\theta \lesssim 9.5^\circ$) initial misorientation, since two QCs can rotate toward $\theta = 0^\circ$ (cf. **(a)**). Conversely, there are many dislocations when two QCs cannot minimize the misorientation between them. The error bars were calculated from multiple dislocation analyses to retain consistency of our approach. *Contribution by the Shahani Group.*

3.3.4 Evolution of Local Grain Orientation Upon Collision of Two Misoriented Grains

Fig. 3.10 **(a-e)** shows the time evolution of coarse-grained LGOs for seeds with 6° misorientation. At early timesteps (Fig. 3.10 **(a-b)**), we observe two grains (labelled A and B) with good alignment to seed orientation (yellow-orange and blue regions, seeds A and B, respectively). Immediately after collision, grain A remains well aligned with seed A and a GB is clearly visible (Fig. 3.10 **(b)**). Both grains continue to rotate and reduce misorientation (darkening of both grains, Fig. 3.10 **(b-e)**) over the next $\sim 4.33 \times 10^6$ timesteps. The GB grooves (Fig. 3.10 **(b-c)**, arrows) gradually flatten during rotation. This confirms the formation of a single grain, mimicking the experimental results (Fig. 3.3 **(b)**).

For comparison to our dec-QC system in Figs. 3.6 and 3.10, we show results from a FCC simulation with seeds at a fixed distance of $15.5a$, where $a = 4\frac{d}{\sqrt{2}}$ is the lattice constant, $d = 1.1$ is average bond length in the FCC grain, and 3° misorientation between seeds. The results are shown in Fig. 3.11, where the image is colored using the same method used in Figs. 3.6 and 3.10, where alignment with seeds A and B (labeled in Fig. 3.11 **(a)**) are indicated by a yellow-orange and blue color, respectively, and fluid-like regions are represented by white. In contrast to our dec-QC

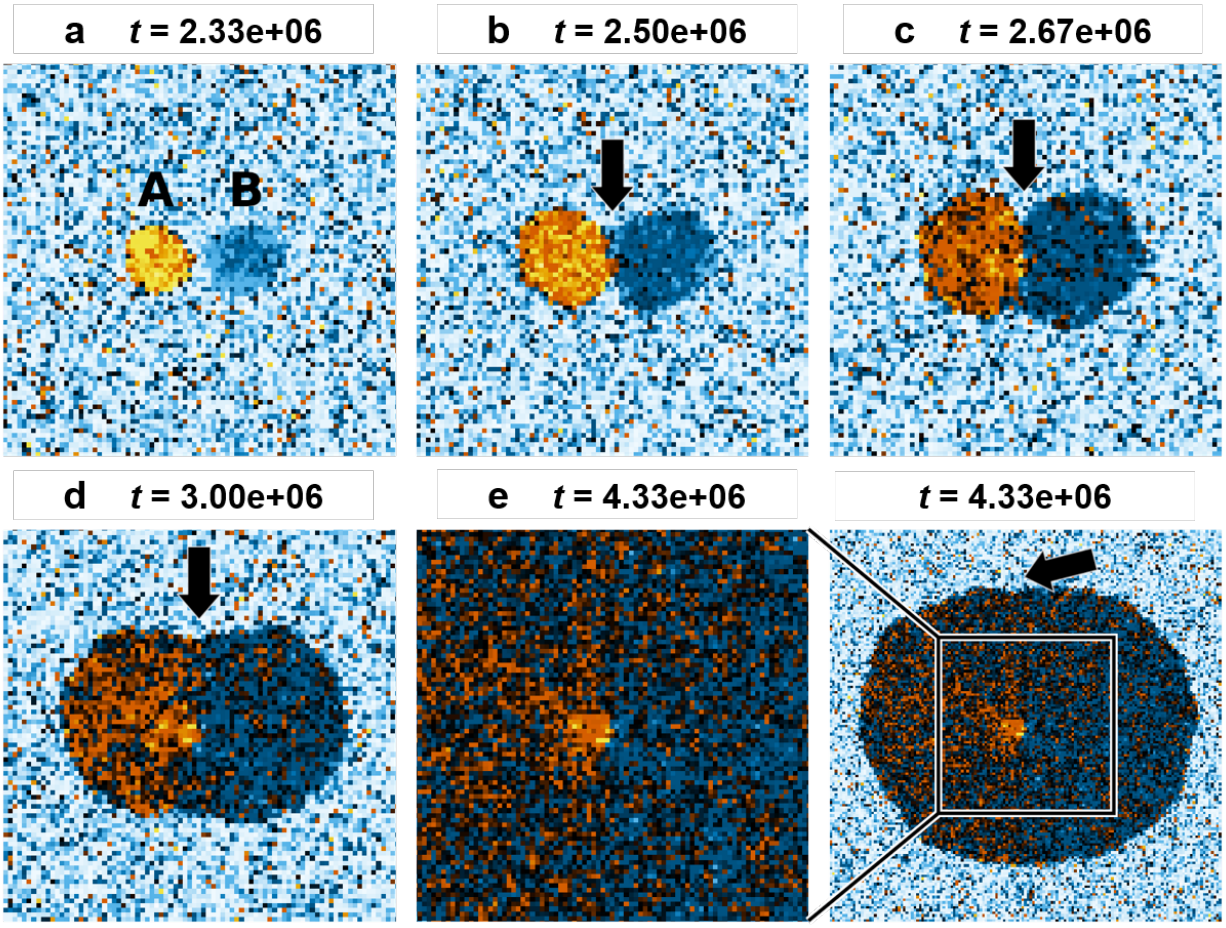

Figure 3.10: **Growth of a single dec-QC from two seeds.** [52] Seeds are labeled A and B in **(a)** with 6° misorientation. Here, coarse-grained images of the aperiodic {00001} plane show the LGOs of dec-QC grains **(a)** during early stages of grain growth; **(b)** immediately after collision; **(c)** after collision, grain rotation to minimize grain misorientation; **(d)** early stages of grain coalescence; **(e)** after grain coalescence. All heatmaps are cropped according to **(e)** from the total volume. Subplots **(a-e)** are colored on the basis of an expected particle seed distribution, as shown in the middle column of Fig. 3.6. Contiguous regions of white in subplots **(a-e)** correspond to liquid regions. Arrows in **(b)** and **(c)** point to the GB grooves at the QC-liquid interfaces. Arrows in **(d)** and **(e)** point to regions where the GB groove has flattened.

results, simulations of FCC grains (Fig. 3.11) show clear GB grooves at all stages of growth and more localized changes in misorientation (Fig. 3.11 **(b-e)**). We note that, even after coalescence, small regions remain well aligned with the initial d-QC seeds (Figs. 3.6 **(a, b)** and Fig. 3.10 **(e)**), despite rotation through the bulk of the crystal. This is due to our decision to fix the seed position throughout the entire simulation, preventing rotation of the nucleation sites of each grain.

3.4 Discussion

3.4.1 Grain Coalescence in Periodic Crystals

The phenomenon of grain coalescence is well documented in polycrystalline materials[23, 55, 93, 135]. Mechanisms for grain coalescence are driven by reduction of GB free energy and are categorized broadly by GB migration and grain rotation, as alluded to earlier. In embedded grains,

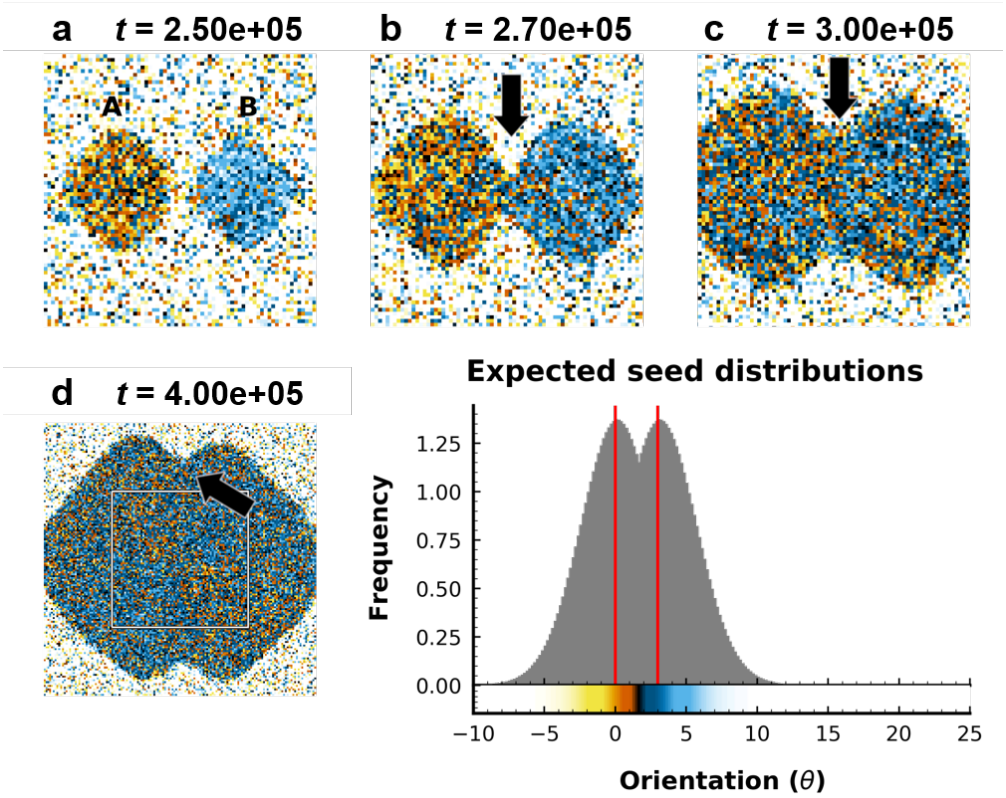

Figure 3.11: **Growth of two FCC grains with** $3°$ **misorientation.** [52] Growth at **(a)** 2.50×10^5, **(b)** 2.70×10^5, **(c)** 3.00×10^5, **(d)** 4.00×10^5 timesteps. **(a-c)** Frames from early stages of growth are cropped to show more detail. The area cropped is shown by the white outline in **(d)**. **(e)** shows the colorbar for this figure, where alignment with seed A corresponds to yellow-orange and alignment with seed B corresponds to blue color. Here, the grey peaks represent the expected probability density functions (PDFs) for reference grain ($\theta = 0°$) and the misoriented grain ($\theta = 3°$). The colorbar is cropped from the maximize range of orientation (-10° to $\sim$ 80°) for clarity. Black area indicates angles along the shortest arc between $0°$ and the misoriented seed, and white areas correspond to angles along the longest arc between $0°$ and the misoriented seed. GB grooves are present during all stages of growth for both orientations, despite rotation of both grains to $0°$ misorientation (see arrows in **(b-d)**). Although we observe global rotation of misoriented grains toward $0°$ misorientation, a persistent grain boundary groove suggests unresolved phonon strain along the grain boundary due to incommensurate distances between FCC lattices.

GB migration is typically coupled with rigid sliding [23, 55, 135, 137] (termed *coupling*), which is identified by a translation of the GB and a concomitant, continuous change in misorientation (i.e., lattice rotation) near the GB [23]. In contrast, uncoupled GB sliding manifests as a uniform, global change in grain orientation, as we observed in Figs. 3.10- and 3.11. Measurements of grain rotation rates as a function of initial grain misorientation (Fig. 3.12) show strong and qualitative agreement with classical equations for the dependence of GB free energy (γ_{gb}) on misorientation (θ)[103] and driving pressure of sliding, $P_{\parallel} \approx -\frac{d\gamma_{gb}}{d\theta}\frac{1}{\mathcal{R}}$, where $\mathcal{R}$ denotes grain radius [23]. The presence of sliding and the gradual disappearance of the GB groove in Fig. 3.10 suggests dec-QCs are able to eliminate GBs with pure rotation. This is unexpected – due to the aperiodic, long-range translational order present in QC lattices, translational mismatch between lattices grown from two seeds is likely, even when misorientation between grains is 0°. It should not be possible to eliminate translational mismatches with rotation alone. This is consistent with our simulations of FCC grains (Fig. 3.11), wherein the GB groove remains stationary and prominent, despite rotation towards 0° misorientation between grains. This finding also means that, although GBs are not observed in the physical space of our dec-QCs, evidence of translational mismatches may be found in the phason space of the crystal.

We note a few caveats to consider when applying this theoretical framework to experiment. First of all, since the sliding velocity is directly proportional to the driving pressure, $P_{\parallel}$, and $P_{\parallel}$ is itself inversely proportional to the radius, $\mathcal{R}$, of the grain [23], a smaller $\Delta\theta_{crit}$ and slower rotation rate are expected in the XRT experiment, compared with the simulation. Second, in experiment, grains are anchored onto a substrate. Even so, grains may rotate if the applied torque is sufficient to overcome any interaction between grains or with an external substrate [29, 49, 58]. This suggests that the presence of external constraints may impact the kinetics of rotation; nevertheless, grain rotation is still possible. A case in point is Figs. 3.3 **(a-b)** from our own work, showing grain rotation on experimental time-scales in the limit of small initial misorientation.

3.4.2 Grain Coalescence in Quasicrystals

Due to the unique symmetries of QCs, all dislocations in dec-QCs contain phasonic components [41]. These phasonic components represent excitations in QC lattice; they contribute to an increase in the system's phason strain, which may be relaxed over diffusive timescales. In contrast, dislocations in periodic crystals are purely phononic. Previous work shows that motion of dislocations through dec-QCs results in a wall of phasons along the slip plane [136]. This suggests that the dislocation reactions which enable sliding to occur (vide supra) redistribute the phonon strain from lattice mismatches as phason strain through a combination of dislocation annihilation mechanisms and phason flips. Due to the complexity and variety of dislocations in dec-QCs, however, we re-

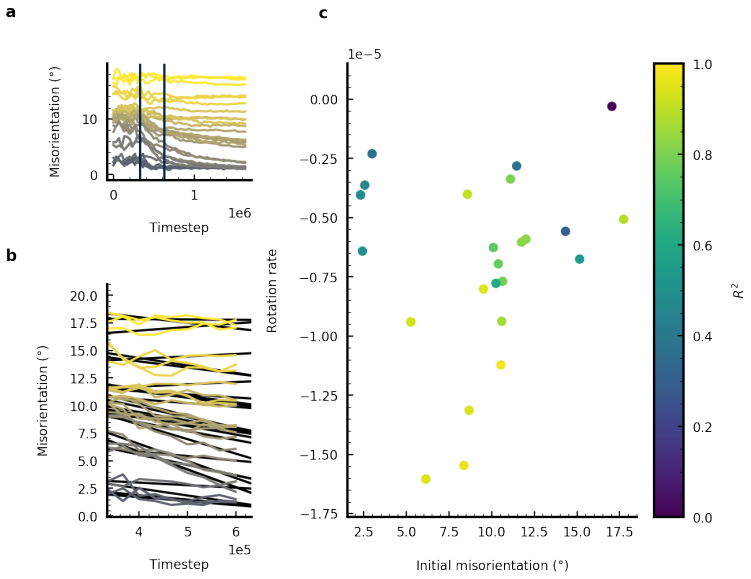

Figure 3.12: **Rotation rates of dec-QCs.** [52] Misorientations between dec-QC grains during growth in simulation. Here, **(a)** shows the change in misorientation between grains over 1 million timesteps, where timesteps are expressed as dimensionless time, τ, and $t = 0$ indicates the start of the simulation. We may estimate each timestep, τ, to be in the order of magnitude of 10^{-13} to 10^{-12} seconds. Lines are colored according to seed misorientation, where yellow (light grey) indicates large misorientation and grey indicates small misorientation. Grain rotation begins when grain collision occurs around $\sim 3 \times 10^5$ timesteps, then continues with a linear trend until $\sim 6 \times 10^5$ timesteps. This region of linear grain rotation is indicated between dark blue lines on **(a)** and expanded in **(b)**. In **(b)**, yellow and grey lines correspond to the same seed misorientations as in **(a)**. We use linear regression to model rotation in each simulation (black lines), and determine rotation rates from the slope of each line. In **(c)**, we plot rotation rate as a function of average grain misorientaion before collision. We use average grain misorientation before collision, rather than seed misorientation because there are small fluctuations in grain orientation during growth. These fluctuations are observed even in growth of single grains and can drastically affect the rotation rates when misorientation is near $\Delta\theta_{crit}$. Rotation rates are colored according to the linear correlation coefficient, R^2, where $R^2 = 1$ is yellow (light grey) and $R^2 = 0$ is purple (dark grey). Here, we observe faster rotation as initial misorientation increases from $\sim 2.5^\circ$ to $\sim 6^\circ$. Then, as misorientation approaches $\Delta\theta_{crit} \approx 9^\circ$, we observe a rapid decrease in the magnitude of the rotation rate. These results are consistent with a driving force of $\gamma'_{gb} = \frac{d\gamma_{gb}}{d\Delta\theta}$, where γ_{gb} is grain boundary energy and $\Delta\theta$ is grain misorientation. Typically, γ_{gb} increases with $\Delta\theta$ until it reaches some critical point ($\Delta\theta_{crit}$), above which λ is a much weaker function of $\Delta\theta$. This means we should expect the driving force, γ'_{gb} to show a decline around $\Delta\theta_{crit}$, which is reflected in the drastic decrease in rotation rates around $\Delta\theta \approx 9^\circ$.

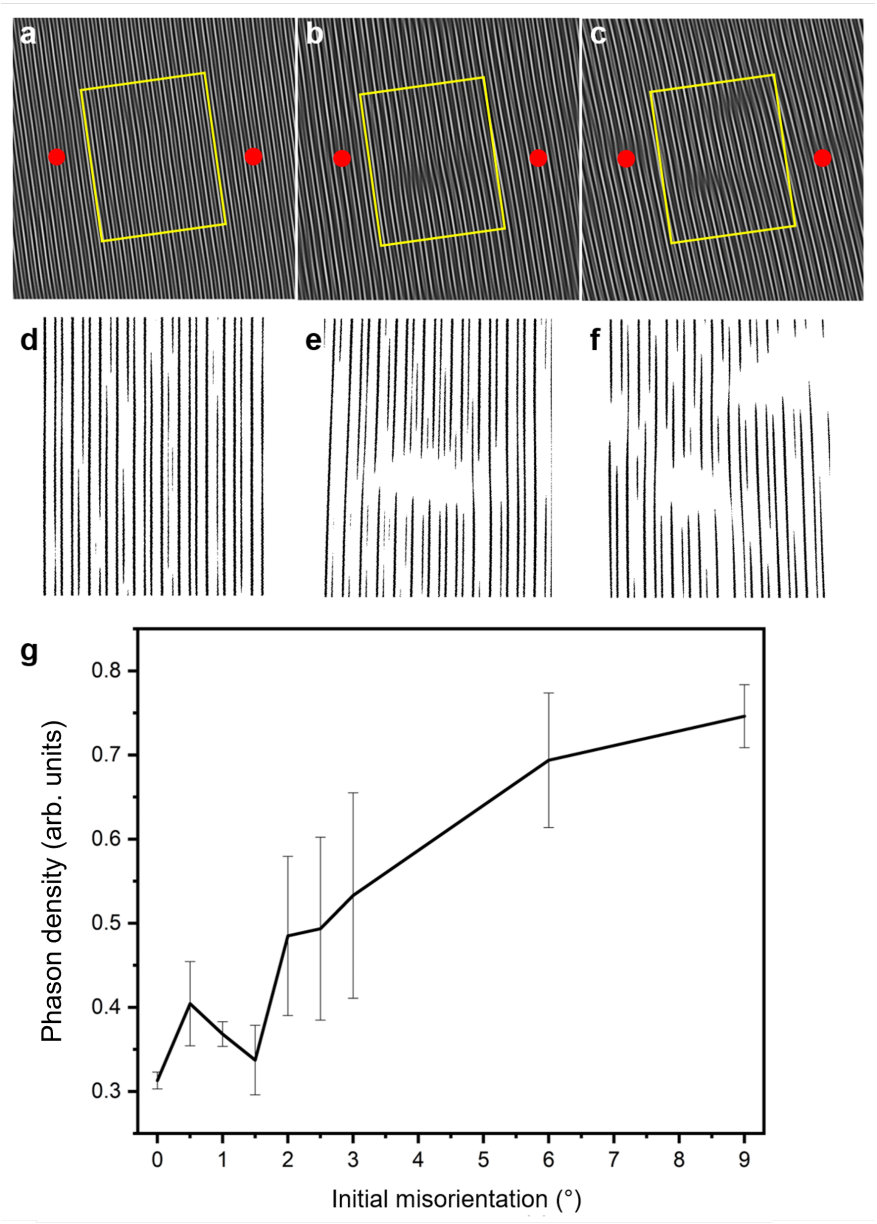

Figure 3.13: **Phason density of coalesced structure.** [52] Phason density modes obtained by filtering two pairs of Bragg peaks [43] from the merged quasicrystals with **(a)** $0°$, **(b)** $3°$, and **(c)** $9°$ of initial misorientations at timestep 4.0×10^5 from MD simulations. The red dots indicate the seed positions and the region highlighted with yellow rectangles is binarized for quantitative analysis of phason strain. **(d)**, **(e)** and **(f)** correspond to **(a)**, **(b)** and **(c)**, respectively. **(g)** Phason densities calculated as a function of initial misorientation between seeds, using the method introduced by Freedman et al. [43]. The phason density was determined from the binarized images based on the areas inside of the yellow rectangles for misorientations of multiple $0°$, $0.5°$, $1°$, $1.5°$, $2°$, $2.5°$, $3°$, $6°$, and $9°$ cases. For consistency of our results, we repeated analyses on different MD simulation datasets, which explains the origin of the error bars. *Contribution by the Shahani Group.*

serve quantitative analysis of phasonic motion and dislocation kinetics for future work. Instead, we examine simulations where grain coalescence occurs for residual phason strain as a potential signature of dislocation motion during grain coalescence (Fig. 3.13).

The density modes (Figs. 3.13 **(a-c)**) are obtained by filtering two pairs of Bragg peaks from the diffraction image of the merged QC. They represent the two different length scales (e.g., golden ratio) in QCs. The region boxed in Figs. 3.13 **(a-c)** with yellow rectangles is further processed for the phason strain analysis with an appropriate threshold (Figs. 3.13 **(d-f)**). According to Freedman et al. [43], the 'jags' in the stripes pattern are the signature of the phason strain in the quasiperiodic lattice. We quantified the fraction of 'jags', which are longer than zero and shorter than the longer edge of the yellow rectangles in Figs. 3.13 **(a-c)**, along the direction of the stripes. Fig. 3.13 **(g)** shows that a higher phason strain is accumulated within the grain boundary region as the initial misorientation increases in the simulation timescale, which supports the hypothesis that phonon strain is redistributed as phason strain during coalescence. This is in good agreement with the coalescence mechanisms shown in [110], where coalescing grains were shown to transform from structures with phonon and phason strain, to a structure with phason strain, which is later relaxed.

We expect phason strain relaxation occurs over diffusive time scales [43]. This means that, although we expect dec-QCs to gradually relax to a low or no phason strain state over time, phason strain introduced during grain coalescence should be observable. Thus, we expect phason strain relaxation to occur over experimental timescales near regions where the hard collision occurred (Fig. 3.13). Indeed, there is ample evidence of phason strain relaxation, obtained from recent in situ experiments. For example, Nagao et al.[95] observed grain boundary migration in QCs through an 'error-and-repair' process, wherein phason strain at the grain boundary region is relaxed to generate an ideal quasicrsytalline lattice. In addition, we confirm the relaxation of phason strain in our slow-cooling experiments, evidenced by the linear relationship between $G_{||}$ and FWHM of the peaks in the diffraction pattern (Fig. 3.4).

3.5 Conclusion

We elucidated the growth interaction between two dec-QCs with fixed-seed positions via 4D XRT and MD simulation. To the best of our knowledge, this is the first experimental study to investigate the structural continuity between two quasicrystalline crystals after a hard collision. With our joint analyses, we were able to provide a cohesive picture for the conditions that give rise to grain coalescence: (i) parallel periodic axes and (ii) small misorientation between quasiperiodic crystals. In this operating regime, we observed grain rotation toward 0° misorientation in order to minimize grain-boundary energy. This process occurs through a dislocation-mediated mechanism that allows the dec-QCs to redistribute phonon strain due to lattice mismatch as phason strain, by local

rearrangement of dislocations into valid tilings. Taken all together, our integrated approach highlights the exciting opportunity for microstructure optimization via control of the grain boundaries – that is, defect engineering. It provides the knowledge base for fabrication of defect-free QCs (e.g., through a controlled sintering process), thereby widening their potential uses and applications.

CHAPTER 4

Quasicrystal-Pore Growth Interactions

This contents of chapter will be submitted for publication in a peer-reviewed journal.

Quasicrystals (QCs) are solids that possess long-range orientational order but lack transitional periodicity. They exhibit mechanical and transport properties that are highly unexpected for their composition [65], which arise due the unique geometries of these materials [65, 99, 133, 147]. These properties made QCs attractive candidates for solar light absorbers [37], as an alternative to Teflon [37, 65], as mechanical reinforcement of tools as a coating or nanoparticles [37], and insulation [37, 65]. Yet, despite the practical and intellectual interests surrounding these materials, little is known about the mechanisms governing QC growth.

Here, our collaborators, Dr. Insung Han and Professor Ashwin J. Shahani, through real-time and 3D imaging, the formation of a single decagonal quasicrystals (dec-QCs) arising upon collision with pores in an Al-Co-Ni melt. Through corresponding molecular dynamics (MD) simulations, we examine the underlying kinetics of QC coalescence and investigate the effects of pore-QC collision conditions on phason and phonon strain. In this work, we highlight the importance of multiple length scales (l_1, l_τ) in phason-mediated coalescence upon QC collision of growth fronts. At early stages, we see the formation of highly-strained structures, and a sharp increase in the relative frequency of the longer length scale, l_τ. Over time, we seed the rapid relation of real space strain and positional disorder, and, remarkably, a drop in potential energy along the region of coalesence. We observe this trend across all 958 of our simulations, and find that the amount of order introduced and the amount of time required to relax disorder introduced upon collision is nearly independant of pore shape or size. Our joint experimental-computational discovery paves the way toward fabrication of single, large-scale QCs for novel applications.

4.1 Introduction

The growth mechanisms of QCs have attracted great interest [68, 71] due to their distinctive, complex structures. QCs possess long range orientational [116] and positional order [124], yet they lack translational periodicity [116]. Arising from this lack of translational periodicity and the presence of long-range quasiperiodicity are *phasons* [119], an additional degree of freedom unique to aperiodic crystals like QCs, where *phason strain* measures deviation from quasiperiodicity [43, 128] and phason flips are characterized by discrete particle motions [41] that result in a change in tiling configuration. These changes in tiling configurations are representative of phason excitations and relaxations, and do not introduce real space defects into the crystal [119].

Although past studies of QC growth mechanisms extend our understanding of phason contributions to stability in a bulk QC [68, 71, 129], studies on phason contributions to the formation and relaxation of localized strain remain limited [52, 110]. Researchers have shown how the additional degree of freedom arising from aperiodicity, or phasons, enable QCs to form defect free QCs upon collision of two grains with small misorientation [52, 110]. In [52], specifically, we found that dec-QC were able to redistribute phonon strain due to lattice mismatches via local rearrangements of dislocations into valid tilings. These local rearrangements resulted in a region of concentrated phason strain along the region of coalesence. Here, we continue to investigate the phason-mediated grain coalesence in the context of QC collisions with shrinkage pores formed during casting.

Porosity is a major solidification defect with potentially detrimental effects on the mechanical properties of castings [15, 24, 56, 101, 108]. Due to the negative impacts porosity may have on a casting's properties, there exists a rich body of literature that discuss the mechanisms of pore formation and the mechanical effects of pores on castings. Yet, to the best of our knowledge, research investigating the effects of porosity on QC growth remains absent. It is critical, then, to understand how the presence of shrinkage pores affects QC growth.

Here, our experimental collaborators in the Shahani group investigate the growth dynamics of a thermodynamically-stable dec-QC grain [141] upon solidification of an $Al_{79}Co_6Ni_{15}$ alloy. They used synchrotron-based, four-dimensional (*i.e.*, 3D space plus time-resolved), x-ray tomography (XRT) to resolve dec-QC crystal growth interactions upon collision with a shrinkage pore. This experimental technique has opened a paradigm shift in solidification science, allowing our collaborators to capture transient microstructural dynamics in optically opaque materials [4, 7, 115]. To the best of our knowledge, their *in situ* experiments provide the first-ever demonstration of QC-pore collision. On the basis of their experimental results, we performed MD simulations to identify the mechanism of grain growth around the pore at the atomic scale. We examine evolution of order along the *region of coalesence*, or the site of growth front collision upon engulfment of a pore, and discuss the role of phasons in facilitating the formation of defect-free dec-QCs upon engulment of

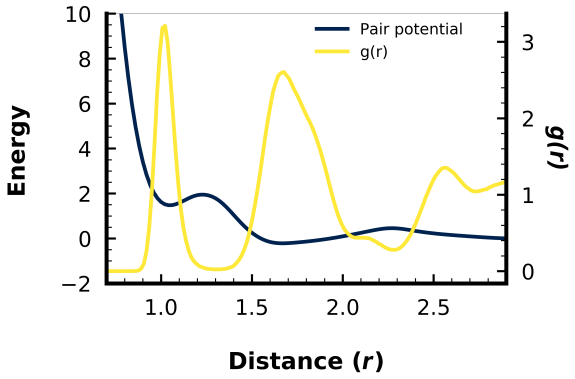

Figure 4.1: **Tabulated pair potential and radial distribution function for QC simulations.** [52] The single-component, isotropic pair potential (dark blue) used for all dec-QC simulations is derived from the potential mean of force of a diamond-forming system [30]. The radial distribution function is shown in yellow, $g(r)$, for a single seeded dec-QC simulation after 19.7×10^6 timesteps.

pores and obstacles in the melt. Our combined efforts provide the first direct evidence of single crystal formation between incommensurate structures, such as QCs.

4.2 Methods

4.2.1 Decagonal Quasicrystal Simulations

We performed MD simulation with HOOMD-blue[6] in the canonical (NVT) ensemble. Simulations used reduced units of energy (ϵ), length ($d = 1.02$) in arbitrary units, mass (m), and time $\left(\tau = \sqrt{\frac{md^2}{\epsilon}}\right)$. Particles interacted through an oscillatory, double-well potential [32] (Fig. 4.1), previously shown to form dec-QCs (Eqn. 3.1).

Each simulation was performed with 1×10^6 particles and with periodic boundary conditions in 3 dimensions. Pores and cylindrical walls were constructed from particles frozen in a fluid-like configuration. Cylindrical walls were introduced to reduce the influence of periodic boundary conditions on dec-QC growth along the quasiperiodic plane (Fig. 4.2 **(a)**, yellow [lighter color] regions). Simulations were also carried out in quasi-2D boxes (slabs) with target dimensions of $(456 \times 456 \times 10)$. The use of quasi-2D boxes allowed us to maximize the size of the quasiperiodic plane for analysis while minimizing computational overhead.

4.2.1.1 Simulation Setup

Systems were initialized in a low density simple cubic (SC) lattice ($\rho = 2$, where $\rho = N/V$ is the number density), then randomized at $T^*_{init} = 2.5$ for 5×10^4 simulation time steps, where

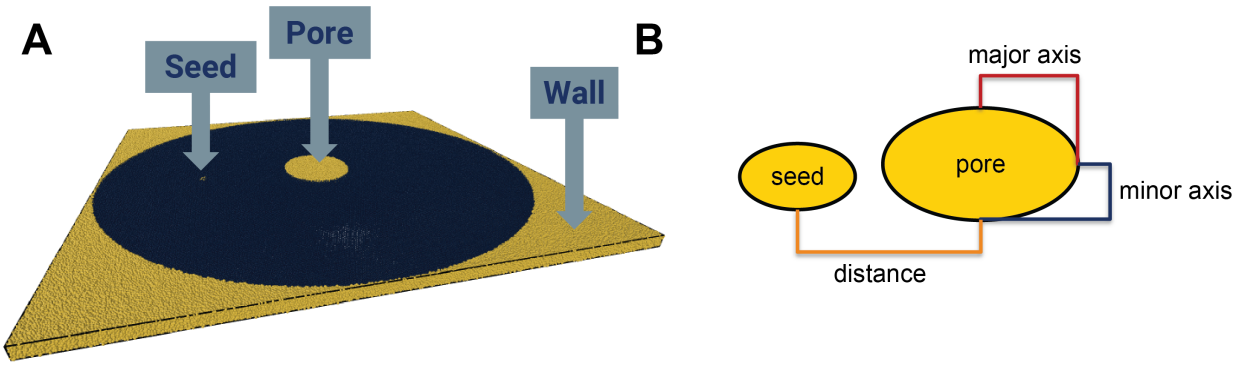

Figure 4.2: **Slab-like simulation for pore-crystal growth simulations. (a)** Snapshot of a 1×10^6 particle seeded simulation with fluid-like walls (yellow, lighter color) and pore. The pore shown here has an axis ratio of 1 and radius of 15, and the distance between the center of the pore and the center of the dec-QC seed is 100. **(b)** Schematic depicting pore parameters varied througho

temperature was expressed in a reduced unit of $T^* = \frac{k_b T}{\epsilon}$ and k_b is the Boltzmann constant.

Next, simulations were compressed from cubic boxes ($126 \times 126 \times 126$) to slab-like boxes ($456 \times 456 \times 10$; $\rho = 0.98$) over 5×10^4 simulation time steps at a constant temperature of $T^* = 2.5$, then held for 2×10^5 simulation time steps. Once the boxes were compressed to the appropriate density and dimensions, we introduce cylindrical walls along the quasiperiodic plane and pores. To construct cylindrical walls, we freeze particles in a fluid-like configuration along the edge of the simulation box. We set the radius of the cylinder as 255. This value was chosen to reduce the effects of periodic boundary conditions on our simulation. The minimum thickness of the wall is approximately $2 \cdot r_{cut}$, where $r_{cut} = 2.9$. Meanwhile, we fix the center of the pore at the center of the simulation box and vary the axes ratio, pore orientation, and pore minor axis (Fig. 4.2 **(b)**). Here, we define axes ratio as the ratio of the pore's minor axis to the pore's major axis, $R = R_{minor}/R_{major}$ and we define pore orientation with respect to the major axis.

After walls and pores were introduced, simulations were held at $T^*_{init} = 2.5$ for 5×10^4 simulation time steps, then linearly cooled from a liquid-like configuration ($T^*_{init} = 2.5$) to a temperature near but below the melting point ($T^*_{end} = 0.4$) over 5×10^4 time steps.

Once cooling was complete, the dec-QC was introduced to the simulation and the system was held at $T^*_{end} = 0.4$ for 20 million simulation time steps.

4.2.1.2 Simulation Parameters

Our simulations consisted of one fixed seed where distance between pore and seeds ranged from $64-100$, minor axis ranged from $10-55$, axis ratio ranged from $1-4$, and pore orientation ranged from $0-\frac{\pi}{2}$ radians. We ran $5-7$ trials of each pore parameter for statistics, resulting in a total of 958 simulations, each containing 1 million particles. The computational workflow and general

data management in particular was primarily supported by the signac data management framework [3].

4.2.2 Body-Centered Cubic Crystal Simulations

For comparison, we carried out additional MD simulations of an body-centered cubic (BCC) forming system via the Lennard-Jones (LJ)-Gauss pair potential [36],

$$V_{LJGauss} = \epsilon \left[\left(\frac{d}{r} \right)^{12} - 2 \left(\frac{d}{r} \right)^{6} \right] - \varepsilon \exp \left[-\frac{(r - r_0)^2}{2\sigma^2} \right] \tag{4.1}$$

that is truncated at $r_{cut} = 2.5d$. Here, $\sigma = \sqrt{0.02}d$, $\varepsilon = 3.0\epsilon$, $r_0 = 1.8d$, and r is the distance from the center of a particle, expressed in units of d. Temperature was fixed at $kT = 6$. All periodic simulations contained 1×10^6 particles. Each seed contained 256 particles. The potential was shifted and smoothed so that both the potential and its derivative are zero at the cutoff.

4.2.3 Orientational Order Parameter

We used the bond-orientational order parameter for k-atic rotational symmetry[127] to identify the local orientational symmetry of each particle m:

$$\psi_k(m) = \frac{1}{n} \sum_{j}^{n} e^{ki\theta_{mj}} \tag{4.2}$$

where n is the number of neighboring particles and θ represents the angle between local bond orientations and a fixed basis with k-atic rotational symmetry. For a dec-QC, we use the value of $k = 10$, so that $\psi_{10}(m)$ refers to the decatic order parameter. For BCC simulations, we computed $\psi_4(m)$, or the quadratic order parameter, on the 2D projection of the crystal down the 2-fold rotational axis. We note that the projected structure resembles a simple square lattice, resulting in 4-fold, rather than 2-fold rotational symmetry in the 2D lattice. We determine neighbors for particle m as the k nearest neighbors in 3D to ensure that measurements reflect the local atomic environment of each particle. Data analysis for this order parameter utilized the *freud* library[102].

4.2.3.1 Solid-Liquid Separation

Due to the local heterogeneity inherit to dec-QCs, we found that ψ_k alone is insufficient to separate crystalline regions from liquid regions during growth. To address this, we introduce three additional steps to account for local thermal fluctuations in crystal structures. First, for each particle

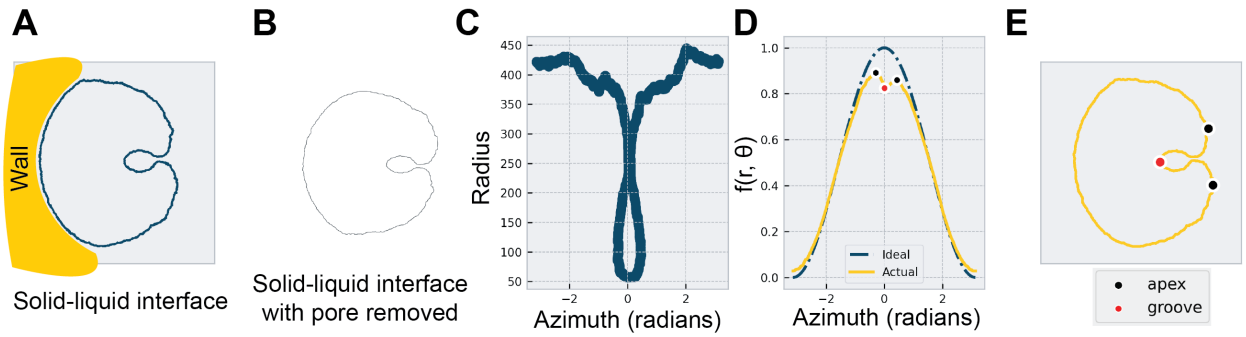

Figure 4.3: **Extracting solid-liquid growth interface and features from simulation.** **(a)** Solid-liquid interface of a dec-QC simulation at 9.1×10^6 time steps. Here, the distance between the pore and seed is 100, the minor axis is 22.7, the axes ratio is 1.50, and the relative orientation is 0.0 radians. **(b)** In frames where the crystal completes growth around the pore, we remove the pore from the interface. Then, **(c)** we map the interface to polar coordinates and **(d)** we detect the *apex* (black dots) and groove (red dot) from the smoothed and normalized signal in polar coordinates. Then, finally, **(e)** we transform the detected apex (black dots) and groove positions back to Cartesian coordinates.

in the simulation, we average ψ_k over its 10 nearest neighbors. Next, we take the averaged ψ_k for each particle, then average it again over its 20 nearest neighbors. Finally, we assign each particle the maximum, double-averaged ψ_k value from its 20 nearest neighbors.

For dec-QCs, we labeled any particle with $||\psi_{10}|| > 0.3$ as solid. For BCC systems, we labeled any particle with $||\psi_4|| > 0.4$ as solid. Here, we define $||\vec{a}|| = \sqrt{\sum a_i^2}$.

4.2.4 Groove and Apex Detection

Using the procedure outlined in Fig. 4.3, we tracked the formation and persistence of grooves during crystal growth around a pore. Here, we also track the *apex*, or, the regions where the growth front remains unaffected by the pore or groove. The apex serves as a reference point for the solid-interface's growth front in the absence of the pore.

To begin, we extract the solid-liquid interface using the binary labels computed using the procedure outlined in Section 4.2.3.1 and *freud*'s [102] `Interface` module. Here, we define interface points as any liquid particle with at least one solid particle neighbor with $r_{\max} > 1.1d$, where $r_{\max}$ is the maximum distance to find neighbors (Fig. 4.3 **(a)**).

Next, we remove the pore from interface calculations in frames where the crystal has completed growth around the pore. This is necessary to prevent the introduction of noise and artifacts during apex and groove detection. To do this, we first projected interface points to 2D and mapped them onto a 2D histogram with dimensions $D_i = 64 \cdot \left\lfloor \sqrt{2 \cdot \max(|\vec{x}_i|)} \right\rceil$, where $|\cdot|$ denotes absolute value, $\lfloor \cdot \rceil$ denotes rounding to the nearest integer, $\vec{x}_i$ is an $N \times 1$ vector of N particle coordinates along

dimension i, and $i = 0, 1$ for a 2D system. Setting grid size based on maximum grain dimensions ensured that we could maintain appropriate resolution of interface features during early stages of growth without the need for extensive computational speed and memory consumption during later stages of growth. Next, we apply a Gaussian filter with $\sigma = 0.8$, where σ is the standard deviation of the Gaussian kernel to fill in any potential gaps in discretized interface. Then, we binarize the image and fill any remaining holes in the image and recover the interface using a Laplace filter (Fig. 4.3 **(b)**). Occasionally, we may detect false interfaces using this procedure. Since these false positives were rare and small compared to the crystal, we identified and removed them by counting the number of connected elements in each unique feature of our image, and removing all but the largest cluster.

Then, we converted the interface positions to evenly spaced polar coordinates (θ, r), where the center of the coordinate system is aligned with the center of mass. This representation was convenient because it allowed us to treat the interface as a 1D signal rather than a 2D image. However, minor fluctuations along the interface and uneven growth fronts due to the presence of cylindrical walls meant that we were unable to reliably detect the proper reference points for the growth front. For example, in Fig. 4.3 **(c)**, we can see that is not straight forward to identify where active growth front is from raw polar coordinates. If we take the maximum radius, we get a point along the interface that has already hit the wall (yellow region, Fig. 4.3 **(a)**).

We reduce noise and enhance desired features in the 1D signal as follows:

1. We normalize and map the radial component to a shifted cosine,

$$\tilde{r}_i = 0.5 \cdot \left| \frac{r_i}{\max \vec{r}} \cos(\theta) + 1 \right|$$

   where $\vec{r}$ is the $N \times 1$ array containing all radial coordinates for the N interface points, and $|\cdot|$ denotes absolute value. Mapping r to a cosine helps accentuate the strength apex points' signals when compared to the raw, polar interface positions.

2. Before we can apply any filters to reduce noise in our system, we must determine the appropriate window size for our filters. Since the size of our images varies based on the size of the grain, we need to compute the window size for each frame of the simulation. To do this, we compute the cross-correlation of $\tilde{r}$ with the shifted and normalized cosine (Fig. 4.3 **(d)**, dotted blue line), $g(\theta) = 0.5(\cos(\theta_i) + 1)$, and we determine the first point where $g(\theta^*) = 0$. Taking a window of θ^* would be too large (for example, taking a median filter with window size θ^* would yield something that strongly resembled a cosine wave, effectively smoothing

out all of the desired features in the signal). Instead, we take the window as:

$$\text{window} = 2\left\lfloor 0.5\sqrt{\theta^*} \right\rceil + 1$$

to ensure that the window is sufficiently small and odd.

3. Once we determine the appropriate window size, we apply a minimum filter $\hat{f}_{\min}(\tilde{r})$ and maximum filter $\hat{f}_{\max}(\tilde{r})$ to $\tilde{r}$ and compute the element-wise product of that signal $f(r,\theta) = \hat{f}_{\max}\hat{f}_{\min}$ (Fig. 4.3 **(d)**, yellow line). We find that the product of the maximum and minimum filtered signals was the most effective way to preserve the sharpness of the groove while and remove noise due to thermal fluctuations in the signal. From Fig. 4.3 **(d)**, we can see that the peaks detected in $f(\tilde{r})$ correspond to points where the growth front in the simulation begins to resemble an ideal, isotropic growth front.

4.2.5 Bragg Peak Filtering and Positional Order Parameter

We remove liquid from our simulations using the protocol outlined in Method 4.2.3.1. Next, we projected our points down the z axis, and expanded the box size from the original simulation box size (456×456 for dec-QCs simulations and 246×246 for BCC simulations) to 512×512. Then, we converted the projected simulation to a 2048 image by computing a 2D histogram of our simulation. We computed the Fourier Transform (FT) using the Fast Fourier Transform (FFT) algorithm [28].

We detect the five brightest peak pairs from a reference pore-free simulation, then scale those five peak pairs by $\tau = \frac{1+\sqrt{5}}{2}$, the scaling ratio associated with our dec-QC.

We recenter our reference peaks by searching for the brightest point on the power spectrum (i.e. the absolute value of the FT) for each simulation frame. Recentering searches were performed within a 32 sized region, centered at the reference peak coordinate. Once peaks were recentered onto the power spectrum of a given simulation frame, we filtered all 20 peaks (10 peak pairs) in the FT using the Hamming window, and positional order was computed as the inverse Fourier Transform (iFT) of the filtered FT.

4.3 Experimental Results

The contents of this section were performed by and contributed by the Shahani Group.

For comparison with our simulation study, we present the experimental results obtained by our experimental collaborators, Dr. Insung Han and Professor Ashwin J. Shahani.

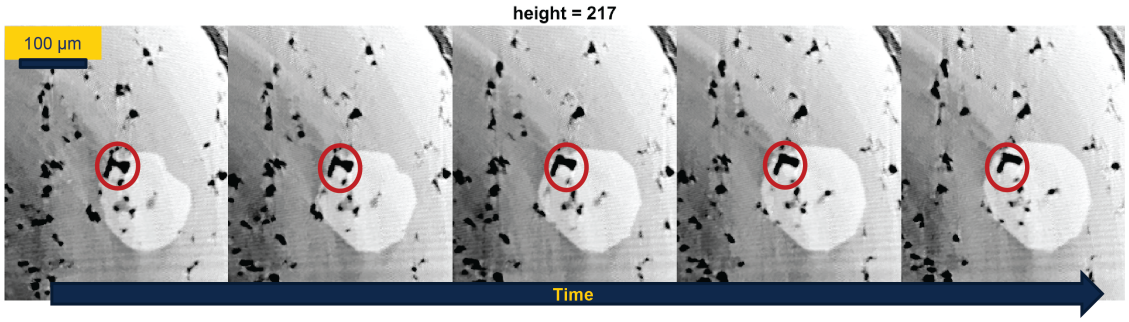

Figure 4.4: **Dislocation free growth of a dec-QC around a shrinkage pore.** Birds-eye view ($\hat{x} - \hat{y}$) of a dec-QC (lighter region) growth around a shrinkage pore (black region, red circle), recorded via XRT. Results were recorded every 10 minutes via XRT with 20s scan time over 50 min of cooling (1 °C/min) from 1030 °C. *This image is contributed by Dr. Insung Han and Professor Ashwin J. Shahani.*

Fig. 4.4 depicts the time-evolution of a single dec-QC upon collision with a shrinkage pore in an alloy of $Al_{79}Co_6Ni_{15}$ upon slow cooling (1° C / min) from above the liquidus (≈ 1026°C) to below. The growth sequences of the as-grown dec-QCs were recorded via XRT every 10 mins with 20 s scan time, starting from 1020 °C (at which point the sample was in a fully liquid state). The key advantage of using XRT is that our collaborators can unambiguously visualize the morphologies, misorientations, and growth dynamics of the QCs in real-time and in 3D, without needing to repeatedly quench their specimen. Quenching is known to distort the shapes and orientations of the solid-liquid interfaces [25].

In Fig. 4.4, we selectively focus on collisions between dec-QCs with a shrinkage pore, where Fig. 4.4 displays a bird's eye (or cross-sectional) view of the growth sequences from the quasiperiodic planes. In aluminum-based alloys, porosity arises due two major factors: gas solubility and thermal shrinkage, and is associated with dentritric growth in pure metals and alloys with periodic structures [15, 24, 56, 101, 108]. Fig. 4.4 collision and defect-free engulfment of a shrinkage pore in the absence of dendritic structures or grain boundaries (GBs).

4.4 Simulation Results

We use MD simulations to overcome spatial and temporal limitations of XRT and to isolate the effects of QC structure and pore geometry on dislocation formation. In an effort to understand how aperiodicity suppresses GB and defect formation in the presence of pores, we use quasi-2D boxes to maximize the surface area along the aperiodic plane, $\{00001\}$. We introduce cylindrical walls of particles frozen in a fluid like configuration to minimize the effects of periodic boundary conditions on our growth simulations. Pores are similarly constructed from particles frozen in

fluid-like configurations. We fix the positions of dec-QC seeds throughout our simulations to match experimental conditions, where grains were 'anchored' to the sample surfaces. A detailed description of the simulation setup and analysis is provided in Section 4.2.

Fig. 4.5 shows the evolution of the solid-liquid interface in a simulated dec-QC, where the distance between the pore and seed centers is 99.8, the minor axis is 29.0, the axis ratio is 2.43, and the orientation is 0 radians. Immediately after the dec-QC grows around the pore (Fig. 4.5 **(b-c)**, red line around 7.5×10^6 simulation time steps), we see the formation of a deep, V-shaped groove along the region of coalescence (Fig. 4.5 **(a)**, red dots). Over the next $\approx 5 \times 10^6$ time steps, the groove rapidly diminishes in depth and eventually disappears (Fig. 4.5 **(c)**).

We observe the formation and gradual disappearance of these deep, V-shaped grooves in all of our simulations, where the depth of the groove is largely dependant on the size of the pore (Fig. 4.6 **(a - d)**). the pore is large or the distance between the pore and the seed are large. In these cases, we see the formation of a deep, V-shaped groove upon collision of growth fronts around the pore. These V-shape grooves rapidly diminish in depth, and eventually disappear. Corresponding correlation matrices for Fig. 4.6 can be found in Appendix A.

The appearance of the groove is surprising, since our collaborator's XRT experiments (Fig. 4.4), show that the dec-QC was able to grow around the shrinkage pore with little to no distortions to the decaprismatic morphology of the solid-liquid interface [53]. In solidification experiments, GBs have been shown to create macroscopic depressions (grooves) in the solid-liquid interface of the crystal [18, 46, 106, 114]. According to Young's law [61], the groove angle, ϕ, is related to the GB energy, γ_{gb}, as $\gamma_{gb} = 2\gamma_{sl}\cos(\phi/2)$, where γ_{sl} is the solid-liquid interfacial free energy. If the GB groove persists during growth, it can be inferred that the GB is stable and fixed to the groove, while the disappearance of the V-shaped groove ($\phi \rightarrow 0^\circ$) suggests the annihilation of the GB during growth. This suggests the that formation of the deep, V-shaped grooves in our simulations may correspond to the formation and eventual annihilation of a high energy GB.

To understand why we see the formation of V-shaped grooves in simulation, we first measure potential energy (Fig. 4.7 **(a-e)**), bond orientational order (ψ_k, where $k = 10$ for dec-QCs; Fig. 4.7 **(f)**), and long-range positional order ($||\xi||$; Fig. 4.7 **(g)**) with respect to the pore center. Potential energy is computed based on the pair potential (Fig. 4.9 **(a)**; dark, solid red line), while the k-atic order parameter, $||\psi_k||$, is computed based on the $k = 10$ nearest neighbors (Methods 4.2.3), and positional order, $||\xi||$, is computed from the iFT of a Bragg peak filtered FT of the simulated dec-QC (filtered peaks circled in red Fig. 4.7 **(a)**, inset; Methods 4.2.5). Here, $||\cdot||$ denotes the norm of some vector $\vec{a}$: $\sqrt{\vec{a} \cdot \vec{a}^*}$, where $\vec{a}^*$ is the complex conjugate of $\vec{a}$. Full details of each calculation may be found in corresponding subsections of Methods.

Here, we use the per-particle potential energy as a proxy for strain, while $||\psi_{10}||$ is a measure of local orientational order. per-particle potential energy and $||\psi_k||$ are strictly measures of local order,

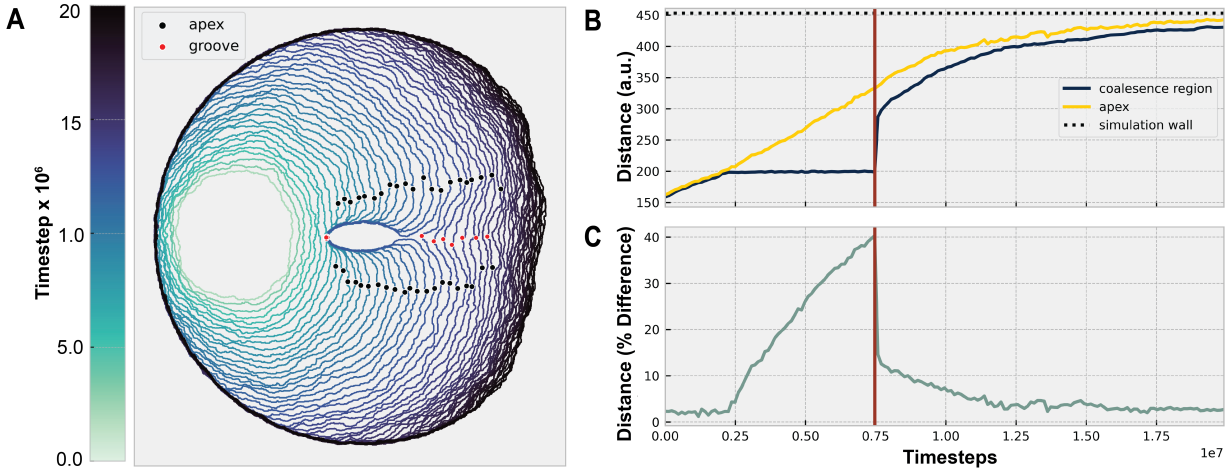

Figure 4.5: **Solid-liquid interface of simulated dec-QC growth around an obstacle. (a)** Solid-liquid interface over 20×10^6 simulation time steps. Light green (lighter color) indicates earlier time steps. Black (darker color) indicates later time steps. Black dots correspond to *apex* locations, or the region where the growth front remains unaffected by the presence of the groove. Red dots correspond to regions where the groove is deepest. **(b)** Tracks the distance of the groove and apex with respect to the seed center (nucleation site) throughout the simulation. Here, yellow (lighter color line) corresponds to growth along the apex (black dots), while blue (darker color line) corresponds to growth along the groove (red dots). The vertical red line denotes the time step right before coalesence occurs, and the dotted black line corresponds to the location of the simulation wall, with respect to the growth front. **(c)** Shows the evolution of the groove depth throughout the simulation. Here, we plot groove depth with respect The vertical red line denotes the time step right before coalesence occurs.

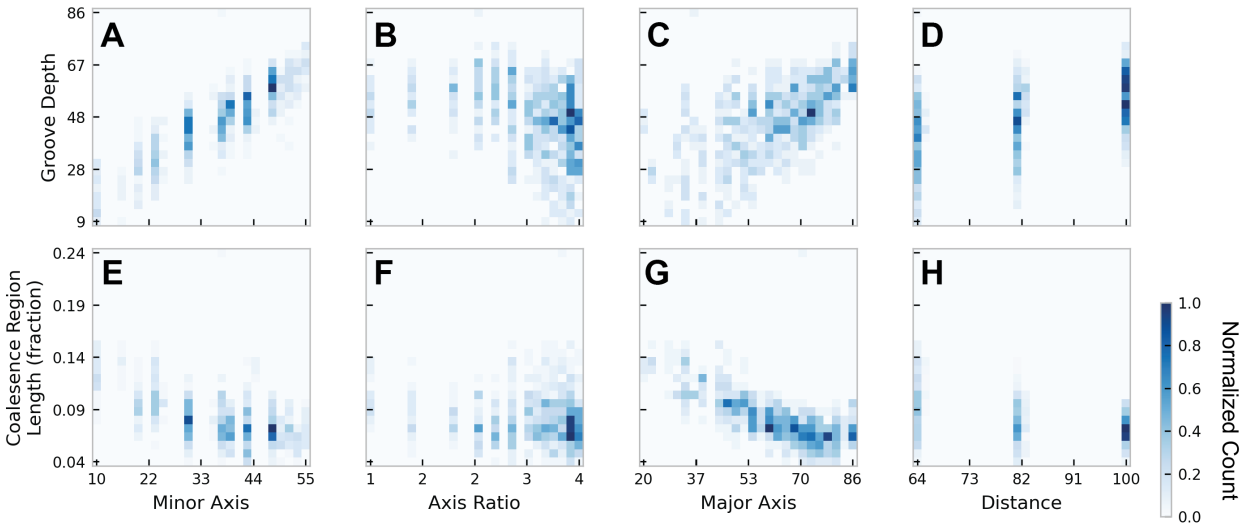

Figure 4.6: **Effects of QC-pore collision conditions on groove depth and characteristics.** We compute the **(a-d)** groove depth and the **(e-h)** size of the region of coalesence upon collision of growth fronts as a function of the pore's **(a, e)** minor axis, **(b, f)** axis ratio, **(c, g)** major axis, and **(d, h)** distance between the pore center and the seed center (nucleation site). Size of the coalesence region up collision was measured relative to the distance between the furthest edge of the pore and the wall. Corresponding correlation matrices can be found in Appendix A.1.

where regions of high phonon strain or per-particle potential energy are typically associated with defects, dislocations, and other classical defects traditionally associated with GBs and disorder in periodic crystals. Meanwhile, $||\xi||$ captures both phononic and phasonic strain (short and long range order).

4.4.1 Bragg Peak Filtering and Quasiperiodic Functions

We say that $||\xi||$ is a measure of long range positional order because of its relationship to Fourier space. The FT of the crystal allows us to capture the global, spatial symmetries of an entire system in the frequency domain. When we filter a set of frequencies associated with the global symmetries of the system (e.g. Bragg peak filtering), we zero all frequencies in the FT outside of the frequencies associated with a given basis vector, $\vec{b}_k$, or a set of basis vectors. Then, when we map them back to real space via the iFT, $||\xi||$, we essentially transform our representation of the crystal from one of discrete particles to a sum of plane wave with frequencies described by $\vec{b}_k$ (see Secs. 2.3 and 2.7 for more details).

Among the possible options to measure quasi-long range order associated with QCs and QC-like structures, the Fourier space description was most attractive for several reasons: (1) We can extend the procedure for analysis of periodic crystals to QCs with little to no modification to

our workflow. (2) We can map *phason strain*, or deviations from quasi-long range order, to real space (Fig. 4.7 **(a-e)**), and (3) the FFT algorithm [28] allows us to quickly and efficient process large batches of simulation data. Similar procedures have been used previously to measure phason strain in photonic quasicrystals [43] and in our previous work (Chapter 3, [52]), where phason strain measurements were obtained by binarizing the iFT magnitude, after filtering two pairs of Bragg peaks, where the two pairs of Bragg peaks were select such that they represented the two length scales associated with the QC.

We adopt this protocol with a few modifications: First, rather than filtering two pairs of Bragg peaks in the FT, we filter all Bragg peaks pairs associated with the two length scales of the dec-QC (10 pairs of peaks in total, where 5 pairs are associated with the 5 basis vectors of the dec-QC and 5 pairs associated with the 5 basis vectors, scaled by τ; red circles in inset of Fig. 4.7, **(a)**). We do this because filtering all Bragg peaks associated with a length scale of the dec-QC, rather than a pair of Bragg peaks, measure deviations from quasi-long range order in the QC along all of the relevant $\vec{b}_k$. Meanwhile, filtering a pair of Bragg peaks measures deviations from the single basis vector $\vec{b}_k$. In some cases, dislocations introduce strain along some, but not all basis vector (e.g. a screw dislocation), or dislocations may introduce strong distortions along one or two $\vec{b}_k$, and very weak distortions along another $\vec{b}_k$. This means that we may miss certain types of defects and dislocations when we filter by a single pair of Bragg peaks associated with a $\vec{b}_k$, or by filtering two pairs of Bragg peaks that represent the two length scales of our dec-QC ($\tau = \frac{1+\sqrt{5}}{2}$, $\vec{b}_k$ and $\tau\vec{b}_k$). Second, we do not binarize the output of the filtered FT, $||\xi||$, since it was more straight forward for us to automate strain detection from the raw $||\xi||$.

We note, however, that it is not straightforward to decouple phason strain from phonon strain using this method (for more details Fig. 2.9 in Sec. 2.7.3). This effect is similar to how traditional dislocations and defects can also cause decreases in iFT magnitude (see Sec. 2.7 and Chapter 5 for a more detailed discussion on Bragg peak filtering in periodic crystals). Previous studies have suggested that filtering two pairs of Bragg peaks, $\vec{b}_k$ and $\tau\vec{b}_k$, allows us to measure both phason and phonon strain, whereas filtering one pair of Bragg peaks measures phonon strain in a system [43]. Our results suggest that phason strain can still be detected when filtering only a single pair of Bragg peaks – though a change in $||\xi||$ is much weaker and harder to detect in these cases.

In light of these results, we compare $||\xi||$ (Fig. 4.7 **(a-e)**) to measures of local order (potential energy and $||\psi_{10}||$ in Fig. 4.7 **(f-g)**) to help decouple the effects of phonon strain and phason strain on our system.

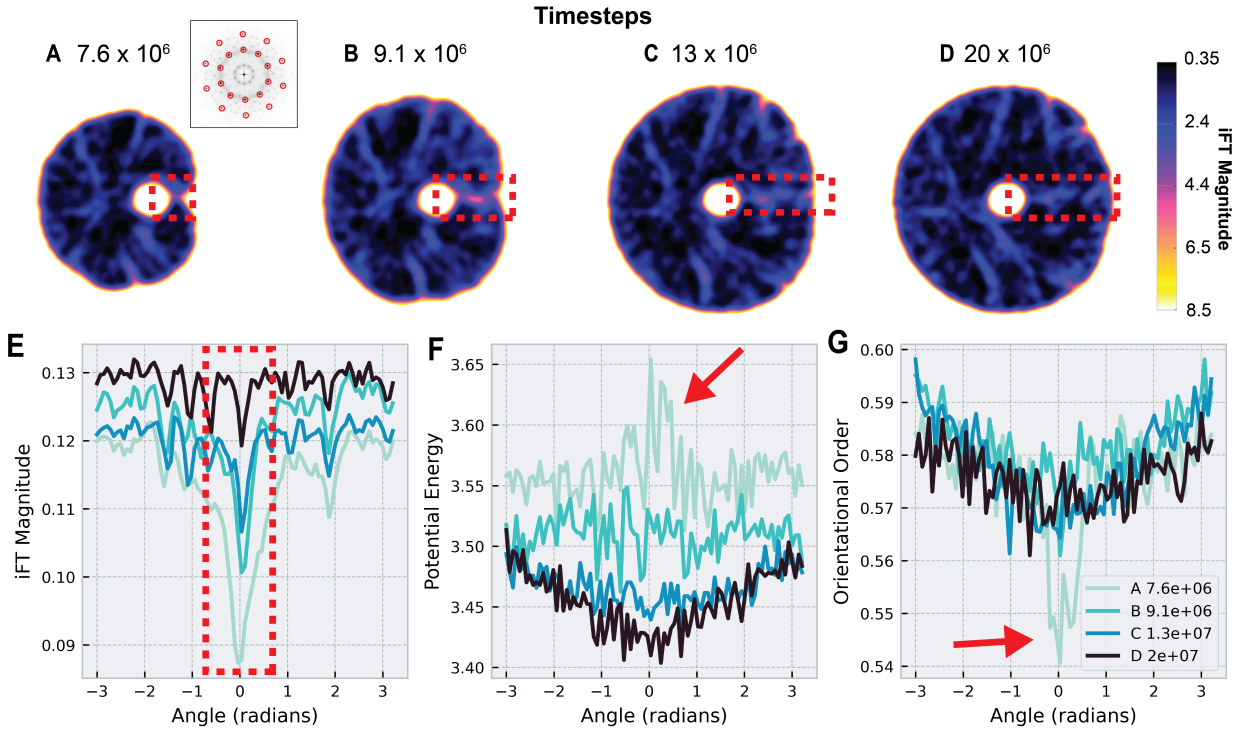

Figure 4.7: **Evolution of potential energy, orientational order, and positional order of a QC upon collision with a pore.** Positional order of a dec-QC simulation upon collision with a pore at **(a)** 7.6×10^6, **(b)** 9.1×10^6, **(c)** 13×10^6, and **(d)** 20×10^6. Here high $||\xi||$ (black) corresponds to strong positional order, while low $||\xi||$ (white) corresponds to poor positional order (e.g. liquid), and $||\xi||$ is the iFT magnitude of the 10 brightest pairs of peaks (red circles in the power spectrum shown in **(a)**, inset). To examine the effects of coalescence (red boxed regions, **(a-e)**) on positional order, $||\xi||$, potential energy and orientational order $||\psi_{10}||$, we converted our particle positions from Cartesian to polar coordinates. Then, we binned our positions based on the azimuth (4° per bin), and compute the means of **(e)** $||\xi||$, **(f)** potential energy, and **(g)** $||\psi_{10}||$ for each bin. We see a sharp decrease in $||\xi||$ along the region of coalescence persists throughout the simulation (boxed region, **(e)**). When growth fronts first meet at **(a)** (light blue-green lines in **(e-g)**), we see a sharp increase in potential energy (red arrow, **(f)**) and a sharp decrease $||\psi_{10}||$ (red arrow, **(g)**), which are consistent with a strong decrease in local positional order in the dec-QC upon collision of growth fronts.

4.4.2 Phason Strain and Phonon Strain Measurements in a Simulated Quasicrystal

Upon the collision of two growth fronts, we see a sharp decrease in $||\xi||$ along the *region of coalescence* (Fig. 4.7 **(a-e)**, red boxed regions). This sharp decrease in $||\xi||$ slowly fades through the early stages of coalescence around the pore (Fig. 4.7 **(a-c)**), until it becomes virtually indistinguishable from normal fluctuations (Fig. 4.7, **(d)** and black line in **(e)**). This suggests that a region of high phason and/or phonon strain forms along the region of coalescence upon collision of growth fronts, then relaxes to insignificant levels during growth.

To determine if this sharp decrease in $||\xi||$ is due to phasons or to a combination of phason and phonon contributions, we examine mean particle potential energy and particle orientational order $||\psi_{10}||$ as proxies for phonon strain. If the sharp decrease in $||\xi||$ is primarily due to phonon strain, we expect to see similar, sharp increases in potential energy along the region of coalescence, and sharp declines in orientational order along the region of coalescence, that fade slowly over time.

At very early stages of collision (Fig. 4.7 **(f, g)**; light blue-green lines, red arrows), we see a sharp spike in the average per-particle potential energy, and sharp dips in $||\psi_{10}||$ along the region of coalescence. These results are consistent with a strong decrease in local positional order seen in Fig. 4.7 **(e)**, and suggest that the interface formed upon collision of growth fronts is more disordered than the rest of the QC. As the QC continues to grow, however, the potential energy along the region of coalescence becomes virtually indistinguishable from the surrounding crystal ($\approx 5 \times 10^5$ time steps; Fig. 4.7 **(f)**, blue-green line associated with **(b)** 7×10^6 time steps), yet positional disorder (Fig. 4.7 **(a-e)**) and orientational order remain (Fig. 4.7 **(f)**, red arrow).

Interestingly, during later stages of the simulation, we see a significant *decrease* in the relative average potential energy along the region of coalescence during later stages of growth (Fig. 4.7 **(f)**), despite the presence of residual orientational order, $||\psi_{10}||$ (Fig. 4.7 **(g)**). Meanwhile, positional disorder, $||\xi||$, appears to relax to nearly indistinguishable levels (Fig. 4.7 **(d)**, boxed region, and **(e)**, black line).

In Fig. 4.9 **(a)**, we plot the histogram of bond lengths for the five nearest neighbors of each particle in a pore-free QC simulation (dotted blue line) against the pair potential used to self-assemble the crystal (solid dark red line). Since these simulations are held at finite temperature, thermal fluctuations and entropy can result in particle distances that do not align perfectly with the local minima in our pair potential (Fig. 4.9 **(a)**; solid dark red line). Rather, we a bimodal distribution of bond lengths in our simulation, with means centered near the local minima of our pair potential (Fig. 4.9 **(a)**, where the dotted blue line is the histogram of bond lengths of the five nearest neighbors of each solid particle in a pore-free simulation). This means that, on average, the distribution of bond lengths in our self-assembled QC align well with the local minima in the

pair potential (Fig. 4.9 **(a)**; black arrows). This also means that mean per-particle potential energy may act as a proxy to measure bond order and strain, where we may expect higher mean per-particle potential energy in the presence of significant direct space strain or GBs and lower mean per-particle potential energy in regions with low direct space strain and minimal dislocations.

Similarly, we expect bond orientational order to decrease in the presence of real space strain or dislocations. It follows then, that decreases in $||\xi||$ due to real space strain or a GB (an array of real space dislocations) should result in an increase mean per-particle energy and a decrease mean orientational order, $||\psi_{10}||$. In the absence of real space strain or GBs, we expect uniform distributions of potential energy and $||\psi_{10}||$ when averaged over angular coordinates. Instead, we see divergent trends between potential energy and $||\psi_{10}||$ after $\approx 10 \times 10^6$ time steps. Along the site of collision, the orientational order along the site of collision remains lower than the surrounding crystal (Fig. 4.7 **(f)**; black arrow), and yet mean per-particle potential energy along the site of collision remains lower than the surrounding crystal. If mean per-particle potential energy was a perfect analogue for direct space strain (i.e. significant deviations from one of the two length scales of our QC, as defined by the pair potential), then, this dip in mean per-particle potential energy along the site of collision would suggest that we see lower strain, and potentially, higher structural order in the QC where coalescence occurred. To understand why we see lower mean per-particle potential energy along the region of coalesence when compared to the rest of the crystal, and to understand why we see divergent trends in orientational order and mean per-particle potential energy, then, we must investigate our assumptions surrounding per-particle potential energy's relationship to order in our simulations.

4.4.3 Bond Length Distributions in Quasicrystal-Pore Simulations

The differences between well depth and shape in our double-well pair potential (Fig. 4.9 **(a)**; solid, dark red line), may be the source of the conflicting measurements between mean per-particle potential energy and $||\psi_{10}||$, where the well associated with the first length scale is narrower and higher in energy than the well associated with the second length scale. This suggests that the decrease in potential energy along the region of coalesence may be due changes in the QC's configuration. Specifically, if the decrease in mean pre-particle potential energy is due to a change in ratio of length scales we see in the system, we should expect to see more open structures along the region of coalesence, such as decagons and nonagons, rather than pentagons or hexagons, since these favor the longer length scales associated with the dec-QC (Fig. 4.8).

Here, it's interesting to note that, as a consequence of self-similarity in mathematically ideal QCs, the incommensurate frequencies associated with a zero phason strain QC are also reflected in the relative frequency of different tiles types [38], and, by extension, the ratio of length scales in

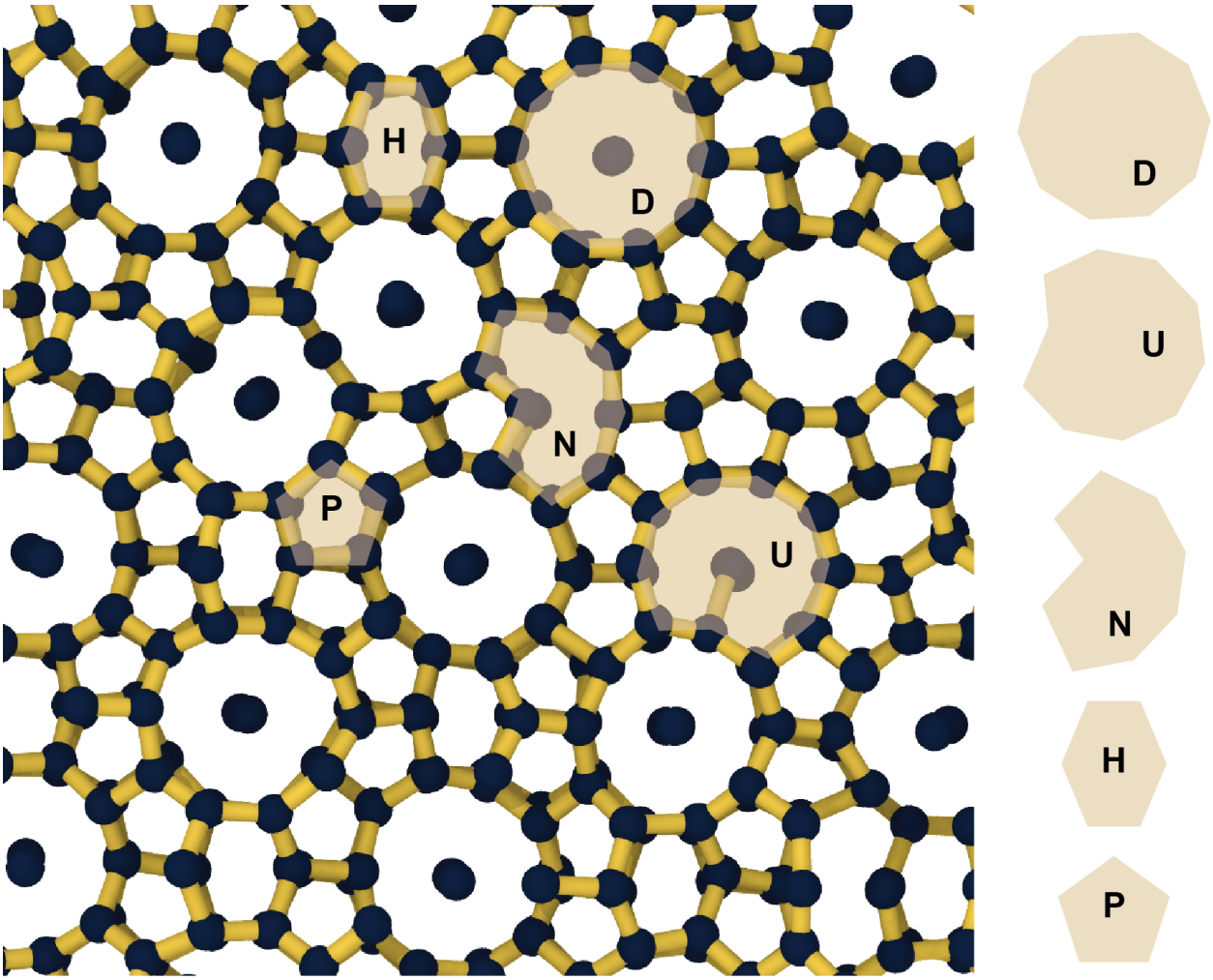

Figure 4.8: **Snapshot of a Tübingen tiling-like dec-QC simulation.** The Tübingen tiling is constructed from 5 prototiles: decagon (D), u-tile (U), nonagon (N), hexagon (H), and pentagon (P).

a given system. A simple example of this phenomenon is observed in the 1D Fibonacci sequence. The Fibonacci sequence consists of long and short segments which appear with a specific ratio: $R_{1,\tau} = N_1/N_\tau \to \frac{1}{\tau}$, where $R_{1,\tau}$ is the ratio between length the two length scales associated with the Fibonacci sequence, N_1 is the number of short segments in a given sequence, and N_τ is the number of long segments in a given sequence. Meanwhile, in an approximate Fibonacci sequence, the ratio between length scales reflects the Fibonacci ratio associated with that approximate: $R_{\tau,1} = 1, \frac{1}{2}, \frac{2}{3}, \frac{3}{5}, \cdots$. (for more details see Sec. 2.5.1; Nagao et al. [95] also provides a helpful schematic illustrating this phenomenon). While the relationship between $R_{1,\tau}$ and τ is less straightforward in our self-assembled, quasi-2D dec-QC than those seen in a mathematically ideal, 1D quasi-crystal analogue, we can still borrow some important intuition from this example. Specifically, we see that the ratio of length scales, $R_{1,\tau}$, in a given system is fundamentally related to the presence of

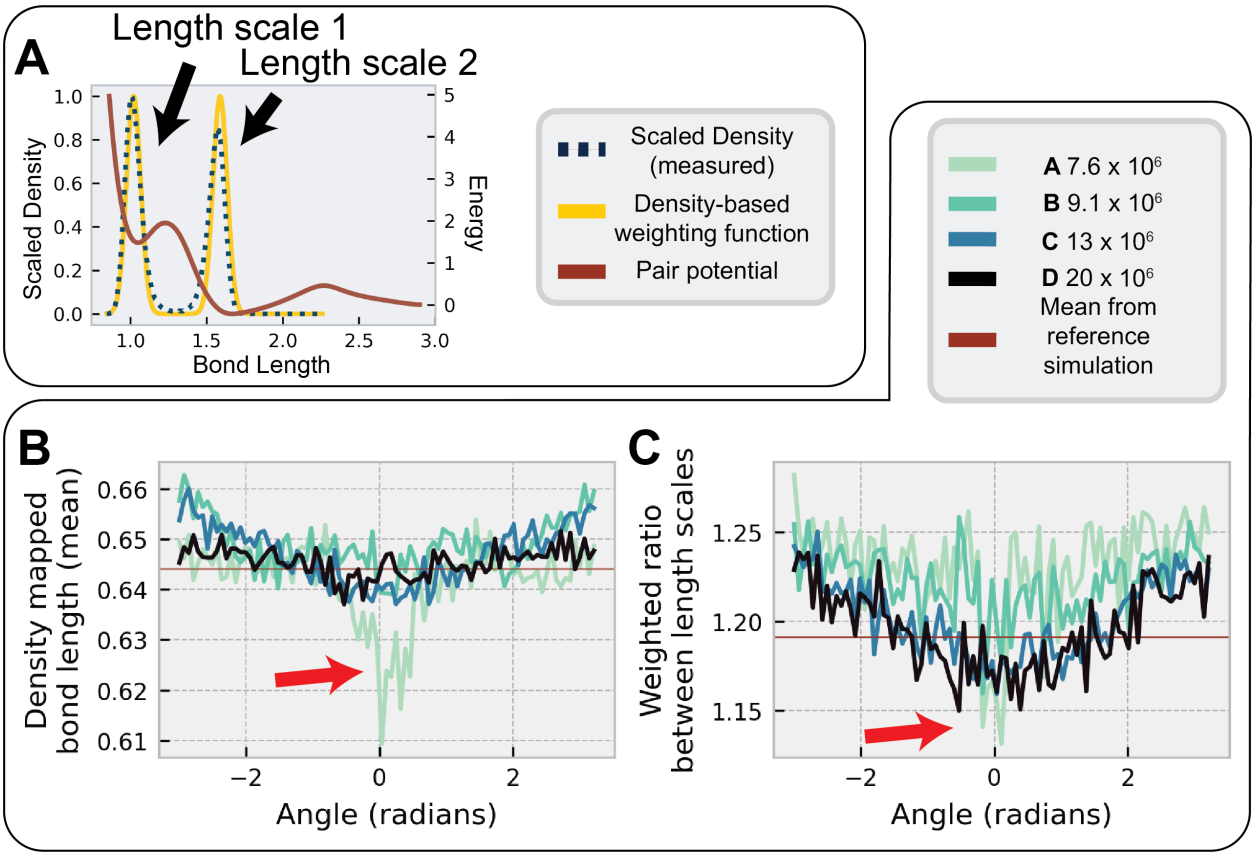

Figure 4.9: **Evolution of Gaussian mapped bond lengths upon QC collision with a pore.** **(a)** We histogram bond lengths for the 5 nearest neighbors of each particle from a pore-free simulation (dotted, dark blue line), and compute the mean and standard deviations associated with each length scale. Then, we sum together two, evenly weighted Gaussians based (solid yellow line), and map bond lengths to **(b)** both length scales, and we compute the **(c)** the ratios between the Gaussian weighted sum of both length scales over 7.6×10^6, 9.1×10^6, 13×10^6, and 20×10^6 time steps with respect to the average density mapped bond lengths (red line in **(b)**), and the weighted ratio between length scales (red line in **(c)**).

phasons and phason strain.

In fact, in pore-free simulations, we see higher $R_{1,\tau}$ during early stages of growth, and lower values of $R_{1,\tau}$ during later stages of growth. Similarly, we see global increases in $|\xi|$ as the QC continues to grow (Fig. 4.7 **(e)**), a phenomenon not seen in simulations in periodic systems (Fig. 4.11 **(e)**). It is well known that QC grow with phason defects that are subsequently relaxed to a nearly zero-phason strain structure over time [67, 95]. This decrease in $R_{1,\tau}$ in pore-free simulations suggests that $R_{1,\tau}$ is a proxy for the phason strain of a system when paired with other measures of order. For comparison to our QC-pore simulations, we plot the mean value of $R_{1,\tau}$ from pore-free simulations after 20×10^6 simulation time steps in Fig. 4.9 **(c)** (straight red line at 1.19),

To determine if the unexpected trends observed in Fig. 4.7 originates from a change in the

ratio of length scales in a given region, we compute a histogram of bond lengths for the five nearest neighbors of each particle in 7 pore-free simulations. We find that the bond lengths follow a bimodal, Gaussian-like distribution with means centered near the minima of the pair potential wells (Fig. 4.9 **(a)**, solid red line). Despite the width of the well associated with the second length scale, we find that the Gaussians associated with each well have nearly equal standard deviations, $\sigma_1 \approx \sigma_\tau$, where σ_1 is the standard deviation associated with the first length scale, and σ_τ is the standard deviation associated with the second length scale.

Based on distributions measured from pore-free simulations, we parameterize density-based weighting functions, $w_i(\vec{r})$, for each length scale:

$$w_1(\vec{x}_j) = \sum_k^5 \exp(-0.5(\vec{r_{j,k}} - \mu_1)^2/\sigma_1^2),$$
$$w_\tau(\vec{x}_j) = \sum_k^5 \exp(-0.5(\vec{r}_{j,k} - \mu_\tau)^2/\sigma_\tau^2),$$

and $w_{1,\tau} = w_1 + w_\tau$ (Fig. 4.9 **(a)**; yellow line), where μ_1 is the bond length associated with the first length scale, μ_τ is the bond length associated with the second length scale, $\vec{x}_j$ is the position particle j, and $\vec{r}_{j,k}$ is distance between the particle j and particle k, and $k = 1, \ldots, 5$ denotes the five nearest neighbors of the particle j.

The density-based weighting functions, w_1 and w_τ, are proportional to the probability density functions associated with each length scale. By weighting these density-based functions evenly in $w_{1,\tau}$, we are able to construct an unbiased metric with which we can determine the relative numbers and quality of bonds QC.

When the distance between two particles is equal to the first length scale, $\mu_1 = \vec{r}_{j,k}$, then $w_1 = 1$ and $w_{1,\tau} = 1$. When the distance between two particles is equal to the second length scale, $\mu_\tau = \vec{r}_{j,k}$, then $w_\tau = 1$ and $w_{1,\tau} = 1$. Meanwhile, $\vec{r}_{j,k}$ that deviate from $w_i = \sum_k^5 \exp(-0.5(r_{j,k} \vec{-} \mu_i{}^2)/\sigma_\tau^2)$ will approach 0. Here, we treat w_i as a proxy for strain, where $w_i \to 1$ corresponds to a lattice with ideal bond lengths, and $w_i \to 0$ corresponds to a lattice with non-ideal bond lengths.

If we look at the density-based weights for both length scales, $w_{1,\tau}$, (Fig. 4.9 **(b)**), we see an initial, sharp drop in $w_{1,\tau}$ (red arrow, Fig. 4.9 **(b)**). This result is consistent with those seen in Fig. 4.7, where we see a spike in potential energy and a sharp decline in positional and orientational order upon collision of growth front. When we look at $w_{1,\tau}$ at later time steps (Fig. 4.9 **(b)**, darker lines), however, we see that the disorder along the region of coalescence quickly relaxes to values nearly indistinguishable from the rest of the QC. Additionally, we find that $w_{1,\tau}$ approach values consistent to those observed in pore-free simulations (Fig. 4.9 **(a)**, horizontal red line). This

suggests that any deviations from real-space order, as measured by $w_{1,\tau}$, are fully relaxed to levels comparable to pore-free simulations during later stages of growth.

Next, we examine the weighted ratio between length scales ($R_{1,\tau}$, Fig. 4.9 **(c)**). Initially, we do not see any strong, spatial dependence in $R_{1,\tau}$ – meaning, we do see any significant difference between the ratio of length scales at the region of coalesence and more mature regions of the QC upon collision. During later stages of growth ($\geq 13^6$ time steps; darker lines), however, we see a spatial dependence in $R_{1,\tau}$. Specifically, we see significantly lower $R_{1,\tau}$ along the region of coalescence than the surrounding regions. This initial sharp decrease in $R_{1,\tau}$ upon collision means that there is an increase in w_τ, which corresponds to an increase in the the number of bonds associated with the longer length scale, during coalescence, and a decrease in w_1, which corresponds to a decrease in the number of bonds associated with the shorter length scale. This suggests that open structures associated with the longer length-scale of the QC can help mediate grain coalesence upon collision (see Fig. 4.8; D, U, and N prototiles).

Since $w_{1,\tau}$ and $||\xi||$ remain high and relatively uniform in those regions where we see a decrease in $R_{1,\tau}$. These results show that the decrease in mean per-particle potential energy near the region of coalesence (Fig. 4.7 **(f)**) is due to a change in $R_{1,\tau}$. They also suggest that the open structures formed along the region of coalesence have relatively high positional order (as measured by $||\xi||$) and low strain (as measured by $w_{1,\tau}$ and potential energy), despite the persistent decrease in orientational order along the region of coalesence.

Taken together, these results show how the presence of two, incommensurate length scales in the QC enable help QCs mitigate translational mismatches in the lattice upon collision of two growth fronts. Revisiting Fig. 2.6 (Ch. 2), we see an example of how phasons may enable a 1D QC to compress in direct space without introducing and defects or strain to the sequence. In Fig. 2.6, we also see the relationship between the phason strain introduced during this "compression" of the 1D quasiperiodic sequence, and length scale ratios. We can take this relative decrease in $R_{1,\tau}$ along the region of coalescence as evidence of the same phenomenon illustrated in Fig. 2.6. That is, the additional, configurational degree of freedom conferred by the loss of translational periodicity (i.e. phasons and the presence of multiple, space-filling configurations of QC prototiles) plays a key role in preventing the formation of GBs or high strain structures in situations where we may expect the formation of GBs or high strained regions in periodic crystals

4.4.4 Influence of Growth Conditions and Interface Characteristics on Quasicrystal Order

Finally, we examine the evolution of relative positional order ($||\xi||$; Fig. 4.10 **(a)**), orientational order ($||\psi_{10}||$, Fig. 4.10 **(b)**), mean potential energy (Fig. 4.10 **(c)**), and distribution-mapped bond

Lower Limit	Upper Limit	Correlation Level
0	<0.20	very weak
0.20	<0.40	weak
0.40	<0.60	moderate
0.60	<0.80	strong
0.80	1.00	very strong

Table 4.1: Correlation strength with respect to correlation coefficient magnitude. Categories were based on recommendations from [42].

lengths ($w_{1,\tau}$; Fig. 4.10 **(d)**). We fixed the position of the groove as the angular coordinate corresponding to the global minimum in angularly-binned $||\xi||$ upon coalesence, and we fix the reference position as the angular coordinate corresponding to the global maximum in angularly-binned $||\xi||$ upon coalesence. We use fixed coordinates to compute our ratio to avoid biasing R_i during later stages of growth, and we do not use groove locations computed from the interface, since we find that the location of the V-shaped groove can move throughout growth, and does not always align well with the region of coalesence.

We compute Pearson's correlation and Spearman's rank correlation for each order parameter (see Appendix A). For a given correlation coefficient, r, where $-1 <= r <= 1$, we will describe the strength of each correlations according to the limits in Table 4.1. We found weak correlations between our measures of order and pore parameters (minor axis, axis ratio, and distance between pore and seed), and between order and interface characteristics upon collision (length of coalesence region and groove depth). Positional order, in particular, had very weak to no correlation with any of our pore parameters and groove depth. Immediately after collision, we do see some weak correlation ($r_{\text{pearsons}} = 0.23$) between $||\xi||$ and the length of the coalesence region upon coalesence, however, this correlation drops quickly within the next $100,000$ time steps (Appendix A.2).

Meanwhile, mean per-particle potential energy and weighted bond lengths ($w_{1,\tau}$) showed very weak to no correlation with most pore parameters and interface characteristics. We observed some weak correlation between mean per-particle potential energy with respect to the major axis length ($r_{\text{spearman}} = -0.29$ to 0.23 between $500,000$ and 2×10^6 time steps after coalesence; Appendix A.5), length of the coalesence region ($r_{\text{spearman}} = 0.21$ at 1×10^6 time steps after coalesence; Appendix A.5), and groove depth ($r_{\text{pearsons}} = -0.24$ at 1×10^6 time steps after coalesence; A.4) at intermediate stages of growth. We observed similar trends between $w_{1,\tau}$ and our various measures of growth conditions, though the correlations seen are lower than those seen in per-particle potential energy.

Of the order parameters measured, orientational order, $||\psi_{10}||$, showed the strongest correlations with growth conditions – though it's important to note that even the strongest correlations

observed were rather weak ($|r| < 0.4$). Specifically, we see weak Spearman's correlations and Pearson's correlations between $||\psi_1 0||$ and major axis length, coalesence region length, and groove depth immediately upon collision. These correlations quickly drop to very weak levels as the QC continues to grow, after which Pearson's correlation coefficients remain very weak, but Spearman's rank correlation coefficients increase to weak levels for minor axis, major axis, distance, coalesence region length, and groove depth (Appendix A.7) around $\times 10^6$ time steps. This disparity between Spearman's rank corrrelation and Pearson's correlation suggests that the relationship between $|\psi_{10}|$ and growth conditions must be monotonic, but highly non-linear.

These calculations show that positional disorder, changes in mean per-particle potential energy, and $w_{1,\tau}$ are relatively independent of the growth conditions and measured interface characteristics. Meanwhile, $||\psi_{10}||$ exhibits some weak, non-linear dependence on growth conditions. Overall, however the even the highest correlations observed are relatively weak, $\max|r| < 0.4$. This suggests that the mechanism behind QC coalesence around a pore is largely dependent on the structure and symmetries of the QC itself, rather than any characteristic of the pore, and that findings in simulation should reproduce experiments.

4.4.5 Evolution of Decagonal Quasicrystal Order Upon Collision with a Pore

Since dec-QC order appears to be relatively uncorrelated with growth conditions, we find that we can aggregate our measures of positional order ($||\xi||$; Fig. 4.10 **(a)**), orientational order ($||\psi_{10}||$; Fig. 4.10 **(b)**), per-particle potential energy (Fig. 4.10 **(c)**), and density-weighted bond lengths ($w_{1,\tau}$; Fig. 4.10 **(d)**) across all of our simulations, and get an approximate trend regarding the evolution of dec-QC order after collision with a pore of arbitrary size and shape. Here, we follow the same protocol used in previous plots, where we transform our particle positions from Cartesian coordinates to polar coordinates, then bin everything by their angular coordinate. We track each respective order parameter along the initial site of collision (solid blue line; circular points), and along the region of highest positional order at the time of collision (dotted red line; triangular points). We fix the positions based on minimum and maximum $||\xi||$, rather than interface characteristics, because we find that the interface groove can move during growth, and does not always align with the regions most associated with coalescence (see Fig. 4.6).

During early stages of collision and growth, we see that $||\xi||$ and $||\psi_{10}||$ exhibits logarithmic-like growth along the region of coalescence (Fig. 4.10 **(a,b)**). These results are consistent with those observed in Fig. 4.7 **(a-e, g)**, where we see an initial, disordered region that relaxes slowly over time. Meanwhile, positional and orientational order remain relatively stable and independent of the order present at the site of coalesence (dashed yellow lines). Here, it's important to note, again,

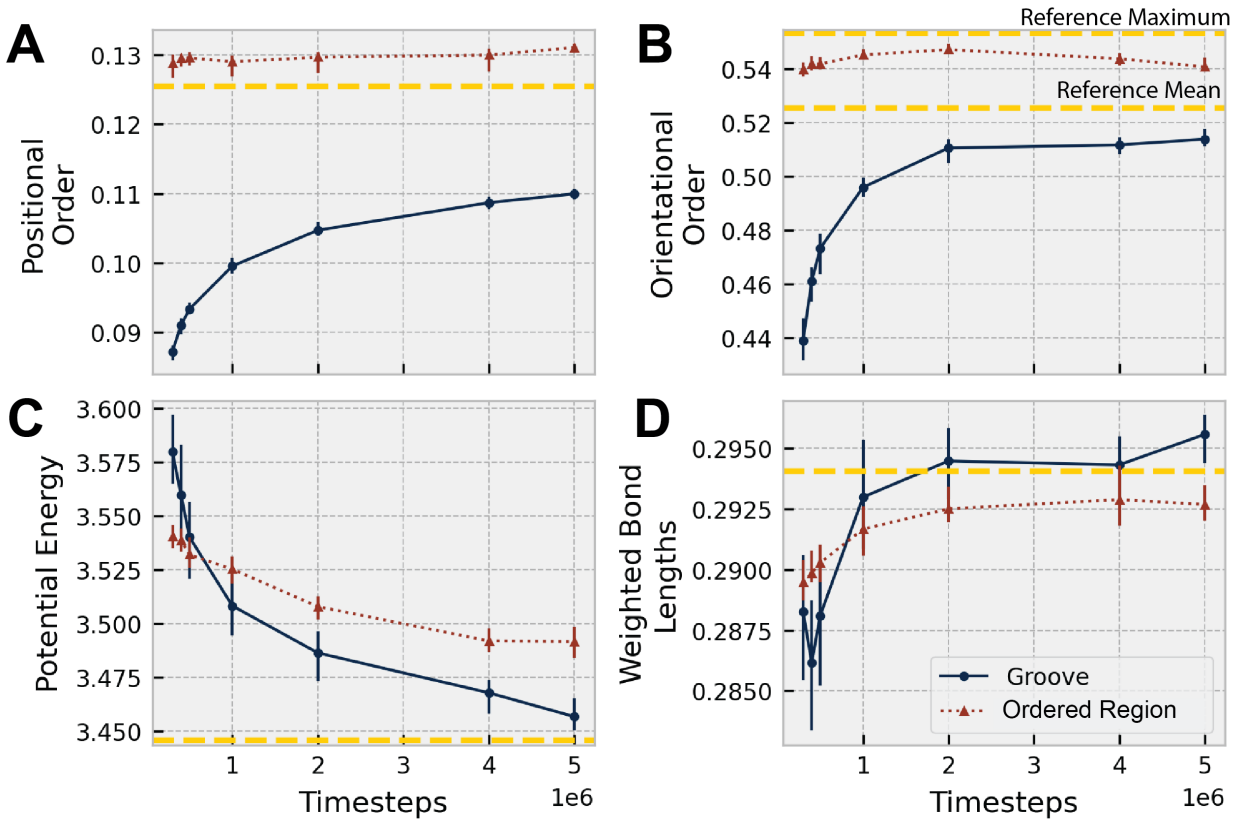

Figure 4.10: **Aggregated measures of QC order over simulated time steps after collision with pore.** Evolution of **(a)** positional order $||\xi||$, **(b)** orientational order $||\psi_{10}||$, **(c)** potential energy, and **(d)** density-weighted bond lengths, $w_{1,\tau}$ after grain coalesence across all of our dec-QC-pore collision simulations, where 0×10^6 corresponds to the point at which growth fronts collide. Points correspond to the median value of each order parameter at a given time step, while bars correspond to the 95% confidence interval. Blue lines with circular points correspond to the order parameter near the initial site of collision. Red lines with triangular points correspond to the order parameter at the most ordered region at the initial time of collision. We measure the evolution of each order parameter over time with respect to these fixed locations. Dotted yellow lines in **(a, c-d)** correspond to the mean value of the corresponding order parameter in a pore-free simulation after 20×10^6 time steps. Dotted yellow lines in **(b)** correspond to the maximum value and mean values of $||\psi_{10}||$ in a pore-free simulation after 20^6 time steps.

that we fixed the center of our polar coordinate system at the center of the pore. This means that the region we chose as a reference point (dotted red lines, labeled "Ordered Region" in Fig. 4.10), may be biased towards higher-than-average values when compared to our pore-free simulations.

Potential energy and $w_{1,\tau}$, two fundamentally related measures of order, also show the same, unexpected trends seen in Fig. 4.7 **(f)** and Fig. 4.9. We see higher per-particle potential energy and lower $w_{1,\tau}$ immediately upon collision. This suggests, once more, that we see the formation of strained structures along the growth front. Within a few 1×10^5 time steps, however, we see that

the strain in the ordered region decrease rapidly, until the region along the region of coalesence becomes *lower* in energy than the surrounding crystal and $w_{1,\tau}$ rapidly becomes higher than the surrounding crystal. Based on our results from Fig. 4.9, we can infer that this decrease in potential energy, then, is due to an increase in the number of open structures along the region of coalesence (or a decrease in $R_{1,\tau}$).

4.4.6 Body-Centered Cubic Crystal Growth Around a Pore

In the absence of phasons and associated configurational degrees of freedom we should expect a strong relationship between strain (as measured by our pair potential) and orientational order. We verify our intuitions regarding positional order, potential energy, and orientational order in the absence of phasons via a simulated BCC collision with a pore (Fig. 4.11). We track the evolution of positional order ($||\xi||$; Fig. 4.11 **(a-d)**), mean per-particle potential energy (Fig. 4.11), and orientational order ($||\psi_4||$; Fig. 4.11 **(g)**) after collision and coalesence around a pore. In these simulations, we see the formation of a dislocation upon collision of growth fronts, which introduces a strong, sharp signal in $||\xi||$ (white dot, Fig. 4.11 **(a-d)**; red arrow, Fig. 4.11 **(e)**). We see that the potential energy and bond orientational order, $||\psi_k||$, show strong, inverse relations in Fig. 4.11 **(f, g)**. This confirms our intuition that, in the absence of phasons and associated configurational degrees of freedom we should expect a strong relationship between strain (as measured by our pair potential) and orientational order.

It's important to note, again, that we centered our polar coordinates at the center of the pore. This means that measurements along the angular coordinate are not completely independent of time. Some measures of order, such as potential energy and $||\psi_4||$, will change as the growth fronts mature in a periodic crystal. This, in part, accounts for the triangular shape of the mean per-particle potential energy and $||\psi_{10}||$. Over long time scales, we would expect the mean per-particle potential energy and $||\psi_{10}||$ curves to flatten out, despite the presence of a dislocation.

Even single dislocations, however, introduce topological defects. In Section 4.4.1, we discussed how $||\xi||$ can be thought of as a sum of plane wave, mapped onto real space. This means that $||\xi||$ is essentially a field measuring contributions of each point in the crystal to *long range* positional order. As a result, the discontinuities introduced by dislocations cause a much stronger decrease in $||\xi||$ than continuous deformations (e.g. phonon strain) formed during coalescence (white dot, Fig. 4.11 **(a-d)**). This drop in $||\xi||$ is so strong that even a single real-space dislocation cannot be averaged out over large bins (Fig. 4.11 **(e)**). Mean per-particle potential energy and $||\psi_{10}||$, however, give us bulk measurements of local order. The effects of a single dislocation would not be significant enough to offset bulk measurements. If we had a GB, which we define as a line of dislocations in direct space, then we would expect a sharp increase in mean per-particle potential

energy and and sharp decrease in orientational order, $||\psi_{10}||$ at the site of the GB.

4.4.6.1 Comparison to Quasicrystal Growth Around a Pore

There are a few notable differences between the results for the BCC simulatoins and those seen in our QC system, which can be attributed to the presence of phasons. First, we note that the global increase in $||\xi||$ observed in our dec-QC simulations (Fig. 4.7 **(e)**) is absent in our BCC simulations (Fig. 4.11 **(e)**). This gradual, global shift in positional order is likely attributed to the error-and-repair growth mechanism unique to QCs, where QCs grow with phason defects that are subsequently relaxed to a nearly zero-phason strain structures over time [67, 95]. Second, we note that the disparity between potential energy and $||\psi_{10}||$ observed in our dec-QCs simulations (Figs. 4.7 **(f, g)** and 4.10 **(b, c)**) is absent in our periodic simulations (Fig. 4.11 **(f, g)**). Our calculations of length scale ratios $R_{1,\tau}$ in Fig. 4.9, suggests that this disparity between potential energy and orientational order likely originates from the presence of phasons in QC. As a consequence of translational periodicity (i.e. the presence of a single unit cell that can describe the entire structure), it is impossible to change the ratio in length scales in a periodic crystal without the introduction of defects.

4.5 Discussion

The potentially detrimental effects of porosity on the mechanical properties of castings is well known and well documented in alloys known to form periodic crystals [15, 24, 56, 101, 108]. Typically, shrinkage pores are discussed in the context of dendritic microstructures in the *mushy zone*, or the region of a phase diagram where solidification occurs. In the mushy zone, we typically see the formation of dendritic microstructures. As these dendrites grow and collide, they have complex interactions with the remaining liquid in the mushy zone and pores that form as a result of, e.g., gas dissolution or solid contraction [101]. In the results found by our collaborators, however, we see columnar prismatic morphologies throughout the solidification process (Fig. 4.4), rendering these dendrite-centric discussions moot. Instead, we focus our work on the behavior of crystal grains upon collision and engulfment of pores. Here, we note that there is limited literature regarding the behavior of periodic crystals upon collision and engulfment of pores or obstacles at the atomic level, and so, we conduct simulations of BCC growth around a pore.

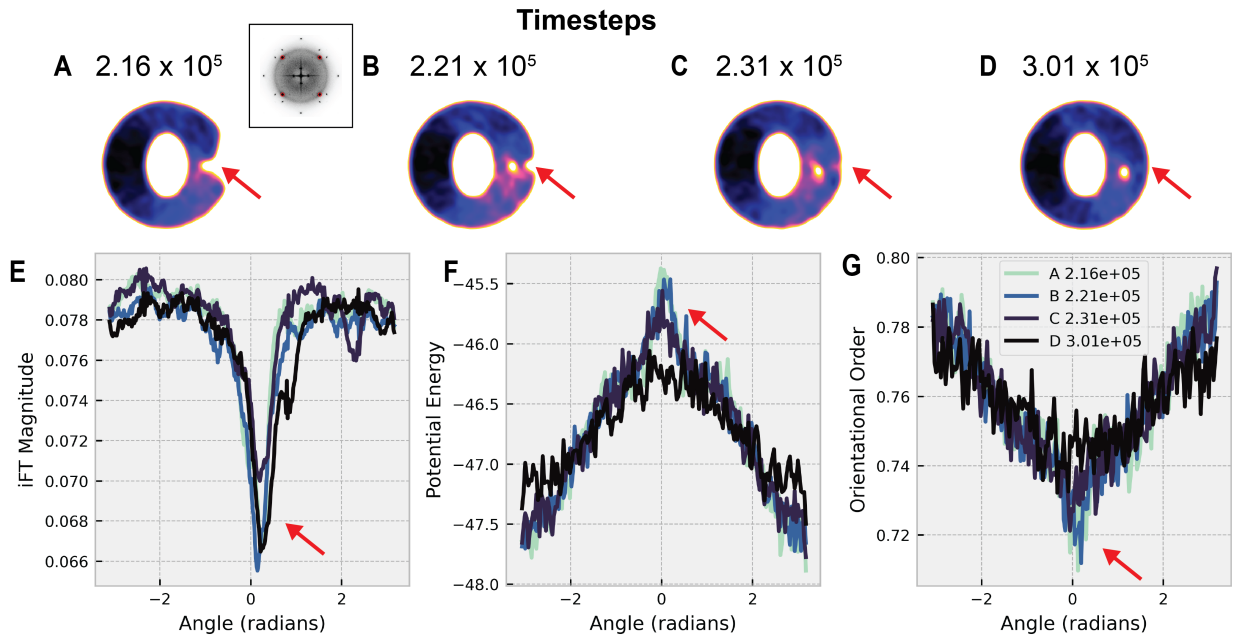

Figure 4.11: **Evolution of potential energy, orientational order, and positional order of a BCC cryastal upon collision with a pore.** Positional order of a BCC simulation upon collision with a pore at **(a)** 2.16×10^5, **(b)** 2.21×10^5, **(c)** 2.31×10^5, and **(d)** 3.01×10^5. Here high $||\xi||$ (black) corresponds to strong positional order, while low $||\xi||$ (white) corresponds to poor positional order (e.g. liquid, dislocations), and $||\xi||$ is the iFT magnitude of the 2 brightest pairs of peaks (red circles in the power spectrum shown in **(a)**, inset). To examine the effects of coalescence (red arrows) on positional order, $||\xi||$, potential energy and orientational order $||\psi_4||$, we converted our particle positions from Cartesian to polar coordinates. Then, we binned our positions based on the azimuth (4° per bin), and compute the means of **(e)** $||\xi||$, **(f)** potential energy, and **(g)** $||\psi_4||$ for each bin.

4.6 Conclusion

We elucidated the growth interaction between dec-QCs grains upon collision with shrinkage pores via 4D XRT and MD simulation. To the best of our knowledge, this is the first simulation-experimental study to investigate QC growth upon collision with shrinkage pores. From our joint analyses, we were able to provide a comprehensive picture of how phasons mediate coalescence upon engulfment of pores or obstacles in the liquid. Upon collision of growth fronts, we see the formation of highly-strained structures and a sharp increase in the relative frequency of long length scales along the side of collision. This suggests that there is an increase in the number of open structures (e.g. decagonal tiles) along the region of coalescence.

Over time, we see the orientational order and positional order increase, and the potential energy decrease, along the region of coalescence. Remarkably, we note that per-particle potential energy changes at a significantly faster rate than orientation along the region of coalescence, ultimately

leading to a lower energy along the side of collision, We attribute the phenomenon to the fact that the ratio of short-to-long length scales remains low along the region of coalescence, when compared to the rest of the crystal. This suggests that the open structures formed upon collision are stable, and that any real-space strain introduced upon collision is absorbed via a phason-mediated mechanism.

Our work shows how phason-mediated coalescence is a powerful mechanism whereby QCs are able to avoid the formation of defects and dislocations in the presence of common solidification defects. Taken all together, our integrated approach highlights the exciting opportunity for microstructure optimization via control of the grain boundaries – that is, defect engineering. It provides the knowledge base for fabrication of defect-free QCs, thereby widening their potential uses and applications.

CHAPTER 5

Mapping Reciprocal Space to Real Space: A Semi-Automated Tool for Advanced Defect Analysis in 3D

This contents of chapter will be submitted for publication in a peer-reviewed journal.

Recent advances in self-assembly and microscopy allow for 3D imaging of complex nanostructures arising in both soft and hard condensed matter systems. At the same time, advances in computing allow for sophisticated simulation models that aid in the understanding and exploration of these systems. However, both experimental and computational analysis of complex crystals at the atomic, molecular and colloidal scales face a common challenge: the lack of generalizable tools for structure, strain, and dislocation analysis. Generalizable methods such as Fourier filtering often rely on manual inspection of structural data, making them impractical for systematic, large-scale studies. Although domain specific tools for automated analysis of 2D electron diffraction patterns exist, these tools are not generalizable to arbitrary 2D and 3D datasets. Here, we present a structure agnostic software tool for analysis of 2D and 3D particle data. Our algorithm is robust to noise originating from liquid, polycrystalline or otherwise disordered regions, and can be used to analyze physical space strain in atomic, molecular and colloidal crystals of varying complexity and from disparate data collection sources. This tool holds promise for advancing structural studies across a variety of domains by providing researchers with a powerful, generalizable tool for understanding and exploring complex crystal structures.

5.1 Motivation

From semiconductors [8, 111, 149] to DNA nanoparticle superlattices [91], defects and dislocations are ubiquitous in self-assembled crystals. The types and quantities of defects greatly impact the quality and properties of a given material, regardless of the crystal's scale or composition

[63, 144, 149]. In some cases the introduction of defects and dislocations can diminish desired properties (e.g. suppression of phonon propagation in thermoelectric materials [149]). In other cases, the introduction of defects such as grain boundaries can be desirable (e.g. work hardening to improve mechanical properties of metals [75] or semi-crystalline polymers [112]).

Recent advances in experimental and simulation techniques give researchers the ability to study growth, dynamics, and phase transitions in ordered matter with extraordinary spatial and temporal resolution. For example, it is now possible to image a variety of soft [90, 91] and hard matter [72, 146] systems with 3D, particle-level resolution. Meanwhile, in simulation, it is now possible to model a variety of complex interactions in experimental systems [143, 145, 150], and to conduct large-scale, exploratory studies [31, 45, 78]. Yet, despite the growing volume of high quality structural data, both experimental and computational analysis of complex crystals at the atomic, molecular and colloidal scales face a common challenge: the lack of generalizable tools for structure, strain and dislocation analysis.

5.2 Background

The characterization and analysis of local particle environments are typically carried out in direct space alone or through Fourier filtering. Among simulationists and experimentalists with access to particle positions in their systems, direct space solutions remain the most popular. Meanwhile, microscopists tend to favor techniques based on reciprocal space filtering for 2D high resolution transmission electron microscopy (HRTEM) images.

Here, we give a brief overview of existing methods for the characterization and analysis of local particle environments using direct space alone, followed by a brief summary of geometric phase analysis (GPA), a Fourier filtered-based method for grain, defect, and dislocation analysis. Finally, we demonstrate the utility of Fourier filtering-based analysis to identify grains, defects, and dislocations in 2D and 3D datasets collected from various sources, and we present a Python-based tool, *PeakyFinders*, to aid in the analysis of crystal structures in Fourier space.

5.2.1 Structural Analysis in Direct Space

5.2.1.1 Local Particle Descriptors

Common measures of local bond order include general descriptors of bond symmetry (e.g. bond orientation order parameters [5, 16, 123]; translational order parameters [5]; Minkowski structure metrics [92]) or algorithms like common neighbor analysis (CNA) [60], dislocation extraction algorithm (DXA) [131, 132], and polyhedral template matching (PTM) [79], which automatically

match crystal structures, dislocations, and grain boundaries in simple condensed phases Meanwhile, general descriptors of local bond order like bond angle order analysis [2] and the Steinhardt order parameter [123], do not require a library of lattices to identify grains or disorder in condensed phases, but still require careful selection of particle neighbors or local symmetry to return meaningful results. Order parameters such as Voronoi-based methods like the Minkowski structure metric [92] and density-based methods [107, 120] attempt to circumvent these issues. However, both the calculation of Voronoi diagrams and density in direct space are computationally expensive. This makes these methods unsuitable for exploratory studies where researchers may get mixed phases of complex, unknown crystals in a single simulation or experiment, or for larger scale studies.

5.2.1.2 Machine Learning

In recent years, numerous machine learning (ML) models have been developed to classify local particle environments [11, 45, 82, 104, 120]. Though powerful, deep, supervised ML models require well labeled data from a variety of crystal structures to return a generalizable model. However, obtaining per-particle labels of local environments in a crystal structure remains challenging and labor intensive. This means supervised ML tend to rely on established order parameters like CNA or Steinhardt to label local environments in training data, and that training data is restricted to structures that researchers can already identify. This limits the variety of structures available to these models and, thus, the model's generalizability to more exotic, complex structures.

Unsupervised ML attempts to circumvent issues with obtaining a variety of labeled, high quality structures that supervised models face. These typically use some combination of clustering and dimensionality reduction to classify particle environments based on particle positions and some set of general descriptors [12, 13, 26, 50, 104, 120]. These methods have been used to effectively classify structures in complex phase diagrams [120], to segment grains in polycrystalline samples [13], to separate growing grains from fluid [104], and, more recently, to identify defects in crystals [12, 26, 50].

Though effective at classification of large domains in a crystal structure, these application of these types of models to the detection of point defects, line dislocations, and the like, remains limited. Existing models are either restricted to 2D inputs [26], rely on 3D, system specific parameters to return meaningful results [12], or they have low precision [50].

5.2.2 Crystals in Fourier Space

Thermal fluctuations, dislocations, and grain boundaries make it challenging to determine long-range order from local environment descriptors. Without a generalized method to determine the type, or types, of long-range order present in a system, it's difficult to measure where grains,

defects, and dislocations do occur.

One potential solution to this problem is to look at the crystal from reciprocal (Fourier) space first. By definition, crystals have essentially sharp Bragg peaks in their diffraction patterns [48], where it position of any Bragg peak in the diffraction pattern, $\vec{b}$, can be expressed as a linear combination of a crystal's basis vectors in reciprocal space, $\vec{b} = \sum_{k=1}^{N} n_k \vec{b}_k$, where $n_k \in \mathbb{Z}$, $\vec{b}_k$ is a reciprocal basis lattice vector, and $N \geq d$ for an d-dimensional crystal.

5.2.2.1 Fourier Transform of a Cosine Crystal

Because reciprocal space is a measure of spatial frequency, it can help to think of these reciprocal lattice vectors, $\vec{b}$, in terms of plane waves, rather than than discrete points. This relationship can be seen most clearly when we construct a crystal from a sum of cosines, rather than discrete points (Fig. 5.1, top row):

$$H(\vec{r}) = \frac{1}{N} \sum_{k}^{N} \cos(2\pi \vec{r} \cdot \vec{b_k}) \tag{5.1}$$

Where, b_k is the set of N basis vectors and $\vec{r}$ is a point in real (direct) space.

If we take the FT of Equation 5.1, we get a point-like Fourier spectrum, where the points can

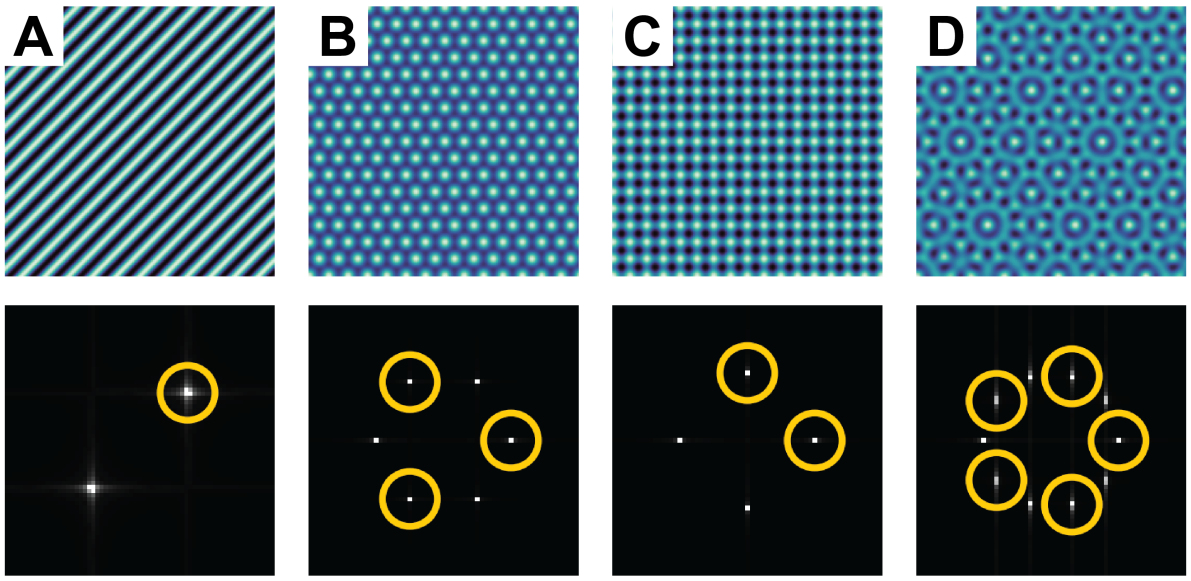

Figure 5.1: **Crystals constructed from a sum of cosines.** Real space (top) and reciprocal space (bottom) images generated from the sum of cosines with basis vectors (circled in yellow) **(a)** $\vec{b_0} = [\cos \pi/4, \sin \pi/4]$; **(b)** $\vec{b_k} = [\cos 2 * k * \pi/3, \sin 2 * k * \pi/3]$ for $k = 0, 1, 2$; **(c)** $\vec{b_0} = [1, 0]$ and $\vec{b_1} = [0, 1]$; and **(d)** $\vec{b_k} = [\cos 2 * k * \pi/5, \sin 2 * k * \pi/5]$ for $k = 0, 1, 2, 3, 4$. For reciprocal space images, plots show the power spectrum (the magnitude of the Fourier Transform (FT)).

be indexed by the basis vectors $\vec{b}_k$ (Fig. 5.1; bottom row, yellow circles correspond to basis vectors used to generate each cosine crystal):

$$F(\vec{x}) = \frac{1}{2N} \sum_{k}^{N} \delta(\vec{x} - \vec{b_k}) + \delta(\vec{x} + \vec{b_k}) \tag{5.2}$$

When we filter a pair of Bragg peaks in the Fourier spectrum, we zero all peaks that are not aligned with some basis vector, b_k. This yields a power spectrum similar to the one seen in Fig. 5.1 **(a)** (bottom) and an inverse Fourier Transform (iFT) similar to the one seen in Fig. 5.1 **(a)** (top). Here, power spectrum refers to the magnitude of the Fourier spectrum, $||F(\vec{x})||$, where $||\cdot||$ denotes the norm of a vector: $\sqrt{\vec{a} \cdot \vec{a}^*}$, and $\vec{a}^*$ denotes the complex conjugate of some vector $\vec{a}$. Typically, diffraction patterns measure $||F(\vec{x})||^2$, or the intensity, rather than the power.

To understand why the FT of a pair of Bragg peaks results in a plane wave, it helps to begin with an understanding of what happens when we filter a single Bragg peak in the Fourier spectrum, $F(\vec{x}) = \delta(\vec{x} - \vec{b}_k)$. Taking the inverse FT of that spectrum, we get the following:

$$\xi_k(\vec{r}) = e^{2\pi i \vec{r} \cdot \vec{b}_k} \tag{5.3}$$

If we contrast this with the positional order parameter[5], which is measured with respect to some $\vec{b}_k$:

$$\chi(\vec{r}) = e^{i \vec{r} \cdot \vec{b}_k} \tag{5.4}$$

we see that the iFT of a filtered Bragg peak is fundamentally related to the positional order parameter, and the iFT of a pair of filtered Bragg peaks is fundamentally related to the cosine representation of a crystal.

Now, if we take the iFT of a pair of Bragg peaks (Eqn. 5.2), we get:

$$\xi_k(\vec{r}) = \frac{1}{2}\left(e^{2\pi i \vec{r} \cdot \vec{b}_k} + e^{-2\pi i \vec{r} \cdot \vec{b}_k}\right) \tag{5.5}$$

Applying Euler's formula to Eqn. 5.5, we get:

$$\xi_k(\vec{r}) = \frac{1}{2} \cos(2\pi \vec{r} \cdot \vec{b}_k) \tag{5.6}$$

When we filter a pair of Bragg peaks for a cosine crystal like those shown in Fig. 5.1, we get one of the individual plane waves used to construct the crystals back out. Filtering a pair of Bragg peaks, or a single Bragg peak for crystals with discrete or point-like particles, however, enables us to transform our representation of a crystal as a set of discrete particles or points, to a finite sum of plane waves.

5.2.3 Application of the Inverse Fourier Transform to Dislocation Analysis

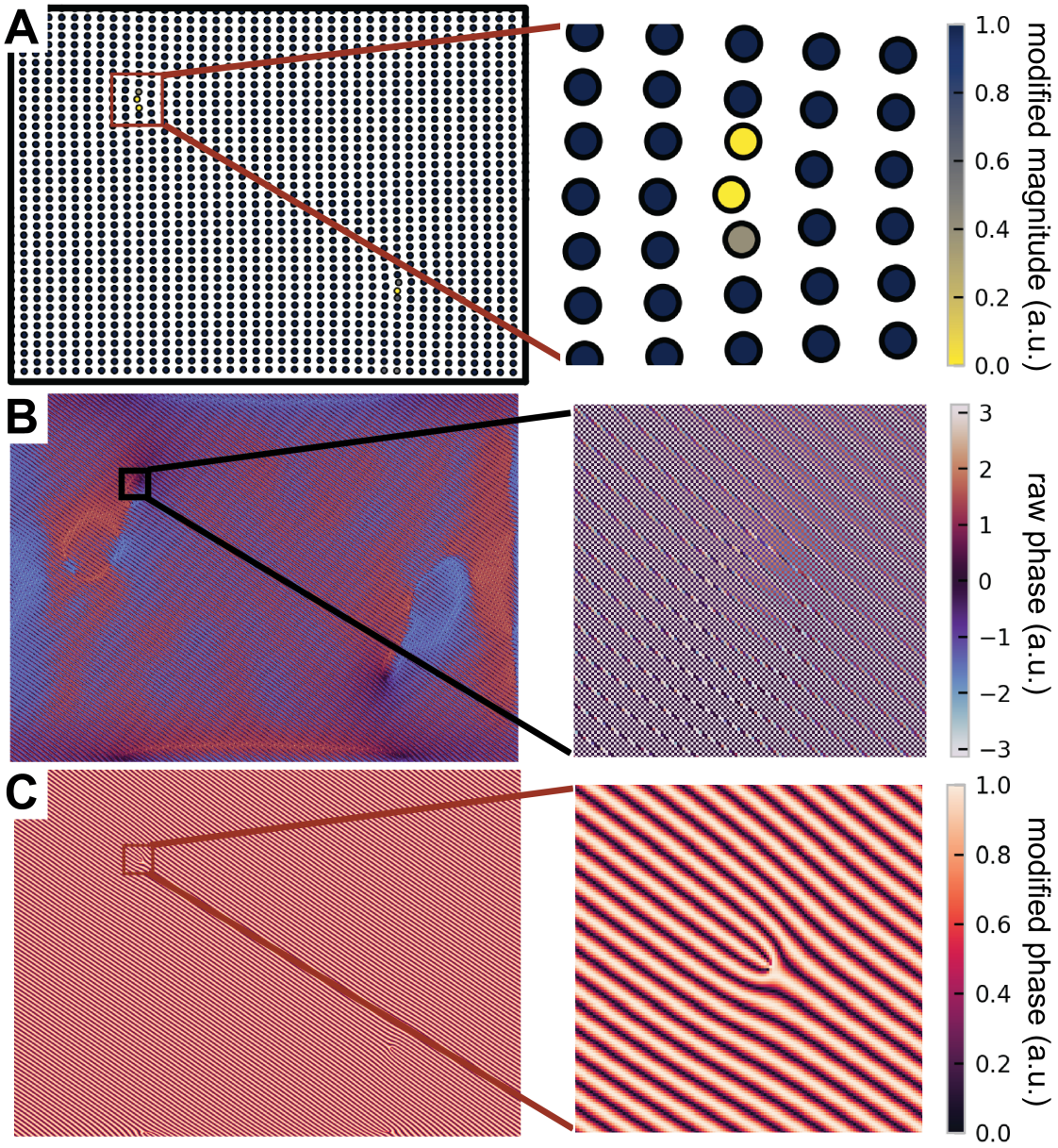

Figure 5.2: **Dislocation detection from Bragg peak filtering using *peakyFinders*.** For a 2D simulation of a dislocation pair in a square lattice: **(a)** Dislocation detected from a single, filtered Bragg peak. The magnitude of the iFT was normalized to 1, then mapped onto a sigmoid centered at 0.3 and scaled to 128. Dark blue (darker color) corresponds to regions aligned with the lattice vector. Yellow (lighter color) corresponds to regions with poor alignment to the lattice vector. Values were mapped from 2D iFT images to 2D simulation points. **(b)** Modified phase of the iFT. We can see changes and distortions in the phase due to the presence of a dislocation. **(c)** Moiré interference pattern due to the dislocation shown in **(a)** and **(b)**. For clarity, phase of the iFT (**(b)**) was mapped to Eqn. 5.8. In **(b)**, blue indicates a value of 0, and yellow indicates a value of 1.

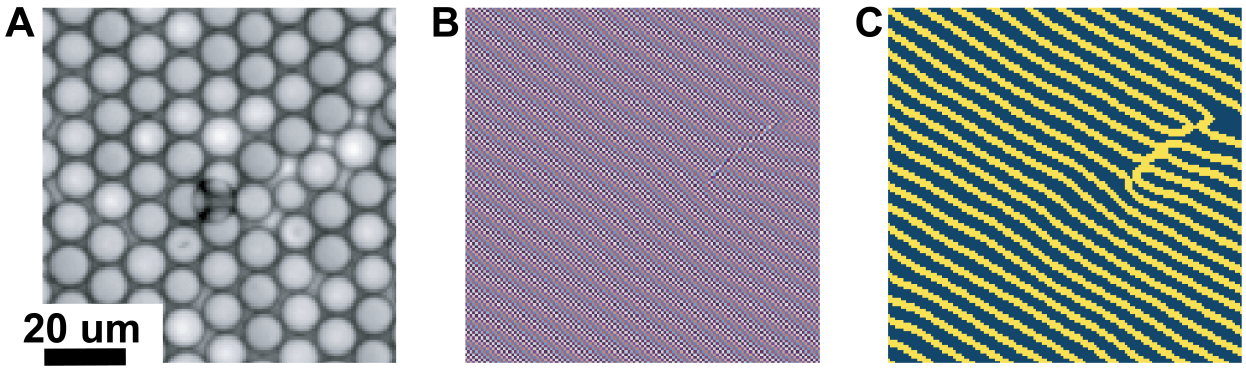

Figure 5.3: **Checkerboard artifacts in the phase due to pixel-level offsets from the peak center.** **(a)** Cropped image of $10\mu m$ glass beads in water. **Source:** "Colloid Crystal 40x Bright Field Glass In Water" [148] by Zephyris, licensed under CC BY-SA 3.0 / Cropped in **(a)**. **(b)** Raw phase, ϕ from the brightest filtered Bragg peak of the image shown in **(a)**. **(c)** Phase modified according to Eqn. 5.8 to remove checkerboard artifact due to pixel-level offsets from the Bragg peak center.

In this plane wave view of crystals, in real (direct) space [62, 105]:

$$H(\vec{r}) = \frac{1}{N}\sum_{k}^{N} \cos(2\pi\vec{r}\cdot\vec{b}_k - 2\pi\vec{r}\cdot\Delta\vec{b}_k) \tag{5.7}$$

These displacement fields, in turn, can cause distortions in the peaks seen in reciprocal space. For a crystal with thermal noise, point defects, and dislocations, we no longer have a perfect, point-like Fourier spectrum. This means that the discrete FT of a crystal behaves like a histogram, where the amplitude of each peak in $||F(\vec{x})||$ (i.e. power spectrum) tells us how many points contribute to a given $\vec{b}_k$. Meanwhile, broadening of these peaks tells us how many particles are strained (i.e. misaligned from the lattice) with respect to a given $\vec{b}_k$. In some ways, we can think about the peak as a sort of 2D or 3D density function, where the density refers to the number of particles displaced by $\Delta\vec{b}_k$ pixels (in the case of a discrete FT).

5.2.3.1 The Magnitude of the Inverse Fourier Transform of a Filtered Bragg Peak

When we filter a single Bragg peak with defects, dislocations, or strain (i.e. displacements or misalignment from the ideal lattice), we can get one of two measurements from ξ. We can think of the magnitude, $||\xi||$, as a way to map the density functions associated with the filtered $\vec{b}_k$ back to real space. That is, $||\xi||$ maps the contributions of each point in the crystal to the positional order, as measured by $\vec{b}_k$ (i.e. how well aligned a given point with $\vec{b}_k$ is with respect to some distribution represented by the filtered Bragg peak). Meanwhile, filtering Bragg peaks associated with multiple $\vec{b}_k$s gives us a measure of how a point $\vec{r}$ in the crystal aligns with, or deviates from,

all of the filtered Bragg peaks. This means that $||\xi||$ can tell us how much a single point aligns with the globally averaged structure, or how much a single point aligns with a globally averaged $\vec{b}_k$. In cases where we may not know the crystal or types of crystals that will form in a given system, or in cases where the unit cell of a crystal is complex and the symmetries are difficult to determine, Bragg peak filtering gives us a highly generalizable way to analyze crystal structures.

We note that this view is particularly useful in analyzing complex structures, such as quasicrystals (QCs), where a set of $\vec{b}_k$ alone is insufficient in describing the global structure and order in the system. Due to the complexity of QCs structures, however, we will refrain from further discussion here. More details are provided in Chapter 2 and Section 4.4.1.

5.2.3.2 The Phase of the Inverse Fourier Transform of a Filtered Bragg Peak

Alternatively, one can measure the *phase*, ϕ. The phase, ϕ, is the angle associated with a complex exponential function, $e^{\phi i}$, or, alternatively, the angle associated with a plane wave, $\cos(\phi)$. In the context of crystals and Bragg peak filtering, phase gives us a direct measurement of displacement field $\Delta\vec{b}_k$. Electron microscopists have long used a type of phase analysis called geometric phase analysis (GPA) [62, 105] to analyze defects and dislocations in electron microscopy and scanning transmission electron microscopy (STEM) images. This technique is powerful and precise, and can even measure displacements in atomic lattices at the picometer scale ($< 10pm$) [109].

5.2.3.3 Analysis of a Dislocation using Bragg Peak Filtering

In Fig. 5.2, we see examples of $||\xi||$ computed by filtering the brightest Bragg peak. Here, we normalized and mapped $||\xi||$ onto a simple square lattice with a dislocation pair (Fig. 5.2 **(a)**), where dark blue (darker color) corresponds to regions aligned with the associated lattice vector and yellow (lighter color) corresponds to regions with poor alignment to the lattice vector. We see here that there is a notable difference in the value of $||\xi||$ at the site of the dislocation when compared of the rest of the crystal.

Figs. 5.2 **(b)** and 5.3 **(b)** show the raw phase, ψ, obtained from a model simple cubic lattice with a dislocation pair and bright field microscope image of $10\mu m$ glass beads in water (Source: "Colloid Crystal 40x Bright Field Glass In Water" [148] by Zephyris, licensed under CC BY-SA 3.0), respectively. Meanwhile, in Fig. 5.2 **(c)** and 5.3 **(c)**, we plot a modified version of the phase, φ, for clarity. From Fig. 5.2 **(c)** (zoomed in inset) and 5.3 **(c)**, we can see how topological defects like dislocations introduce jags and discontinuities φ. Meanwhile, continuous deformations to the lattice can be seen as gradual bends and general "waviness" in the grating lines associated with φ (and, by extension ϕ).

Typically, in GPA, the basis vector, $\vec{b}_k$, associated with the filtered Bragg peak is subtracted

from the raw phase to obtain the displacement field: $\phi - \vec{b}_k = \Delta\vec{b}_k$ (see Eqn. 5.7). In this work, we focus on the advantages of using $||\xi||$ on various systems, rather than generalizing implementations of GPA to 3D systems. Although GPA can achieve picometer level precision [109] it is not without its disadvantages.

5.2.4 Artifacts in Phase Analysis

Achieving this level of precision, however, requires, pixel perfect measurements of peak centers. Slight offsets can create artifacts in the phase, or even produce dubious results. For example, filtering a peak with even a half pixel offset from the peak center can result in a checkerboard-like pattern in the phase (Figs. 5.2 **(b)** and 5.2 **(b)**). This appears to be a cosmetic issue, however, as we found that checkerboard artifacts can be fixed by modifying the phase with:

$$\varphi = |cos(\phi)| \tag{5.8}$$

where $|\cdot|$ represents absolute value.

In other instances, however, phase analysis can return false or misleading measurements (e.g. identifying regions of order where they do not exist or identifying dislocations in regions where there is no crystal). In Fig. 5.4, we see that from phase analysis alone, we are unable to detect polycrystallinity. Instead, we see strain lines, regularly spaced lines (i.e. gratings) on misoriented regions (blue regions, Fig. 5.4 **(a)**). These straight lines suggest that these regions are unstrained and aligned with the filtered Bragg peak, yet we know from analysis in Sec. 5.4.1 that these regions are misaligned with the filtered Bragg peak.

Additionally, we see several of what look like dislocations (jags, breaks, and other distortions and discontinuities to the straight lines) in these regions unaligned with the grain (blue regions in Fig. 5.4 **(a)**). An example of one of these defects can be seen in the white, circled regions in **(a)** and **(c)**. Examining the original photo suggests that defects do not exist in the circled region.

Overall, the examples shown in Figs. 5.2, 5.3, and 5.4 show how phase analysis is vulnerable to several types of artifacts when used incorrectly, or when Bragg peaks are miscentered by pixel-level offsets.

5.2.5 Backround Summary

Although crystallographers have long used Fourier-base analysis to identify structures and measure deformations in 2D electron microscopy images of crystals, applications of these techniques have seen limited usage among simulationists and in other fields of microscopy. Tools such as crysTbox [73, 74] have been developed specifically for the automated analysis of 2D electron diffraction

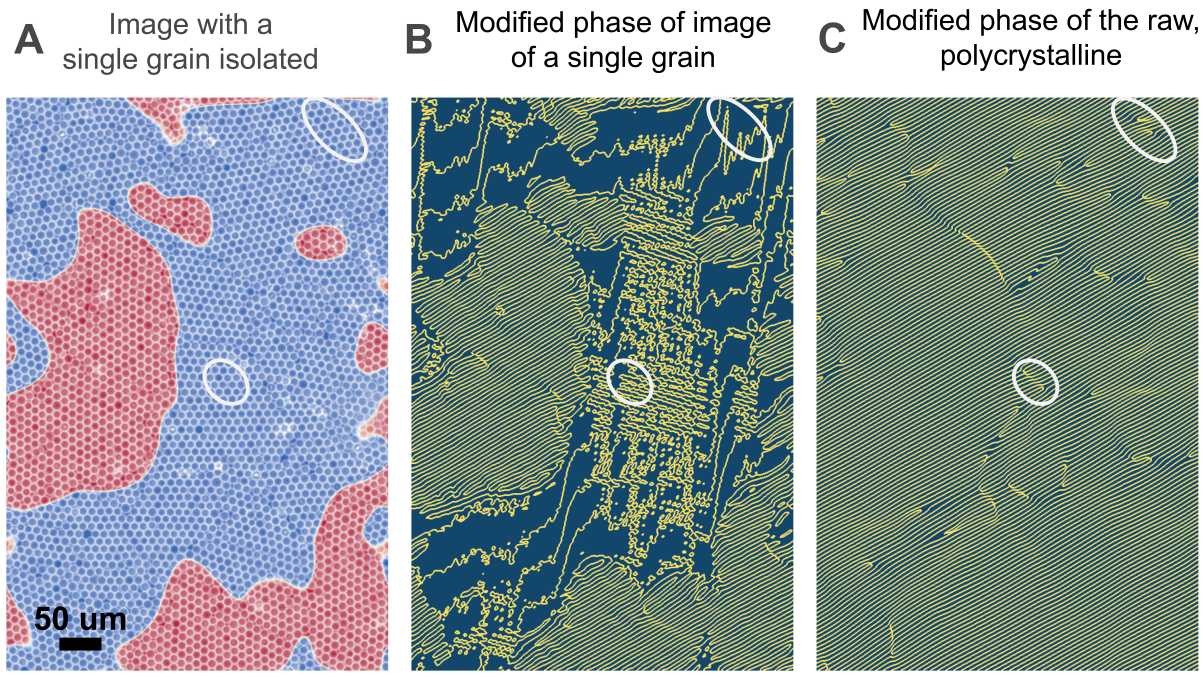

Figure 5.4: **Phase artifacts in polycrystals.** **(a)** Bright field microscopy image of $10\mu m$ glass beads in water with all aligned crystal grains highlighted, where the grain mask, ς, corresponds to red regions. **(b)** Modified phase computed from the masked image. **(c)** Modified phase computed from the raw image. Blue (darker color) corresponds to $|\cos\phi| = 0$ and yellow (lighter color) corresponds to $|\cos\phi| = 1$. Bends in the yellow lines should correspond to strain, while breaks, jags, and swirls (see white circles) correspond to disclinations and dislocations. Spectra computed from: "Colloid Crystal 40x Bright Field Glass In Water" by Zephyris [148], licensed under CC BY-SA 3.0.

patterns and electron microscopy images. These tools are not designed for use on 3D data, nor are they designed for use on arbitrary 2D image inputs. Additionally, phase-based methods like GPA require pixel-level precision to return meaningful results. Adapting these tools to higher dimensions, and automating analysis for large batches of data with variable structures, particle types, and levels of noise would be particularly challenging.

Recently, researchers have used $||\xi||$ obtained via Bragg peak filtering as a way to segment out particle positions in 3D reconstruction of a colloidal crystal self-assembled from DNA grafted gold nanoparticle self-assembly [91]. Unfortunately, this workflow relied on manual inspection of structural data, making it impractical for systematic, large-scale studies. Instead, we propose the use of the iFT magnitude, $||\xi||$, rather than phase, as a way to segment grains, detect dislocations, and measure order in a variety of 2D and 3D systems, and we develop a Python-based tool to assist in peak detection and Bragg peak filtering for 2D and 3D inputs. In this work, we show that using $||\xi||$ to develop masks and mapping to real space data is a highly robust and reliable measure of

positional order.

5.3 Algorithm Development

5.3.1 Fourier Spectrum Preprocessing

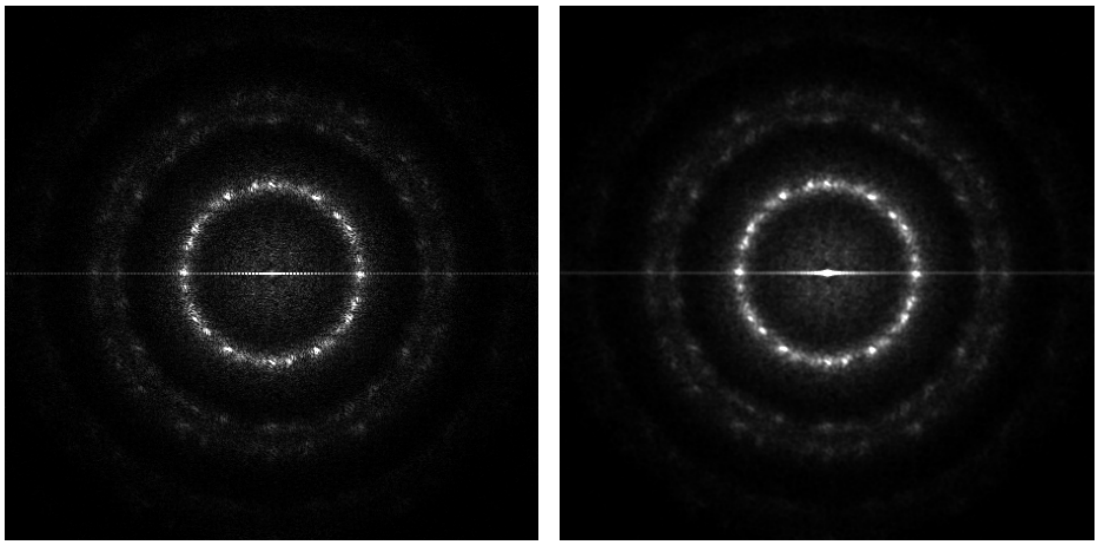

Figure 5.5: **Comparison between filtered and power spectra.** 2D spectra **(a)** unfiltered power spectrum and **(d)** power spectrum with Gaussian filter ($\sigma = 1$), of $10\mu m$ glass beads in water. Spectra computed from: "Colloid Crystal 40x Bright Field Glass In Water" by Zephyris [148], licensed under CC BY-SA 3.0.

Fourier Transforms (FTs) are generated from input image arrays using a Fast Fourier Transform (FFT) algorithm. For low noise FTs, we detect peaks directly from the amplitude spectrum Fig. 5.5 **(a)**. For high noise FTs, we give users the option to apply a user defined function, such as an N-D Gaussian filter Fig. 5.5 **(b)**, to the FT.

5.3.2 Bragg Peak Finding

We perform peak detection on the filtered or unfiltered power spectrum, $||F(\vec{x})||$, as follows:

1. We use *scipy*[139] to perform 1D peak detection along each dimension of $||F(\vec{x})||$, where peaks are defined as any sample whose value is greater than its two neighboring values, and whose prominence is greater than a percentile-based threshold Fig. 5.6 **(a - b)**. Percentile

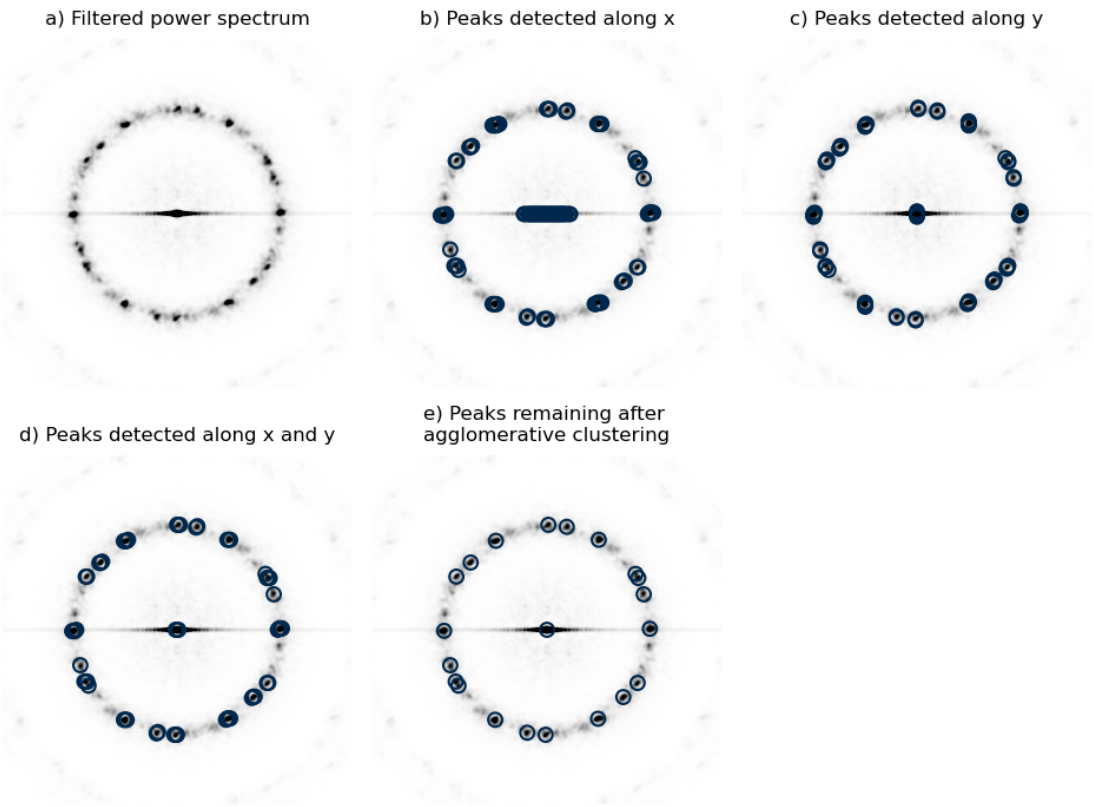

Figure 5.6: **Peak detection algorithm.** Peak detection from filtered power spectrum of polycrystalline $10\mu m$ glass beads in water. **(a)** Power spectrum computed from Gaussian filtered amplitude spectrum ($\sigma = 1$). **(b)** Peaks detected along x with prominence greater than 99.9 percent. **(c)** Peaks detected along y with prominence greater than 99.9 percent. **(d)** Peaks detected along x and y within 1 pixel of each other. **(e)** Peaks remaining after network-based clustering (distance threshold of 2 pixels).

thresholds range from 99.9 percent (most experimental systems) to 99.99 percent (most simulated systems) of all values in $||F(\vec{x})||$. This method is sensitive to noise and produces many false positives.

2. To reduce the number of false positives, we perform a distance-based neighbor search between points detected along each dimension, where points detected within 1 pixel of each other along all dimensions of the image are kept as valid peaks Fig. 5.6 **(d)**.

3. We perform network-based clustering [102] with a user-defined distance threshold to eliminate any remaining duplicate peaks Fig. 5.6 **(e)**.

Although the prominence threshold greatly reduces the number of false positive detections, it can result in a loss of low intensity peaks. Due to the presence of noise and artifacts in tested

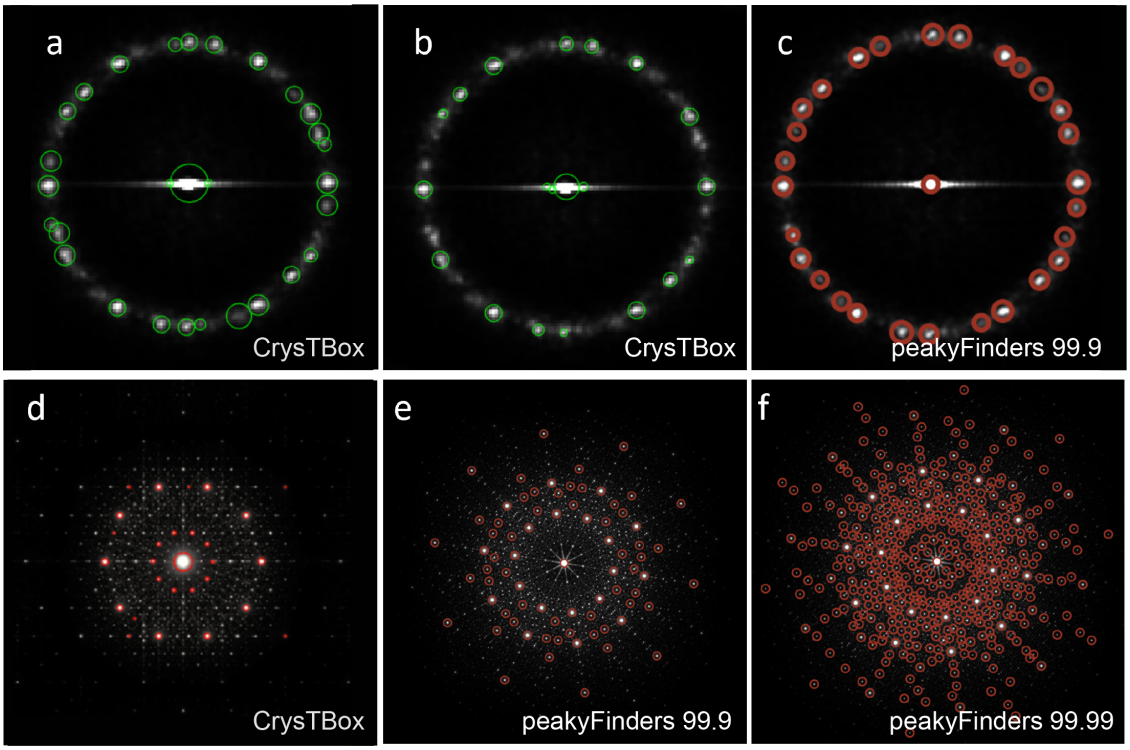

Figure 5.7: ***PeakyFinders* peak detection algorithm compared to CrysTBox.** Peak detection from filtered power spectrum of polycrystalline $10\mu m$ glass beads in water (**a-c**) and Tuebingen Triangle Tilings (TTTs) (**c-f**). **(a)** Peaks detected with CrysTBox[73, 74], Hessian response[87]. **(b)** Peaks detected with CrysTBox[73, 74], difference of Gaussians[87]. **(c)** Peaks detected with Method 5.3.2 (99.9 percentile). **(d)** Peaks detected with CrysTBox[73, 74], Hessian response[87]. **(e)** Peaks detected with *peakyFinders* (99.99 percentile). **(f)** Peaks detected with Method *peakyFinders* (99.9 percentile). Difference between spectra in **(d)** and **(e - f)** are due to down sampling by CrysTBox. Spectra computed from: "Colloid Crystal 40x Bright Field Glass In Water" by Zephyris [148], licensed under CC BY-SA 3.0.

spectra, we found it best to favor specificity over sensitivity and provide additional methods to recover higher order peaks (see Methods 5.3.4).

We note that for 2D datasets, our peak detection algorithm produces comparable results to more sophisticated algorithms used for electron diffraction analysis [73, 74] and image matching [87] (Fig. 5.7). Although our methods requires more user intervention than these state-of-the-art diffraction analysis tools [73, 74], our code generalizes to 3D with little overhead or modifications.

5.3.3 Bragg Peak Filtering

Bragg peaks are filtered with a window function. By default, we apply a Hamming window with a width equal to 8 times a Bragg peak's estimated full width at half maximum (FWHM) along one dimension. The window is centered on each peak's maximum and applied to the unfiltered FT. For

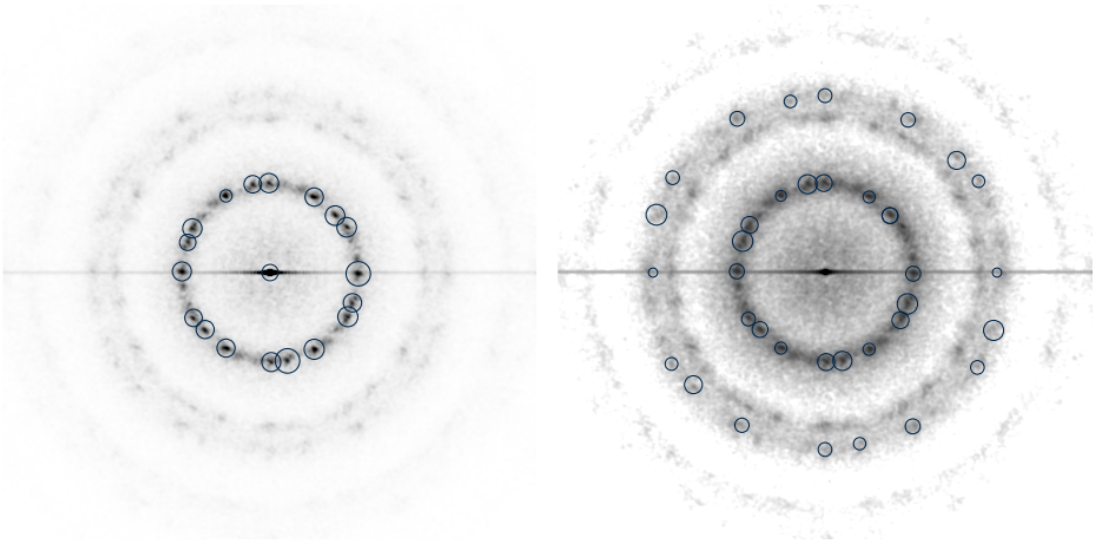

Figure 5.8: **Scaling detected peaks using *peakyFinders*. (a)** Ring of peaks detected in the power spectrum of polycrystalline $10\mu m$ glass beads in water and **(b)** peaks scaled by twice the peak coordinates detected in **a**. Scaled peaks are re-centered at the local maxima within a 20 pixel window of the scaled peaks. In **b**, we show the log of the power spectrum to highlight low intensity peaks in the spectrum. spectra computed from: "Colloid Crystal 40x Bright Field Glass In Water" by Zephyris [148], licensed under CC BY-SA 3.0.

flexibility, our code includes implementations for the Hamming window or a user defined window function.

5.3.4 Recovery of Higher Order Bragg Peaks

Users have the option to recover higher order peaks by scaling existing peaks, $\vec{b}_k$, and searching for a local maximum within some user defined grid (see example in Fig. 5.8).

5.3.5 Bragg Peak Width Estimates

Peak widths are estimated using *scipy*'s [139] *peak_width* method.

5.3.6 PeakyFinders Workflow

PeakyFinders accepts raw Fourier spectra, 2D grayscale image arrays, 3D grayscale image arrays, or particle positions as inputs (Fig. 5.9 **(a)**). If the Fourier spectrum is not provided, but a grayscale image array is provided, *peakyFinders* computes the FT directly from the image using the FFT [28] algorithm. If particle positions are provided, the inputs are first discretized into a d-dimensional

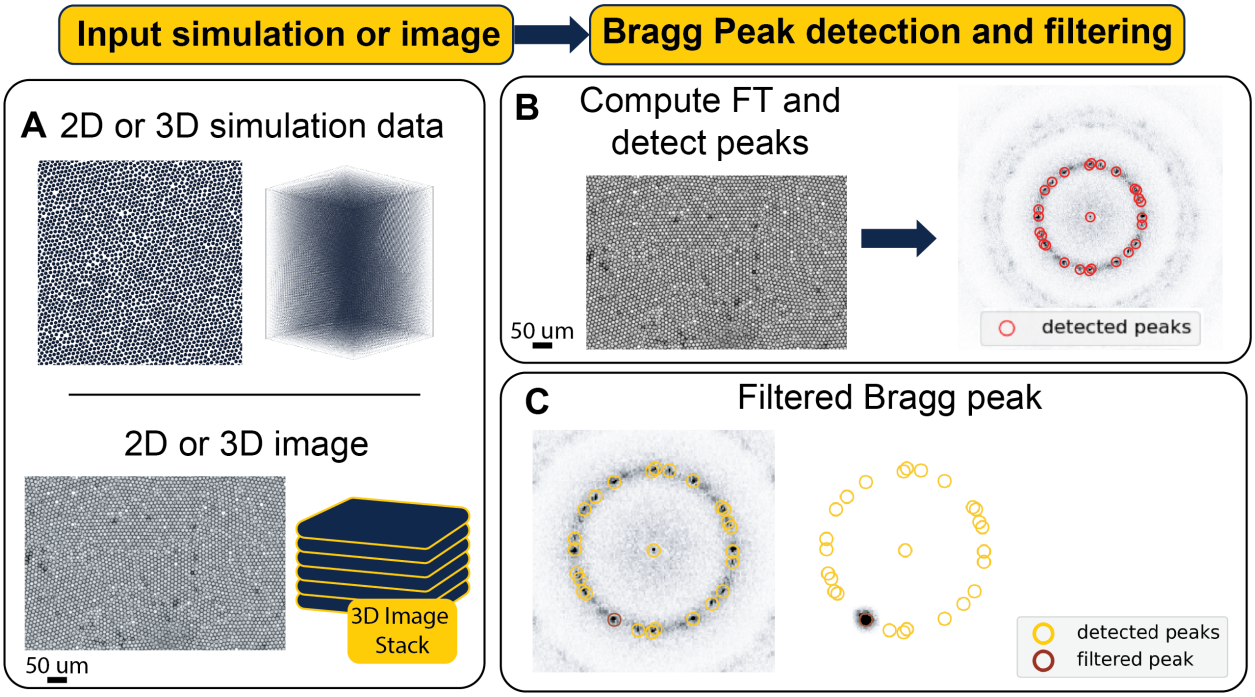

Figure 5.9: **Peak detection and filtering with *peakyFinders*** *PeakyFinders* accepts either **(a)** 2D or 3D simulations (top), 2D experimental images (bottom left), or 3D image stacks (bottom right) as input. From these inputs, **(b)** we compute the FT of the input. We plot the power spectrum computed from the FT (left) and bright field microscope image of $10\mu m$ glass beads in water (right). We perform Bragg peaks detection on the computed spectrum (red circles). To segment out a grain, **(c)** we filter the brighted peak detected in **(b)**. Source (image of glass beads in **(a, b)**): "Colloid Crystal 40x Bright Field Glass In Water" by Zephyris [148], licensed under CC BY-SA 3.0.

histogram, where d is the dimension of the particle point cloud. Then, the Fourier spectrum is computed from the histogram array using the FFT algorithm. The resolution of the histogram is set to 5 pixels per distance unit by default, but may be modified by the user.

Next, peaks are detected in the power spectrum of the computed or input Fourier spectrum (Fig. 5.9 **(b)**, red circles) and transformed back to real space using the inverse FFT algorithm. For cases where the Bragg peaks may be less prominent due to noise or polycrystallinity, users have the option to apply a Gaussian filter or any arbitrary, user specified function to improve the signal-to-noise ratio. Once peaks are detected, users can filter a single peak or pairs of peaks (Fig. 5.9 **(c)**). Using this output, it's possible to either segment grains in a polycrystalline system (Fig. 5.10 **(a-d)**), or to find defects and dislocations in a single crystal (Fig. 5.10 **(e-h)**).

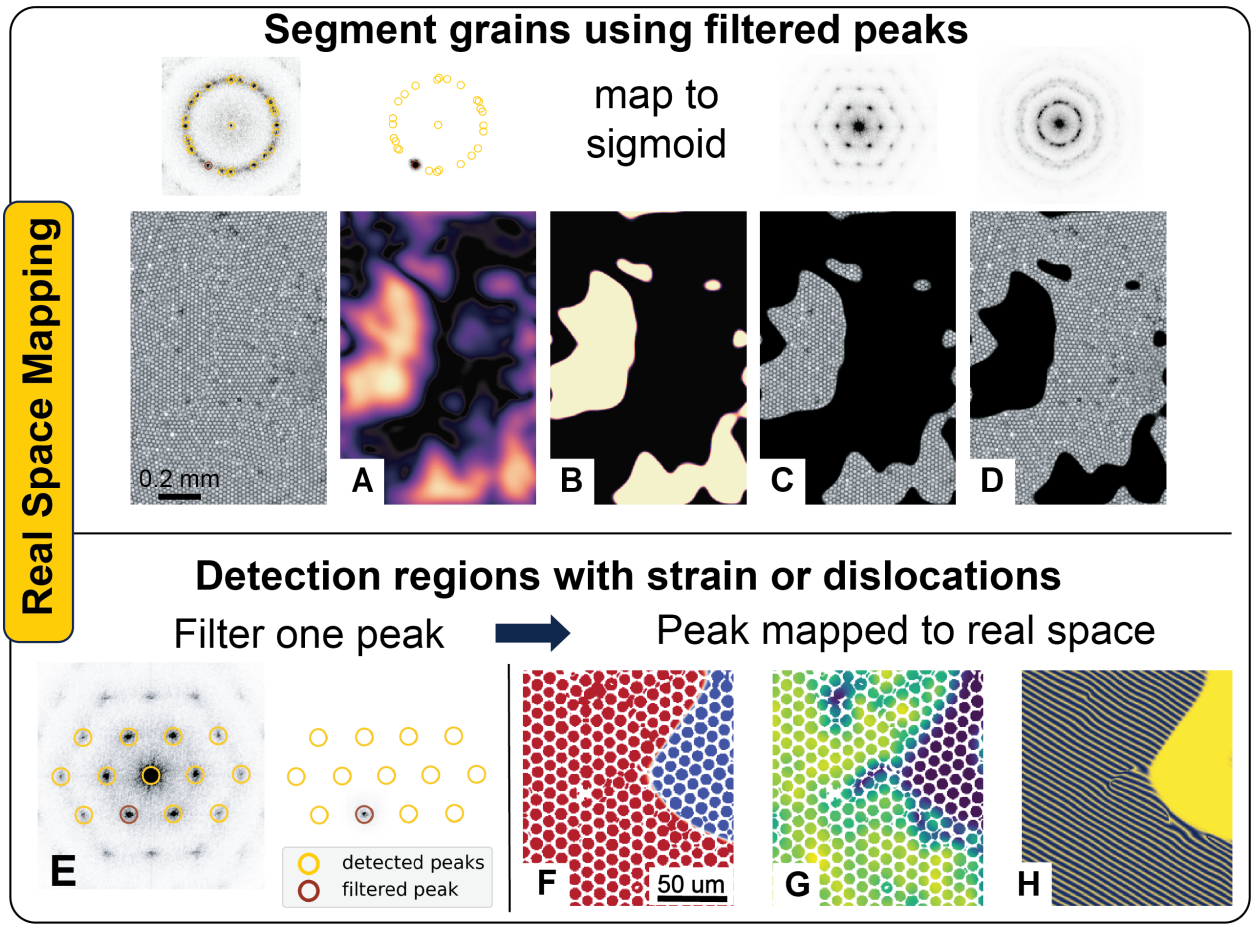

Figure 5.10: **Bragg peak filtering workflow for grain and dislocation detection. (a)** We filter the selected Bragg peaks (power spectrum of the filtered FT, top), and we compute the inverse Fourier Transform (iFT), ξ, of the filtered Bragg peaks (bottom). Next, to segment out grains associated with a peak or set of peaks, **(b)** we create a mask by normalizing and mapping ξ onto a scaled and shifted sigmoid, ς. We apply the **(c)** mask and the **(d)** inverse mask to the input image (bottom) and recompute the FT (power spectra of the respective FTs, top). **(e)** Power spectrum and filtered peak from the masked input image shown in **(d)**. Zoomed in region of the input image showing: the **(f)** grain (red) identified in **(d-f)**. **(g)** iFT of the Bragg peak filtered in **(h)**. Yellow and green (lighter color) indicate regions of high translational order, while purple (darker color) indicates regions of low translational order, with respect to the filtered Bragg peak. **(h)** Raw phase information for the given domain. Source (image of $10\mu m$ glass beads): "Colloid Crystal 40x Bright Field Glass In Water" [148] by Zephyris, licensed under CC BY-SA 3.0 / Original, first on top row. Adapted in **(b, c, f, g)**. Masked in **(c, d)**

5.4 Validation in 2D Systems

Here, we present a structure agnostic tool for semi-automated analysis of 2D and 3D particle data called *peakyFinders*.

First, we test our code's ability to identify grains and dislocations on 2D, polycrystalline images (Fig. 5.9 and 5.10). Next, we test our code's robustness to peak shape arising from non-circular/spherical particle shapes (Fig. 5.12), and we verify our code's generalizability to model 3D systems (Fig. 5.13 and 5.14). Then, we test our code on simulated 3D systems (Fig. 5.17). Finally, we demonstrate our code's utility in on 3D tomography data (Fig. 5.15 and 5.16).

We find that although our peak detection algorithm is relatively simple, it is robust to noise originating from liquid or polycrystallinity, and distortions in peaks due to particle shape. We also find that the Bragg peak filtering methodology extends easily to 3D systems of varying complexity.

5.4.1 Analysis of a 2D Image of Polycrystalline Glass Beads

We test our peak finding algorithm's ability to detect peaks in polycrysatlline samples on brightfield microscope image of $10\mu m$ glass beads in water (Fig 5.9 **(a-g)**, Source: "Colloid Crystal 40x Bright Field Glass In Water" [148] by Zephyris, licensed under CC BY-SA 3.0), and we find that our peak detection algorithm is robust to noise arising from the presence of multiple, misoriented crystal grains (Fig. 5.9 **(b)**, red circles).

5.4.1.1 Grain Segmentation

Next, we isolate all grains aligned with the brightest detected peak (Fig. 5.9 **(c)**, red circle; Fig. 5.9 **(d)**, top). To do this, we first map the filtered Bragg peak to real space (Fig. 5.9 **(d)**, bottom) using the inverse Fast Fourier Transform (FFT) (ξ). From the magnitude of the filtered inverse Fourier Transform (iFT), $||\xi||$, we can identify two grains (Fig. 5.9 **(d)**, light yellow) that are well aligned with the associated reciprocal vector.

In order to identify a domain with well defined edges, we map $|\xi(\vec{r})|$ onto a sigmoid using the following procedure: First, we normalize the iFT, $|\hat{\xi}(\vec{r})|$, so that the minimum value is 0 and the maximum value is 1. Next, we map $\hat{\xi}(\vec{r})$ to a sigmoid:

$$\varsigma(\vec{r}) = \frac{1}{1 + e^{-(||\hat{\xi}(\vec{r})|| - c_1)c_2}} \tag{5.9}$$

where $||\hat{\xi}(\vec{r})||$ is the iFT of the filtered Bragg peak (Equation 5.3), c_1 defines the point where $\varsigma(\vec{r}) = 0.5$ and c_2 is a shape parameter that controls the slope of $\varsigma(\vec{r})$. In practice, c_1 determines the threshold of the domain mask and c_2 determines the visual sharpness of the domain mask.

Setting $c_1 = 0.5$ and $c_2 = 1$ returns nearly identical results to the normalized iFT. Increasing c_1 increases the threshold of the domain mask, while increasing c_2 sharpens the domain mask. For most cases we tested, we found that the best parameters for creating domain masks are $c_1 = 0.3$ and $c_2 = 128$ (Fig. 5.10 **(f)**; bottom, red is the aligned grain and blue is regions not aligned with the associated reciprocal vector).

5.4.1.2 Dislocation Detection

The procedure for dislocation detection follows a similar protocol to grain detection, with a few additional caveats:

- Dislocation detection must be performed on the Fourier Transforms (FTs) of single crystal grains, otherwise, distortions to the phase from other grains may introduce artifacts to the analysis.
- In order to capture distortions from dislocations, Bragg peak filtering must be done over a larger radius (typically 6 - 8 times the estimated peak width) than for grain detection (typically 1 times the estimated peak width).
- The inverse Fourier Transforms (iFTs)'s phase (Fig. 5.10 **h**) and magnitude (Fig. 5.10 **(g)**) are both effective means to measure strain along a given basis vector. Each method has a specific set of advantages and disadvantages:
  - **Phase (ϕ):** Phase analysis has long been used for measurements of lattice displacement (Δb_k in Eqn. 5.7) in electron microscopy images [62, 105, 109] and in studies of melting transitions in hard disks [5, 39]. However, geometric phase analysis (GPA) requires exact measurement of the basis vector $\vec{b}_k$ to return meaningful results. Even pixel-level or half pixel-level deviation in $\vec{b}_k$ can return artifacts in phase analysis.
  - **Magnitude ($||\xi||$):** In Fig. 5.10 **(g)**, we plot the magnitude of $||\xi(\vec{r})||$, rather than the phase. The purple (dark) correspond to dislocations or high displacement with respect to $\vec{b}_k$ of the filtered peak (low positional order), while yellow (light) correspond to low displacement with respect to $\vec{b}_k$ (high positional order). We see a close relationship between the displacement field, $\Delta\vec{b}_k$ and $||\xi(\vec{r})||$. This suggests that the $||\xi(\vec{r})||$ can also be used to measure $\Delta\vec{b}_k$. Unlike GPA, however, we are able to obtain this measurement without the need to center $||\xi(\vec{r})||$ with respect to a precise measurement of $\vec{b}_k$. However, further theoretical development is necessary to obtain more precise measurements of $\Delta\vec{b}_k$ from this analysis.

5.4.2 Analysis of a 2D Photograph of Self-Assembled Cubes

Next, we tested *peakyFinders* on 2D photographs of self-assembled $\frac{3}{8}$ inch acrylonitrile butadiene styrene (ABS) cubes. This is an important test because particle shape can cause changes to the Bragg peak's shape. Conceptually, this is similar to how the atomic form factor causes changes in the Bragg reflections in the X-ray scattering of a crystal.

Using our experimental system of hard cubes, we show our peak detection algorithm's generalizability to Fourier spectra with non-point like peaks (Fig. 5.11 **(a)**, red circles), and show that the methodology used in Section 5.4.1 can be easily extended to systems with non-spherical or point-like particles, with some caveats and modifications.

5.4.2.1 Peak Detection

We found that, despite the changes in peak shape in the power spectrum (Fig. 5.12 **(a-c)**, top), we could use nearly identical settings as those used in Section 5.4.1 to detect peaks in the power spectrum. The only setting we needed to change in the peak finding procedure was the distance threshold for network-based clustering (see Methods 5.3.2, step 3), where a distance threshold of 4 pixels was used for the image of glass beads, while a distance threshold of 7 pixels was used for the image of ABS cubes.

5.4.2.2 Grain Segmentation and Disclinations

Due to the presence of disclinations (white arrows in Fig. 5.11; white and yellow arrows in Fig. 5.12) and changes in peak shape, we required higher order peaks and larger windows for peak filtering (large window shown in Fig. 5.11 **b**, small window shown in Fig. 5.11 **(f)**). When filtering by lower order peaks (Fig. 5.12 **(b-i)**) or smaller windows (Fig. 5.11 **(f)**), we find that the disorder introduced by disclinations are nearly indistinguishable from misaligned grains in the iFT magnitude (Fig. 5.11 **(g, h)**, white arrows; Fig. 5.12 **(b, e, h)**; black indicates low translational order and yellow/purple indicates translational order).

We filter higher order peaks by taking the coordinates of the brightest peak, scaling the coordinates by a factor of 3 (Methods 5.3.4; Fig. 5.11 **(a, b)** larger blue circle). and filtering multiple, higher order peaks along a given $\vec{b}_k$ (Fig. 5.11 **(b)**). This helps us better capture these regions of disorder in the grain (Fig. 5.11 **(d)**, white arrows).

We note that, when filtering more than one peak, ξ no longer returns a single, continuous domain (Fig. 5.11 **(d)**). Instead, we get a grating-like pattern, similar to the one seen in Fig. 5.1 **(a)**. To understand why this is the case, it's important to remember that the process of Bragg peak filtering helps us transform our discrete representation of particles to the frequency domain. If we return to our discussion of crystals in Fourier space (Sec. 5.2.2), we see that the output of $||\xi||$ from a

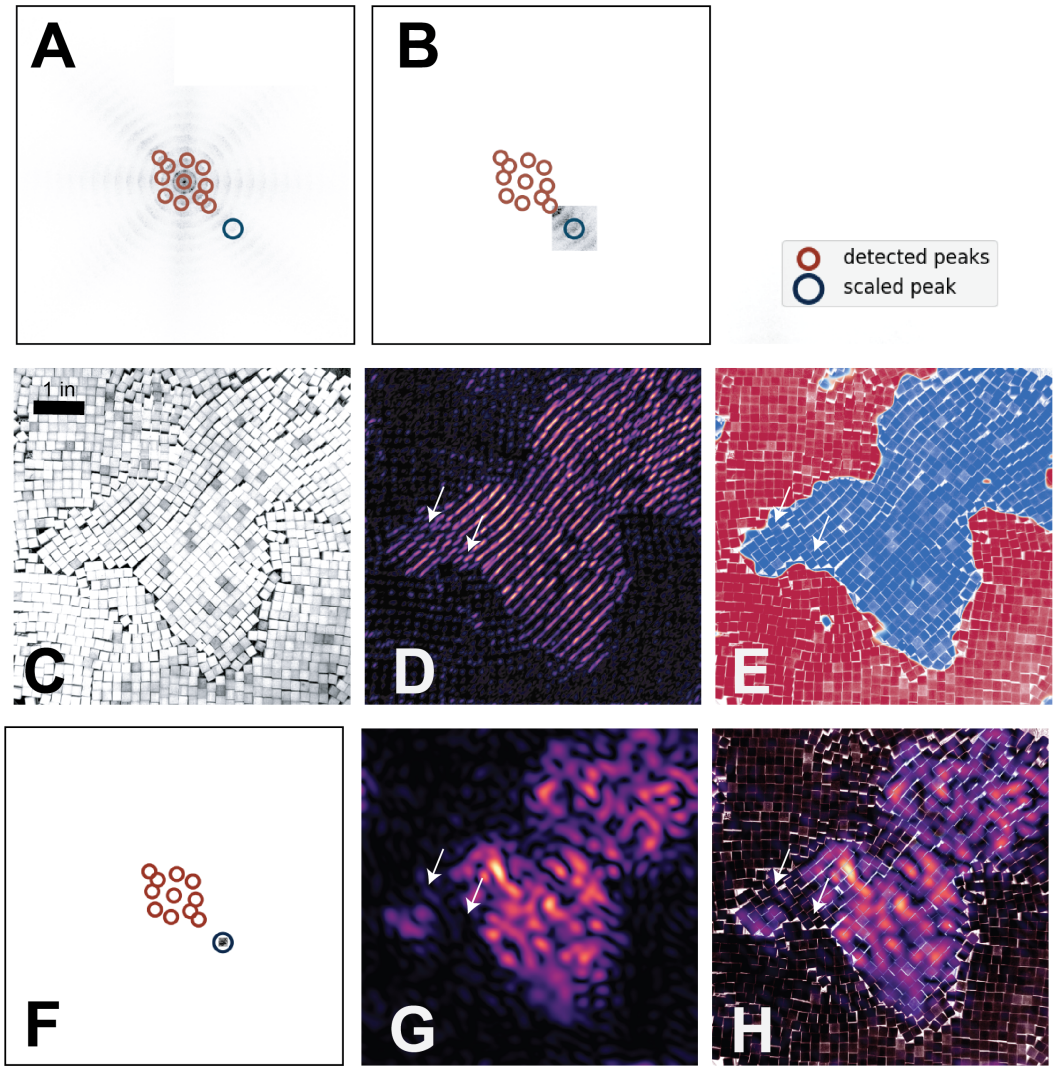

Figure 5.11: **The effect of peak width on Bragg peak filtering in a photograph of self-assembled ABS cubes.** **(a)** Power spectrum and **(c)** photograph of 3D printed, $\frac{3}{8}$ inch ABS cubes on a metal tray self-assembled via mechanical agitation. **(a-b)** Peaks detected with *peakyFinders* are circled in red. The vector associated with the brightest peak was selected, then scaled by a factor of 3 (larger, blue circle), while the peak with was scaled by a factor of 5. The resulting, filtered power spectrum is shown in **(b)**. **(d)** inverse Fourier Transform (iFT) of the filtered FT, $||\xi||$, where black indicates low translational order (with respect vectors associated with the filtered region), and yellow/purple indicates translational order (with respect vectors associated with the filtered region). **(e)** Domain mask computed by normalizing and mapping $||\xi||$ onto a scaled and shifted sigmoid, ς. Blue corresponds to the grain associated with the filtered region, while red corresponds to regions not associated with the filtered region. **(f, g)** Shows a filtered power spectrum where the vector associated with the brightest peak was selected, then scaled by a factor of 3 (larger, blue circle), but the peak with was scaled by a factor of 1, rather than 5. The resulting $||\xi||$ is unable to capture the full grain in these cases, due to the presence of disclinations (white arrows), values mapped to the photograph shown in **(h)**).

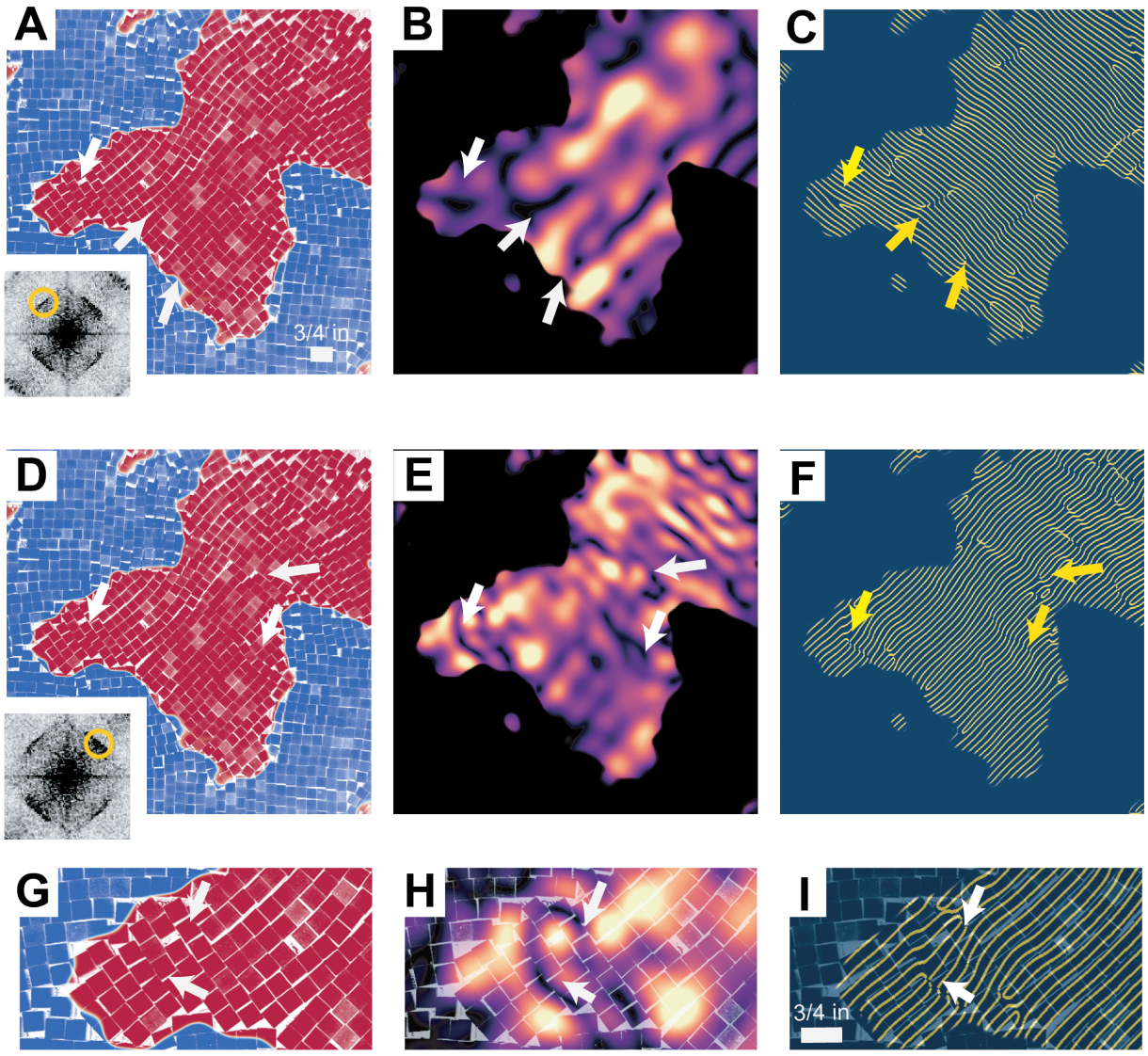

Figure 5.12: **Defect detection in a photograph of self-assembled ABS cubes.** We examine the effects of disclinations and strain (white and yellow arrows) on **(a, e, h)** positional order, $||\xi||$, masked with the grain domain (red region in **(a)**) and **(c, f, i)** modified phase, $|\cos\phi|$, masked with the grain domaian (red region in **(a)**). We see that, for non-circular or spherical particles, **(b, e, h)** $||\xi||$ is more sensitive to disorder than **(c, f, i)** phase. In **(b, e, h)**, black indicates low translational order (with respect vectors associated with the filtered region), and yellow/purple indicates translational order (with respect vectors associated with the filtered region). In **(c, f, i)**, blue (darker color) corresponds to $|\cos\phi| = 0$ and yellow (lighter color) corresponds to $|\cos\phi| = 1$. Bends in the yellow lines correspond to strain, while breaks, jags, and swirls (see arrows) correspond to disclinations and dislocations.

single, filtered Bragg peak is loosely analogous to positional order (Eqn. 5.4). When filtering a pair of peaks (Eqn. 5.2), however, it's better to adopt the viewpoint of ξ as a sum of plane waves. This grating-like pattern (Fig. 5.11 **(d)**) can be thought of as the pattern that results from the sum of two plane waves with different frequencies.

Because we filtered multiple peaks associated with $\vec{b}_k$ at different scales, we can think of these plane waves as a way to refine where and how we see order along a given $\vec{b}_k$. Conceptually, then, we can think of these brighter regions as corresponding to "particle positions", as recognized by the FT. This means that in simulations we can easily normalize and map the raw output of the iFT magnitude to particle positions. For images, however, we want to identify a large, continuous domain for a given grain. In these cases, we apply a Gaussian filter to the iFT magnitude, normalize the output, then map to a sigmoid (Fig. 5.11 **(e)**). We found that, following this procedure, we were able to use the same parameters as those used in Section 5.4.1 (Eqn. 5.9) to create the domain mask.

5.4.3 Conclusion of 2D Cubes Example

We find that *peakyFinders*' peak detection algorithm generalizes well to a variety of 2D systems. We first test our code on a simulated model system of a dislocation, then, we show that the algorithm and workflow generalize well to 2D experimental systems of variable particle types and shapes.

5.5 Validation in 3D Systems

5.5.1 Validation of a Model 3D Systems

To begin, we tested *peakyFinder*'s generalizability to 3D simulations in 3 model systems, constructed using *atomsk* [59]: a body-centered cubic (BCC) crystal with a glide loop dislocation (Fig. 5.13 **(a)**), a BCC crystal with a screw dislocation (Fig. 5.13 **(c)**), and a polycrystalline hexagonal diamond crystal (Fig. 5.14 **(a)**), and we verify our results against volumetric strain and dislocation extraction algorithm (DXA) calculations.

5.5.1.1 Peak Detection

We found that we could use nearly identical settings as those used in 2D systems to detect peaks on the power spectrum. The only setting we needed to change in the peak finding procedure was the distance threshold for network-based clustering (see Methods 5.3.2, step 3), where a distance threshold of 8 pixels for all of our model systems.

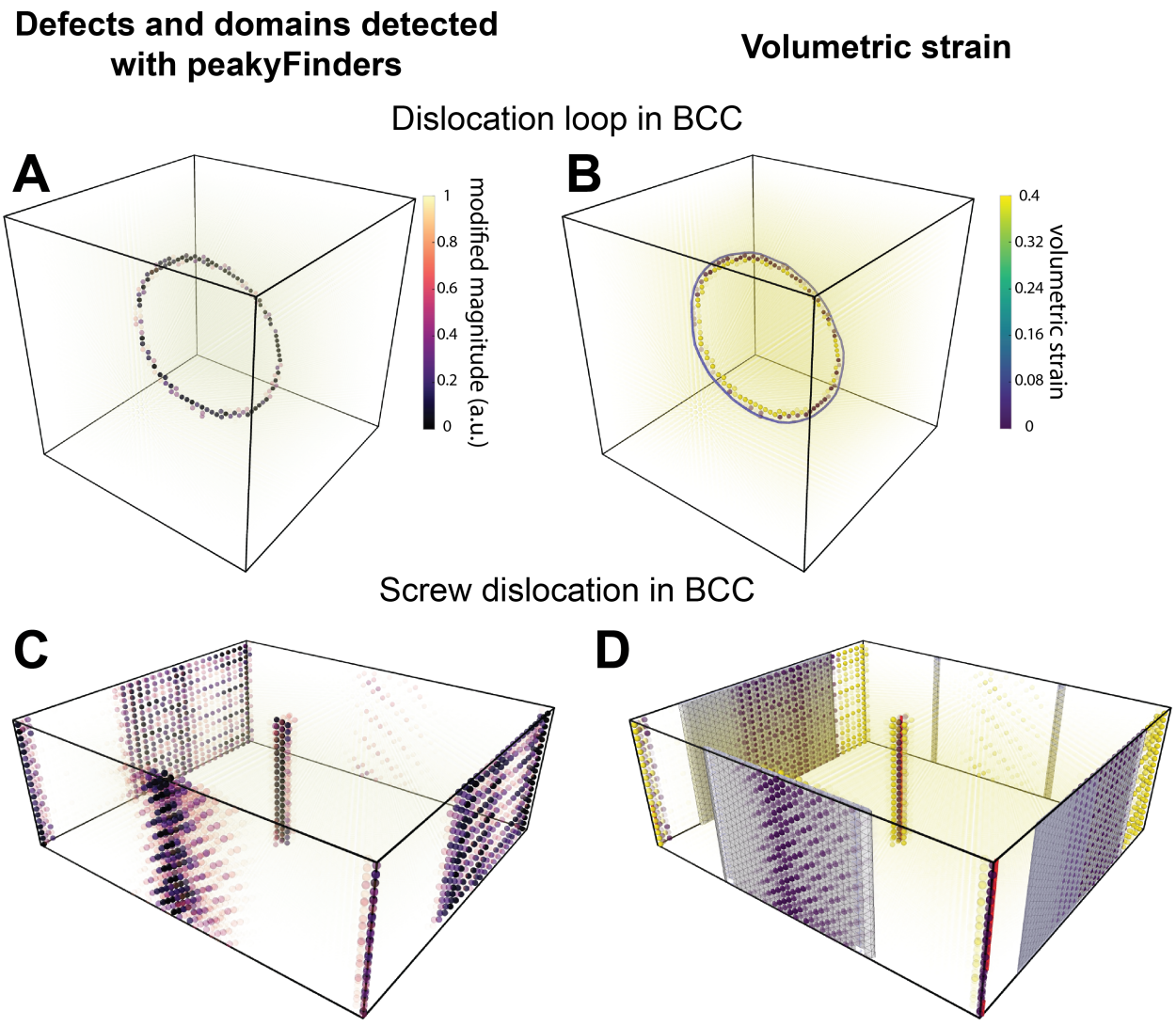

Figure 5.13: **Dislocation detection in model 3D systems of body-centered cubic (BCC) crystals with a dislocation loop and screw dislocation.** We compare the sigmoid-mapped inverse Fourier Transform (iFT) magnitude, $\varsigma(\vec{x})$, computed using *peakyFinders* ([right column, **(a, c)**] to volumetric strain measurements and dislocation extraction algorithm (DXA) calculations in 3D systems [left column, **(b, d)**] with a **(a, b)** BCC crystal with a dislocation loop and **(c, d)** BCC crystal screw dislocation. Particle opacity is inversely related to ς, where opaque particles have low ς (black in **(a, c)**), and transparent particles have high ς (pale yellow in **(a, c)**), where low ς corresponds to particles with low positional order, and high ς corresponds to particles with high positional order, and positional order was computed from the iFT magnitude after filtering all detected Bragg peaks with a peak width scale of 1. Plots **(b, d)** are colored according to volumetric strain, where high strain corresponds to yellow (lighter color) and low strain corresponds to purple (dark color). Dislocation lines (**(b)** blue loop and **(d)** red lines. and dislocation meshes (**(d)**) using DXA. These results show that *peakyFinders* and the defect and dislocation protocol presented in 2D systems generalizes well to model 3D systems.

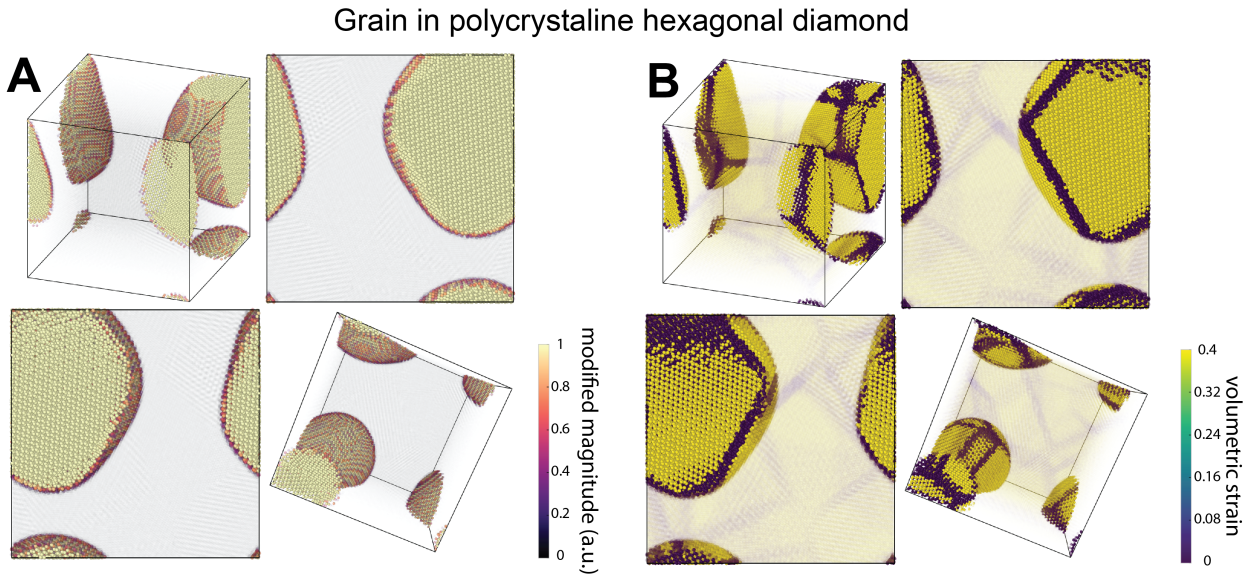

Figure 5.14: **Grain segmentation in model 3D systems of polycrysatlline hexagonal diamond.** We compare the sigmoid-mapped inverse Fourier Transform (iFT) magnitude, $\varsigma(\vec{x})$, computed using *peakyFinders* ([right column, **(a)**] polycrystalline hexagonal diamond, Here, particle opacity is proportional to ς. where opaque particles have high ς and high positional order (black in **(a)**), and transparent particles have low ς and low positional ordder (pale yellow in **(a)**). Positional order was computed from the iFT magnitude after filtering all detected Bragg peaks with a peak width scale of 1. For comparison, we compute **(b)** volumetric strain, where high strain corresponds to yellow (lighter color) and low strain corresponds to purple (dark color). These results show that *peakyFinders* and the grain segmentation procedure presented in 2D systems generalizes well to model 3D systems.

5.5.1.2 Dislocation Detection

For single crystal systems, we computed the sigmoid-mapped inverse Fourier Transform (iFT) magnitude, $\varsigma(\vec{x})$, after filtering all detected peaks in the Fourier Transform (FT) using a peak width scaled by a factor of 16, $c_1 = 0.5$, and $c_2 = 128$. This means that the ς values shown in Fig. 5.13 **(a, c)** measure displacements from all basis vectors $\vec{b}_k$ associated with the given crystal, rather than displacement from a single basis vector.

For glide loop dislocation shown in Fig. 5.13 **(a - b)**, we saw strong agreement between ς (Fig. 5.13 **(a - b)** high particle opacity corresponds to low ς and **(a)** dark regions correspond to low ς) and the dislocation circuit computed using DXA (Fig. 5.13 **(b)**, blue line). Here, we were unable to reliably detect the glide loop dislocation using volumetric strain (Fig. 5.13 **(b)**; yellow corresponds to low strain, purple corresponds to high strain), but we were able to reliably detect the glide loop dislocation using Bragg peak filtering.

For screw dislocations shown in Fig. 5.13 **(d - e)**, we also saw strong agreement between ς (Fig. 5.13 **(c - d)** high particle opacity corresponds to low ς and **(c)** dark regions correspond to low

ς), the dislocation circuit computed using DXA (Fig. 5.13 **(d)**, red line mesh), and volumetric strain calculations (Fig. 5.13 **(d)**; yellow corresponds to low strain, purple corresponds to high strain).

5.5.1.3 Grain Segmentation

For polycrystalline hexagonal diamond, we computed the sigmoid-mapped iFT magnitude, $\varsigma(\vec{x})$, after filtering the brightest Bragg peak in the FT. We scaled the estimated peak width by a factor of 7 and used ς parameters of $c_1 = 0.3$, and $c_2 = 128$. The segmented grain (Fig. 5.14) shows a single, well defined domain. Volumetric strain calculations and structure factor verify that the segmented regions were associated with a single hexagonal diamond grain.

5.5.2 Analysis of 3D Reconstruction of DNA Grafted Gold Nanoparticles

After we verified out algorithm's generalizability to 3D systems and defects, we test *peakyFinders*' robustness to noise and applicability to experimental systems by testing our workflow on a 3D reconstruction of 20 nm DNA grafted gold nanoparticles [91]. We find that our peak finding algorithm extends well to FTs of 3D images, and we find that our workflow for grain segmentation and dislocation detection extends well to experimental 3D systems.

5.5.2.1 Peak Detection

We found that we could use nearly identical settings as those used in 2D systems and model 3D systems to detect peaks in the power spectrum of the experimental 3D colloidal crystal (Fig. 5.15 **(a)**). The only setting we needed to change in the peak finding procedure was the distance threshold for network-based clustering (see Methods 5.3.2, step 3). Here, we used a distance threshold of 3 pixels.

5.5.2.2 Grain Segmentation

From visual inspection of a slice of the 3D reconstruction (Fig. 5.15 **(d)**), we can see that the assembled structure contains a mixture of disordered phases and two, misoriented crystal grains. To isolate a single grain from the 3D image, we follow the same protocol outlined in previous sections. We computed the sigmoid-mapped iFT magnitude, $\varsigma(\vec{x})$, after filtering the brightest Bragg peak in the FT. We scaled the estimated peak width by a factor of 19 and used ς parameters of $c_1 = 0.2$, and $c_2 = 128$. Here, the choice of $c_1 = 0.2$ for ς is lower than the typical value of $c_1 = 0.3$ used for grain segmentation in 2D experimental systems and model 3D systems. The peak width scale factor of 19 is also significantly higher than the scale factors used in previous sections.

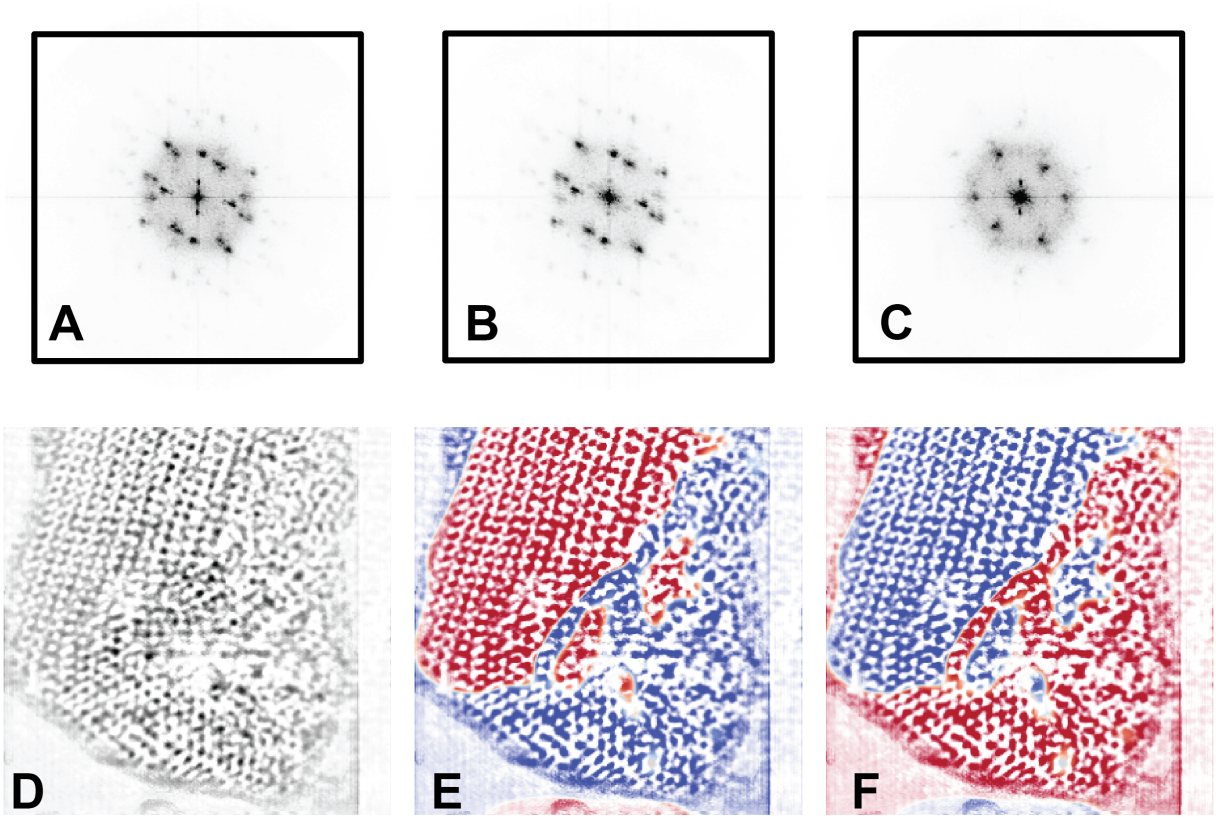

Figure 5.15: **Grain identified via Bragg peak filtering in a 3D reconstruction of a system of 20 nm DNA grafted gold nanoparticles [91].** The power spectrum of **(a)** the raw, 3D reconstruction obtained from [91], **(b)** a grain, obtained by masking ς over the 3D reconstruction, and **(c)** the inverse of the grain mask, $1 - \varsigma$, times the normalized intensities of the 3D reconstruction. Power spectra were computed as the magnitude of the FT of the 3D reconstruction. For plots **(a-c)**, the 3D spectra were projected down the viewing axis. **(d)** shows slice of the raw, 3D reconstruction obtained from [91], while **(e)** shows the grain mask applied to the 3D reconstruction and **(f)** shows the inverse of the grain mask applied to the 3D reconstruction. In **(e, f)**, red corresponds to the domain used to compute corresponding power spectra **(b)** and **(c)**, respectively, while blue corresponds to regions excluded from the respective power spectrum calculations.

We note here that although the peak width detection generalizes relatively well to highly non-spherical shapes seen in Fig. 5.12 **(a)** and to model 3D systems, the peak width estimates struggle in the presence of noise inherent to the self-assembled structures. Using $c_1 = 0.3$ returns a similar, single, well-defined domain, with the exception that we lost the edge of the crystal (Fig. 5.15 **(d)**, highlighted region). This is likely due to a combination of limited image resolution and variations in image brightness and contrast towards the edge of the imaged structure.

Overall, however, we were able to obtain a single, well defined domain with which we could segment a single crystal grain (Fig. 5.15 **(e)**, red region), with little modification to our workflow.

5.5.2.3 Dislocation Detection

Once we isolated a single crystal grain, we re-ran peak detection on the FT computed from the isolated domain (Fig. 5.15 **(b)**), using the same peak detection parameters outlined in Sec. 5.5.2.1. Here, we note that *peakyFinders* is able to return reasonable peak width estimates. This is likely due to the fact that the spectrum computed from the isolated grain (Fig. 5.15 **(b)**) has significantly less noise than the spectrum computed from the raw, 3D reconstruction (Fig. 5.15 **(a)**).

Next, we filtered the brightest Bragg peak in the FT with a width scale of 4. In Fig. 5.16, we can see the results of $||\xi||$ mapped onto a slice of the 3D reconstruction (Fig. 5.16 **(b)**), and the raw $||\xi||$ (Fig. 5.16 **(d)**, where purple (darker color) corresponds to disordered regions or dislocations, and yellow (lighter color) corresponds to highly ordered regions. Meanwhile, in Fig. 5.16 **(c)**, blue (darker color) corresponds to $|cos(\phi)| \cdot \varsigma = 0$, while yellow (lighter color) corresponds to $|cos(\phi)| \cdot \varsigma = 1$. From Fig. 5.16 **(b, d)** (circled region), we can clearly see the presence of a grain boundary (GB). Meanwhile, discontinuities in Fig. 5.16 **(c)** (white arrow), allow us to identify dislocations with particle-level resolution (Fig. 5.16 **(a)**, red arrow).

5.5.3 Analysis of a 3D Simulation with Hexagonal/Cubic Diamond Stacking Faults

Finally, we test the utility of *peakyFinders* in differentiating structures that are traditionally challenging to analyze. Here, we chose a system of 50,000 hard truncated tetrahedrons with edge truncation of 1.20, vertex truncation of 2.16, and particle volume fraction of 0.58, self-assembled via Monte Carlo simulations (obtained from [80]). This system contains a mixture of liquid and hexagonal diamond/cubic diamond stacking faults.

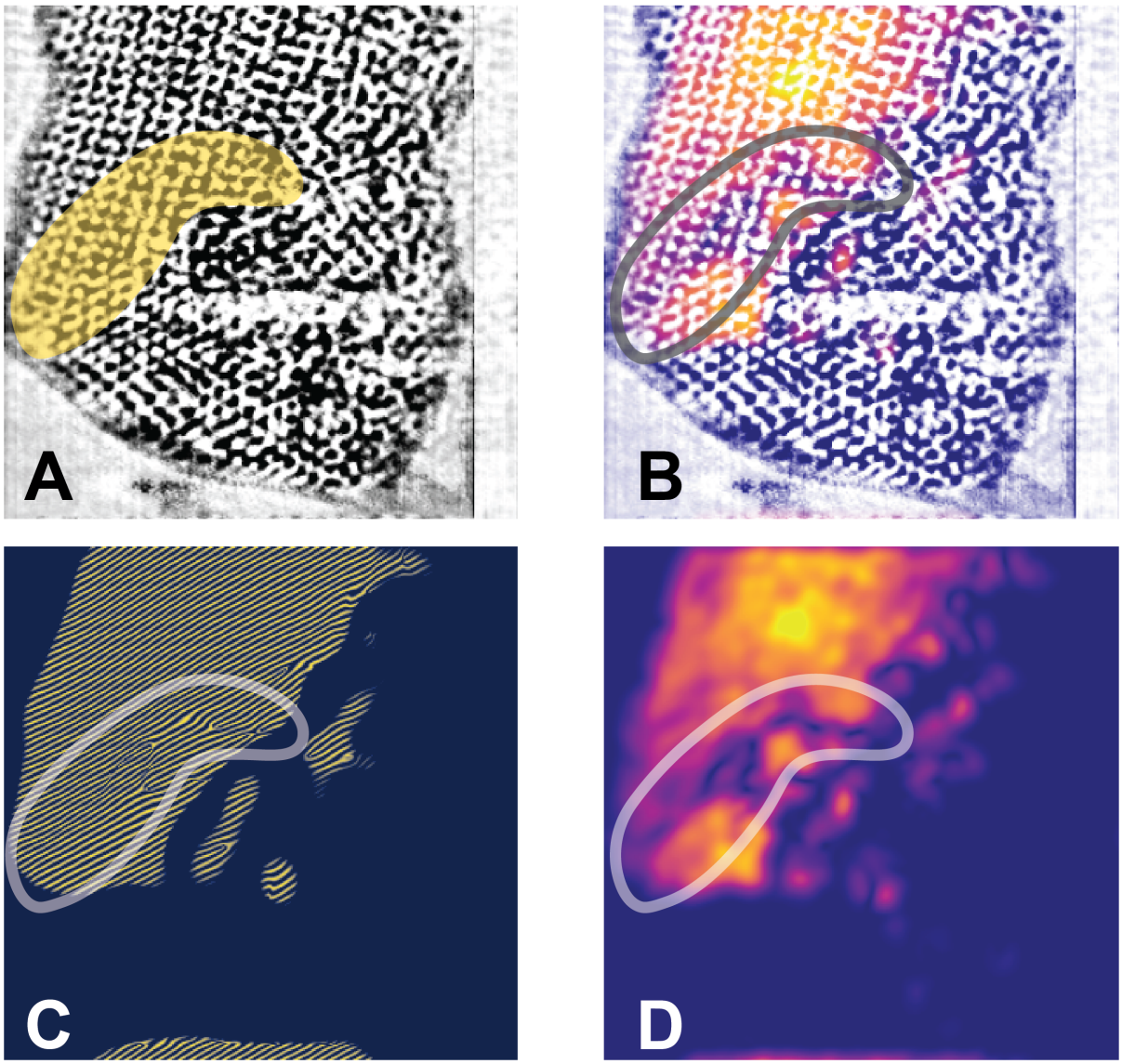

Figure 5.16: **Dislocations detected via Bragg peak filtering in a 3D reconstruction of a system of 20 nm DNA grafted gold nanoparticles.** **(a)** Contrast-enhanced slice of raw, 3D reconstruction obtained from [91]. **(b)** $||\xi||$ of a single, filtered Bragg peak, mapped onto **(a)**. **(c)** Modified phase of ξ and **(d)** $||\xi||$ of the slice shown in **(a)**, where purple (dark regions) correspond to dislocations or high displacement with respect to $\vec{b}_k$ of the filtered peak (low positional order), while yellow (light regions) correspond to low displacement with respect to $\vec{b}_k$ (high positional order). For clarity, the phase of the iFT, ξ, (**(c)**) was mapped to $|\cos(\theta)|$. Here, blue indicates a value of 0, and yellow indicates a value of 1. Analyses of the phase and magnitude of ξ show a series of dislocations along the outline regions in **(a-d)**.

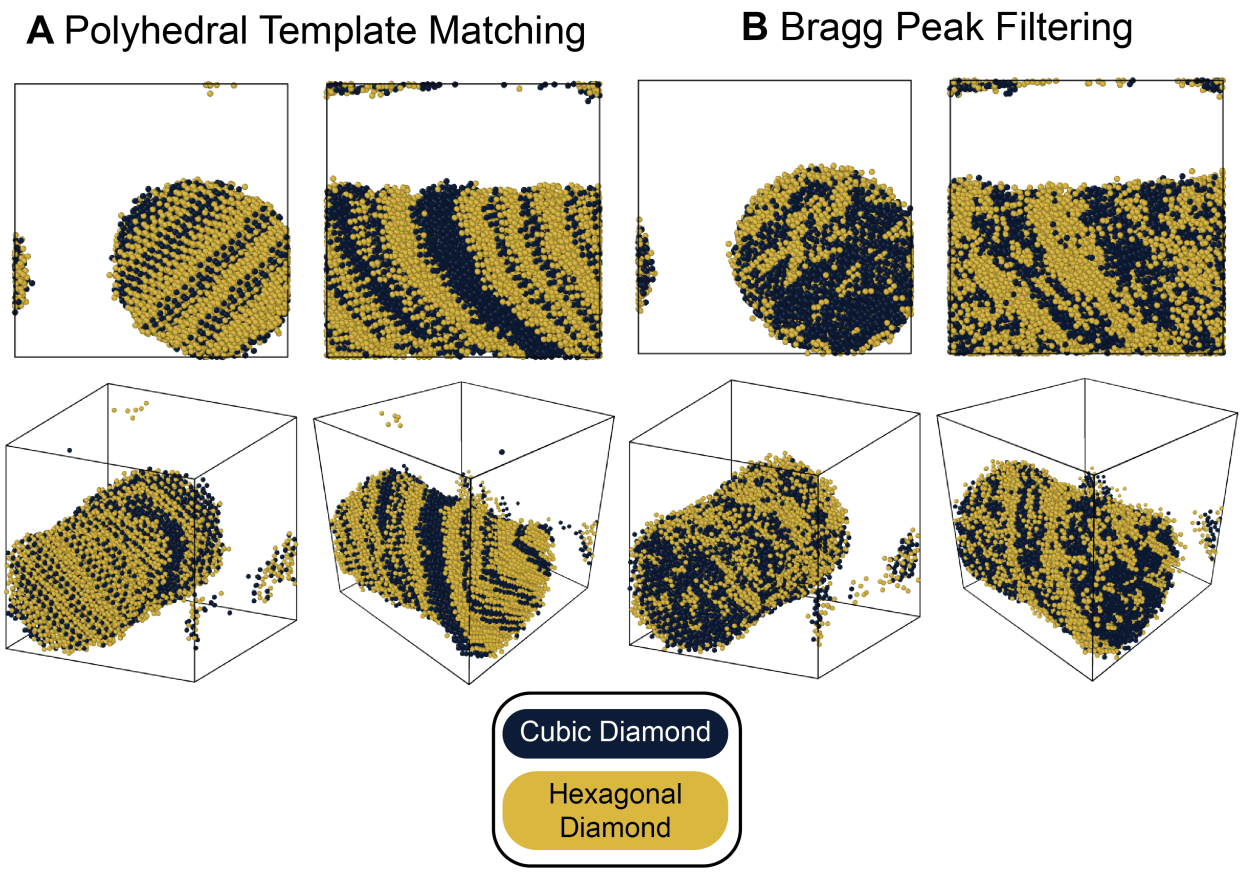

Figure 5.17: **Bragg Peak filtering in a simulation with hexagonal/cubic diamond stacking faults.** Hexagonal/cubic diamond stacking faults self assembled from Monte Carlo simulations of 50,000 hard truncated tetrahedrons with edge truncation of 1.20, vertex truncation of 2.16, and particle volume fraction of 0.58 obtained from [80]. Hexagonal diamond phases are labeled in yellow (lighter color) and cubic diamond phases are labeled in blue (darker color) using **(a)** polyhedral template matching (PTM) and **(b)** Bragg peak filtering. Bragg peak filtering was carried out in two steps: First, we separate solid from liquid by computing the positional order parameter, $||\xi_1||$ based on all detected Bragg peaks, then mapping to a sigmoid, ς_1. Then, we mask regions of the simulation with $\varsigma_1 > 0.5$, and computed $||\xi_2||$ from the second brightest Bragg peak of the masked simulation. We note that, although the results for PTM show sharper, more well defined boundaries, PTM identifies local structures by comparison with a library of known lattices. Meanwhile, Bragg peak filtering methods are more general, and can be used to analyze the structure of any unknown crystal(s).

5.5.3.1 Peak Detection

We found that we could use nearly identical settings as those used for peak detection in previous sections of this chapter. Once more, the only setting we needed to adjust in the peak finding procedure was the distance threshold to 8 pixels for network-based clustering (see Methods 5.3.2, step 3).

5.5.3.2 Solid-Liquid Separation

Here, we found that the presence of both fluid and stacking faults made it difficult to separate hexagonal diamond domains from cubic diamond domains. We also note that, just as in our previous case study with DNA- coated nanoparticle assemblies, the presence of liquid negatively affects out peak width estimates. Instead, we first separate crystalline regions from disordered regions. To separate crystal from disordered regions, we filter all detected peaks using a width scale of 5. Because we must filter multiple Bragg peaks to seperate all solid regions from disordered regions, we adopt a similar protocol to that used to segment grains in a 2D image of self-assembled acrylonitrile butadiene styrene (ABS) cubes (Sec. 5.4.2.2).

Because we filter more than one peak in this protocol, we get a patchy, patterned domain rather than a smooth, continuous one (see discussion in Sec. 5.4.2.2 for more details regarding why this is the case). To obtain a smooth domain, we follow a similar protocol to Sec. 5.4.2.2, where we apply a Gaussian filter with $\sigma = 1$ to the $||\xi||$ (after filtering all detected peaks). This enabled us to obtain a smooth, continuous domain associated with the crystalline region of the simulation. Next, we computed the sigmoid-mapped iFT magnitude, $\varsigma(\vec{x})$, from the Gaussian filtered $||\xi||$. Using this protocol and ς parameter setting of $c_1 = 0.5$ and $c_2 = 128$, we were able to effectively segment the crystal from the liquid.

5.5.4 Differentiating Hexagonal and Cubic Diamond

Next, we separate hexagonal diamond layers from cubic diamond layers using Bragg peak filtering and *peakyFinders*. To begin, we performed peak detection on the isolated, crystallized region of the simulation. As with the 3D DNA-grafted gold nanoparticle system, we found that peak width detection worked reasonably well in absence of noise due to fluid.

In order to obtain a relatively clear separation between stacking fault layers, we found it necessary to iterate through a few combinations of lower intensity peaks. We note that here, that we did not do an extensive search of all peak combinations.

Ultimately, we were able to find a combination of two peaks that allowed us to obtain a decent separation between hexagonal and cubic diamond layers, shown in Fig. 5.17 **(b)**, where blue (darker color) is cubic diamond and yellow (lighter color) is hexagonal diamond. For both filtered

peaks, we used a width scale of 9 and ς setting of $c_1 = 0.3$ and $c_2 = 128$, then mapped ς back onto our simulation points.

For comparison, we show cubic and hexagonal diamond domains identified via the PTM implementation in Ovito [130] (Fig. 5.17). We see good agreement between PTM outputs and our Bragg peak filtering results, though the boundaries of our Bragg peak filtering results are less well defined than PTM. It's important to note here, however, that PTM is a *template matching* protocol – meaning PTM performs an exhaustive comparison of each point and its neighbors with a library of crystal structures. This means that the structures of interest must be present in the existing library of structures for a given PTM implementation, or the user must know *a priori* what structure(s) are present in their system, then add it into the library of structures available to PTM.

In contrast, Bragg peak filtering does not require prior knowledge of the structure or types of structures present in the system. The fundamental relationship between Bragg reflections and crystal symmetry, too, means that this method should be applicable to any crystal that can be represented in a 2D or 3D image.

5.5.5 Conclusion of 3D Examples

These results show that the Bragg peak filtering procedure and *peakyFinders* generalize to 3D, and that *peakyFinders* can be used to segment grains and detect defects and dislocations with particle-level precision.

5.6 Conclusion

In this chapter, we showed the how the Bragg peak filtered inverse Fourier Transform (iFT), magnitude, $||\xi||$, can be applied to the segment grains, detect dislocations, and measure order in a variety of 2D and 3D systems, and we develop an Python-based tool (*peakyFinders*) to assist in peak detection and Bragg peak filtering for 2D and 3D inputs. We find that the peak detection and sigmoid masking in *peakyFinders* are robust to noise and distortions arising from highly non-spherical particle shapes (e.g. hard cubes) and noise arising from liquid or disorder in 2D and 3D and we find that our existing protocol is easily extensible to a variety of 2D systems and simple, 3D crystals, and that our workflow can be extended to more complex structures and particle shapes with the few additional steps in our workflow. In fact, we were able to use nearly identical settings for peak detection and simulation masking for nearly all of our test cases. We compared our dislocation and grain segmentation results to volumetric strain calculations and dislocation extraction algorithm (DXA) for model dislocation cases and polyhedral template matching (PTM) for our stacking fault case. We found that our Bragg peak filtering protocol can reliably reproduce outputs

from each of these methods, and we developed a Python based tool, *peakyFinders*, which will be available as an open source package in 2024.

This last point is particularly notable – Bragg peak filtering allowed us to reproduce results from a variety of different measures of order using the same, or nearly the same, protocol and setting and no prior knowledge of the structures present in the system. Taken all together, this work highlights a new framework with which we can approach the analysis of order in complex crystals and develop fast, reliable, and transparent models for structural analysis.

CHAPTER 6

Concluding Remarks

Quasicrystals (QCs) have long attracted interest, due to their unique properties and their fascinating structures. Unfortunately, the commercial application of QCs remains limited due to challenges surrounding the synthesis of large, high quality samples. Meanwhile, research detailing experimentally relevant growth mechanisms remain limit and analysis of these systems remains challenging.

In this thesis, we addressed some of these gaps in literature, and methodology. Namely, we elucidated the role phasons play in defect-free QC growth and we developed a robust framework to measure order in crystalline systems. Our main contributions include:

1. Providing large scale, systematic analysis of experimentally relevant QC growth interactions.
2. Establishing the role of phasons in redistributing strain upon collision of growth fronts.
3. Detailing the role of multiple length scales in phason-mediated grain coalesence.
4. Developing *peakyFinders*, a Python-based tool for Bragg peak detection and filtering.
5. Developing a masking-based methodology for Bragg peak filtering. This method avoids some of the common artifacts traditional Fourier filtering analysis faces and requires less precise measurements of Bragg reflection centers.

In Ch. 3, we worked alongside the Shahani group to provide a cohesive picture for the conditions that give rise to grain coalescence in QCs upon collision of two misoriented decagonal quasicrystals (dec-QCs) grains. Using molecular dynamics (MD) simulations we observed grain rotation toward 0° misorientation upon collision of grains with small ($< 9^\circ$) misorientation. We observed a dislocation-mediated mechanism, wherein the dec-QCs redistribute phonon strain due to lattice mismatch as phason strain via phason flips.

We continued our collaboration with the Shahani group, and built on these findings in Ch. 4. Using large scale simulation studies, we investigated the mechanisms driving coalesence upon QC

collision and engulfment of shrinkage pores. Our work highlighted the role of multiple length scales in phason-mediated coalesence. Specifically, our results showed that, after collision, the mean per-particle potential energy of particles along the region of coalescence rapidly decreases, until they form a low energy region along the site of collision. We found that this low energy region originates from a low ratio of short-to-long length scales along the region of coalescence when compared to the rest of the crystal. This is a phenomon that is unique to QCs – in periodic crystals, it impossible for the ratio of length scales without the introduction of grain boundaries. This highlights how phasons can help prevent the formation of grain boundaries or dislocations upon collision of growth fronts.

Taken together, our results highlight how the unique symmetries of QCs enable defect-free growth in situations where periodic crystals might form defects, grain boundaries, and dislocations.

Throughout this work, we were able to build a stronger understanding of order in both QCs and periodic crystals. In Ch. 5, we built on this insight and developed *peakyFinders*, a robust Python-based tool for Bragg peak detection and filtering. We demonstrated how inverse Fourier Transform (iFT) magnitude of Bragg peak filtered spectrums are more robust to noise and artifacts when compared to traditional, phase-based analysis, while still maintaining particle-level defect and grain detection. We show how this methodology can be applied to the segment grains, detect dislocations, and measure order with particle level precision in a wide variety of 2D and 3D systems. Then, finally, we show how our workflow can be extended to more complex structures and particle shapes. Ultimately, Ch. 5 highlights a new framework with which we can approach the analysis of order in complex crystals

Taken all together, our work with QCs highlights an exciting opportunity for defect engineering in QCs and deepens the knowledge base for fabrication of defect-free QCs. Through insight gleaned in our QC work, we develop a new, highly generalizable approach to grain, defect, and dislocation detection in crystalline systems.

6.1 Future Directions

This dissertation deepens our understanding of phason contributions to QC growth, and, more generally, highlights how Fourier-based analysis can be harnessed to analyze complex crystals.

6.1.1 Phason Contributions to Quasicrystal Defect Formation

A natural progression of the work presented in this thesis is the systematic investigation of order upon collision of growth fronts at various temperatures. System temperature is important for two reasons: (1) Phason strain relaxation occurs via particle motion. As system temperature changes,

then, we may also expect changes in the frequency and types of phason flips that occur in a system. It follows, then, that phason-mediated mechanisms and phason strain relaxation are affected by system temperature. (2) Annealing is a fundamental step in material processing and manufacturing. Understanding the effects of temperature on phason relaxation will give experimentalists the tools they need to develop better manufacturing processes for commercially viable quasicrystal coatings.

Another interesting study that could be carried out in tandem with annealing and temperature-based studies, is a study of particle motion and phasonic motion; that is, tracking the motion of particles near the site of collision over long periods of time. Specifically, it would be to see if certain structures are more or less stable than others, or if some regions are more prone to correlated phason flips than others. Here, work by Engel et al. [41] would serve as a good model for this type of study.

Extension of this work to other types of QCs is another promising avenue. The pair potential used in our dec-QC may have played a role in the types of structures formed after growth front collision. Comparing the results of Ch. 4 to entropically assembled QCs, or with pair potentials where the difference between well shapes and depths are minor can offer some additional insight on the nature of phason-mediated grain coalesence.

6.1.2 PeakyFinders

There are two promising directions for *peakyFinders* development.

A first direction is the addition of machine learning (ML) and further automation to the *peakyFinders* pipeline. A major drawback for *peakyFinders* when dealing with complex structures, is the need to iterate over multiple peaks. Future development should focus on developing a pipeline to automate this process, and to use ML to assist in reducing the number of parameters in the analysis workflow. Here, it's not necessary to use any neural networks or multi-layer perceptions, rather, the focus should be on unsupervised models to tune parameters, and to determine which peaks are, or are not, relevant for analysis of specific domains. Additionally, care should be taken with regards to computational cost of these algorithms. *peakyFinders* is intended to be a package which users can do quick, exploratory analysis. While some overhead may be expected for more sophisticated implementations, we should always favor the simpler, more transparent algorithms to achieve the desired outcome.

A second direction is the development of either a guided user interface or interactive tutorials. While we expect *peakyFinders* users to possess some working level of Python proficiency, these types of tools will make *peakyFinders* and the Bragg peak filtering workflow easier to work with. There is an inherently visual component to these types of analyses Giving new users the ability to experiment and explore can help them build intuition on the relationship between reciprocal space,

Bragg peak filtering, and order in their systems.

In addition to these two major directions, there are several parameters and algorithms in *peakyFinders* that could benefit from further iteration. These include:

- Improvements to the Bragg peak width estimation method.
- Replacing the duplicate Bragg peak window parameter with a metric that is relative to image size.
- Better support to account for highly irregular form factors.
- General improvements to Bragg peak categorization.
- Support for rotating, scaling, and matching a set of reference Bragg peaks to a given Fourier Transform (FT) or power spectrum.

6.1.3 Quasicrystals, Reciprocal Space, and Bragg Peak Filtering

The field of QC research would benefit greatly from a more rigorous, but accessible treatment of Bragg peak filtering outputs. There are a number of papers that discuss the crystallography of QC in the context of diffraction [66, 88, 126]. While these are useful resources to build intuition, diffraction patterns cannot be used to map long-range structural order back to real space positions. Most of these papers talk about the effects of phason strain and phonon strain on the shape and intensity of the Bragg peak, as well as shifts in the spectrum. While these are undoubtedly useful topics to review, they should be reviewed alongside literature regarding geometric phase analysis (GPA), modulated phases, and, perhaps, an introduction to topological defects [44].

6.2 Final Comments

As we deepen our understanding of how phasons contribute to the unexpected growth behavior of QCs seen in experiment, we also deepened our understanding of order in periodic systems. Studying QCs and reciprocal space-based methods for crystal analysis has potential to broaden our understanding of not just QCs but other unconventional or complex crystals. We hope that this thesis will help enable the development of new and better theories of QC growth, and to aid in the development of analysis techniques for challenging and complex structures.

APPENDIX A

Correlations Martrices for Quasicrystal-Pore Simulations

A.1 Interface Characteristic Dependence on Pore Parameters

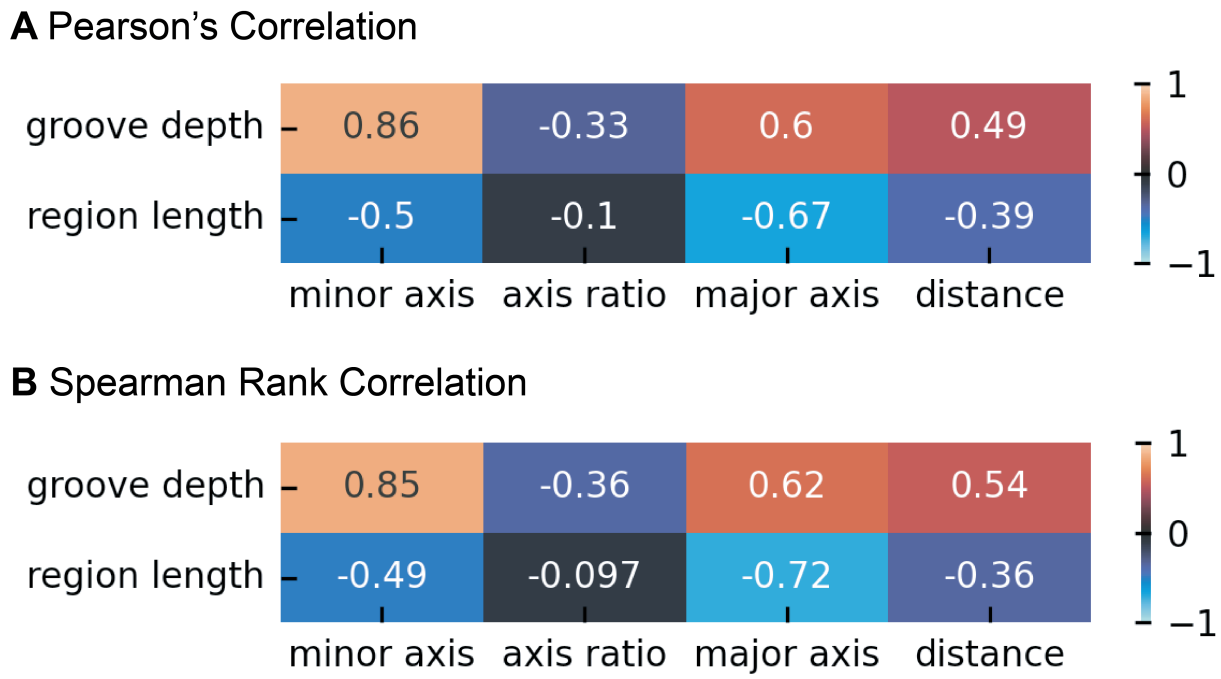

Figure A.1: (a) Pearson's correlation and (b) Spearman rank correlation between interface characteristics (groove depth and coalescence region length).

A.2 Positional Order Dependence on Pore Parameters and Interface Characteristics

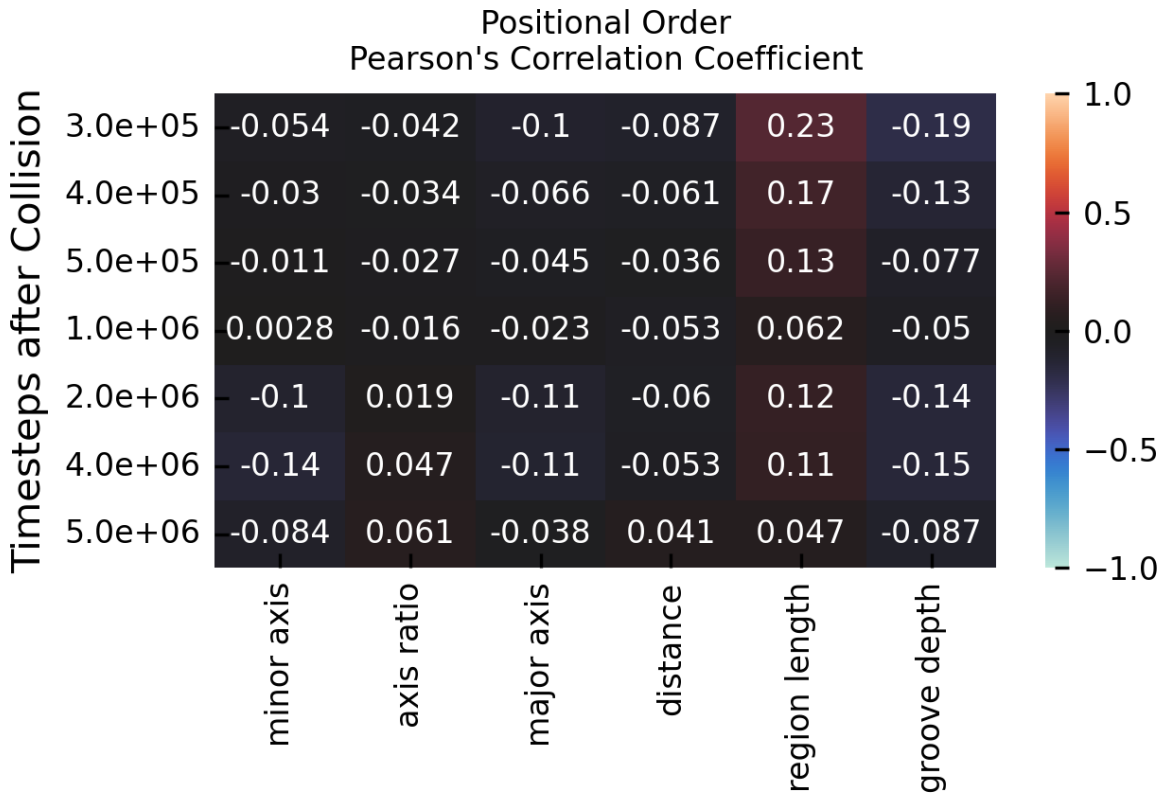

Figure A.2: Pearson's correlation between positional order and pore parameters at various timesteps after coalescence.

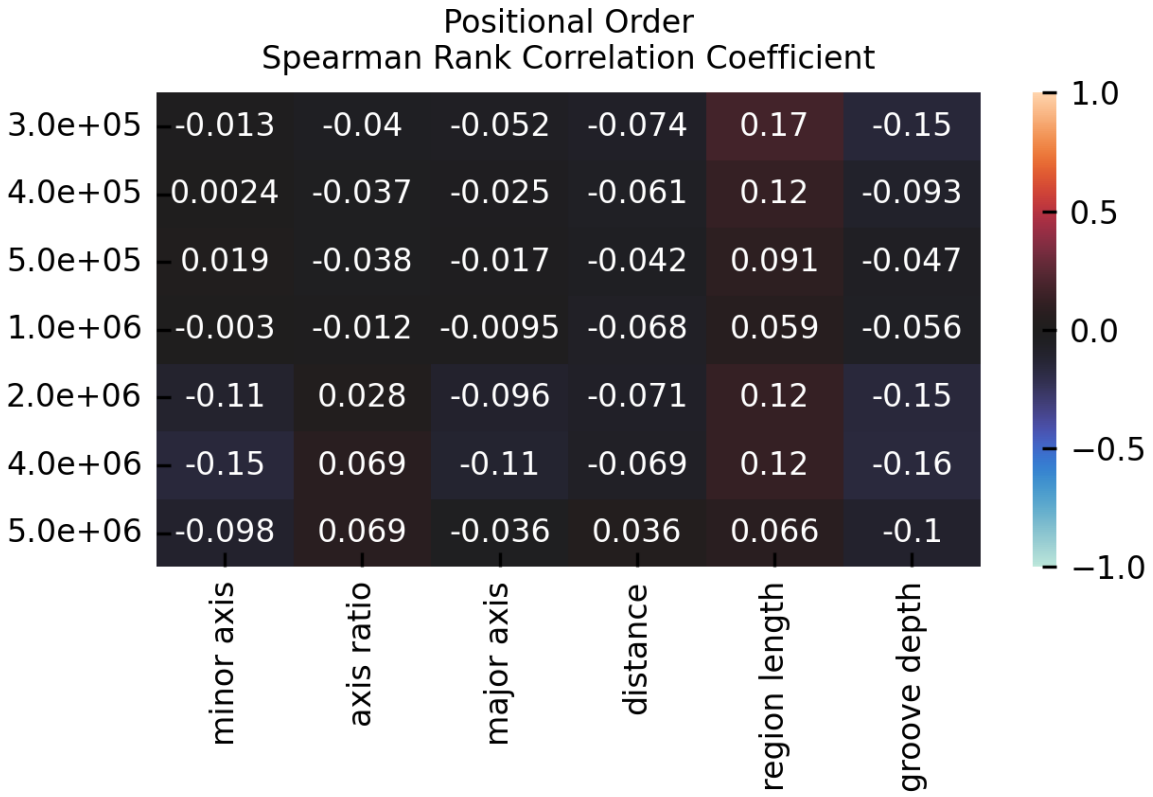

Figure A.3: Spearman correlation between positional order and pore parameters at various timesteps after coalescence.

A.3 Mean Per Particle Potential Energy Dependence on Pore Parameters and Interface Characteristics

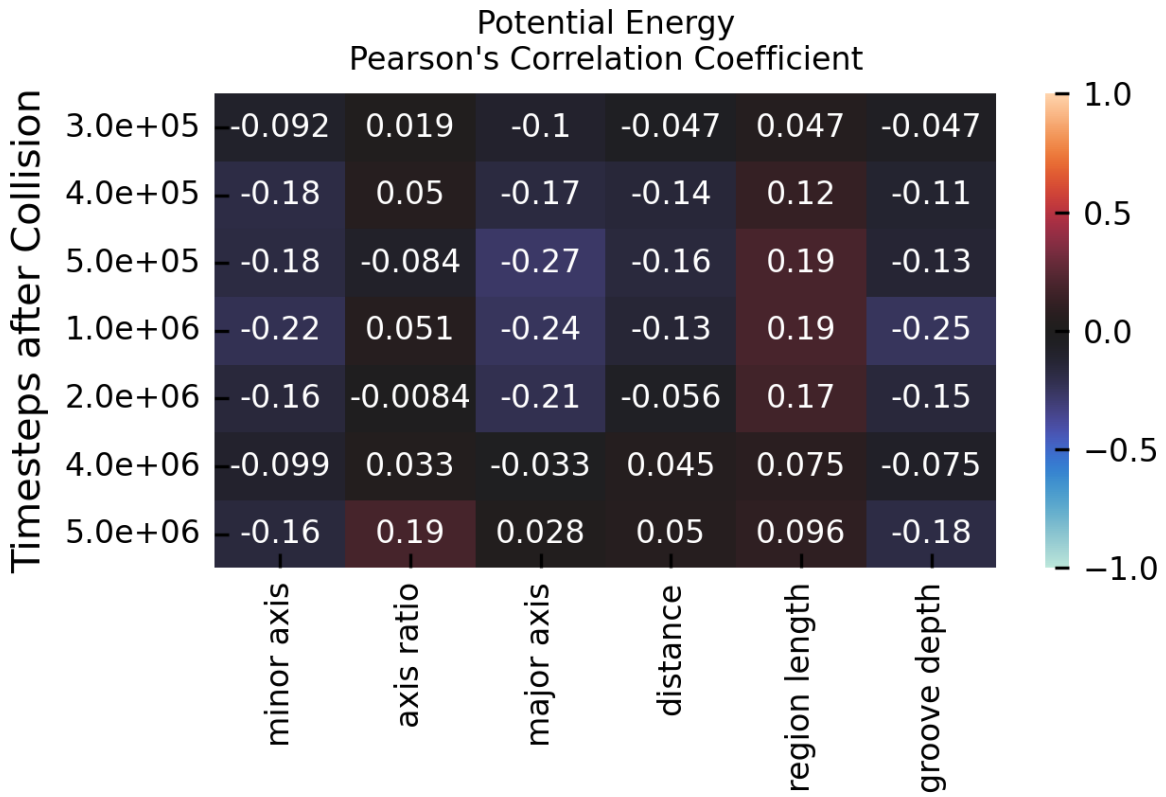

Figure A.4: Pearson's correlation between mean per particle potential energy and pore parameters at various timesteps after coalescence.

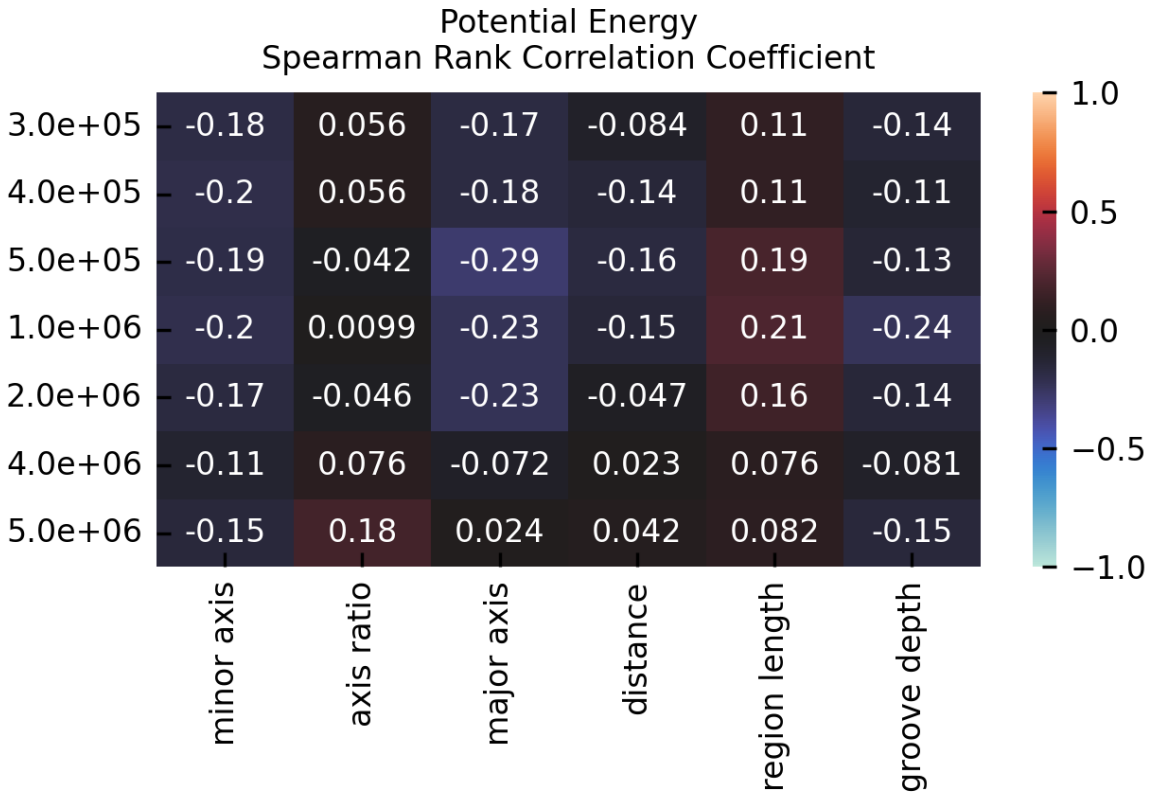

Figure A.5: Spearman correlation between mean per particle potential energy and pore parameters at various timesteps after coalescence.

A.4 Orientational Order Dependence on Pore Parameters and Interface Characteristics

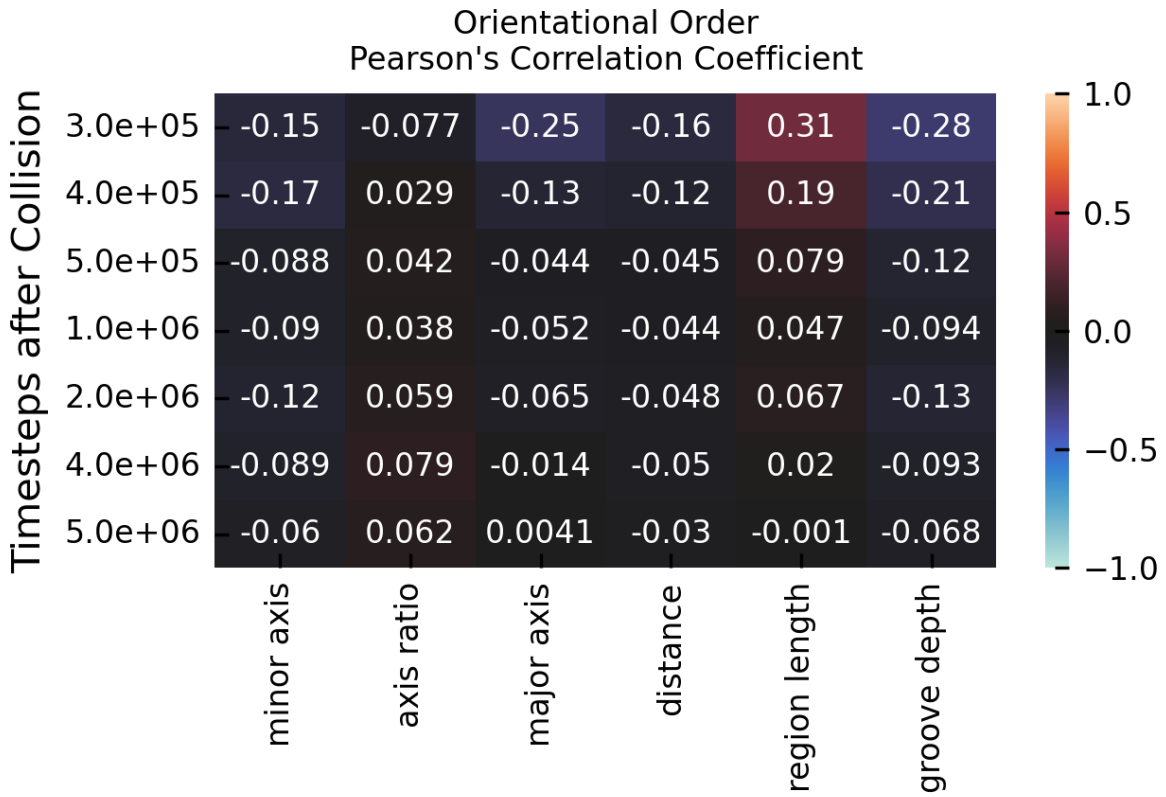

Figure A.6: Pearson's correlation between orientational order and pore parameters at various timesteps after coalescence.

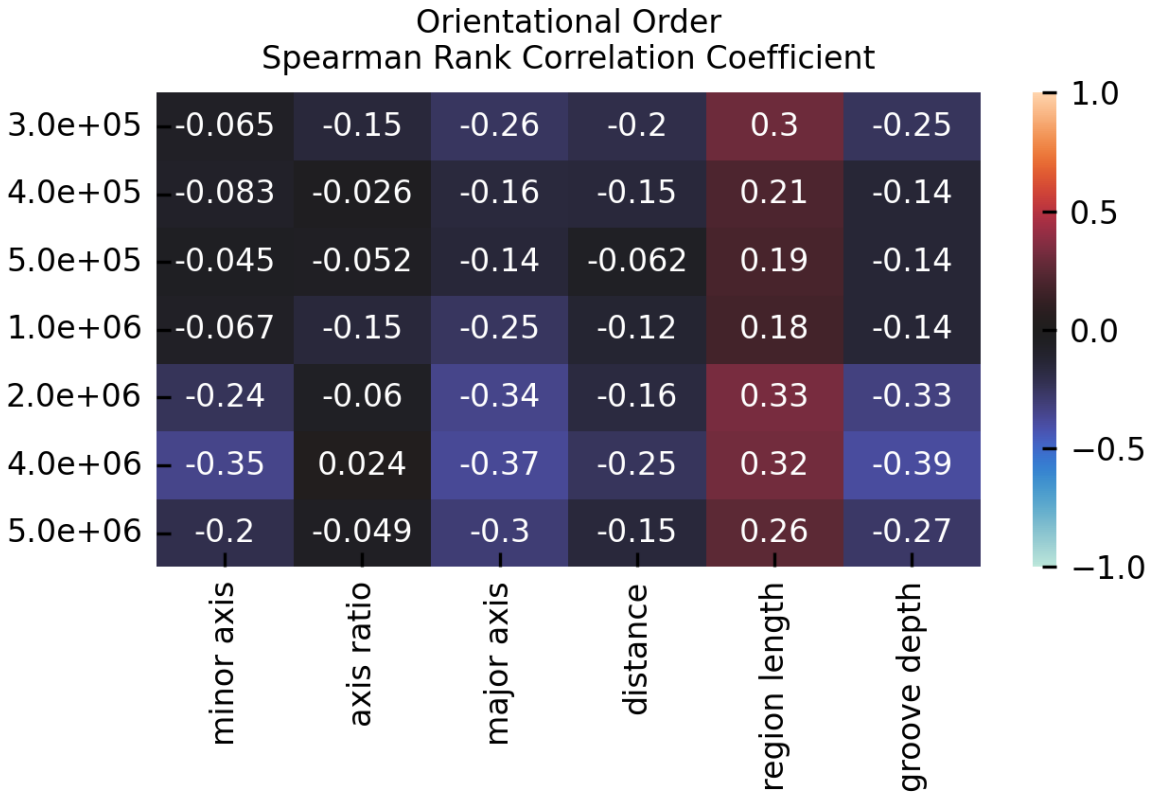

Figure A.7: Spearman correlation between mean orientational order and pore parameters at various timesteps after coalescence.

A.5 Gaussian-Weighted Bond Lengths Dependence on Pore Parameters and Interface Characteristics

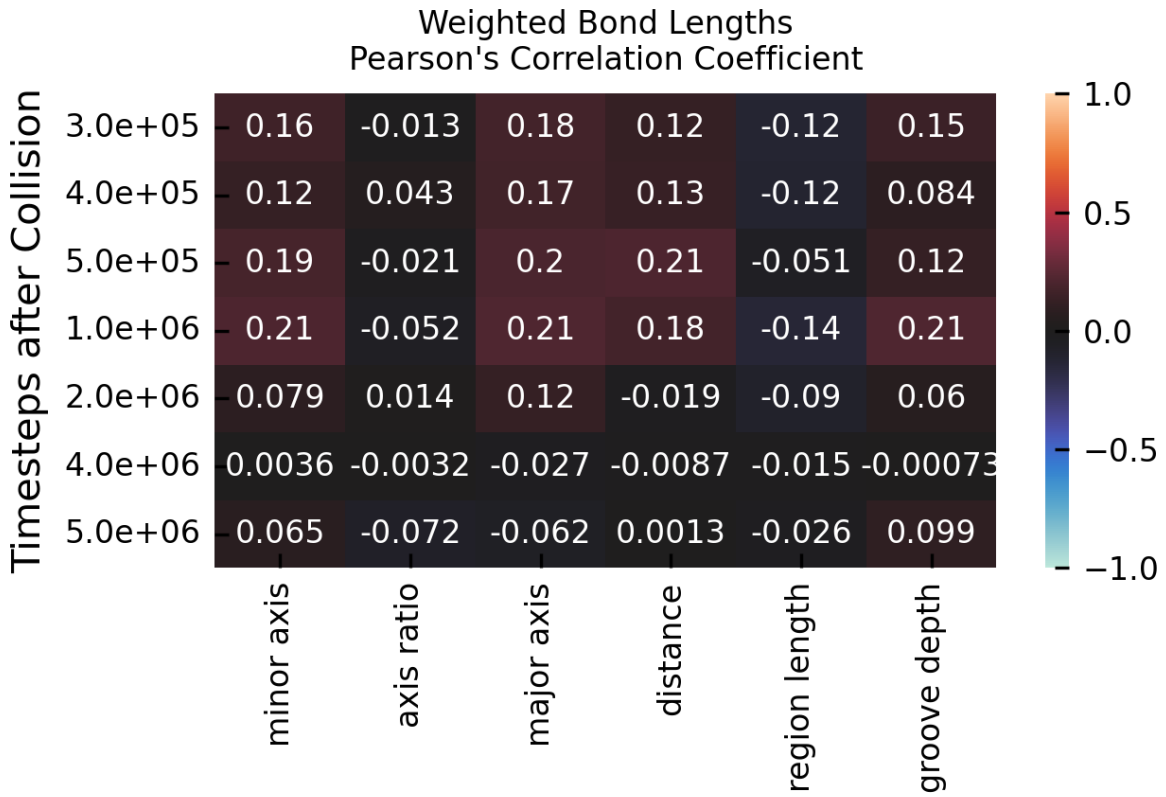

Figure A.8: Pearson's correlation between density-mapped bond lengths and pore parameters at various timesteps after coalescence.

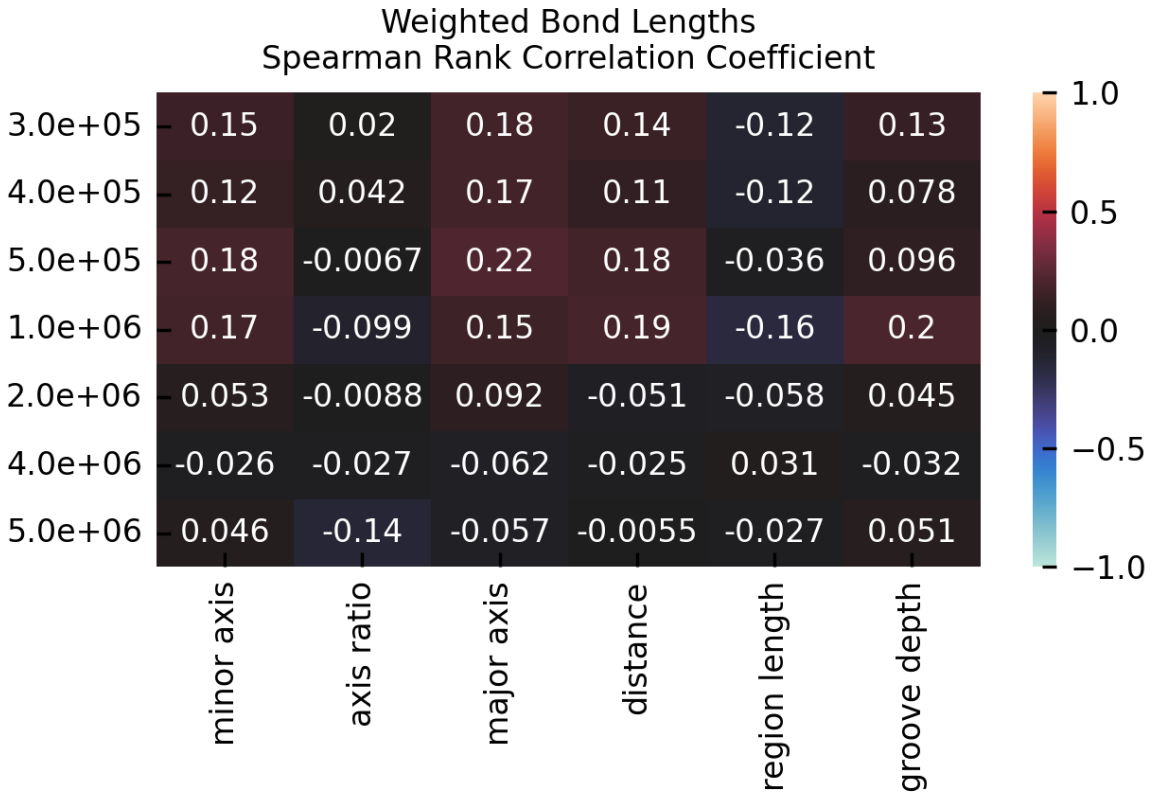

Figure A.9: Spearman correlation between density-mapped bond lengths and pore parameters at various timesteps after coalescence.

BIBLIOGRAPHY

[1] Nobel Prize Outreach AB. The nobel prize in chemistry 2011.

[2] Graeme J. Ackland and Andy P. Jones. Applications of local crystal structure measures in experiment and simulation. *Physical Review B*, 73(5):054104, 2006.

[3] Carl S. Adorf, Paul M. Dodd, Vyas Ramasubramani, and Sharon C. Glotzer. Simple data and workflow management with the signac framework. *Computational Materials Science*, 146:220–229, 2018.

[4] Silvère Akamatsu and Henri Nguyen-Thi. In situ observation of solidification patterns in diffusive conditions. *Acta Materialia*, 108:325–346, 2016.

[5] Joshua A Anderson, James Antonaglia, Jaime A Millan, Michael Engel, and Sharon C Glotzer. Shape and symmetry determine two-dimensional melting transitions of hard regular polygons. *Physical Review X*, 7(2):021001, 2017.

[6] Joshua A. Anderson, Jens Glaser, and Sharon C. Glotzer. Hoomd-blue: A python package for high-performance molecular dynamics and hard particle monte carlo simulations. *Computational Materials Science*, 173:109363, 2020.

[7] Lars Arnberg and Ragnvald H. Mathiesen. The real-time, high-resolution x-ray video microscopy of solidification in aluminum alloys. *Jom*, 59(8):20–26, 2007.

[8] Song Bai, Ning Zhang, Chao Gao, and Yujie Xiong. Defect engineering in photocatalytic materials. *Nano Energy*, 53:296–336, 2018.

[9] Gordon L. J. Bailey and Harry C. Watkins. Surface tensions in the system solid copper-molten lead. *Proceedings of the Physical Society. Section B*, 63(5):350, 1950.

[10] Vsevolod N. Balbyshev, Alexander N. Khramov, David J. King, Benjamin S. Phillips, Linda S. Kasten, and Michael S. Donley. Investigation of nanostructured al-based quasicrystal thin films for corrosion protection. *Progress in Organic Coatings*, 47(3-4):357–364, 2003.

[11] Suvo Banik, Debdas Dhabal, Henry Chan, Sukriti Manna, Mathew Cherukara, Valeria Molinero, and Subramanian KRS Sankaranarayanan. CEGANN: Crystal Edge Graph Attention Neural Network for multiscale classification of materials environment. *npj Computational Materials*, 9(1):23, 2023.

[12] Armand Barbot and Riccardo Gatti. Unsupervised learning for structure detection in plastically deformed crystals. *Computational Materials Science*, 230:112459, 2023.

[13] Guillermo Bárcena-González, Andrei Hernández-Robles, Álvaro Mayoral, Lidia Martinez, Yves Huttel, Pedro L Galindo, and Arturo Ponce. Unsupervised learning for the segmentation of small crystalline particles at the atomic level. *Crystal Research and Technology*, 58(3):2200211, 2023.

[14] Simon Bäuerle, Robert Fiedler, and Hartmut Hetzler. An engineering perspective on the numerics of quasi-periodic oscillations: A comparison of two hyper-time approaches based on a unified framework. *Nonlinear Dynamics*, 108(4):3927–3950, 2022.

[15] Peter Beeley. *Foundry technology*. Elsevier, 2001.

[16] Etienne P. Bernard and Werner Krauth. Two-step melting in two dimensions: First-order liquid-hexatic transition. *Physical review letters*, 107(15):155704, 2011.

[17] Harald Bohr. Zur theorie der fast periodischen funktionen: I. eine verallgemeinerung der theorie der fourierreihen. *Acta Mathematica*, 45(1):29–127, 1925.

[18] Tamas Börzsönyi, Silvère Akamatsu, and Gabriel Faivre. Dynamics of a faceted nematic–smectic-b front in thin-sample directional solidification. *Physical Review E*, 65(1):011702, 2001.

[19] Martin J. Buerger. Crystallographic symmetry in reciprocal space. *Proceedings of the National Academy of Sciences*, 35(4):198–201, 1949.

[20] Martin J. Buerger. *Elementary crystallography*. John Wiley & Sons, 1956.

[21] Sergei E. Burkov. Structure model of the Al-Cu-Co decagonal quasicrystal. *Physical review letters*, 67(5):614, 1991.

[22] John W Cahn. Quasicrystals. *Journal of research of the National Institute of Standards and Technology*, 106(6):975, 2001.

[23] John W. Cahn and Jean E. Taylor. A unified approach to motion of grain boundaries, relative tangential translation along grain boundaries, and grain rotation. *Acta Materialia*, 52(16):4887–4898, 2004.

[24] John Campbell. *Castings*. Elsevier, 2001.

[25] Bertrand L. Chamberland. Crystal growth of CrO2. *Materials Research Bulletin*, 2(9):827–835, 1967.

[26] Danpeng Cheng, Wuxin Sha, Zuo Xu, Shide Li, Zhigao Yin, Yuling Lang, Shun Tang, and Yuan-Cheng Cao. Atomgan: unsupervised deep learning for fast and accurate defect detection of 2d materials at the atomic scale. *Science China Information Sciences*, 66(6):160410, 2023.

[27] Mikhail A. Chernikov, Hans R. Ott, Andrea Bianchi, Albert Migliori, and Tim W. Darling. Elastic Moduli of a Single Quasicrystal of Decagonal Al-Ni-Co: Evidence for Transverse Elastic Isotropy. *Physical Review Letters*, 80(2):321–324, Dec 1998.

[28] James W. Cooley and John W. Tukey. An algorithm for the machine calculation of complex fourier series. *Mathematics of computation*, 19(90):297–301, 1965.

[29] Jules M. Dake, Jette Oddershede, Henning O. Sørensen, Thomas Werz, J. Cole Shatto, Kentaro Uesugi, Søren Schmidt, and Carl E. Krill. Direct observation of grain rotations during coarsening of a semisolid al–cu alloy. *Proceedings of the National Academy of Sciences*, 113(41):E5998–E6006, 2016.

[30] Pablo F. Damasceno, Michael Engel, and Sharon C. Glotzer. Crystalline assemblies and densest packings of a family of truncated tetrahedra and the role of directional entropic forces. *ACS Nano*, 6(1):609–614, 2011.

[31] Pablo F. Damasceno, Michael Engel, and Sharon C. Glotzer. Predictive self-assembly of polyhedra into complex structures. *Science*, 337(6093):453–457, 2012.

[32] Pablo F. Damasceno, Sharon C. Glotzer, and Michael Engel. Non-close-packed three-dimensional quasicrystals. *Journal of Physics: Condensed Matter*, 29(23):234005, 2017.

[33] Jonathan A. Dantzig and Michel Rappaz. *Solidification: -Revised & Expanded*. EPFL press, 2016.

[34] Marc de Boissieu. Ted Janssen and aperiodic crystals. *Acta Crystallographica Section A: Foundations and Advances*, 75(2):273–280, 2019.

[35] Pieter M. De Wolff. The pseudo-symmetry of modulated crystal structures. *Acta Crystallographica Section A: Crystal Physics, Diffraction, Theoretical and General Crystallography*, 30(6):777–785, 1974.

[36] Julia Dshemuchadse, Pablo F. Damasceno, Carolyn L. Phillips, Michael Engel, and Sharon C. Glotzer. Moving beyond the constraints of chemistry via crystal structure discovery with isotropic multiwell pair potentials. *Proceedings of the National Academy of Sciences*, 118(21):e2024034118, 2021.

[37] Jean-Marie Dubois. Properties- and applications of quasicrystals and complex metallic alloys. *Chemical Society Reviews*, 41(20):6760, 2012.

[38] Michael Engel. *Dynamics and defects of complex crystals and quasicrystals : perspectives from simple model systems*. PhD thesis, Institut für Theoretische und Angewandte Physik, 2008.

[39] Michael Engel, Joshua A. Anderson, Sharon C. Glotzer, Masaharu Isobe, Etienne P. Bernard, and Werner Krauth. Hard-disk equation of state: First-order liquid-hexatic transition in two dimensions with three simulation methods. *Physical Review E*, 87(4):042134, 2013.

[40] Michael Engel and Hans-Rainer Trebin. Stability of the decagonal quasicrystal in the Lennard–Jones–Gauss system. *Philosophical Magazine*, 88(13-15):1959–1965, 2008.

[41] Michael Engel, Masahiro Umezaki, Hans-Rainer Trebin, and Takashi Odagaki. Dynamics of particle flips in two-dimensional quasicrystals. *Physical Review B*, 82(13):134206, 2010.

[42] James D. Evans. *Straightforward statistics for the behavioral sciences.* Thomson Brooks/Cole Publishing Co, 1996.

[43] Barak Freedman, Ron Lifshitz, Jason W. Fleischer, and Mordechai Segev. Phason dynamics in nonlinear photonic quasicrystals. *Nature materials*, 6(10):776–781, 2007.

[44] Sébastien Fumeron and Bertrand Berche. Introduction to topological defects: from liquid crystals to particle physics. *The European Physical Journal Special Topics*, pages 1–21, 2023.

[45] Fengyi Gao, Jens Glaser, and Sharon C. Glotzer. The role of complementary shape in protein dimerization. *Soft Matter*, 17(31):7376–7383, 2021.

[46] Supriyo Ghosh, Alain Karma, Mathis Plapp, Silvère Akamatsu, Sabine Bottin-Rousseau, and Gabriel Faivre. Influence of morphological instability on grain boundary trajectory during directional solidification. *Acta Materialia*, 175:214–221, 2019.

[47] Chaim Goodman-Strauss. Matching rules and substitution tilings. *Annals of Mathematics*, pages 181–223, 1998.

[48] Uwe Grimm. Aperiodic crystals and beyond. *Acta Crystallographica Section B: Structural Science, Crystal Engineering and Materials*, 71(3):258–274, 2015.

[49] Robert Grupp, Michael Nöthe, Bernd Kieback, and John Banhart. Cooperative material transport during the early stage of sintering. *Nature Communications*, 2(1), Apr 2011.

[50] Yueming Guo, Sergei V. Kalinin, Hui Cai, Kai Xiao, Sergiy Krylyuk, Albert V. Davydov, Qianying Guo, and Andrew R. Lupini. Defect detection in atomic-resolution images via unsupervised learning with translational invariance. *npj Computational Materials*, 7(1):180, 2021.

[51] Christopher A. Guryan, Alan I. Goldman, Peter W. Stephens, K. Hiraga, An Pang Tsai, Akihisa Inoue, and Tsuyoshi Masumoto. Al-Cu-Ru: An icosahedral alloy without phason disorder. *Physical review letters*, 62(20):2409, 1989.

[52] Insung Han, Kelly L. Wang, Andrew T. Cadotte, Zhucong Xi, Hadi Parsamehr, Xianghui Xiao, Sharon C. Glotzer, and Ashwin J. Shahani. Formation of a single quasicrystal upon collision of multiple grains. *Nature Communications*, 12(1):5790, 2021.

[53] Insung Han, Xianghui Xiao, and Ashwin J. Shahani. Probing the growth and melting pathways of a decagonal quasicrystal in real-time. *Scientific reports*, 7(1):1–10, 2017.

[54] Insung Han, Xianghui Xiao, Haiping Sun, and Ashwin J. Shahani. A side-by-side comparison of the solidification dynamics of quasicrystalline and approximant phases in the Al–Co–Ni system. *Acta Crystallographica Section A: Foundations and Advances*, 75(2), 2019.

[55] Jian Han, Spencer L. Thomas, and David J. Srolovitz. Grain-boundary kinetics: A unified approach. *Progress in Materials Science*, 98:386–476, 2018.

[56] Richard A. Hardin and Christoph Beckermann. Effect of porosity on deformation, damage, and fracture of cast steel. *Metallurgical and Materials Transactions A*, 44:5316–5332, 2013.

[57] Karen E. Harris, Varun V. Singh, and Alexander H. King. Grain rotation in thin films of gold. *Acta materialia*, 46(8):2623–2633, 1998.

[58] Dirk Heinen, Hans G. Bohn, and Werner Schilling. Internal friction in free-standing thin al films. *Journal of applied physics*, 78(2):893–896, 1995.

[59] Pierre Hirel. Atomsk: A tool for manipulating and converting atomic data files. *Computer Physics Communications*, 197:212–219, 2015.

[60] J Dana Honeycutt and Hans C Andersen. Molecular dynamics study of melting and freezing of small lennard-jones clusters. *Journal of Physical Chemistry*, 91(19):4950–4963, 1987.

[61] James M. Howe. *Interfaces in materials: atomic structure, thermodynamics and kinetics of solid-vapor, solid-liquid and solid-solid interfaces*. Wiley-Interscience, 1997.

[62] Martin J. Hÿtch. Geometric phase analysis of high resolution electron microscope images. *Scanning Microsc*, 11:53–66, 1997.

[63] Amir Jangizehi, Friederike Schmid, Pol Besenius, Kurt Kremer, and Sebastian Seiffert. Defects and defect engineering in soft matter. *Soft Matter*, 16(48):10809–10859, 2020.

[64] Aloysio Janner and Theo Janssen. Symmetry of periodically distorted crystals. *Physical Review B*, 15(2):643, 1977.

[65] Christian Janot. The properties and applications of quasicrystals. *Europhysics News*, 27(2):60–64, 1996.

[66] Theo Janssen, Gervais Chapuis, and Marc de Boissieu. *Aperiodic crystals: from modulated phases to quasicrystals*. Oxford University Press, 2018.

[67] Kwanghwi Je, Sangmin Lee, Erin G. Teich, Michael Engel, and Sharon C Glotzer. Entropic formation of a thermodynamically stable colloidal quasicrystal with negligible phason strain. *Proceedings of the National Academy of Sciences*, 118(7):e2011799118, 2021.

[68] Dieter Joseph and Veit Elser. A model of quasicrystal growth. *Physical review letters*, 79(6):1066, 1997.

[69] Magzhan Kairanbay and MJ Hajar. A review and evaluations of shortest path algorithms. *International journal of scientific & technology research*, 2(6):99–104, 2013.

[70] Dimitris Kammer and Peter W. Voorhees. The morphological evolution of dendritic microstructures during coarsening. *Acta materialia*, 54(6):1549–1558, 2006.

[71] Aaron S. Keys and Sharon C. Glotzer. How do quasicrystals grow? *Physical Review Letters*, 99(23):235503, 2007.

[72] Byung Hyo Kim, Junyoung Heo, Sungin Kim, Cyril F Reboul, Hoje Chun, Dohun Kang, Hyeonhu Bae, Hyejeong Hyun, Jongwoo Lim, Hoonkyung Lee, et al. Critical differences in 3d atomic structure of individual ligand-protected nanocrystals in solution. *Science*, 368(6486):60–67, 2020.

[73] Miloslav Klinger. More features, more tools, more crystbox. *Journal of Applied Crystallography*, 50(4):1226–1234, 2017.

[74] Miloslav Klinger and Aleš Jäger. Crystallographic tool box (crystbox): automated tools for transmission electron microscopists and crystallographers. *Journal of applied crystallography*, 48(6):2012–2018, 2015.

[75] Ulrich F. Kocks and Heinrich Mecking. Physics and phenomenology of strain hardening: the fcc case. *Progress in materials science*, 48(3):171–273, 2003.

[76] Liron Korkidi, Kobi Barkan, and Ron Lifshitz. Analysis of dislocations in quasicrystals composed of self-assembled nanoparticles. In *Aperiodic Crystals*, pages 117–124. Springer, 2013.

[77] Uwe Köster, Wei Liu, H. Liebertz, and M. Michel. Mechanical properties of quasicrystalline and crystalline phases in $A1 - Cu - Fe$ alloys. *Journal of Non-Crystalline Solids*, 153-154:446–452, 1993.

[78] R Allen LaCour, Carl Simon Adorf, Julia Dshemuchadse, and Sharon C. Glotzer. Influence of softness on the stability of binary colloidal crystals. *ACS nano*, 13(12):13829–13842, 2019.

[79] Peter Mahler Larsen, Søren Schmidt, and Jakob Schiøtz. Robust structural identification via polyhedral template matching. *Modelling and Simulation in Materials Science and Engineering*, 24(5):055007, 2016.

[80] Sangmin Lee and Sharon C. Glotzer. Entropically engineered formation of fivefold and icosahedral twinned clusters of colloidal shapes. *Nature Communications*, 13(1):7362, 2022.

[81] Sangmin Lee, Erin G Teich, Michael Engel, and Sharon C. Glotzer. Entropic colloidal crystallization pathways via fluid–fluid transitions and multidimensional prenucleation motifs. *Proceedings of the National Academy of Sciences*, 116(30):14843–14851, 2019.

[82] Andreas Leitherer, Angelo Ziletti, and Luca M. Ghiringhelli. Robust recognition and exploratory analysis of crystal structures via bayesian deep learning. *Nature Communications*, 12(1):6234, 2021.

[83] Dov Levine, T. C. Lubensky, Stellan Ostlund, Sriram Ramaswamy, Paul Joseph Steinhardt, and John Toner. Elasticity and dislocations in pentagonal and icosahedral quasicrystals. *Physical Review Letters*, 54(14):1520–1523, Aug 1985.

[84] Dov Levine and Paul J. Steinhardt. Quasicrystals: a new class of ordered structures. *Physical review letters*, 53(26):2477, 1984.

[85] Dov Levine and Paul J Steinhardt. Quasicrystals. I. Definition and structure. *Physical Review B*, 34(2):596, 1986.

[86] Lili Liu, Miaoqing Qing, Yibo Wang, and Shimou Chen. Defects in graphene: generation, healing, and their effects on the properties of graphene: a review. *Journal of Materials Science & Technology*, 31(6):599–606, 2015.

[87] David G Lowe. Distinctive image features from scale-invariant keypoints. *International journal of computer vision*, 60:91–110, 2004.

[88] T. C. Lubensky, Joshua E. S. Socolar, Paul J. Steinhardt, Peter A. Bancel, and Paul A. Heiney. Distortion and peak broadening in quasicrystal diffraction patterns. *Physical review letters*, 57(12):1440, 1986.

[89] S. Martin, Arthur F. Hebard, A. R. Kortan, and F. A. Thiel. Transport properties of Al_{65} Cu_{15} Co_{20} and Al_{70} Ni_{15} Co_{15} decagonal quasicrystals. *Physical review letters*, 67(6):719, 1991.

[90] Arnaud Mayence, Dong Wang, German Salazar-Alvarez, Peter Oleynikov, and Lennart Bergström. Probing planar defects in nanoparticle superlattices by 3d small-angle electron diffraction tomography and real space imaging. *Nanoscale*, 6(22):13803–13808, 2014.

[91] Aaron Michelson, Brian Minevich, Hamed Emamy, Xiaojing Huang, Yong S. Chu, Hanfei Yan, and Oleg Gang. Three-dimensional visualization of nanoparticle lattices and multimaterial frameworks. *Science*, 376(6589):203–207, 2022.

[92] Walter Mickel, Sebastian C. Kapfer, Gerd E. Schröder-Turk, and Klaus Mecke. Shortcomings of the bond orientational order parameters for the analysis of disordered particulate matter. *The Journal of chemical physics*, 138(4), 2013.

[93] Dorel Moldovan, Dieter Wolf, and Dieter R. Phillpot. Theory of diffusion-accommodated grain rotation in columnar polycrystalline microstructures. *Acta Materialia*, 49(17):3521–3532, 2001.

[94] William W. Mullins. Theory of thermal grooving. *Journal of Applied Physics*, 28(3):333–339, 1957.

[95] Keisuke Nagao, Tomoaki Inuzuka, Kazue Nishimoto, and Keiichi Edagawa. Experimental observation of quasicrystal growth. *Physical review letters*, 115(7):075501, 2015.

[96] Joachim Neubüser, Hans Wondratschek, and Rolf Bülow. On crystallography in higher dimensions. i. general definitions. *Acta Crystallographica Section A: Crystal Physics, Diffraction, Theoretical and General Crystallography*, 27(6):517–520, 1971.

[97] International Union of Crystallography. Report of the executive committee for 1991. *Acta Crystallogr., Sect. A: Found. Crystallogr.*, 48(6):922–946, 1992.

[98] International Union of Crystallography. https://dictionary.iucr.org/Crystal, Mar 2021.

[99] Jeong Young Park, D. Frank Ogletree, Miquel Salmeron, Raquel A. Ribeiro, Paul C. Canfield, Cynthia J. Jenks, and Patricia A. Thiel. High frictional anisotropy of periodic and aperiodic directions on a quasicrystal surface. *Science*, 309(5739):1354–1356, 2005.

[100] Fabian Pedregosa, Gaël Varoquaux, Alexandre Gramfort, Vincent Michel, Bertrand Thirion, Olivier Grisel, Mathieu Blondel, Peter Prettenhofer, Ron Weiss, Vincent Dubourg, et al. Scikit-learn: Machine learning in python. *J. Mach. Learn. Res.*, 12:2825–2830, 2011.

[101] Ch. Pequet, Michel Rappaz, and M. Gremaud. Modeling of microporosity, macroporosity, and pipe-shrinkage formation during the solidification of alloys using a mushy-zone refinement method: applications to aluminum alloys. *Metallurgical and Materials Transactions A*, 33:2095–2106, 2002.

[102] Vyas Ramasubramani, Bradley D. Dice, Eric S. Harper, Matthew P. Spellings, Joshua A. Anderson, and Sharon C. Glotzer. freud: A software suite for high throughput analysis of particle simulation data. *Computer Physics Communications*, 254:107275, 2020.

[103] W. T. Read and William Shockley. Dislocation models of crystal grain boundaries. *Physical review*, 78(3):275, 1950.

[104] Wesley F. Reinhart. Unsupervised learning of atomic environments from simple features. *Computational Materials Science*, 196:110511, 2021.

[105] Jean-Luc Rouviere and E Sarigiannidou. Theoretical discussions on the geometrical phase analysis. *Ultramicroscopy*, 106(1):1–17, 2005.

[106] David J. Rowenhorst and Peter W. Voorhees. Measurements of the grain boundary energy and anisotropy in tin. *Metallurgical and Materials Transactions A*, 36(8):2127–2135, 2005.

[107] Ali Sadeghi, S Alireza Ghasemi, Bastian Schaefer, Stephan Mohr, Markus A Lill, and Stefan Goedecker. Metrics for measuring distances in configuration spaces. *The Journal of chemical physics*, 139(18), 2013.

[108] Agnes M Samuel, Ehab Samuel, Victor Songmene, and Fawzy H Samuel. A review on porosity formation in aluminum-based alloys. *Materials*, 16(5):2047, 2023.

[109] Benjamin H Savitzky, Ismail El Baggari, Alemayehu S. Admasu, Jaewook Kim, Sang-Wook Cheong, Robert Hovden, and Lena F Kourkoutis. Bending and breaking of stripes in a charge ordered manganite. *Nature communications*, 8(1):1883, 2017.

[110] Michael Schmiedeberg, Cristian V. Achim, Johannes Hielscher, Sebastian C. Kapfer, and Hartmut Löwen. Dislocation-free growth of quasicrystals from two seeds due to additional phasonic degrees of freedom. *Physical Review E*, 96(1):012602, 2017.

[111] Edmund G. Seebauer and Kyong Wook Noh. Trends in semiconductor defect engineering at the nanoscale. *Materials Science and Engineering: R: Reports*, 70(3-6):151–168, 2010.

[112] Roland Séguéla. On the natural draw ratio of semi-crystalline polymers: review of the mechanical, physical and molecular aspects. *Macromolecular Materials and Engineering*, 292(3):235–244, 2007.

[113] Marjorie Senechal. Structures beyond superspace. *Acta Crystallographica Section B: Structural Science, Crystal Engineering and Materials*, 71(3):250–251, 2015.

[114] Ashwin J. Shahani, E. Begum Gulsoy, Stefan O. Poulsen, Xianghui Xiao, and Peter W. Voorhees. Twin-mediated crystal growth: an enigma resolved. *Scientific reports*, 6(1):1–11, 2016.

[115] Ashwin J. Shahani, Xianghui Xiao, Erik M. Lauridsen, and Peter W. Voorhees. Characterization of metals in four dimensions. *Materials Research Letters*, 8(12):462–476, 2020.

[116] Dan Shechtman, Ilan Blech, Denis Gratias, and John W. Cahn. Metallic phase with long-range orientational order and no translational symmetry. *Physical review letters*, 53(20):1951, 1984.

[117] Tadaharu Shibuya, Tatsuo Hashimoto, and Shin Takeuchi. Anisotropic conductivity in a decagonal quasicrystal of al70ni15co15. *Journal of the Physical Society of Japan*, 59(6):1917–1920, 1990.

[118] Ana Smontara, I Smiljanić, Jovica Ivkov, D Stanić, Osor S Barišić, Z Jagličić, Peter Gille, M Komelj, P Jeglič, M Bobnar, et al. Anisotropic magnetic, electrical, and thermal transport properties of the y-al-ni-co decagonal approximant. *Physical Review B*, 78(10):104204, 2008.

[119] Joshua E. S. Socolar, T. C. Lubensky, and Paul J. Steinhardt. Phonons, phasons, and dislocations in quasicrystals. *Physical Review B*, 34(5):3345, 1986.

[120] Matthew Spellings and Sharon C Glotzer. Machine learning for crystal identification and discovery. *AIChE Journal*, 64(6):2198–2206, 2018.

[121] Paul Steinhardt. *The second kind of impossible: the extraordinary quest for a new form of matter*. Simon and Schuster, 2019.

[122] Paul J. Steinhardt and Hyeong-Chai Jeong. A simpler approach to penrose tiling with implications for quasicrystal formation. *Nature*, 382(6590):431–433, 1996.

[123] Paul J. Steinhardt, David R. Nelson, and Marco Ronchetti. Bond-orientational order in liquids and glasses. *Physical Review B*, 28(2):784, 1983.

[124] Peter W Stephens and Alan I Goldman. Sharp diffraction maxima from an icosahedral glass. *Physical review letters*, 56(11):1168, 1986.

[125] Walter Steurer. Quasicrystals - a paradigm shift in crystallography? *Chimia*, 68:45–8, 02 2014.

[126] Walter Steurer and Sofia Deloudi. *Crystallography of quasicrystals: concepts, methods and structures*. Springer, 2009.

[127] K. J. Strandburg, J. A. Zollweg, and G. V. Chester. Bond-angular order in two-dimensional lennard-jones and hard-disk systems. *Physical Review B*, 30(5):2755–2759, 1984.

[128] Katherine J. Strandburg. Random-tiling quasicrystal. *Physical Review B*, 40(9):6071, 1989.

[129] Katherine J. Strandburg, Leihan Tang, and Marko V. Jaric. Phason elasticity in entropic qnasicrystals. *Physical Review Letters*, 63(3):1943–1946, 1989.

[130] Alexander Stukowski. Visualization and analysis of atomistic simulation data with ovito–the open visualization tool. *Modelling and simulation in materials science and engineering*, 18(1):015012, 2009.

[131] Alexander Stukowski and Karsten Albe. Extracting dislocations and non-dislocation crystal defects from atomistic simulation data. *Modelling and Simulation in Materials Science and Engineering*, 18(8):085001, 2010.

[132] Alexander Stukowski, Vasily V Bulatov, and Athanasios Arsenlis. Automated identification and indexing of dislocations in crystal interfaces. *Modelling and Simulation in Materials Science and Engineering*, 20(8):085007, 2012.

[133] Shin Takeuchi. Bulk mechanical properties of quasicrystals. *MRS Online Proceedings Library (OPL)*, 553:283, 1998.

[134] John Towns, Timothy Cockerill, Maytal Dahan, Ian Foster, Kelly Gaither, Andrew Grimshaw, Victor Hazlewood, Scott Lathrop, Dave Lifka, Gregory D Peterson, et al. Xsede: accelerating scientific discovery. *Computing in science & engineering*, 16(5):62–74, 2014.

[135] Zachary T. Trautt and Yuri Mishin. Grain boundary migration and grain rotation studied by molecular dynamics. *Acta Materialia*, 60(5):2407–2424, 2012.

[136] Hans-Rainer Trebin, Ralf Mikulla, and Johannes Roth. Motion of dislocations in two-dimensional decagonal quasicrystals. *Journal of non-crystalline solids*, 153:272–275, 1993.

[137] M. Upmanyu, David J. Srolovitz, E. Lobkovsky, A, James A. Warren, and W. C. Carter. Simultaneous grain boundary migration and grain rotation. *Acta Materialia*, 54(7):1707–1719, 2006.

[138] Sander van Smaalen. Aperiodic crystals and their atomic structures in superspace: an introduction. *Rendiconti Lincei. Scienze Fisiche e Naturali*, pages 1–8, 2023.

[139] Pauli Virtanen, Ralf Gommers, Travis E. Oliphant, Matt Haberland, Tyler Reddy, David Cournapeau, Evgeni Burovski, Pearu Peterson, Warren Weckesser, Jonathan Bright, Stéfan J. van der Walt, Matthew Brett, Joshua Wilson, K. Jarrod Millman, Nikolay Mayorov, Andrew R. J. Nelson, Eric Jones, Robert Kern, Eric Larson, C J Carey, İlhan Polat, Yu Feng, Eric W. Moore, Jake VanderPlas, Denis Laxalde, Josef Perktold, Robert Cimrman, Ian Henriksen, E. A. Quintero, Charles R. Harris, Anne M. Archibald, Antônio H. Ribeiro,

Fabian Pedregosa, Paul van Mulbregt, and SciPy 1.0 Contributors. SciPy 1.0: Fundamental Algorithms for Scientific Computing in Python. *Nature Methods*, 17:261–272, 2020.

[140] Lihua Wang, Jiao Teng, Pan Liu, Akihiko Hirata, En Ma, Ze Zhang, Mingwei Chen, and Xiaodong Han. Grain rotation mediated by grain boundary dislocations in nanocrystalline platinum. *Nature communications*, 5(1):4402, 2014.

[141] Yao Wang and Gabriele Cacciamani. Experimental investigation and thermodynamic assessment of the Al-Co-Ni system. *Calphad*, 61:198–210, 2018.

[142] R. Wittmann, Knut Urban, M. Schandl, and Erhard Hornbogen. Mechanical properties of single-quasicrystalline $AlCuCoSi$. *Journal of Materials Research*, 6:1165–1168, 1991.

[143] Alexa M. Wong, Kwanghwi Je, Cindy Y. Zheng, Liban Jibril, Ziyi Miao, Sharon C. Glotzer, and Chad A. Mirkin. Arrays of colloidal single crystals engineered with dna in lithographically defined microwells. *Nano letters*, 23(1):116–123, 2022.

[144] Yu Wu, Weiqing Xu, Lei Jiao, Yinjun Tang, Yifeng Chen, Wenling Gu, and Chengzhou Zhu. Defect engineering in nanozymes. *Materials Today*, 52:327–347, 2022.

[145] Shengsong Yang, R. Allen LaCour, Yi-Yu Cai, Jun Xu, Daniel J. Rosen, Yugang Zhang, Cherie R. Kagan, Sharon C. Glotzer, and Christopher B. Murray. Self-assembly of atomically aligned nanoparticle superlattices from pt–fe3o4 heterodimer nanoparticles. *Journal of the American Chemical Society*, 145(11):6280–6288, 2023.

[146] Yongsoo Yang, Chien-Chun Chen, MC Scott, Colin Ophus, Rui Xu, Alan Pryor, Li Wu, Fan Sun, Wolfgang Theis, Jihan Zhou, et al. Deciphering chemical order/disorder and material properties at the single-atom level. *Nature*, 542(7639):75–79, 2017.

[147] Wang Yun-ping, Zhang Dian-lin, and L. F. Chen. Universality of the hall-effect anisotropy in decagonal quasicrystals. *Phys. Rev. B*, 48:10542–10545, Oct 1993.

[148] Zephyris. Colloid crystal 40x brightfield glass in water. https://commons.wikimedia.org/wiki/File:ColloidCrystal_40xBrightField_GlassInWater.jpg, Jul 2010.

[149] Yun Zheng, Tyler J. Slade, Lei Hu, Xian Yi Tan, Yubo Luo, Zhong-Zhen Luo, Jianwei Xu, Qingyu Yan, and Mercouri G Kanatzidis. Defect engineering in thermoelectric materials: what have we learned? *Chemical Society Reviews*, 50(16):9022–9054, 2021.

[150] Wenjie Zhou, Yein Lim, Haixin Lin, Sangmin Lee, Yuanwei Li, Ziyin Huang, Jingshan S. Du, Byeongdu Lee, Shunzhi Wang, Ana Sánchez-Iglesias, et al. Colloidal quasicrystals engineered with dna. *Nature materials*, pages 1–5, 2023.